FINAL REPORT

FOR

DELIVERY ORDER 41/NAS8-36955

PROCESS MODELLING FOR SPACE STATION EXPERIMENTS

Center for Microgravity and Materials Research
The University of Alabama in Huntsville

FINAL REPORT

FOR

DELIVERY ORDER 41/NAS8-36955

PROCESS MODELLING FOR SPACE STATION EXPERIMENTS

J. IWAN D. ALEXANDER AND FRANZ ROSENBERGER

PRINCIPAL INVESTIGATORS

AND

ARUNAN NADARAJAH

JALIL OUAZZANI

SAKIR AMIROUDINE

CO-INVESTIGATORS

CENTER FOR MICROGRAVITY AND MATERIALS RESEARCH

THE UNIVERSITY OF ALABAMA IN HUNTSVILLE

TABLE OF CONTENTS

SECTION PAGE

1. GENERAL

The work completed under the Delivery order contract DO-41 comprised the final part of a three year study of the sensitivity of low gravity experiments to residual acceleration experienced aboard a spacecraft in low earth orbit. The sensitivity analyses were carried out using "generic models" which were representative of the types of experiment that would take place on Space Station. This report summarizes all the work carried out over the period 7/5/89-10/4/90 .

The following papers have been published, accepted for publication or are in preparation for submission for publication:

1. A. Nadarajah, F. Rosenberger and J.I.D. Alexander, Modelling the solution growth of triglycine sulfate in low gravity, J. Crystal Growth 104 (1990) 218-232.
2. J. I. D. Alexander and F. Rosenberger, Bridgman crystal growth in low gravity: A scaling analysis, to appear in Low Gravity Fluid Dynamics and Transport Phenomena, J. Koster and R. Sani (eds.) AIAA, (1990).
3. J.I. D. Alexander and J. Ouazzani, A Pseudospectral Collocation Method Applied to the Problem of Convective-Diffusive Transport in Fluids Subject to Residual Acceleration, Proc. 6th International Conference on Numerical Methods in Laminar and Turbulent Flow, C. Taylor, P. Gresho, R. L. Sani and J. Haüser (eds.) Pineridge, Swansea (1989) 1035.
4. J. I. D. Alexander, Low-Gravity Experiment Sensitivity to Residual Acceleration: A Review, Microgravity Science and Technology 3, (1990) 52-68.
5. F. Rosenberger, J.I.D. Alexander, A. Nadarajah and J. Ouazzani, Influence of Residual Gravity on Crystal Growth Processes, to appear Microgravity Science and Technology (1990).
6. J.I.D. Alexander, S. Amiroudine, J. Ouazzani and F.Rosenberger F.: Analysis of the Low Gravity Tolerance of the Bridgman-Stockbarger Technique. II: Transient and Periodic Accelerations, to be submitted to the J. Crystal Growth (1990).
7. A. Nadarajah, F. Rosenberger and J.I.D. Alexander, Modelling Crystal Growth by Physical Vapor Transport in Closed Ampoules, to be submitted to the J. Crystal Growth (1990).

In addition to the above publications, the results of our work have been presented at the following conferences

1. "Commercial Numerical Codes: To Use or Not to Use, Is This The Question?" presented by J.I.D Alexander at the Microgravity Fluids Workshop, Westlake Holiday Inn, Cleveland Ohio, August 7-9, 1990.
2. "Sensitivity of Crystal Growth Experiments to Residual Accelerations, presented by J.I.D. Alexander, the Gordon Conference on Gravitational Effects in Materials and Processes", July 30 -

August 4, 1989, Plymouth State College, Plymouth, New Hampshire.

3. "Low Gravity Accelerations: Influence on Dopant Redistribution During Directional Solidification", presented by J.I.D. Alexander at the Third International Symposium on Experimental Methods for Microgravity Materials Science Research, COSPAR XXVIII Plenary Meeting, June 25-July 6, 1990.

4. "Modelling the Solution Growth of TGS Crystals in Low Gravity", presented by J.I.D Alexander, at the Third International Symposium on Experimental Methods for Microgravity Materials Science Research, COSPAR XXVIII Plenary Meeting, June 25-July 6, 1990.

5. "Modelling the Solution Growth of TGS Crystals in Low Gravity", presented by A. Nadarajah at the Eighth American Conference on Crystal Growth, Vail, Colorado July (1990).

6. "Influence of Residual Gravity on Crystal Growth Processes," presented By F. Rosenberger at the First International Microgravity Congress, Bremen September (1990).

The results of the work carried out under DO-41 are presented in the following sections. The work has mostly been concerned with the effects of time-dependent accelerations during directional solidification by the Bridgman technique, steady acceleration during crystal growth by physical vapor transport (PVT) and the completion of a study of steady and time-dependent acceleration effects during TGS solution growth. In **section 2** we review work related to the analysis of the sensitivity of residual acceleration. In **section 3** we present the latest results for the analysis of the sensitivity of the Bridgman technique to time-dependent residual acceleration. The results include the effect of oscillatory accelerations as well as acceleration time-series synthesized from measured disturbances on spacelab-3. In **section 4** we present the results of our analysis of the process of crystal growth by Physical Vapor Transport. The results of the study of the TGS solution growth system are given in the appendix (**section 5.2**)

2. EXPERIMENT SENSITIVITY TO RESIDUAL ACCELERATION: A REVIEW

2.1. Introduction

It has been recognized for some time that the low-gravity acceleration environment associated with a spacecraft in low earth orbit offers an opportunity to study certain physical processes which are difficult to investigate under the gravitational acceleration experienced at the earth's surface. Our experience with such opportunities has led us to realize that the residual acceleration environment on board an orbiting spacecraft is not as low or as steady as would be desired for certain classes of experiments . The sources of the residual acceleration include [1-5] crew motions, mechanical vibrations (pumps, motors, excitations of natural frequencies of spacecraft structures), spacecraft maneuvers and basic attitude motion, atmospheric drag and the earth's gravity gradient. The accelerations are characterized by temporal variations in both magnitude and orientation. Such disturbances will, in particular, affect those experiments susceptible to buoyancy induced fluid motion [6]. Indeed, recent studies [7,9] indicate that transient disturbances can have undesirable long term effects. The analysis of the sensitivity of any proposed flight experiment is

necessary for a variety of reasons. These include the need to optimize the use of the limited time available for flight experiments, the interpretation of experimental results and the determination of tolerable acceleration levels to be used in planning for NASA's Space Station [3].

Examples of experiments that are conducted in the low-gravity environment include critical point studies [10], crystal growth [11-18], and diffusion experiments [19,20]. Since these experiments involve density gradients in the fluid phase, they are inherently sensitive to the effects of buoyancy-driven fluid motion [21-25]. For certain types of systems it is known [7,8,26-37] that the associated physical processes (mass transfer, heat transfer, convection, oscillation and distortion of free surfaces) are sensitive to time-dependent accelerations. For example, the transfer of mass and heat in fluid systems can be significantly affected by oscillatory flows [28-37]. The effect of oscillation enhanced transport conditions on the local variation in composition during crystal growth is not well characterized for most of the systems relevant to crystal growth under microgravity conditions. Order of magnitude analyses [7,8,38] suggest that for certain combinations of physical properties and growth conditions, oscillations in the residual acceleration may adversely affect the mass transport conditions. For instance, the DMOS experiment [39] on STS 51-D showed extensive evidence of convective mixing of liquids. The degree of mixing is greater than can be attributed to the quasi-steady low-gravity component, but can be accounted for when oscillations in effective gravity are included in the description of the transport conditions.

It is possible that in future space laboratories some experiments will require isolation from vibration. The design of efficient isolation systems, however, requires determination of the tolerable acceleration levels (amplitudes and frequencies) for given experiments. The results of sensitivity analyses can be used in the development of vibration isolation systems to identify those experiments that will need isolation and by supplying data concerning frequency dependence, the effect of transients etc.. The system can then be designed to filter out those bandwidths to which the experiment is predicted to respond adversely.

Low-gravity experiments which involve liquids with free surfaces are most likely to be sensitive to vibrations. Experiments of this type include studies of liquid bridges, equilibrium shapes of drops and bubbles [40-43] and thermocapillary flow experiments [43-46]. Evidence for the oscillation of liquid zone shapes was found on the D-1 mission. Long liquid bridges were more sensitive to residual gravity, and exhibited random oscillations in zone shape [40].

It should be recognized that the sensitivity of a given process to the overall low-gravity environment will depend on one or more of the following factors:

a) magnitude and direction of accelerations

b) system geometry

c) boundary conditions (eg. insulated or conducting walls, solute sources and sinks), and

d) physical properties of the participating materials (viscosity, thermal and solute diffusivities).

Any analysis of the sensitivity to oscillatory accelerations and transient disturbances characteristic

of the anticipated environment aboard Space Station, or any other spacecraft, must take these factors into account. In general, a full mathematical characterization may not be practical. However, identification of sensitive experiments in combination with a judicious choice of simplified numerical models can be used to choose operating parameters that will optimize the use of the low-gravity environment. With this in mind, we review work related to the effects of steady and time-dependent residual accelerations, and associated work concerning transport in oscillating flows.

In section 2 we describe the components of the low-gravity environment. In section 3 previous work involving order of magnitude (OM) estimates is discussed. The application of OM analyses to acceleration-sensitivity determination is discussed in 3.1. The results of simple analytical models are summarized in section 3.2. Work related to linear stability in the presence of modulated gravity is briefly discussed in section 3.3. The results of direct numerical simulations are reviewed in section 3.4. In section 4., the results and utility of residual acceleration analyses are summarized and discussed.

2.2. The microgravity environment

The low-gravity environment of a spacecraft has been referred to as a "zero gravity" environment. This is because any object within the craft is subject to roughly the same acceleration due to the earth's gravitational field. Thus, a free object may move along approximately the same orbital path as the spacecraft. As a consequence, to an observer in the space craft objects appear to behave as if no gravity were present. However, any body capable of motion relative to the spacecraft will experience an acceleration relative to the mass center of the spacecraft. This relative acceleration arises from several sources which include the gravity gradient of the earth, atmospheric drag and attitude motions, as well as machinery vibrations and crew activities.

The relative acceleration that is associated with the earth's gravity gradient is defined as follows. The mass center of the spacecraft is subject to a force $\mathbf{F}(\mathbf{r}_o)$ due to the gravitational attraction of the earth, where $\mathbf{r}_o$ is the position of the mass center of the craft with respect to the mass center of the earth. A particle at a position $\mathbf{r}$ within the spacecraft is subject to a force $\mathbf{F}(\mathbf{r})$. If, as a first approximation, we ignore the interaction between the spacecraft and the mass of the particle, and if the distance $|\mathbf{r} - \mathbf{r}_o|$ is small compared to the semi-major axis of the spacecraft orbit, the difference between the forces applied at $\mathbf{r}$ and $\mathbf{r}_o$ define the gravity gradient $\mathbf{G}$ as follows [2-6]

$$\mathbf{F}(\mathbf{r}) - \mathbf{F}(\mathbf{r}_o) = \mathbf{G}\mathbf{z}, \quad \mathbf{z} = \mathbf{r} - \mathbf{r}_o . \tag{1}$$

If the spacecraft maintains a fixed orientation, for example with respect to the sun, there is no rotation of the spacecraft frame relative to the geocentric frame. In this type of orbit both the magnitude and the orientation of the residual acceleration vector change as a function of time and there will be no steady residual acceleration.

In addition to the gravity gradient acceleration the atmospheric drag force on the spacecraft can be significant [2-6], despite the fact that the atmospheric density at typical shuttle altitudes is only on the order of 10^{-12} kg m^{-3}. Atmospheric drag causes a slow inward spiral of the spacecraft.

To an observer in the spacecraft the effect of atmospheric drag is to produce a relative acceleration that is equal in magnitude but opposite in sign to the atmospheric drag force. Table 1 gives atmospheric drag acceleration estimates and relative acceleration related to the gravity gradient and centrifugal force in μg per meter from the mass center of a spaceraft that is in a circular orbit with a gravity gradient stabilized attitude. X_1 is parallel to the local vertical and X_2 is perpendicular to the orbital plane. For this attitude the acceleration points away from the mass center along X_1 and toward the mass center along X_2.

If the spacecraft does not maintain such a fixed orientation then, in addition to (1), centrifugal, Coriolis and Euler accelerations will become apparent in the spacecraft reference frame. They arise in conjuction with spacecraft attitude motions and depend on the nature of the rotation of the spacecraft frame of reference relative to a fixed geocentric frame. If a spacecraft in a quasi-circular orbit continuously rotates relative to the fixed geocentric frame such that a given direction in the spacecraft frame is always oriented parallel to the craft's position vector $\mathbf{r}_o$, a centrifugal acceleration will augment the gravity gradient in the direction parallel to the position vector, and cancel the component tangent to the flight path. Under these conditions there will be a steady component to the residual acceleration vector. In practice this situation arises, for example, in the so-called gravity gradient stabilized attitude.

Euler accelerations arise when the rate of rotation of the spacecraft frame changes as a function of time, as it would in a non-circular orbit, or as the semi-major axis of the orbit changes as the craft slowly spirals inward due to atmospheric drag. Coriolis accelerations will also be apparent but are proportional to the velocity of an object relative to the spacecraft. Thus, unless relative velocities are large, the Coriolis effect will be insignificant [6].

In addition to the above, there are a variety of residual acceleration components that occur over a broad range of amplitudes and frequencies. The nature and sources of these accelerations have been discussed in [1-3]. Figures 1 and 2 are examples of residual accelerations measured on orbit.

2.3. Analyses of residual acceleration effects

As discussed in the introduction, many experiments are undertaken in orbiting spacecraft in order to reduce or eliminate unwanted effects of buoyancy driven motions in fluids. Sources of buoyancy in fluids include discrete interfaces, as they occur, for example between immiscible fluids, solid particles and fluids, and bubbles and fluids with different densities, other buoyancy sources are internal density gradients that arise as a consequence of gradients in temperature and concentration. The nature of the response of a bulk fluid to the effective body force associated with a low-gravity environment will depend, in part, on the relative orientation of the residual acceleration vector and the density gradient. In particular, if the integral of the effective body force $\rho\mathbf{b}$ (where ρ is the density and $\mathbf{b}$ the effective acceleration) acting on any closed circuit within the fluid is non-zero, motion will immediately ensue. That is, if

$$\int_C d\mathbf{c}\cdot\rho\mathbf{b} = \int_S d\mathbf{A}\cdot\text{curl}\ \rho\mathbf{b} = \int_S d\mathbf{A}\cdot[\text{grad}\ \rho\wedge\mathbf{b} + \rho\ \text{curl}\ \mathbf{b}] \neq 0, \qquad (2)$$

motion will occur. Note also, that even if there is no density gradient motion will occur if

$$\int_S d\mathbf{A}\cdot\text{curl}\ \rho\mathbf{b} \neq 0. \qquad (3)$$

This includes the case of "precessional stirring" [48]. This could occur, for example, when a spacecraft orbiting in a radial attitude (i.e. it continuously rotates about an axis perpendicular to the orbital plane) underwent an additional rotation about some axis other than the basic orbital axis.

There have been three appraoches to the determination of experiment sensitivity to the residual acceleration environment.

a) order of magnitude analyses [38,49-52],
b) analytical models [5,6,39,53-59], and
c) direct numerical simulation [9,3,60-73].

In addition to work directly related to microgravity, there is extensive literature on mass and heat transport in oscillatory flows [26-36], the effect of gravity modulation on the classical Bénard problem [74-77] and the linear stability of planar fluid surfaces [78,79].

2.3.1. Order of magnitude analyses

An order of magnitude (OM) or dimensional analysis of a physical process involves the examination of the system of equations that are assumed to govern the process. For fluid physics and material science experiments, the relevant physical processes are governed by equations describing the transport of heat, mass and momentum in single and multi-component fluid systems. The usual approach to OM analyses [51] involves the definition of reference quantities which appropriately characterize the physical system (i.e. reference scales for velocity, time, length, forces, etc.). Application of these scales to the (dimensional) governing equations, followed by the definition of characteristic dimensionless groups admits a comparison of the order of magnitude of every term in each equation. There are several comprehensive discussions of OM analyses applied to low-gravity situations (eg. [38,49-51]).

The advantage of the OM approach is that a great deal of information pertaining to the sensitivity of a given experiment can be obtained with little computational effort. The disadvantages are related to the fact that the choice of characteristic reference quantities for length, velocity, time etc. are not, in general, known *a priori* [80]. Thus, in cases for which the chosen characteristic scale is not (for a given set of conditions) representative of the actual process, the results of the analysis may be in error, often by several orders of magnitude. In addition,

application of OM analyses to the problem of g-sensitivity has invariably involved implicit linearization and often poorly represents the multi-dimenional nature of the physical process. This can also lead to incorrect OM predictions. Finally, analyses are generally restricted to the examination of a single component disturbance (e.g. ~ sin(ωt)). As a result, they may not properly indicate the response of the system to the typically complex multi-frequency disturbances characteristic of the spacecraft environment. It is nonetheless useful to examine the general trends predicted by such analyses since they can provide at least qualitative guidance for more detailed analytical and numerical studies.

The determination of tolerable g-levels using OM analyses is based upon estimations of the response of a system to either steady accelerations or time-dependent disturbances of the form

$$\mathbf{g}(t) = \mathbf{a}\cos(\omega t), \tag{4}$$

where ω is the angular frequency of the disturbance. The susceptibility of an experimental system to such disturbances is defined via the magnitude of a particular response (say a temperature, compositional or velocity fluctuation) which must not be exceeded in order to bring the experiment to a successful conclusion. The most obvious trend predicted by analyses to date is shown in Figs. 3 - 5. The curves depict the maximum tolerable residual acceleration magnitude as a function of frequency, $f = \omega/2\pi$, for given experiments and have the form

$$g_{max} = F(\omega, \Pi_{crit}, p_i), \tag{5}$$

where Π_{crit} is the magnitude of the maximum allowable response, and the p_i, i=1,N represent the N material properties of the system (such as viscosity, thermal and species diffusivities). In general, below 10^{-2} to 10^{-3} Hz the response is expected to be either independent or weakly dependent on frequency. At higher frequencies the analyses indicate that the allowable residual acceleration magnitude increases as approximately the square of the frequency. This behavior can be understood upon consideration of the following OM estimates [38] (used to obtain Fig. 3) for velocity, temperature and concentration changes associated with the acceleration (4):

$$V_g \sim \frac{g^*\Delta\rho/\rho}{(\omega^2 + \nu^2/L^4)^{1/2}} \tag{6}$$

$$\delta T \sim V_g \frac{\Delta T/L}{(\omega^2 + \kappa^2/L^4)^{1/2}}, \tag{7}$$

$$\delta C \sim V_g \frac{\Delta C/L}{(\omega^2 + D^2/L^4)^{1/2}}, \tag{8}$$

where g^* is the residual acceleration magnitude, ρ is the mass density, and $\Delta\rho/\rho$ is the relative change in density due to temperature and/or composition; $\Delta T/L$, $\Delta C/L$ and L are, respectively, a characteristic temperature gradient, concentration gradient and length; κ is the thermal diffusivity. The sensitivity limits are obtained by using either δT, δC or V_g as a sensitivity parameter and setting g^* equal to the allowable residual acceleration g_{max}.

For situations which involve mixed thermocapillary convection and buoyancy-driven convection the governing dimensionless groups are [51]: the Bond number, $B_o = \rho g^* L^2/\gamma$, the Grashof number $Gr = \Delta T\,|\beta_T|\, g^* L^3/\nu^2$, the Prandtl number $Pr = \nu/\kappa$, and the Surface Reynolds number $Rs = |\gamma_T|\Delta T L/\mu\nu$. Here $|\gamma_T|$ is the rate of change of surface tension γ with temperature, β_T is the coefficient of thermal expansion, ν is the kinematic viscosity, μ is the shear viscosity These groups respectively represent the ratios of buoyancy force to surface force, buoyancy force to inertial force, thermal and momentum timescales, and surface force to inertial force.

The relative importance of gravity and thermocapillary forces can then be estimated upon considering the relative magnitudes of the velocity due to buoyancy and the velocity due to thermocapillary effects [50,51]. The latter is given by

$$V^* = \frac{|\gamma_T|\Delta T}{\mu}. \tag{9}$$

For thermocapillary flow to dominate, the ratio of V_g to V^* must be less than one. For this to occur, the maximum magnitude of the acceleration must satisfy:

$$g^* < |\gamma_T| \frac{(\omega^2 + \nu^2/L^4)^{1/2}}{\nu\beta_T}. \tag{10}$$

Equation (10) can be re-interpreted in terms of the ratio of the Grashof number, Gr, and the surface Reynolds number Rs. The condition for buoyancy and thermocapillary forces to be the same magnitude is

$$Gr = Rs(St^2 + 1)^{1/2}, \tag{11}$$

where $St = \omega L^2/\nu$ is the Strouhal number. This condition is illustrated in Fig. 6. Three regimes of interest are identified. These regions are defined by the relative values of the Grashof, Strouhal and surface Reynolds numbers. In region I, the Strouhal number St is less than one, and the condition that thermocapillary forces dominate is equivalent to that for a steady flow. In region II, St is greater than one. In this region, for a fixed value of Rs, the value of Gr required to give buoyancy forces equal weight to thermocapillary forces increases with increasing values of the Strouhal number. This essentially reflects the fact that the characteristic time for the fluid response greatly exceeds the period of the disturbance. Thus, thermocapillary forces dominate at higher values than

in region I. In region III buoyancy forces predominate over thermocapillary forces. For situations here a boundary layer scaling is appropriate i.e Rs >> 1 [50]. The relative importance of buoyancy can be estimated via the ratio

$$Gr = Rs^{5/3}(St^2 + 1)^{1/2} . \qquad (12)$$

Figure 7 depicts the relationship between the estimated tolerable g-level and the frequency of the acceleration for experiments with the physical properties given in Table 2. These figures represent estimates based on two extreme flow regimes, penetrative or "viscous" flow (Fig. 7a) and boundary layer flow (Fig. 7b) and may be respectively considered as "worst" and "best" case estimates for the given sensitivity parameters. The curves have been determined for a sensitivity criterion which requires the tolerable acceleration levels to be such that the buoyancy forces should not exceed 10% of the thermocapillary forces (if the requirement had been 1%, the tolerable accelerations would be an order of magnitude smaller). In terms of acceleration levels predicted for the space station or measured on past missions the practical sensitive ranges are restricted to disturbances with frequencies less than 10 Hz. The majority of the estimates suggest that ,for these experimental parameters, periodic vibrations will generally not lead to significant buoyancy effects.

The above examples estimate the effects of simple single component accelerations. In reality, low-gravity disturbances tend to be associated with more than one frequency. Given that a system may respond to a multi-frequency disturbance in an "additive" way, tolerance curves such as these may underestimate the response to a given low-gravity disturbance. For example, models of the DMOS experiment show that mass transport has an additive response to the (multi-frequency) residual acceleration [39]. Post flight analysis of the experiment results has demonstrated that the amount of mixing observed between organic liquids can be explained by the additive response of the system to a multicomponent disturbance.

In many cases an *a priori* choice of length or time scales may not be obvious. For example, in a study of dopant (solute) uniformity in directionally solidified crystals, the OM estimates of Rouzaud et al. [52] and Camel and Favier [83] are in agreement with the direct numerical simulations of Chang and Brown [84] for a Schmidt number (ratio of the melt's kinematic viscosity to dopant diffusivity) of fifty but overestimate the amount of radial segregation for a Schmidt number of ten.

The results of an order of magnitude or scaling analysis have been compared in [80] with those of numerical simulations of the effects of steady residual acceleration on compositional nonuniformity in directionally solidified crystals. The basic model consisted of a Bridgman-type system with an ampoule translated between hot and cold zones separated by a thermal barrier. In order to apply the Camel-Favier technique [52,83] to the numerical simualtion, it was necessary to evaluate a proportionality constant, x_o^2. This relates the maximum convective velocity obtained in the numerical simulations with the Grashof number. The value of this constant depended on the orientation of the acceleration, and on the chosen length scale. The adiabatic zone length L_a yielded results which best showed the trends predicted by the Camel-Favier approach. Table 3 lists values of x_o associated with different choices of reference length. Having calculated x_o we then

determined the transport regime (see references [52,80,83] for details) by graphing, in Fig. 8, GrSc vs Pe_g for the case of the residual acceleration parallel to the interface. Here Sc (Schmidt number) gives the ratio of kinematic viscosity to thermal diffusivity, and $Pe_g = VL/D$, is a ratio of the translation rate to the characteristic diffusive speed where L is the characteristic diffusion length and D the solute diffusivity. The lateral composition non-uniformities in the crystal obtained from numerical simulations [9] are also given in Fig. 8. A comparison between computed and predicted nonuniformity values showed that at high values of GrSc (region Ic in Fig. 8), the order of magnitude approach meets with some success but is less faithful at low values of GrSc (for example the transition between regions Ib and II). Fig. 8 also contains two cases for which Pe_g is reduced at fixed GrSc. According to the estimates the lower GrSc case should have yielded a higher compositional nonuniformity as the growth rate was reduced, i.e. the estimates predict that the system moves closer to the convective diffusive transition. This was not reflected in the nonuniformity obtained from the numercial simulations. Evaluation of the numerical results showed that the increase in the characteristic diffusion length scale (associated with reduction in growth rate) led to an order of magnitude decrease in the solute gradient at the interface. Hence, because the system-wide variation in composition is small, the interfacial nonuniformity is correspondingly small.

The above results indicate that scaling arguments alone can at best be expected to yield order of magnitude accuracy. The limitations of scaling arguments are hardly surprising if one considers the neglect of the multi-dimensionality (boundary conditions, flow structure, etc.) of the physical situation which is inherent in such scalar descriptions. Of course, prior knowledge of the system behavior can be used to *locally* improve the accuracy of the scaling, (eg. Kimura and Bejan [85]). Similarly, if a system locally exhibits one-dimensional behavior, such as boundary layer flow, then the appropriate scaling for the formal reduction of the transport equations can be used effectively to estimate the local system response. In general, however, our understanding of the response of systems to residual acceleration can be furthered only by an approach which uses scaling, mathematical modelling and, naturally, the results of experiments in a complementary fashion.

2.3.2. Analytical models

A few attempts have been made to assess the effects of time-dependent residual acceleration using analytical models [53-59]. The first attempt to model the effects of disturbances on heat transfer between a fluid and a solid bounding medium was carried out by Gebhardt [53]. Under the assumption that the fluid and its container would be subject to a "sequence of abrupt relative displacements spaced by a time interval τ_c, ...", Gebhardt took τ_c to be a random distributed variable. He showed that as τ_m (the most likely value of τ_c) decreases, the resulting heat transfer was greater than predicted by conduction in the absence of a disturbance. In particular, it was found that for $\tau_m < d^2/\kappa$ (where d is a characteristic length and κ is the thermal diffusivity) the heat transfer increased rapidly as τ_m decreased. The main limitation of this model is that fluid convection (and thus fluid properties such as kinematic viscosity) does not enter the analysis. It is well known that the response of heat transfer to convection varies according to the Prandtl number. In particular, for low-gravity flows (as we shall see later) the temperature field is less sensitive to

convection for low Prandtl number fluids (Pr < 1).

Approximate solutions for transient convection in a cylinder with an azimuthal temperature variation have been obtained by Dressler [54]. Residual accelerations representing the motion of an astronaut and a transient rotation of the spacecraft were imposed on the system. Linear accelerations were imposed perpendicular to the cylinder axis. For kinematic viscosities of 10^{-2} $cm^2\ s^{-1}$, cylinders of radius 1 and 2 cm with a maximum temperature difference of 95 K across the diameter were examined. The maximum fluid velocities consequent to the astronaut motion (modelled by a sequence of two step functions separated by 2 seconds with 4×10^{-4} g magnitude, 0.5 second duration and zero mean, oriented perpendicular to the temperature gradient) were 12 $\mu m\ s^{-1}$ for both the large and small diameter cylinders (see Fig. 9). For the larger cylinder the second pulse reduced the velocity from 12 $\mu m\ s^{-1}$ to 0 by the end of the pulse. The effect of the second pulse was to change the velocity in the small container from 12 to -3 $\mu m\ s^{-1}$ by the end of the pulse. The velocity decayed asymptotically to zero reaching a value close to zero after 15 seconds. The reason the response was different for the two containers can be explained simply in terms of the momentum decay times ($t_{1/2} \sim R^2/\nu$) for each container. The velocity in the larger container had hardly begun to decay when the second impulse arrived. The shorter decay time associated with the smaller container meant that the impulse acted on a smaller magnitude velocity which explains the change in direction of the motion. While the disturbance had a mean value of zero the fluid particles attained a finite displacement (indicated by the value x of the angular displacement in Fig. 6). Similarly, a disturbance corresponding to a simple spacecraft maneuver was examined. The simulated maneuver corresponded to a 90° rotation of the spacecraft at a rate of $1°\ s^{-1}$. The maximum velocities associated with the centrifugal acceleration were, respectively, 40 and 35 $\mu m\ s^{-1}$ for the large and small diameter cylinders.

Experiments involving free surfaces of liquids have a high probability of responding to residual accelerations. Indeed, unexpected results have been attributed to residual accelerations in several cases [40,86-88]. Particular examples of such experiments involve liquid (float) zones. Three types of liquid zones are typically the subject of low-gravity experiments [89]: isothermal and non-isothermal zones suspended between inert solids (i.e. liquid bridges), and non-isothermal zones suspended between a feed rod and a growing crystal. The dimensionless group associated with the shape of isothermal static liquid zones is the Bond number, B_0, defined earlier. It expresses the relative importance of gravitational and surface forces. A comprehensive description of stable zone shapes in zero gravity, and as a function of B_0, is given by Martinez et al. [41]. Fig. 10 displays their results for the stability of static zones with a steady acceleration parallel to the zone axis. In order to relate the Bond number to a given acceleration level they give the value of $B_0 = 1.4$ for a 1 liter volume of water subject to an acceleration of 1 cm s^{-2}. For $B_0 = 0$, the zone volume $V = V^* = \pi R^2 L$ and contact angle $\phi = 90°$ the maximum stable length is $2\pi R$ (the Rayleigh limit). Coriell et al. [90] investigated the effect of B_0 on the maximum length of such zones and compared theoretical predictions with experimental results (see Fig. 11). The actual length of the equilibrium zone is determined by the volume, the contact angle and the static Bond number.

Estimates of the effect on the free surface shape of oscillatory residual acceleration parallel to the axis of an isothermal liquid bridge have been made by Langbein [55]. Not suprisingly, his calculations suggest that the sensitivity of the surface is highest for disturbances with frequencies close to the natural frequency of the bridge, typically in the 0.001-10 Hz range. For the example given in [55], the maximum acceleration magnitudes that can be tolerated by a bridge less than 90% of the maximum stable bridge length (given by the Rayleigh limit) range from 5×10^{-8} to 5×10^{-3} g. The criterion used to determine the tolerable residual acceleration was that the amplitudes of all surface shape excitations with frequencies other than the resonance frequency be kept to 0.1% of the radius of the column. Examples of the results of this analysis are shown in Fig. 12. The curves represent the maximum tolerable axial acceleration for a given aspect ratio (Fig. 12a), and for a surface response with a given number of nodes (Fig. 12b). The results express the maximum tolerable frequency a_0 in terms of the g-jitter frequency ω, the resonant frequency, ω_m, of the liquid zone associated with the m^{th} node of the deformation of the zone surface, the viscosity of the liquid ν and the spatial wavenumber

$$a_0 < \min\left[\sqrt{(\omega^2-\omega_m^2) - \omega\nu q_m}\right], \qquad (9)$$

where $\omega_m^2 = \gamma q_m^2[(q_m R)^2 - 1]/\rho R$, and $q_m = (m+1)\pi/H$, R is the column radius and H the column height. Note that the global minimum, and local minima of the tolerable acceleration curve occur at disturbance frequencies equal to the natural frequencies of the system.

Zhang and Alexander [91] have also analyzed this problem using a slender-body approximation. The problem of determining the axisymmetric response of the shape of the free surface of a cylindrical liquid column bounded by two solid regions is modelled by a 1-D system of non-linear equations. It is found that the sensitivity of the zone to breakage and shape changes depends on the static Bond number, aspect ratio and viscosity as well as the amplitude and frequency of the disturbance. The general trend is an increase in tolerable residual acceleration with increasing frequency. At the eigenfrequencies of the zone, however, there are strong deviations from this trend. At these frequencies this model also shows that the tolerable residual gravity level can be two orders of magnitude lower. These most sensitive frequencies have been found in the 10^{-2}-10^{-1} Hz range (see for example Fig. 13). For the cases examined, maximum tolerable residual gravity levels as low as 10^{-6} g have been calculated. For higher viscosities the tolerable acceleration level is increased for all frequencies. The equilibrium shape, as determined by the steady background acceleration, has a prounounced effect on the response at low frequencies. A change in slenderness of the bridge markedly changes the sensitivity to residual acceleration as the Rayleigh limit is approached. It is clear that for liquid bridges, small magnitude accelerations cannot be ignored.

For non-isothermal zones, the dimensionless groups introduced earlier in section 3.1 govern the problem. For molten silicon Sekerka and Coriell [89] have calculated the values of these groups. They are presented in Table 4. The relative magnitudes of the terms suggest that on earth

the zone shape will be dominated by the capillary effect (large B_O) for typical zone sizes, while under low-gravity conditions the zone shape will be influenced mainly by the temperature gradient along the interface. In addition (as discussed earlier) dynamic distortions may also be important. Considerations of the float zone crystal growth process introduce further complications which ultimately require independent analysis. In the previous cases, the surfaces of the inert solids between which the zone is suspended are usually planar. This is generally not the case for the crystal growth process. The actual shape depends primarily on the thermal conditions. The influence of the meniscus angle at either of the crystal-melt-vapor tri-junctions can also be important and has been analyzed by Heywang [93] and Coriell et al. [94]. In addition to zone failure due to the classical capillary instability (or Rayleigh instablity), a "dewetting" instability is found to be important. The instability arises when the angle between the meniscus and the melt-crystal interface is less than the wetting angle for the liquid melt on the solid crystal. For Si zones of greater than 1 cm radius, zone failure on earth occurs due to the Heywang instability [94,95]. Zone failure by this mechanism is unlikely under low-gravity conditions.

Feuerbacher et al. [56] developed an *ad hoc* model to describe experiment sensitivity to residual accelerations. The model is based on the motion of a body in response to an applied sinusoidal oscillation. The governing equation is that of a damped harmonic oscillator. The tolerable residual accelerations are (as expected) found to increase with increasing frequency of the disturbance. Furthermore, there is a minimum tolerable acceleration at disturbance frequencies corresponding to the natural frequency of the system.

The effect of time dependent accelerations on experiments involving drops and bubbles has been examined for the cases of sinusoidal and Heaviside-function disturbances [57]. The criterion used to define the sensitivity is that the displacement of the drop not exceed 10% of the drop radius. For a given set of physical properties, the admissible accelerations can be expressed as a function of frequency (Fig. 14). The tolerable acceleration levels exhibit trends similar to those depicted in Figs. 4-6.

The influence of the gravity gradient, atmospheric drag and spacecraft attitude motion on the motion of a spherical solid particle immersed in viscous fluid has also been considered [5,6]. The extent and nature of the influence of the gravity gradient and the atmospheric drag on the trajectory of the particle are, for a given value of the Stokes drag coefficient, shown to be dependent on the characteristic orbital attitude, the magnitude of the atmospheric drag accelerations and the distance of the particle from the mass center of the spacecraft.

Amin [59] has investigated the influence of g-jitter on heat transfer from an isothermal sphere maintained at a constant temperature greater than the ambient fluid temperature. The body force was taken to have a single frequency sinusoidal time dependence and a small amplitude. A significant result of the analysis is that the Reynolds stresses associated with the fluctuating flow result in a steady streaming motion. This has implications for both heat and mass transport in oscillating flows. For the low Pr fluids examined, it was concluded that buoyancy induced convection caused by high frequency g-jitter (with amplitudes 10^{-2} g) will result in heat transfer conditions significantly different from pure conduction. However, it was found that in high Prandtl

number fluids with small kinematic viscosities, low frequency g-jitter will influence heat transfer.

Analyses of heat transfer in (laminar) oscillating flows in cylinders and between parallel plates [27-33] have shown that at high frequencies the effective thermal diffusivity is

$$\kappa_{eff} \propto \frac{\omega \Delta x^2}{W_o}, \tag{10}$$

while for low frequencies

$$\kappa_{eff} \propto \omega \Delta x^2 W_o. \tag{11}$$

Here ω is the circular frequency, Δx is the cross-stream average displacement of a fluid element over half the period of the oscillation and $W_o = L(\omega/\nu)^{1/2}$ is the Wormsley number which represents the ratio of the viscous response time to the period of the oscillation. For a given frequency the heat transfer process was found to be most efficient for $Pr = \pi / W_o^2$ i.e. when the characteristic time, $\tau_k = L^2/\kappa$ associated with heat diffusion is equal to half the period of the oscillation. Fig. 15 illustrates this result for fluids with different diffusivities and L = 1 cm.

2.3.3. Linear stability and gravity modulations

The stability of a heated fluid layer of infinite lateral extent is affected by gravity modulation and has received a limited amount of attention for the case of sinusoidally modulated gravity [74-77]. The static case, where the gravity vector is perpendicular to the layer and parallel to the temperature gradient, is stable unless the critical Rayleigh number is exceeded. The effect of gravity modulation is to introduce stability for given combinations of modulation amplitude and frequency for situations which in the absence of modulations would exhibit instability. In contrast, for the case where the gravity vector and the temperature gradient are anti-parallel (which is stable for a steady gravity vector,) instability can occur due to gravity modulation.

The work of Biringen and Peltier [77] focused on the behavior of a 3-D Rayleigh Bénard system subject to spatial and temporal gravity modulation. They used a pseudo-spectral method to examine the system numerically and studied the effects of sinusoidal and random gravity modulations with the gravity vector oriented perpendicular to the fluid layer. It was found that when the base acceleration was reduced from 1g to zero, the system parameters that had resulted in a synchronous response at 1 g led to a conductive state for the modulated zero g case. The spatially random modulations about a zero g base acceleration led to excitations of the 3-D temperature field. These excitations were less pronounced than for the 1 g case. For temporally random modulations about zero g, the cases considered that where excited at 1 g no longer exhibited excitation.

The effect of oscillating accelerations and impulse forcing of an interface separating two immiscible fluids has recently been considered [78,79]. Both these analyses are restricted to time-dependent accelerations with zero mean which are oriented perpendicular to the interface between the fluids. The linear stability of a basic state characterized by a planar interface and an oscillating

pressure was examined. For the case of an arbitrary oscillating disturbance it is shown that the linear evolution of an infinitesimal perturbation of the interface is governed by a single integro-differential equation. Except in the limit of zero surface tension the effect of viscosity is shown to be small. As surface tension becomes dominant, resonant instabilities are excited at lower and lower wavenumbers. The interface is found to be more unstable to impulse type forcing than to sinusoidal forcing [79].

2.3.4. Direct numerical simulation

The effects of low-gravity on the transport of heat and momentum have been examined in a number of articles [37, 60-71]. Robertson et al. [60,61] found that for convection in circular cylinders with azimuthal variations in temperature at the boundary and the gravity vector applied perpendicular to the cylinder axis, the intensity of convection follows the prediction of Weinbaum's first order theory [96] for low Rayleigh numbers. Weinbaum's first order theory predicts a simple sinusoidal dependence of the maximum velocity as a function of orientation of the gravity vector. The effects of a variety of acceleration vectors (sinusoidal, cycloidal and linear periodic) on motion in three fluids corresponding to mercury, helium and water ($10^{-2} < Pr < 10$) were studied by Spradley et al. [62]. They found that the steady mean part of the applied disturbance is more important than the oscillatory part (frequency =1 Hz) in determining the flow field and heat transfer. Kamotani et al. [37] solved a linearized approximation of the Boussinesq equations and investigated the effect of an applied acceleration consisting of a time mean part and an oscillatory part on the temperature and flow fields in a rectangular enclosure. They found that the thermal convection was predominantly oscillatory in nature. In addition they found that the acceleration perpendicular to the temperature gradient is the most important for the generation of fluid motion.

The response of natural convection of a Boussinesq fluid in a cylinder to residual acceleration has been examined by Heiss et al. [64], and Schneider and Straub [97]. In the work of Heiss et al. the calculations are three-dimensional and involve gravity pulses and a rotating gravity vector. The ends of the cylinder are held at different temperatures. The cylinder walls are taken to be either perfectly insulating or perfectly conducting. The results are presented in terms of the relevant dimensionless parameters in the original papers. Figure 16 illustrates their results for impulse disturbances. The physical conditions were taken to correspond to: a cylinder of aspect ratio 1, with diameter = 1 cm, $\nu = 5\times10^{-3}$ cm^2 s^{-1}, $\kappa = 7.14\times10^{-3}$ cm^2 s^{-1}, $\beta = 2.5\times10^{-4}$, and a temperature difference, ΔT, of 25^o K. The magnitude of the acceleration pulse (duration =0.7 seconds) corresponding to a Rayleigh number, Ra^*, of 2000 is $\sim 3\times10^{-3}$ g and results in a maximum velocity of approximately 5.8 cm s^{-1} . The decay time for the flow field is about 5.6 seconds. Notice that for all the results, the decay time of the pulse is independent of the magnitude of Ra*. For a rotating gravity vector of a given magnitude, the maximum velocity of the system is independent of the dimensionless frequency $f = f^* d^2/\kappa$, up to $f \sim 10$ whereupon it decreases rapidly with increasing frequency. For the fluid with the physical properties described in the previous example, f^* corresponds to 7.14×10^{-2} s^{-1}.

Schneider and Straub [97] examined the effect of Prandtl number on the response to g-jitter

for the same system as Heiss et al. They examined the response of the system to pulses of infinite length and sinusoidally varying pulses. For sinusoidal pulses they found for systems with Pr =0.71 and 7.0 (air and water) that the maximum velocity decreased with increasing frequency for dimensionless frequencies, $F=f L^2/\kappa$, greater than 10. At Pr=7 a maximum in the velocity was observed between F = 10 and 100 for the maximum amplitude pulse examined ($Ra = 2\times10^5$, or $|\mathbf{g}| \approx 3\times10^{-4}$ g for a fluid with the properties of water, a 1 cm diameter cylinder and a temperature difference of 10 K). They determined that the system was least sensitive when the transient accelerations acted along the cylinder axis.

The extent to which gravity causes buoyancy-driven fluid motion (and thus, solute redistribution) during directional solidification has been examined using numerical models of buoyancy-driven convection in cylindrical and rectangular geometries[9,65-69,84,98-101]. Except for [9,65-69] these studies are restricted to axisymmetric situations in which a steady gravity vector is oriented parallel to the axis of a cylindrical ampoule. McFadden and Coriell [66] have undertaken 2-D calculations of the effects of time-dependent accelerations on lateral compositional variations during directional solidification. The gravitational acceleration was assumed to have a uniform magnitude and rotation rate. The amount of compositional nonuniformity was found to increase with decreasing rate of rotation (see Fig. 17).

Two- and three- dimensional models of directional solidification from dilute gallium-doped germanium melts have been used to determine the sensitivity of crystal compositional uniformity to both time-dependent and steady residual accelerations [9,67,69]. The specific boundary conditions, thermo-physical properties of the melt, growth rates and ampoule size are all found to play a role in the determination of the experiment sensitivity. For a given set of operating conditions, it is found that at growth rates on the order of 6.5 mm s^{-1} the orientation of the experiment with respect to the steady component of the residual gravity is a crucial factor in determining the suitability of the spacecraft as a means to suppress or eliminate unwanted effects caused by buoyant fluid motion. The worst case appears to be when the acceleration vector is parallel to the crystal interface. At growth rates on the order of microns per second, this orientation leads to compositional non-uniformities of 10-20% when the magnitude of the acceleration is of the order 10^{-6} g. If, however, the growth rate is lowered by an order of magnitude, the nonuniformity is reduced significantly (down to 1- 5% in this case). Table 5 summarizes the results obtained for steady accelerations.

The directional solidification (Bridgman-Stockbarger) process is also extremely sensitive to transient disturbances. The response of the system to a variety of impulses will be discussed. For example, a 3×10^{-3} g impulse of one second duration acting parallel to the interface of a growing crystal produces a response in the solute field which lasts for nearly 2000 seconds. Consequently lateral and longitudinal compositional variations occur over a length of nearly 6 mm in the grown crystal.

The response of the solute field and the lateral nonuniformity to oscillatory accelerations varies from no response at all (at frequencies above 1 Hz with amplitudes below 10^{-3} g) to a significant response at 10^{-3} Hz at amplitudes on the order of 10^{-6} g. In addition, additive effects

were observed for combinations of a steady and a low frequency residual acceleration component. These additive effects gave rise to significant lateral and *longitudinal* non-uniformities in concentration. A number of different types of periodic disturbances were employed. Single frequency disturbances of the form $\mathbf{g}(t) = \mathbf{g}_o + \mathbf{g}_n \cos(2\pi f_n t)$ were examined with $\mathbf{g}_o = 0$, $\sqrt{2}(10)^{-6}$ and $\sqrt{2}(10)^{-5}$ g, oriented parallel, perpendicular and at 45° to the crystal-melt interface. The frequency range examined was $f_n = 10^{-4}$, 10^{-3}, 10^{-2}, 10^{-1}, 1 and 10 Hz. For frequencies greater than 10^{-2} Hz, there were no discernible effects on the solute fields. The velocity field did, however, respond to the oscillatory disturbances. For the case of 10^{-3} Hz (at 5×10^{-6} g) the response of the solute field was significant. Lateral and longitudinal nonuniformity levels in excess of 15% were calculated. Figures 18-20 show the lateral nonuniformity as a function of time and highlights the additive effect of oscillatory and steady components of the residual acceleration.

The effect of a multiple frequency disturbance is illustrated in Figure 20. The acceleration consists of steady and periodic contributions with the form: $\mathbf{g}(t) = \mathbf{g}_0 + \mathbf{g}_1 \cos(2\pi 10^{-3} t) + \mathbf{g}_2 \cos(2\pi 10^{-2} t)$. Here $|\mathbf{g}_0| = \sqrt{2}\times10^{-6}$ g, $|\mathbf{g}_1| = 3\sqrt{2}\times10^{-6}$ g and $|\mathbf{g}_2| = 3\sqrt{2}\times10^{-5}$ g. The magnitude of the compositional nonuniformity ξ is seen to vary with the frequencies of the acceleration. More recently, it has been shown [67] that, particularly at high frequencies, it is important to consider the long time behavior of the system, because for high frequency disturbances ($\approx$ 0.1 - 1 Hz) the transient behavior of the system is more sensitive than the long time behavior. For example, the response to a 1 Hz 10^{-2} g acceleration was found to exhibit a concentration nonuniformity on the order of 10% during the first 80 seconds whereupon it decayed slowly to 1% over a period of 2500 seconds. In addition, calculations have been made using sample acceleration time histories obtained on Spacelab 3 (SL-3). The results varied according to the type of SL-3 data that were input. For the example shown in Fig. 21 the response of the solute field was negligible, although the velocity field fluctuated on the order of the crystal growth rate. The system exhibited some response to transient disturbances (for example the structural response to thruster firings) that were superimposed on background low frequency acceleration. Low frequency ($\leq 10^{-1}$ Hz) acceleration components with amplitudes of 10^{-3} g or more were also found to give rise to undesirable nonuniformity.

Griffin and Mokatef [72,73] modelled the nature of melt convection in a Bridgman system subject to steady and unsteady axial acceleration. They also found that at conditions corresponding to low-gravity the response time of the melt velocity is proportional to the momentum diffusion time (i.e. it is controlled by the characteristic system length scale and melt viscosity). In accord with the general trend exhibited by most physical systems discussed in this article, they found that the velocity response to sinusoidal g-jitter decreased as the inverse square of the momentum diffusion time.

A general conclusion that can be drawn from all attempts to characterize gravity-driven convective effects on directional solidification from two component melts is that the maximum lateral solute nonuniformity (radial segregation for the axisymmetric cases) occurs near the transition from diffusion dominated to convection dominated growth conditions [52,84,9]; that is, when convective velocities are of the same order of magnitude as the diffusive velocities. The

conditions under which this "transition" takes place will depend on the specific nature of the forces driving convection. The orientation of the steady component of the gravity vector is crucial in determining the magnitude of the gravity vector at which this transition occurs. Thus, for a given set of operating conditions the orientation of the gravity vector determines the suitability of a low-gravity environment for directional solidification experiments.

Motivated by the growth of triglycine sulfate (TGS) crystals on Spacelab 3 [11], Nadarajah et al. [102] have examined the acceleration sensitivity of crystal growth from solution. Thermal and solutal convection were included in their analyses and the crystal growth rate was chosen as the sensitivity parameter for the response to convective transport. Simulations were carried out for steady, impulsive and periodic accelerations in order to determine tolerable acceleration levels. Long-time simulations of the experiment were conducted with steady background accelerations of 10^{-6} and 10^{-5}g. Impulsive and periodic disturbances of higher magnitudes were imposed at intermediate points. For steady accelerations the system was shown to have diffusion dominated transport at 10^{-6}g but for 10^{-5}g a transition to convection dominated transport occurs. Figure 22 summarizes the results for oscillatory disturbances. For each case, the numbers correspond to the ratio $g\beta\Delta c/f\,v^*$, which is an estimate of the the ratio of buoyancy to inertial forces. Here β is the solute expansion coefficent, Δc the characteristic concentration difference, f is the frequency of the acceleration and v^* is the calculated characteristic fluid velocity. Clearly, for this example, a simple estimate alone will not suffice to determine the system sensitivity. The system is relatively stable to impulsive and periodic disturbances unless their magnitudes are very large.

2.4. Summary and discussion

The work described in this paper examines the sensitivity of a variety of space experiments to residual accelerations. In all the cases discussed, the sensitivity is related to the dynamic response of a fluid. In some cases the sensitivity can be defined by the magnitude of the response of the velocity field. This response may involve motion of the fluid associated with internal density gradients, or the motion of a free liquid surface. For fluids with internal density gradients, the type of acceleration to which the experiment is sensitive will depend on whether buoyancy-driven convection must be small in comparison to other types of fluid motion (such as thermocapillary flow), or fluid motion must be suppressed or eliminated (such as in diffusion studies, or directional solidification experiments). In the latter case, the experiments (for example diffusion experiments and directional solidification experiments) are sensitive to steady and low frequency accelerations ($< 10^{-2}$ Hz). For experiments such as the directional solidification of melts with two or more components, determination of the velocity response alone is insufficient to assess the sensitivity. The effect of the velocity on the composition and temperature field must be considered, particularly in the vicinity of the melt-crystal interface. As far as the response to transient disturbances is concerned the sensitivity is determined by both the magnitude and frequency of the acceleration and the characteristic momentum and solute diffusion times.

The directional solidification of doped germanium crystals has been carried out on Skylab [17,18,103,104] and the Apollo-Soyuz Test Project (ASTP) [105,106]. The latter involved the directional solidification of seeded Ge melts. Melts were doped with gallium and some were doped

with 1% Si and .001% Sb [105]. The results of these experiments revealed strong asymmetric non-uniformities in the space grown crystals. Lateral variations were also observed in samples grown under terrestrial conditions but were much less pronounced [25]. It has been argued that the asymmetric redistribution of the dopant can be ascribed to "barometric diffusion" of the solutes due to the acceleration gradient in the melt arising from the rotational motion of the spacecraft [105,106]. The basis of the argument, however, appears to ignore the presence of gravity gradient and atmospheric drag effects and does not explicitly account for the spacecraft attitude motions. It has been demonstrated [9] that melt convection can occur in response to a low magnitude steady residual acceleration, and that whenever the acceleration vector is not aligned with the ampoule axis strong asymmetries in composition can occur. Since there is a non-linear dependence of compositional uniformity on convection, there is always the possibility that the observed non-uniformities in the terrestrially grown samples will be smaller than those observed in space grown samples. Thus, convection caused by residual acceleration cannot be discounted as the origin of the non-uniformities.

Thermocapillary flow experiments require that buoyancy effects are small in comparison to capillary effects. The estimated range of accelerations to which they are sensitive lies between 5×10^{-3} Hz and 2 Hz for the most sensitive cases. Unless the magnitude of the effective buoyancy force (expressed through the Grashof number) associated with a given acceleration is on the order of or greater than $Rs(1+ St^2)^{1/2}$, buoyancy effects are not likely to be significant. It is possible that more subtle effects of the acceleration environment might occur (for example influencing the transition from steady to oscillatory flow) but this cannot be determined by order of magnitude analysis. It is more likely that thermocapillary flow experiments will be most sensitive to the motion of the free surface in response to g-jitter.

The response of free surfaces to g-jitter has been examined through analytical and numerical models. For cylindrical liquid bridges this has been undertaken only for axial accelerations. The shape of the surface is most responsive to disturbances close to the natural frequency of the bridge and its harmonics. The sensitive frequencies lie in the 5×10^{-3} -10 Hz range, with maximum tolerable magnitudes from 10^{-8} - 10^{-3} g depending on the sensitivity criterion and the particular model employed.

Figure 23 depicts the range of measured acceleration amplitudes (courtesy of Dr. H. Hamacher, DLR, and M. J. B. Rogers, University of Alabama in Huntsville) as a function of frequency for several "shuttle" missions. It should be remembered that in addition to the accelerations shown here there are gravity gradient and atmospheric drag accelerations with magnitudes on the order of 10^{-6}-10^{-7} g which can be steady (for gravity gradient stabilized type attitudes) or have frequencies that are twice the orbital frequencies (for a solar inertial attitude). In Fig. 24 we depict these together with g-tolerance curves selected from the examples discussed earlier. There is some overlap between the sensitivity curves and measured accelerations. Even if the fact that most of the curves are obtained for order of magnitude estimates is taken into account, it is clear that a careful evaluation of the interaction between experiments and the residual acceleration environment is necessary. Once the experiment sensitivity has been determined

(which may sometimes require a more detailed analysis than any discussed in this review) it should be possible for the experimenter to choose operating conditions which will minimize the effect of the predicted acceleration environment. Since flight opportunities are limited, it is particularly important that the chances of success for any given experiment be greatly improved by detailed modelling prior to flight. This will allow investigators to better anticipate undesirable effects of the prevailing residual acceleration conditions, and will ultimately lead to a better overall understanding of the physical system.

2.5. References

[1] *Chassay, R. P., Schwaniger, Jr., A. J.*: NASA -TM 86585, December, 1986

[2] *Hamacher, H. , Jilg, R., Mehrbold, U.*: Proc. 6th European Symposium Materials Sciences in Microgravity Conditions, Bordeaux, France (ESA SP-256 1987).

[3] Proceedings of the Workshop on Measurement and Characterization of the Accceleration Environment On Board the Space Station , Guntersville Alabama, August 11-14, 1986 (Teledyne Brown Engineering, Huntsville Alabama 1987).

[4] *Hamacher, H.*: in Materials Science in Space, B. Feuerbacher, R. Naumann, H. Hamacher (eds.) Springer, New York 1986, 31.

[5] *Alexander, J. I. D. , Lundquist, C. A.*: AIAA Journal 26 (1988) 34.

[6] *Alexander, J. I. D. , Lundquist, C. A.*: J. Astr. Sci. 35 (1987) 193.

[7] *Camel, D., Favier, J.J., Rouzaud, A.*: ESA Contract Report, Gr- 764.108, March 27 1987.

[8] *Monti, R.*: ESA Contract Report, R-66.525, Technosystems Report TS-7-87, April 1987.

[9] *Alexander, J. I. D., Ouazzani, J. , Rosenberger, F.*: J. Crystal Growth 97 (1989) 285.

[10] *Beysens, D.*: in Materials Science in Space, B. Feuerbacher, R. Naumann, H. Hamacher (eds.)Springer, New York 1986 191.

[11] *Yoo, H-D., Wilcox, W.R., Lal, R.B., Trollinger, J.D.*: in Materials Processing in the Reduced Gravity of Space Vol. 9,.G. E. Rindone (ed.) North Holland, New York 1982 399.

[12] *Van den Berg, L., Schnepple, W.*: in Materials Processing in the Reduced Gravity of Space Vol. 9, G. E. Rindone (ed) North Holland, New York 1982 349.

[13] *Van den Berg, L., Schnepple,W.*: Growth of Mercuric Iodide in Spacelab 3, Nuclear Instruments and Methods in Physics Research A283 (1989) 335.

[14] *Wiedemeier, H., Chandra, D., Klaessig, F. C.*: J. Crystal Growth 51 (1980) 345.

[15] *Cröll, A., Mueller, W., Nitsche, R.*: Proc. 6th European Symposium Materials Sciences in Microgravity Conditions, Bordeaux, France (ESA SP-2561987) 87.

[16] *Camel, D., Favier, J. J., Dupauy, M. D., Le Maguet,R.*: ibid., 317.

[17] *Witt, A. F., Gatos, H. C., Lichtensteiger, M., Lavine M. C., Hermann, C. J.*: J. Electrochem. Soc. 122 (1975) 276.

[18] *Witt, A. F., Gatos, H. C., Lichtensteiger, M., Lavine, M.C., Hermann, C. J.*: J. Electrochem Soc. 127 (1978) 832.

[19] *Frohberg, G., Kraatz, K. H., Wever, H.*: Proc. 6th European Symposium Materials Sciences in Microgravity Conditions, Bordeaux, France (ESA SP-256 1987) 585.

[20] *Malméjac, Y., Frohberg, G.*: in Fluid Sciences and Materials Science in Space, A European Perspective, ed. H. U. Walter (Springer, Berlin 1987) 159.

[21] *Brown, R.A.*: Lecture notes from the 6th Intenational Summer School on Crystal Growth, Edinburgh, Scotland, June 1986.

[22] *Polezhaev, V. I.*: Hydrodynamics, Heat and Mass Transfer during Crystal Growth, in Crystals 10 ed. H. C. Freyhardt (Springer, Berlin, 1984).

[23] *Ostrach, S.* : J. Fluids Engineering 105 (1983) 5.

[24] *Rosenberger, F*:: Fundamentals of Crystal Growth I (Springer, Berlin 1979).
[25] *Hurle, D. J. T. , Müller, G. , Nitsche, R.*: in Fluid Sciences and Materials Science in Space, A European Perspective, ed. H. U. Walter (Springer, Berlin 1987) 313.
[26] *Taylor, G.I.*: Proc. Roy. Soc. London A 219 (1953) 186.
[27] *Aris, R.*: Proc. Roy. Soc. London A 259, (1960) 370.
[28] *Gill, W. N.*: *Sankarsubramanian, R.*: Proc. Roy. Soc. London A 316 (1970) 341.
[29] *Brocher, E.*: J. Fluid Mech. 133 (1983) 245.
[30] *Kurzweg, U. H.*: J. Heat Transfer 107 (1985) 459.
[31] *Kurzweg, U. H.*: J. Fluid Mech. 156 (1983) 291.
[32] *Kavainy, M.*: Int, J. Heat and Mass Transfer 29 (1985) 2002.
[33] *Joshi, C. H., Kamm, R. D., Drazen, J. M., Slutsky, A. S.*: J. Fluid Mech. 114 (1983) 245.
[34] *Smith, R.*: J. Fluid Mech 114 (9182) 379.
[35] *Watson, E. J.*: J. Fluid Mech. 133 (1983) 233.
[36] *Farrell, D., Larsen, W. E.* : Water Resources Res. 9 (1973) 173.
[37] *Kamotani, Y., Prasad, A., Ostrach, S.* : AIAA Journal 19 (1981) 511.
[38] *Monti, R., Favier, J.J., Langbein, D.*: in Fluid Sciences and Materials Science in Space, A European Perspective, ed. H. U. Walter (Springer, Berlin 1987) p. 637.
[39] *Radcliffe, M. D., Drake, M. C., Zvan, G., Fowlis, W. W., Alexander, J. I. D., Roberts, G. D., Sutter, J. K., Bergman, E.*: in Proceedings of the American Chemical Society Meeting, New Orleans 1987.
[40] *Martinez, I.* Proc. 6th European Symposium Materials Sciences in Microgravity Conditions, Bordeaux, France (ESA SP-256 1987) 235.
[41] *Martinez, I., Haynes, J. M., Langbein, D.*: in Fluid Sciences and Materials Science in Space, A European Perspective, ed. H. U. Walter (Springer, Berlin 1987) 53.
[42] *Langbein, D., Roth, U.*: Proc. 6th European Symposium Materials Sciences in Microgravity Conditions, Bordeaux, France (ESA SP-256 1987) 183.
[43] *Padday J. F.*: ibid. 49.
[44] Napolitano, L. G., Monti, R., Russo, G., Golia, C. ibid. 191.
[45] *Schwabe,D., Scharmann, A.*: Proc. 6th European Symposium Materials Sciences in Microgravity Conditions, Schlob Elmau FRG (ESA SP-222 1984) 81.
[46] *Napolitano, L. G., Monti , R., Russo, G.*: ibid. 15.
[47] *Rogers, M. J. B., Alexander, J. I. D.*: submitted to the AIAA Journal of Spacecraft and Rockets, (1990).
[48] Malkus, W. R.: Science, 160 865 (1968).
[49] *Langbein, D.*: ESA Contract Report, BF-R-66.525, April 1987.
[50] *Napolitano, L.*: Ann. N.Y. Acad. Sci. (1983) 278.
[51] *Ostrach, S.*: Ann. Rev. Fluid Mech. 14 (1982) 313.
[52] *Rouzaud, A., Camel, D., Favier, J. J.* : J. Crystal Growth 73 (1985) 149.
[53] *Gebhardt, B.* : AIAA J. 1 (1963) 380.
[54] *Dressler,.R. F.* : J. Crystal Growth 54 (1981) 523.
[55] *Langbein, D.*: Proc. 6th European Symposium Materials Sciences in Microgravity Conditions, Bordeaux, France (ESA SP-256 1987) 221.
[56] *Feuerbacher, B., Hamacher, H.,Jilg, J.* preprint (DFVLR Köln, FRG, 1988).
[57] *Dewandre, Th.*: Applied Microgravity Technology 1 (1988) 142.
[58] *Fowlis, W.W., Roberts, G., Drake, M. , Radcliffe, M.*: Determination of the Flow in the 3M company's space crystal growth experiments, to be published J. Crystal Growth (1989).
[59] *Amin, N.*: Proc. R. Soc. Lond. A 419 (1988) 151.
[60] *Robertson, S. J., Nicholson, L. A.*: Lockheed Report LMSC-HREC TR D867640 (1987).
[61] *Robertson, S. J., Nicholson, L. A., Spradley, L. W.*: Lockheed Report LMSC-HREC TR D867624 (1982).
[62] *Spradley, L. W. Bourgeois, S. W. , Lin, F. N.*: AIAA paper 75-695 (1975).
[63] *Grodzka, P. G., Bannister, T. C.*: AIAA paper 74-156 (1974).

[64] *Heiss, T., Schneider, S., Straub, J.*: Proc. 6th European Symposium Materials Sciences in Microgravity Conditions, Bordeaux, France (ESA SP-256 1987) 517.
[65] *Polezhaev, V. I., Lebedev, A. P., Nikitin, S. A.*: Proc. 5th European Symposium on Materials Sciences under Microgravity, Schloss Elmau FRG, ESA SP-222 (1984), 237.
[66] *McFadden, G. B., Coriell, S. R.*: in Proc. AIAA/ASME/SIAM/APS 1st National Fluid Dynamics Congress, Cincinnati, July 25th-28th (1988) p. 1572.
[67] *Alexander, J. I. D., Ouazzani, J., Rosenberger, F.*: Proc. 3rd International Colloquium on Drops and Bubbles, AIP Conference Proceedings 197, ed. Taylor G. Wang (American Institute of Physics, New York, 1988) p.112.
[68] *Alexander, J. I. D., Ouazzani, J.*: Proc. 6th International Conference on Num. Methods in Laminar and Turbulent Flow, C. Taylor, P. Gresho, R. L. Sani and J. Haüser (eds.) Pineridge, Swansea 1989 1035.
[69] *Alexander, J. I. D., Amiroudine, S., Ouazzani, J., Rosenberger, F.*: Analysis of the Low Gravity Tolerance of the Bridgman-Stockbarger Technique. II: Transient and periodic accelerations, in preparation 1989.
[70] *Arnold, W. A., Jacqmin, D. A., Chang, R., Chait, A.*: AIAA paper No. 89 (1989).
[71] *Ramachandran, N., Winter, C.* AIAA Paper No. 90-0654 (1990).
[72] *Griffin, P. R., Mokatef, S.*: Appl. Microgravity Tech. 2 (1989) 121.
[73] *Griffin, P. R., Mokatef, S.*: ibid. 128.
[74] *Gresho, P. M. Sani, R. L.*: J. Fluid Mech. 40 (1970) 783.
[75] *Gershuni, G. Z., Zhukovitskii, E. M.* Convective stability of incompressible fluids (Israel program for scientific translations, Jerusalem 1976).
[76] *Hadid, H. B. , Roux, B., Randriamapianina, A., Crespo, E., Bontoux, P.*: Proc. NATO Conf. on Phys.-Chem. Hydrodyn. Spain, July (1986).
[77] *Biringen, S., Peltier, L. J.*: Proc. 27th Aerospace Science Mtg., Reno, Nevada 1989, AIAA Paper No. 89-0068.
[78] *Jacqmin, D., Duval, W. M. B.*: J. Fluid Mech, 196 (1988) 495.
[79] *Jacqmin, D., Williams, M. D.*: unpublished research, NASA Lewis Research Center, Cleveland (1988)..
[80] *Alexander, Rosenberger, F.*: Bridgman Crystal Growth in low gravity: A scaling analysis to appear in Low Gravity Fluid Dynamics and Transport Phenomena, J. Koster and R. Sani (eds.) AIAA, 1990.
[81] *Ch-H. Chun*, Proc 6th European Symposium Materials Sciences in Microgravity Conditions, Bordeaux, France (ESA SP-256 1987) 271.
[82] *M. D. Lind*, AIAA-Paper 87-0618 (25th Aerospace Sciences Meeting, Reno, January 19-27, 1987).
[83] *Camel, D., Favier, J.J.* : J. de Physique 47 (1986) 1001.
[84] *Chang, C. J., Brown, R. A.*: J. Crystal Growth 63 (1983) 353.
[85] *Kimura, S., Bejan,* A.: Phy. Fluids 28 (1985) 2980.
[86] *Martinez, I.*: Proc. 5th European symposium on materials sciences under microgravity, Schloss Elmau FRG, ESA SP-222 (1984) 31.
[87] *Haynes, J.*: ibid. 43.
[88] *Padday, J. F.*: ibid. 251.
[89] *Sekerka, R. F., Coriell, S. R.*: Proc. 3rd. Symposium on Material Science in Space, Greneble, France (ESA SP-142, 1989) 55
[90] *Coriell, S.R., Hardy, S.C., Cordes, M.R.*: J. Colliod Interface Sci. 60 (1976) 126.
[91] *Zhang Y. Q., Alexander, J. I. D.*: submitted to Physics of Fluids (1990).
[92] *Chang, C. E., Wilcox, W. R.*: J. Crystal Growth 28 (1975) 8.
[93] *Heywang, W.*, Z. Naturforschg. 11a (1956) 238.
[94] *Coriell, S. R., Hardy, C., Cordes, M. R.*: J. Crystal Growth 42 (1977) 466.
[95] *Duranceau, J. L., Brown, R. A.*: J. Crystal Growth 75 (1986) 367.
[96] *Weinbaum, S.*: J. Fluid Mech. 18 (1964) 409.
[97] *Schneider, S., Straub, J.*: J. Crystal Growth 97 (1989) 235.

[98] *Clark, P. A., Wilcox, W. R.*: J. Crystal Growth 50 (1980) 461.
[99] *Kobayashi , N., Wilcox, W. R.*: J. Crystal Growth 59 (1982) 616.
[100] *McFadden, G. B., Rehm, R. G., Coriell, S. R., Clark, W., Morrish, K. A.*: Metall. Trans. A15 (1984) 2125.
[101] *Adornato, P. M., Brown, R. A.*: J. Crystal Growth 80 (1987) 155.
[102] *Nadarajah, A., Rosenberger, F., Alexander, J. I. D.*: J. Crystal Growth **104** (1990) 218-232.
[103] *Yue, J. T.: Voltmer, F. W.* : J. Crystal Growth 29 (1975) 329.
[104] *Gatos, H. C.*: in Materials Processing in the Reduced Gravity Environment of Space ed. G Rindone (Elsevier, New York, 1982) 355.
[105] *Zemskov, V. S.*: Soviet Physics Dokl. 22 (1977) 170.
[106] *Zemskov, V. S., Shul'pina, I. L., Titkov, A. N., Belokurova, I., Guseva, N. B., Safarov, V. I.*: Soviet Phys. Solid State 21 (1979) 576.

2.6. Tables

Table 1. Changes in residual acceleration components [$\mu g\ m^{-1}$] along the local vertical (X_1) and perpendicular to the oribital plane (X_2) associated with the gravity gradient stabilized attitude, and estimated atmospheric drag accelerations. a and b are, respectively, best and worst drag estimates for the "Shuttle" (1) and NASA's Space Station (2). From [5]

Altitude [km]	X_1	X_2	Drag 1a	Drag1b	Drag 2a	Drag 2b
275	0.414	-0.137	2.10	0.360	10.6	3.1
300	0.410	-0.136	1.20	0.210	6.1	1.8
325	0.405	-0.134	0.69	0.120	3.6	1.1
350	0.401	-0.133	0.41	0.070	2.1	0.6
400	0.392	-0.130	0.24	0.025	0.7	0.2
450	0.383	-0.127	0.05	0.009	0.4	0.1
500	0.375	-0.124	0.02	0.001	0.8	0.02

Table 2. Physical properties and dimensionless groups for various experimental systems: 1- dimethyl silicone oil [44], 2- methanol [81], 3- $NaNO_3$ [45], 4 - indium [82], 5- selenium - [82], 6- silicon [15].

Exp #	μ [g cm s^{-2}]	ν [cm^2 s^{-1}]	κ [cm^2 s^{-1}]	$\lvert\gamma_T\rvert$ [dyne $cm^{-1}K^{-1}$]	ΔT [K]	$\lvert\beta_T\rvert$ [K^{-1}]	L [cm]
1	4.56×10^{-2}	5.01×10^{-2}	8.7×10^{-4}	$6.55\times10\times^{-2}$	32	1.05×10^{-3}	3.8
2	5.8×10^{-3}	7.4×10^{-3}	1.08×10^{-3}	7.7×10^{-2}	10	1.2×10^{-3}	1
3	2.82×10^{-2}	1.48×10^{-2}	1.67×10^{-3}	$5.5\times10\times^{-2}$	15	3.8×10^{-4}	0.5
4	1.94×10^{-2}	2.76×10^{-3}	2.17×10^{-1}	6.2×10^{-2}	5	1.21×10^{-4}	1.5
5	5.3	1.33	4.0×10^{-4}	7.7×10^{-2}	5	2.23×10^{-3}	1.5
6	7.5×10^{-3}	3.0×10^{-3}	1.3×10^{-1}	4.3×10^{-1}	50	1.43×10^{-4}	2

Exp #	$Gr=\frac{\lvert\beta_T\rvert\Delta T H^3 g}{\nu^2}$	$Rs=\frac{\lvert\gamma_T\rvert\Delta T\, L}{\mu\nu}$	Gr/Rs	$GrRs^{-5/3}$	Pr
1	7.1985×10^5 g/g_o	3.486×10^3	206.5 g/g_o	0.898 g/g_o	57.6
2	2.1476×10^5 g/g_o	1.801×10^4	11.9 g/g_o	1.736×10^{-2} g/g_o	6.85
3	3188 g/g_o	1024	3.11 g/g_o	3.06×10^{-2} g/g_o	8.86
4	2.6269×10^5 g/g_o	8684	30.2 g/g_o	7.16×10^{-2} g/g_o	1.27×10^{-2}
5	20.8 g/g_o	8.19×10^{-2}	254 g/g_o	-	595
6	6.228×10^6 g/g_o	1.911×10^6	3.23 g/g_o	2.12×10^{-4} g/g_o	2.3×10^{-2}

Table 3. Comparison of numerical (ξ^*_m) and order of magnitude estimates ($_m$) of compositional nonuniformity for different choices of length scale [80]. The non uniformity ξ in these cases is given by $\xi = | c(0) - c_\infty | / c(0)$, c_∞ is the melt composition far from the crystal and, because $k < 1$, $c(0)$ is the maximum value of the composition at the interface.

g-orientation	L [cm]	x_o	Gr	Sc	ξ^*_m [%]	ξ_m [%]	Pe_g	Regime
Parallel	1.0	0.066	145	10	61	10	5	II (b)
Parallel	0.25	0.27	2.27	10	61	73	1.25	I (b)
Parallel	1.0	0.066	145	15	71	5	7.5	II (b)
Parallel	0.25	0.27	2.27	15	71	40	1.875	II (b)
Parallel	1.0	0.066	145	25	73	2.5	12.5	II (b)
Parallel	0.25	0.27	2.27	25	73	21	3.125	II (b)
Parallel	1.0	0.066	145	10	12	18	0.5	I (b)
Parallel	0.25	0.27	2.27	10	12	8	0.125	I (b)

Table 4. Values of dimensionless groups for silicon calculated from the data of Chang and Wilcox [92]. The length scale is taken to be the zone radius R; β_T is estimated at 1.6×10^{-4} K^{-1}. For space, g_S is taken as 10^{-4}g. ΔT is assumed to be 10 C°. (After Sekerka and Coriell [89]).

	B_o	Gr	$N_3=\frac{\rho v^2}{R\gamma}$	$R_S N_3=\frac{\Delta T\lvert\gamma_T\rvert}{\gamma}$	Pr	R_S
R=1 cm	3.4	1.3×10^{5}	4.3×10^{-8}	6×10^{-3}	2.3×10^{-2}	1.4×10^{5}
$R=10^{-2}$ cm	3.4×10^{-4}	1.3×10^{-1}	4.3×10^{-10}	6×10^{-3}	2.3×10^{-2}	1.4×10^{3}
SPACE						
R=1 cm	3.4×10^{-4}	1.3×10	4.3×10^{-8}	6×10^{-3}	2.3×10^{-2}	1.4×10^{5}

Table 5. Compositional nonuniformity ξ [%] for Ge:Ga [9,80]; $\xi = (c_{smax} - c_{smin})/c_{sav}$, where c_s denotes the crystal composition at the melt-crystal interface.

Residual Acceleration Magnitude [g]		Orientation		Ampoule Width [cm]			
				1		0.5	2.0
				Growth Rate [mm s^{-1}]			
		N	e_g	6.5	0.65	6.5	6.5
A)	10^{-4}			80			
	10^{-5}			92.7	11.9	12.0	
				70.9	11.3		
				6.4	0.95		
	$5(10)^{-6}$			3.2			
				39			
				54.2			
	10^{-6}			11.3	2.0		
				8.0			
				0.7	0.0		
B)	10^{-5}			22.6			64.5
	10^{-6}			2.3			

e_g is the unit vector parallel to **g**, **N** is the normal vector to the crystal. L = 1 cm for all cases. Values in parentheses indicate 3-D results. All calcualtions were undertaken using the Thermo-physical properties of gallium-doped germanium [80] and **A)** and **B)** refer to the operating conditions listed below.

	Operating conditions	
A)	Hot zone temperature (T_h)	1331 K
	Distance between inlet and interface (L)	1.0 cm
	Height of adiabatic zone (L_a)	2.5 mm
	Ampoule width (diameter)	1.0 cm
B)	Hot zone temperature (T_h)	1251 K

2.7. Figures

Fig 1. An example of a relatively "quiet period" measured on SL-3 ($< 4\times10^{-3}$g, g = 9.8 m s^{-2}). a) Total acceleration array. b) Combined amplitude spectrum, note components in the 5-6 Hz and 7-8 Hz, 10-12 Hz, 17Hz and 30-35 Hz ranges. After Rogers and Alexander [47].

Fig 2. "Window" containing three thruster pulses. a) Total acceleration array, maximum magnitude ~1×10^{-2} g. b) Combined amplitude spectrum, dominant frequency components 11 Hz and 17 Hz. After Rogers and Alexander [47].

Fig. 3 Estimated tolerable residual accelerations (in units of g = 9.8 m s^{-2}) as a function of frequency for: 1) a fluid physics experiment involving a temperature gradient, 2) a crystal growth experiment and 3) a thermo-diffusion experiment. After Monti et al. [38].

Fig. 4 Estimated tolerable residual accelerations (in units of g = 9.8 m s^{-2}) for semiconductor and metal solidification experiments. The sensitivity parameter is longitudinal segregation, $\Delta c/c$. $Pe_s = 5$, temperature gradient = 50K cm^{-1}, k=0.1. After Monti et al. [36].

Fig. 5 Estimated tolerable residual acceleration (in units of g = 9.8 m s^{-2}) ranges for diffusion experiments. After Monti et al. [36].

Fig. 6 Tolerable acceleration limits for a thermocapillary flow experiment expressed in terms of Grashof (Gr), Strouhal (St) and Surface Reynolds (Rs) numbers.

Fig. 7 Tolerable acceleration limits (in units of g = 9.8 m s^{-2}) as a function of frequency for the thermo-capillary experiments with properties listed in Table 2. a) Gravity forces 1% of thermo-capillary forces, b) gravity forces 10% of thermo-capillary forces.

Fig. 8 A plot of GrSc vs. Pe_g for the results of numerical simulations for steady accelerations parallel to the crystal-melt interface [80]. The solid and dashed lines delineate the following transport regimes: I a - c convective regime; II advective-diffusive regime [83]. Note that the adiabatic zone length has been used to calculate the Grashof and growth Peclet numbers, and that x_o =0.27. Numbers in parentheses indicate the value of compositional nonuniformity $\xi = |c_{smax} - c_{smin}|/c_{sav}\times 100\%$, where c_s denotes the crystal composition at the melt-crystal interface, associated with each of the numerical results.

Fig. 9 Transient convection in large and small test cells due to residual accelerations caused by astronaut motion after Dressler [54]. Here x is the angular displacement, v the velocity and $t_{1/2}$ is the decay time given by $0.68\times R^2/\nu$.

Fig. 10 Stability limits of an isothermal liquid bridge of volume V and length L suspended between discs of radius R and subject to a steady axial acceleration defined by a Bond number $B_{o,}$ after Martinez et al. [41]. The angle ϕ is defined in the inset.

Fig. 11 The maximum stable zone length of an isothermal liquid zone suspended between inert solids of radius R as a fucntion of Bond number: Comparison of theory and experiment. After Coriell et al. [90].

Fig. 12 Tolerable residual accleration (in units of g = 9.8 m s^{-2}) for experiments investigating resonance frequencies of liquid columns subject to axial acceleration , following Langbein [55]. a) sensitivity for different aspect ratios $\Lambda = L/2\pi R$, b)

change in sensitivity with number of nodes in the deformation for $\Lambda = 0.9999$.

Fig. 13 Curves of tolerable acceleration (in units of g = 9.8 m s^{-2}) versus frequency for a maximum liquid bridge shape change of 10% at B_o=0.002, g_o =1.42×10^{-5} g and C=0.001. The solid curve, the dotted curve and the dotted-dashed curve are the results for aspect ratios L/2R=2.6, 2.826 and 3.024, respectively. From Zhang and Alexander [91].

Fig. 14 Threshold intensity $g^* = g_T R^4 / \nu^2 d_\tau$ as a function of normalized frequency $S = \omega R^2/2\nu$ after Dewandre [57]. Here g_T is the maximum tolerable acceleration, d_τ the admissible displacement and r is the ratio of the drop density to that of the surrounding fluid.

Fig. 15 Plot of effective diffusivity, κ_{eff} vs. Wormsely number W_o, after Kurzweg [31].

Fig. 16 Dimensionless maximum velocity caused by impulse disturbances as a function of Fourier number $F_o = t\kappa^2/d$, after Heiss et al. [64]. Here t is the time [s], κ is the thermal diffusivity [$cm^2\ s^{-1}$], d is the diameter of the cylinder [cm]. The parameter Ra* is the Rayleigh number associated with the disturbance which is of dimensionless duration $F_o^* = 5.5(10)^{-3}$. $Ra^* = \beta_T\ gL^3\Delta T/\nu\kappa$, where L is the cylinder length [cm], ΔT is the temperature difference between the ends of the cylinder [K], β_T is the coefficient of thermal expansion [K^{-1}], g is the magnitude of the acceleration [cm s^{-2}] and ν is the kinematic viscosity [$cm^2\ s^{-1}$].

Fig. 17 Maximum lateral solute segregation $\Delta c/c_\infty$ (where c_∞ is the far-field solute concentration in the melt) in the crystal as a function of the period of the gravitational oscillation, after McFadden and Coriell [66].

Fig. 18 Lateral nonuniformity in composition, ξ, plotted as a function of time for an oscillatory residual acceleration with a maximum magnitude of $3\sqrt{2}(10)^{-6}$ g and a frequency of 10^{-3} Hz, acting parallel to the crystal-melt interface [67]. The initial state was purely diffusive.

Fig. 19 Lateral nonuniformity in composition, ξ, plotted as a function of time for a residual acceleration consisting of a steady part with magnitude $\sqrt{2}(10)^{-6}$ g and an oscillatory part with a maximum magnitude of $3\sqrt{2}(10)^{-6}$ g and a frequency of 10^{-3} Hz, acting parallel to the crystal-melt interface [67]. The calculation was started from a steady flow associated with a $\sqrt{2}(10)^{-6}$ g acceleration acting parallel to the interface.

Fig.20 Lateral nonuniformity in composition, ξ, plotted as a function of time for a multi-component disturbance consisting of a steady low g background plus two periodic components: $\mathbf{g}(t) = \mathbf{g}_o + \mathbf{g}_1 \cos(2\pi 10^{-3} t) + \mathbf{g}_2 \cos(2\pi 10^{-2} t)$, where $|\mathbf{g}_o| = \sqrt{2}(10)^{-6}$, $|\mathbf{g}_1| = 3\sqrt{2}(10)^{-6}$ and $|\mathbf{g}_2| = 3\sqrt{2}(10)^{-5}$ [67]. The calculation was started from a steady flow associated with a $\sqrt{2}(10)^{-6}$ g acceleration acting perpendicular to the interface.

Fig. 21 Lateral nonuniformity $|\xi|$ as a function of time for accelerations taken from a

sample time series (see inset) constructed from data obtained on Spacelab 3 [69]. The acceleration consists of a repeated "noise" segment (length 10 seconds, 10^{-1} Hz $< f <$ 1 Hz) and a thruster firing event (length 10 seconds, 10^{-1} Hz $< f <$ 13 Hz). The latter is introduced at 10 and 80 seconds.

Fig. 22 Sensitivity of crystal growth from solution to various periodic disturbances. The solid line separates tolerable responses (10% or less growth rate fluctuations) from intolerable ones. For each case, the numbers correspond to the ratio $g\beta\Delta c/f\,v^*$, which is an estimate of the the ratio of bouyancy and inertial forces. After Nadarajah et al. [102].

Fig. 23 Residual accelerations measured on orbit (in units of g = 9.8 m s^{-2}). (Data courtesy of Dr. H. Hamacher, DLR, and M.J.B. Rogers Univ. of Alabama in Huntsville.) The Spacelab 3 (SL-3) data are restricted to measured frequencies between 10^{-3} and 1 Hz. The points corresponding to Sled, Hop, Drop, Treadmill, Quiet, FPM ops, Stowage, refer to activities and experiments on the D-1 mission. FPM ops stands for Fluid Physics Module operations, P RCS and V RCS refer to the primary and vernier thrusters. The drag and rotation entries correspond to accelerations arising from slow variations in atmospheric drag during an orbit and attitude changes involving rotation.

Fig. 24 Acceleration sensitivity curves from selected examples discussed earlier superimposed on Fig. 23. Curves 1 and 3 correspond to the cases n=1, Λ=0.9999 and n=1, Λ =0.9 in Fig. 12 a, curve 2 corresponds to n=2 and Λ=0.9999 in Fig. 12 b. Curve 4 corresponds to the most sensitive case of zone shape change in Fig. 13, and curves 5 and 6 respectively correspond to the semi-conductor and metal melt growth experiments from Fig. 4. Curve 7 represents the thermo-diffusion experiment of Fig. 5.

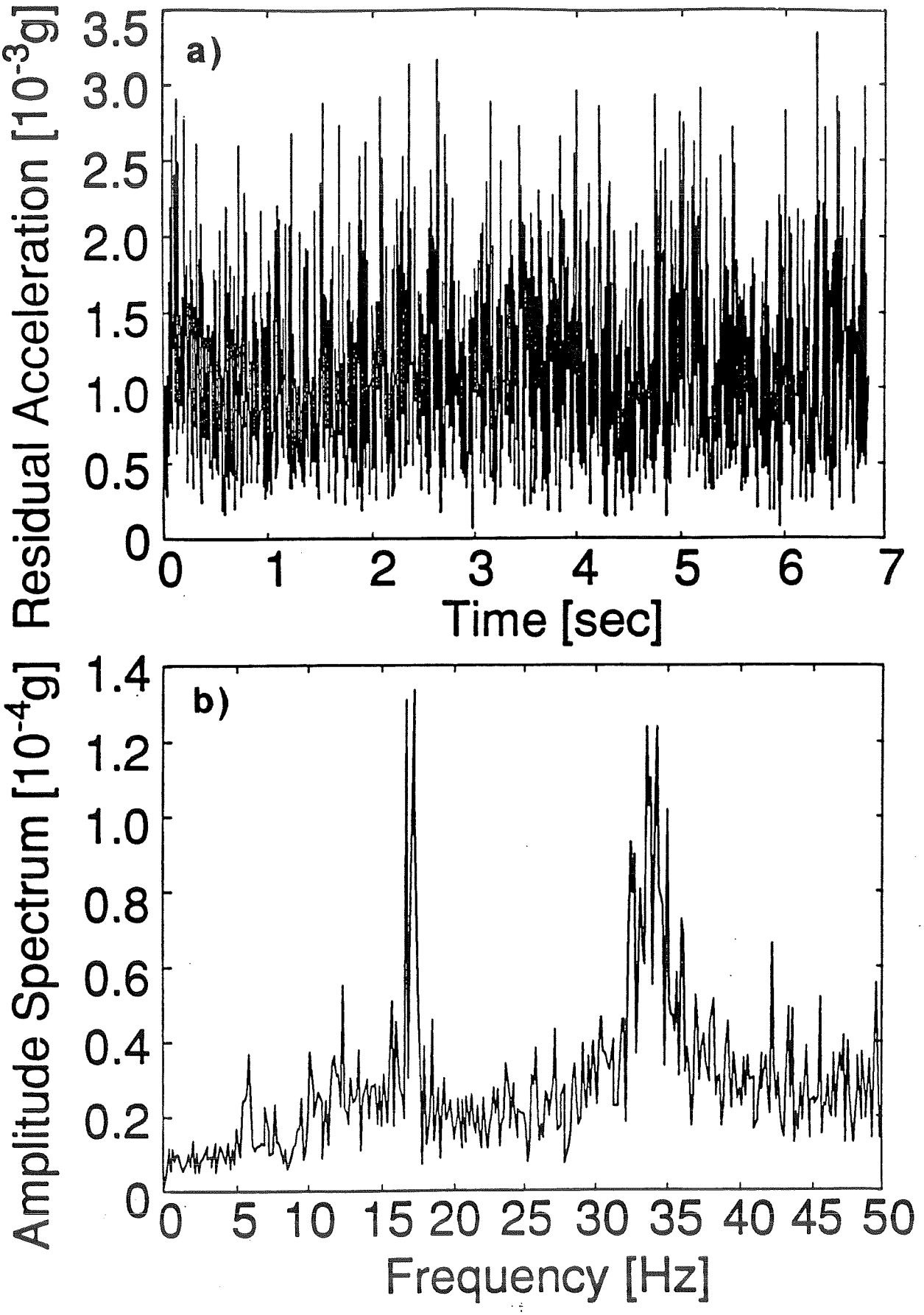
a)
Residual Acceleration [10-3g]
3.5
3.0
2.5
2.0
1.5
1.0
0.5
0
0 1 2 3 4 5 6 7
Time [sec]
b)
Amplitude Spectrum [10-4g]
1.4
1.2
1.0
0.8
0.6
0.4
0.2
0
0 5 10 15 20 25 30 35 40 45 50
Frequency [Hz]

Fig. 1

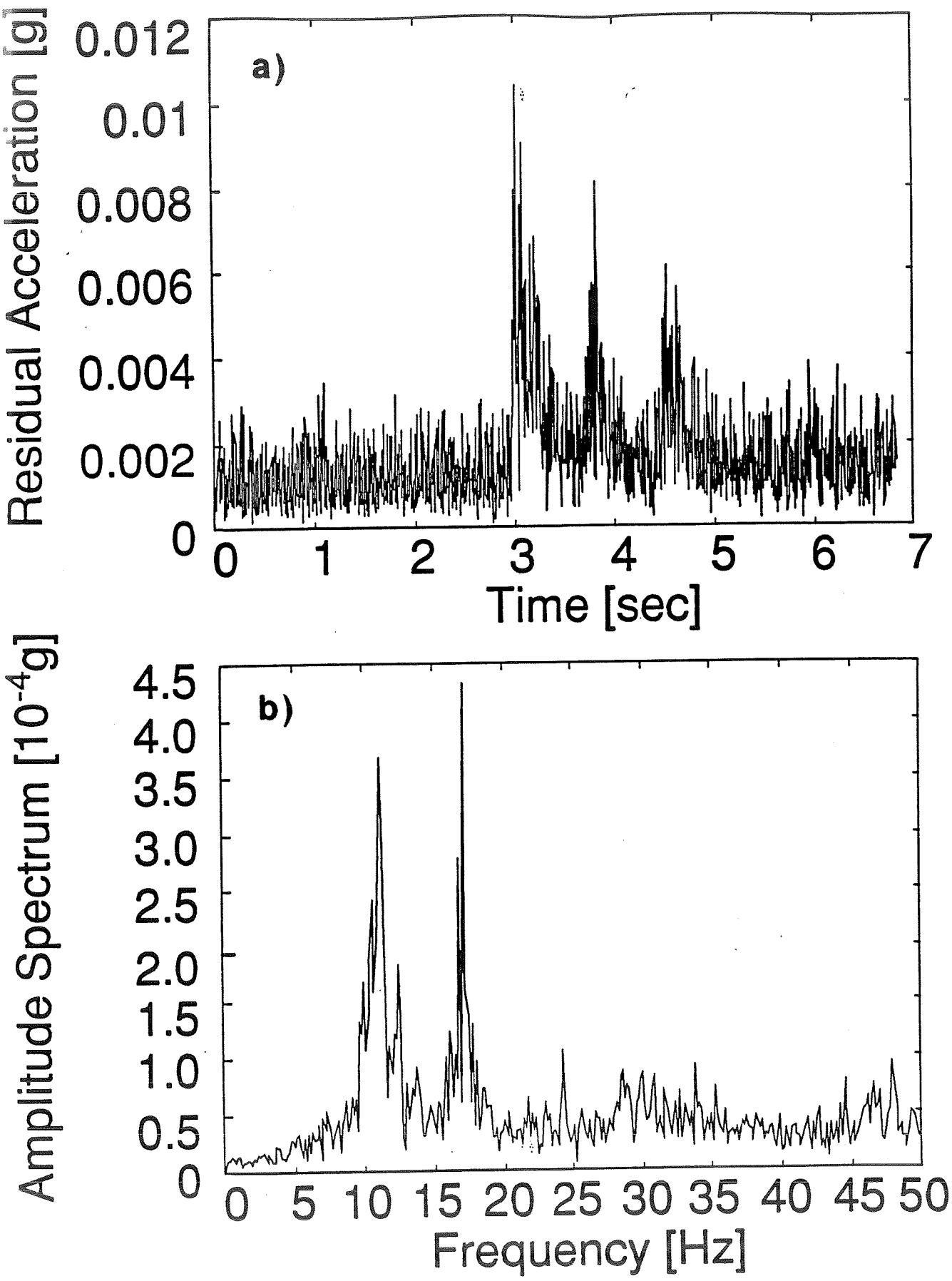
a)
Residual Acceleration [g]
0.012
0.01
0.008
0.006
0.004
0.002
0
0 1 2 3 4 5 6 7
Time [sec]
b)
Amplitude Spectrum [10^{-4}g]
4.5
4.0
3.5
3.0
2.5
2.0
1.5
1.0
0.5
0
0 5 10 15 20 25 30 35 40 45 50
Frequency [Hz]

Fig. 2

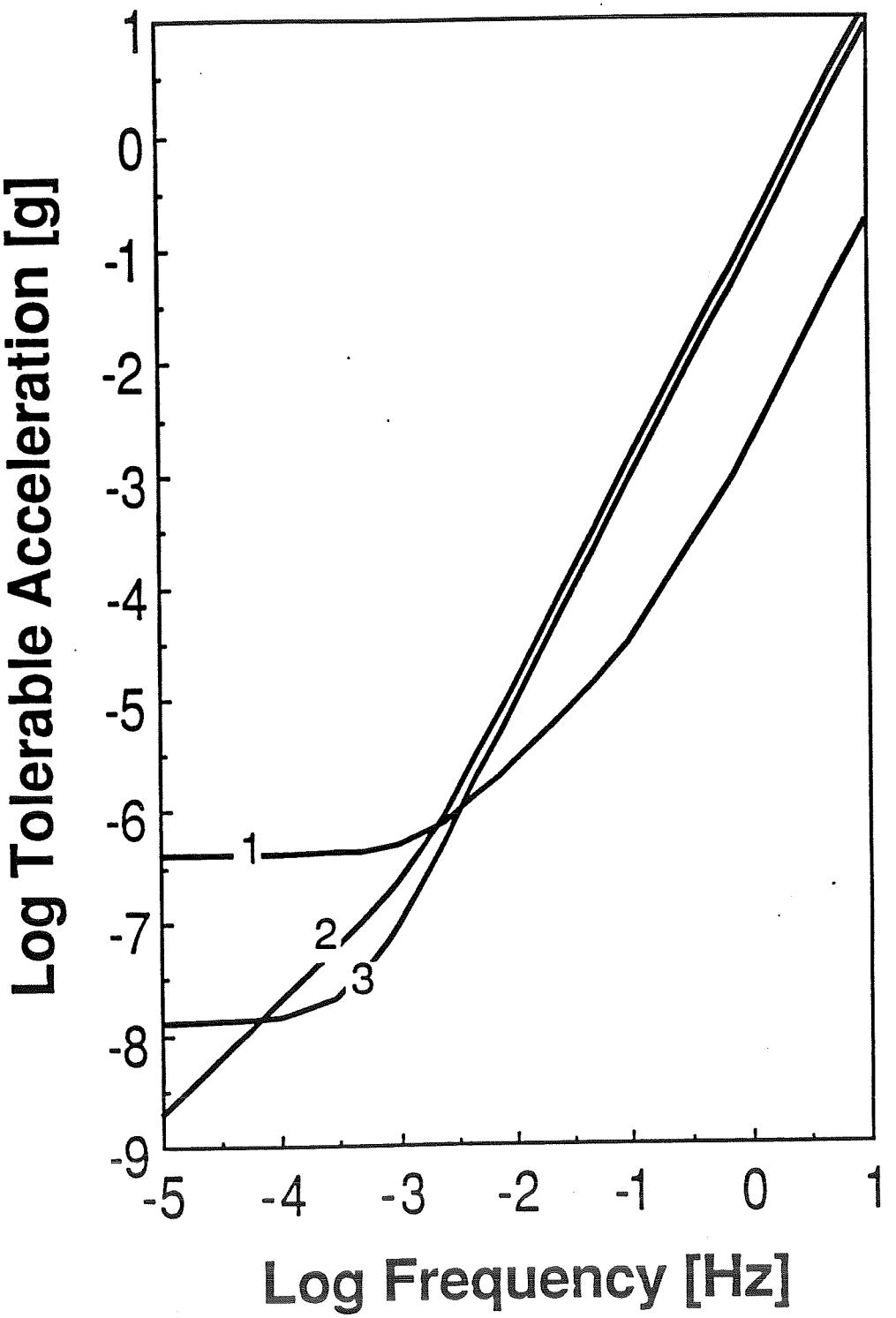
Log Tolerable Acceleration [g]
1
0
-1
-2
-3
-4
-5
-6
-7
-8
-9
-5
-4
-3
-2
-1
0
1
Log Frequency [Hz]
1
2
3

Fig. 3

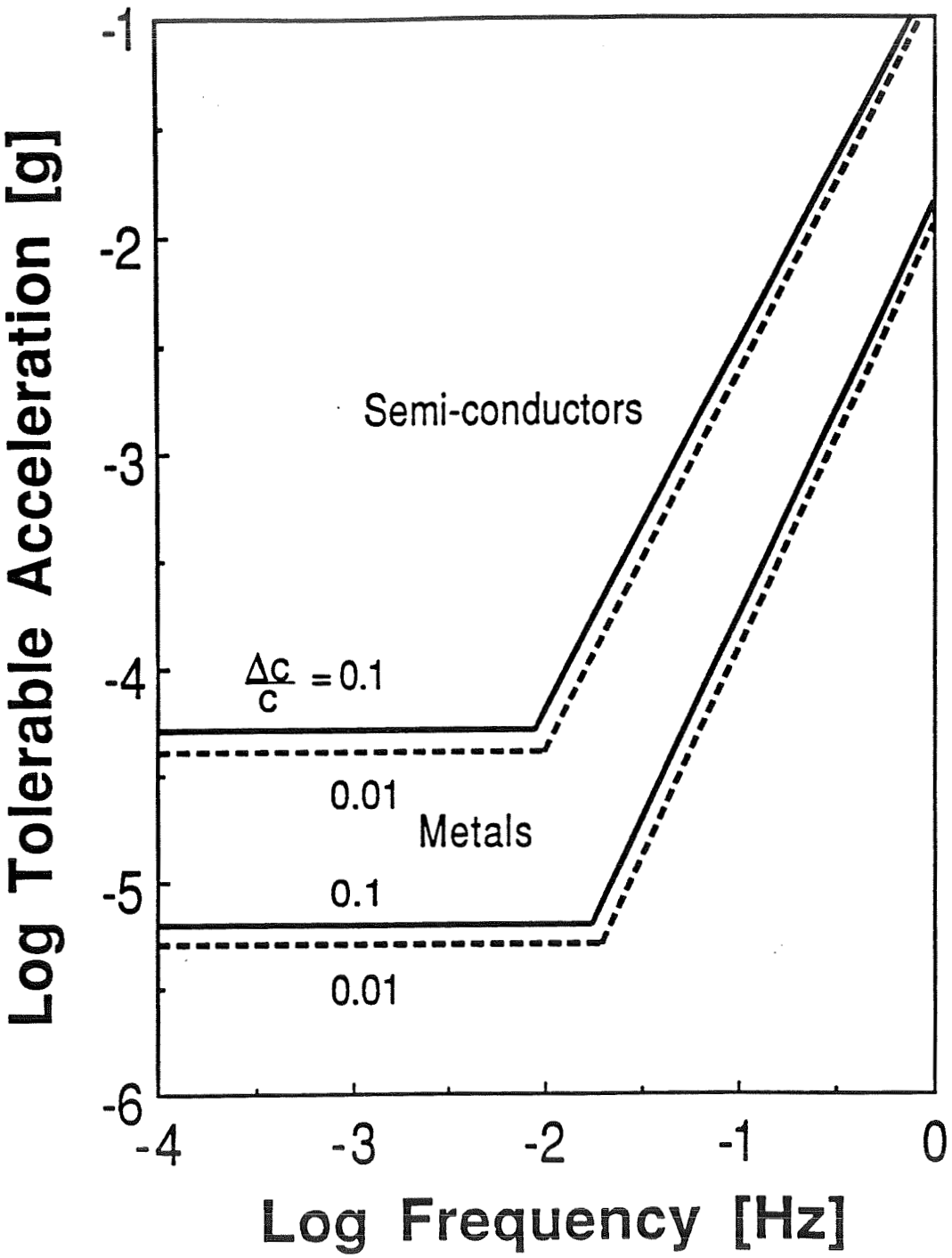
Log Tolerable Acceleration [g]
-1
-2
-3
-4
-5
-6
-4
-3
-2
-1
0
Log Frequency [Hz]
Semi-conductors
Δc/c = 0.1
0.01
Metals
0.1
0.01

Fig. 4

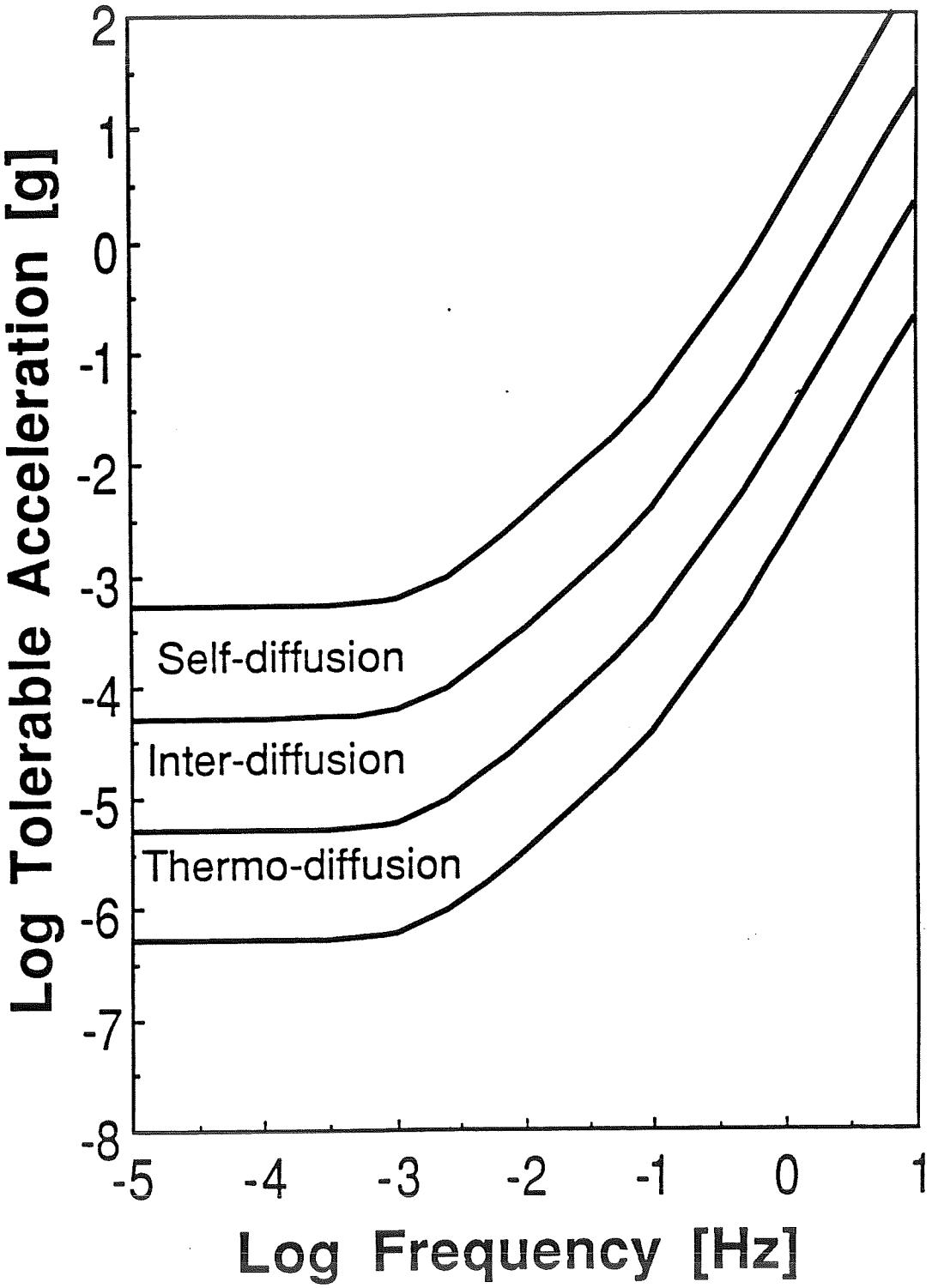
Log Tolerable Acceleration [g]
2
1
0
-1
-2
-3
-4
-5
-6
-7
-8
Self-diffusion
Inter-diffusion
Thermo-diffusion
-5
-4
-3
-2
-1
0
1
Log Frequency [Hz]

Fig. 5

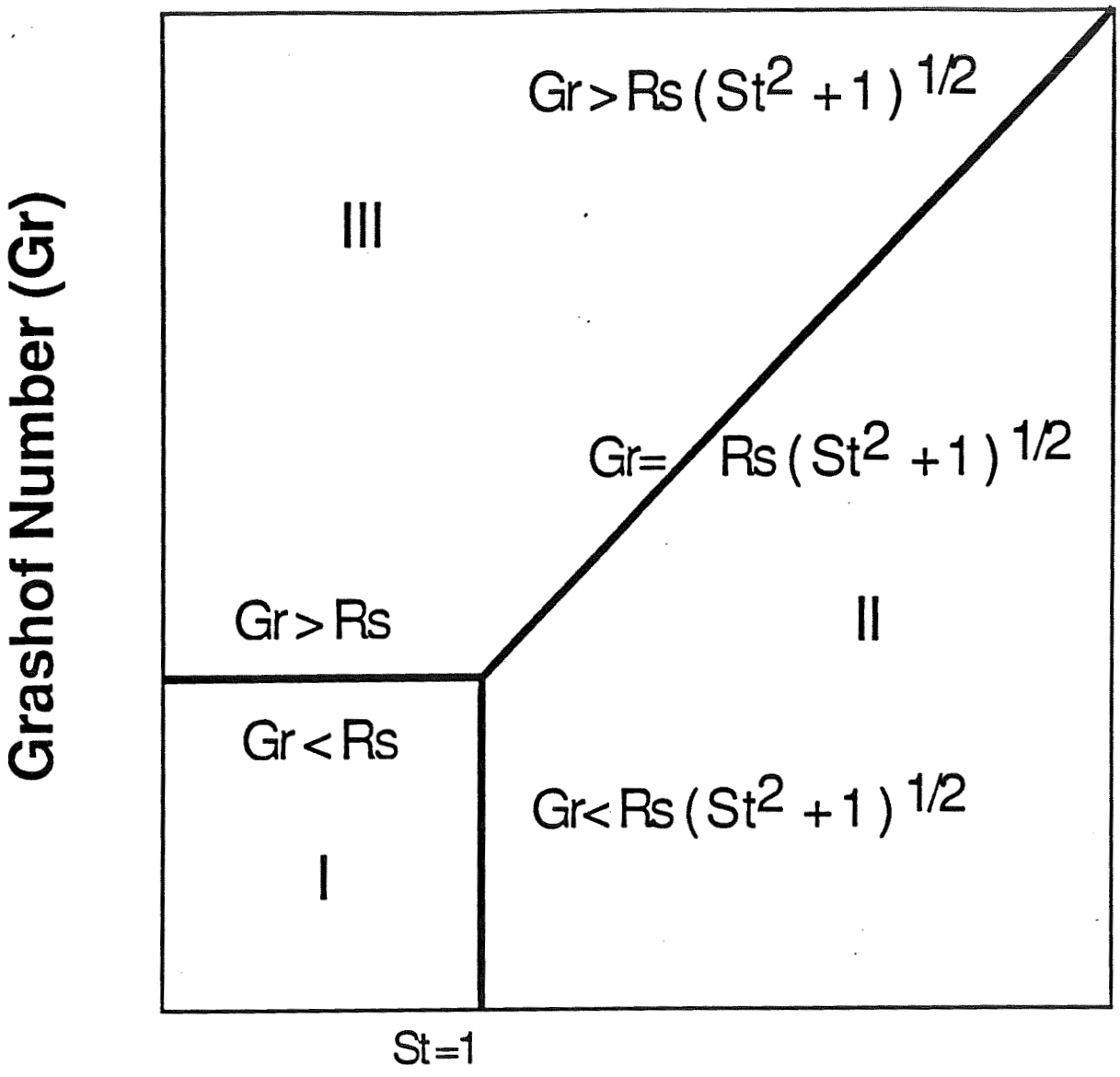
Gr > Rs (St2 + 1) 1/2
III
Gr = Rs (St2 + 1) 1/2
Gr > Rs
II
Gr < Rs
Gr < Rs (St2 + 1) 1/2
I
St = 1
Grashof Number (Gr)
Strouhal Number (St)

Fig.6

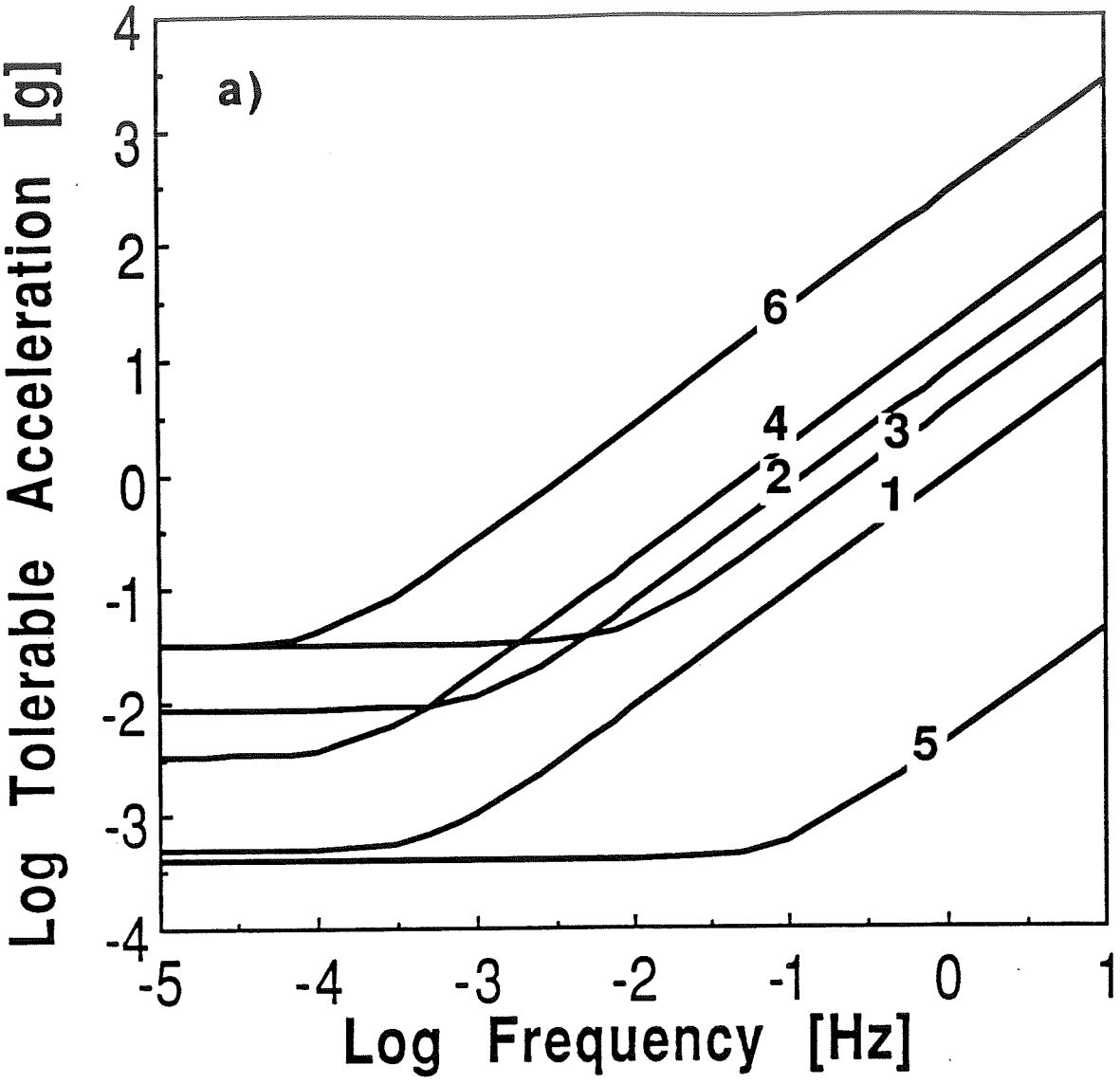
a)
Log Tolerable Acceleration [g]
Log Frequency [Hz]
4
3
2
1
0
-1
-2
-3
-4
-5
-4
-3
-2
-1
0
1
6
4
3
2
1
5

Fig. 7a

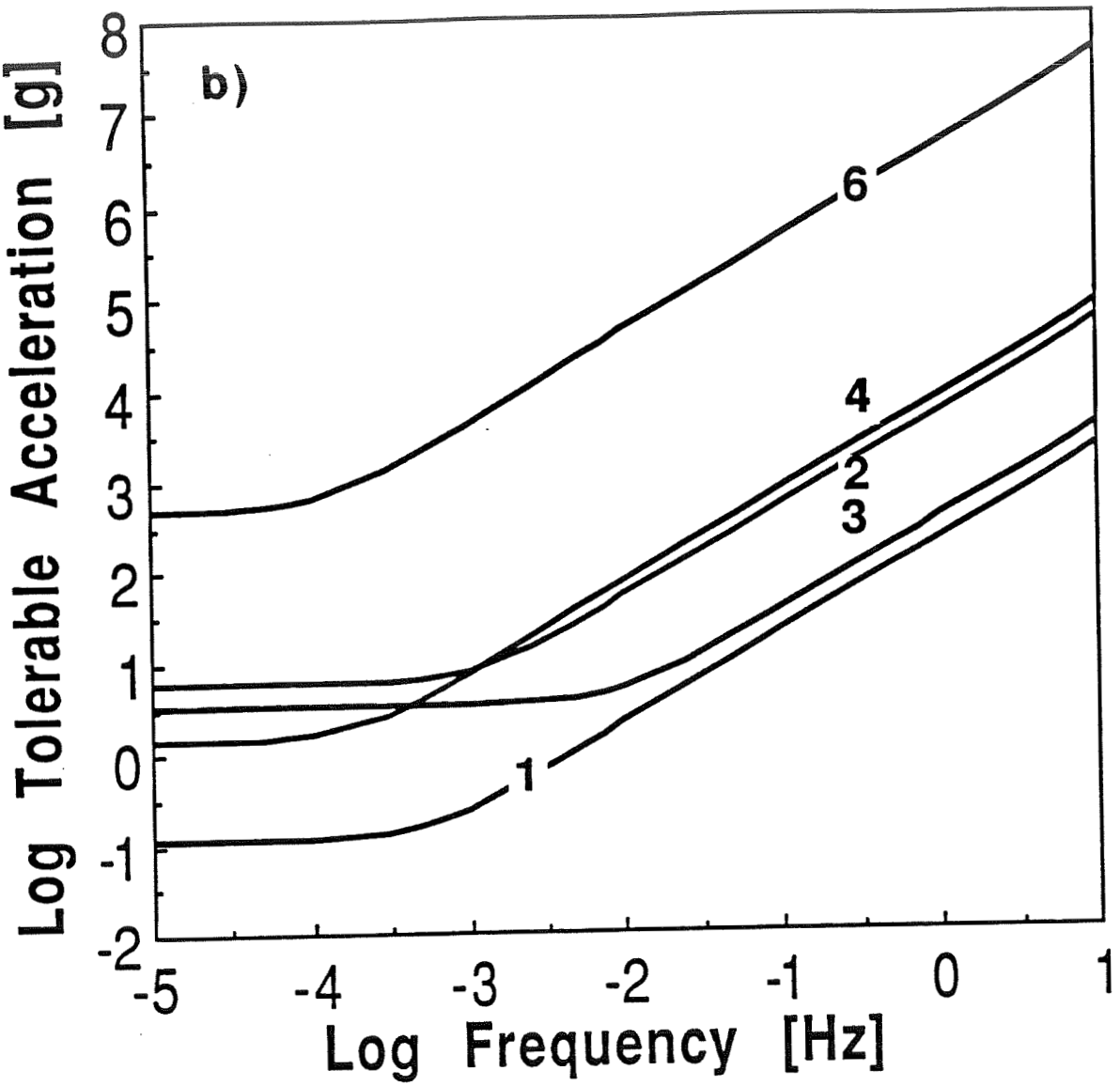
b)
Log Tolerable Acceleration [g]
8
7
6
5
4
3
2
1
0
-1
-2
-5
-4
-3
-2
-1
0
1
Log Frequency [Hz]
6
4
2
3
1

Fig. 7 b

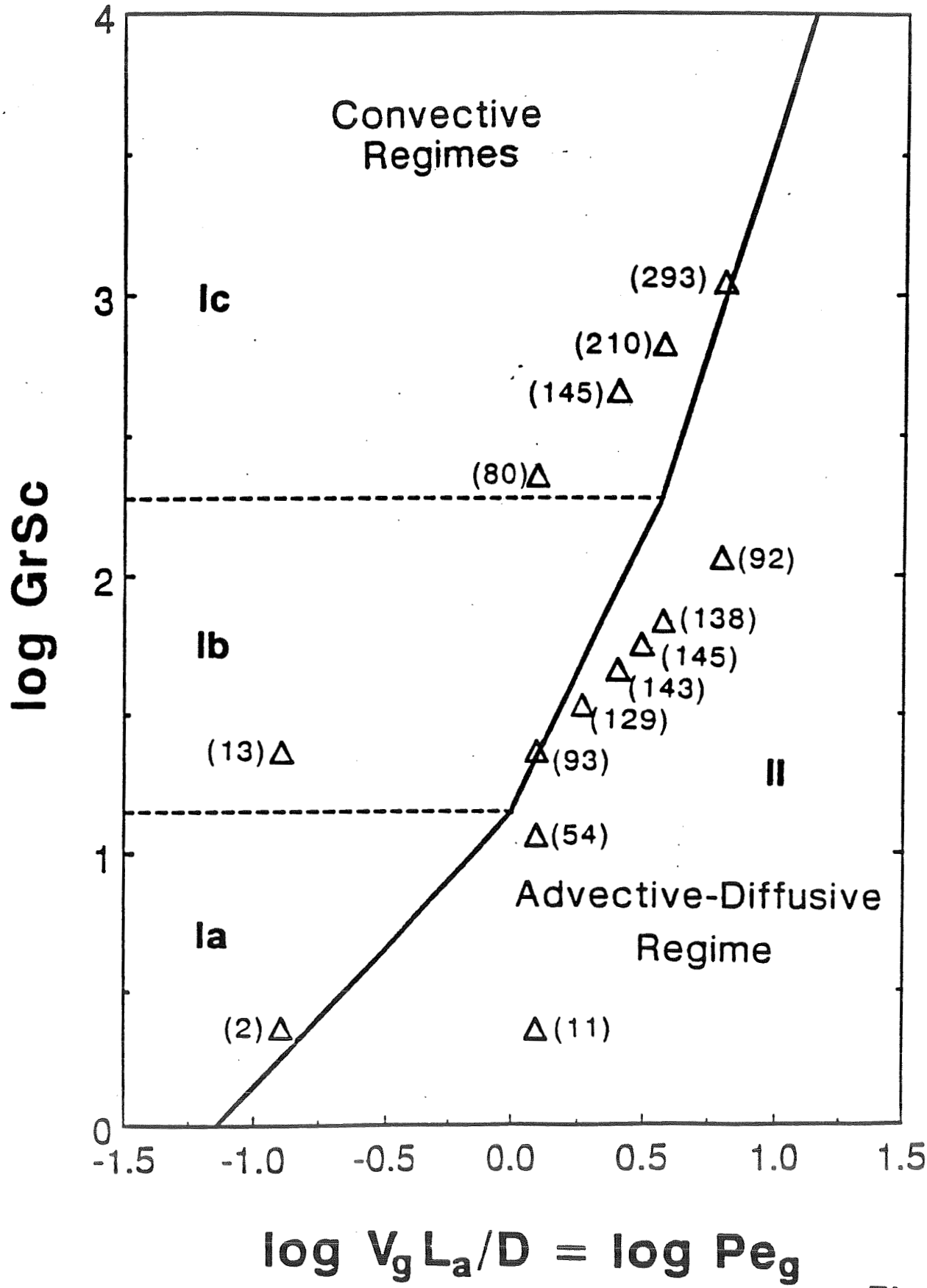
Convective
Regimes
Ic
Ib
Ia
II
Advective-Diffusive
Regime
(293)Δ
(210)Δ
(145)Δ
(80)Δ
Δ(92)
Δ(138)
Δ(145)
Δ(143)
Δ(129)
(13)Δ
Δ(93)
Δ(54)
(2)Δ
Δ(11)
log GrSc
log $V_g L_a/D$ = log Pe_g
4
3
2
1
0
-1.5
-1.0
-0.5
0.0
0.5
1.0
1.5

Fig. 8

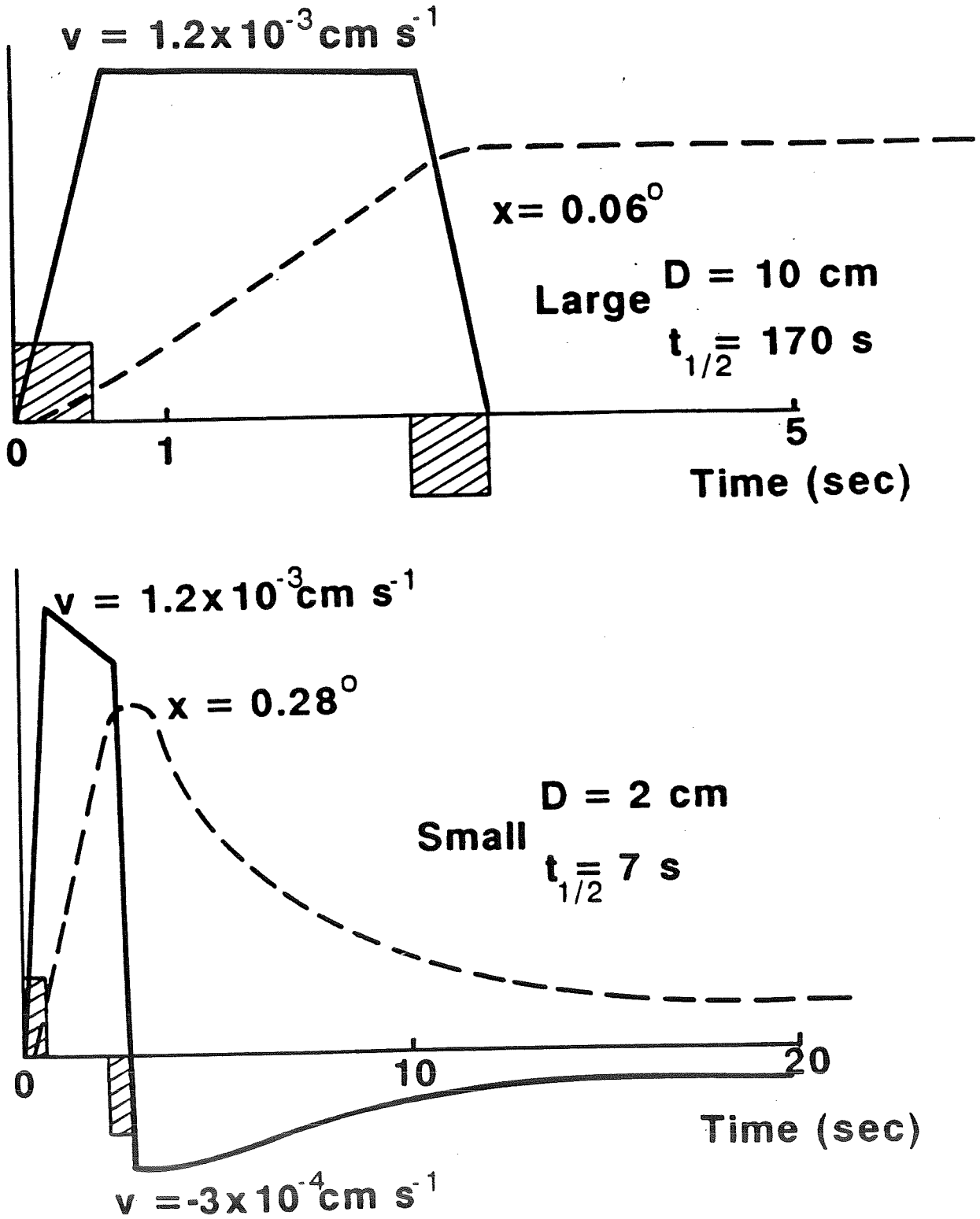
v = 1.2x10⁻³cm s⁻¹
x= 0.06°
Large
D = 10 cm
t1/2 = 170 s
0
1
5
Time (sec)
v = 1.2x10⁻³cm s⁻¹
x = 0.28°
Small
D = 2 cm
t1/2 = 7 s
0
10
20
Time (sec)
v =-3x10⁻⁴cm s⁻¹

Fig. 9

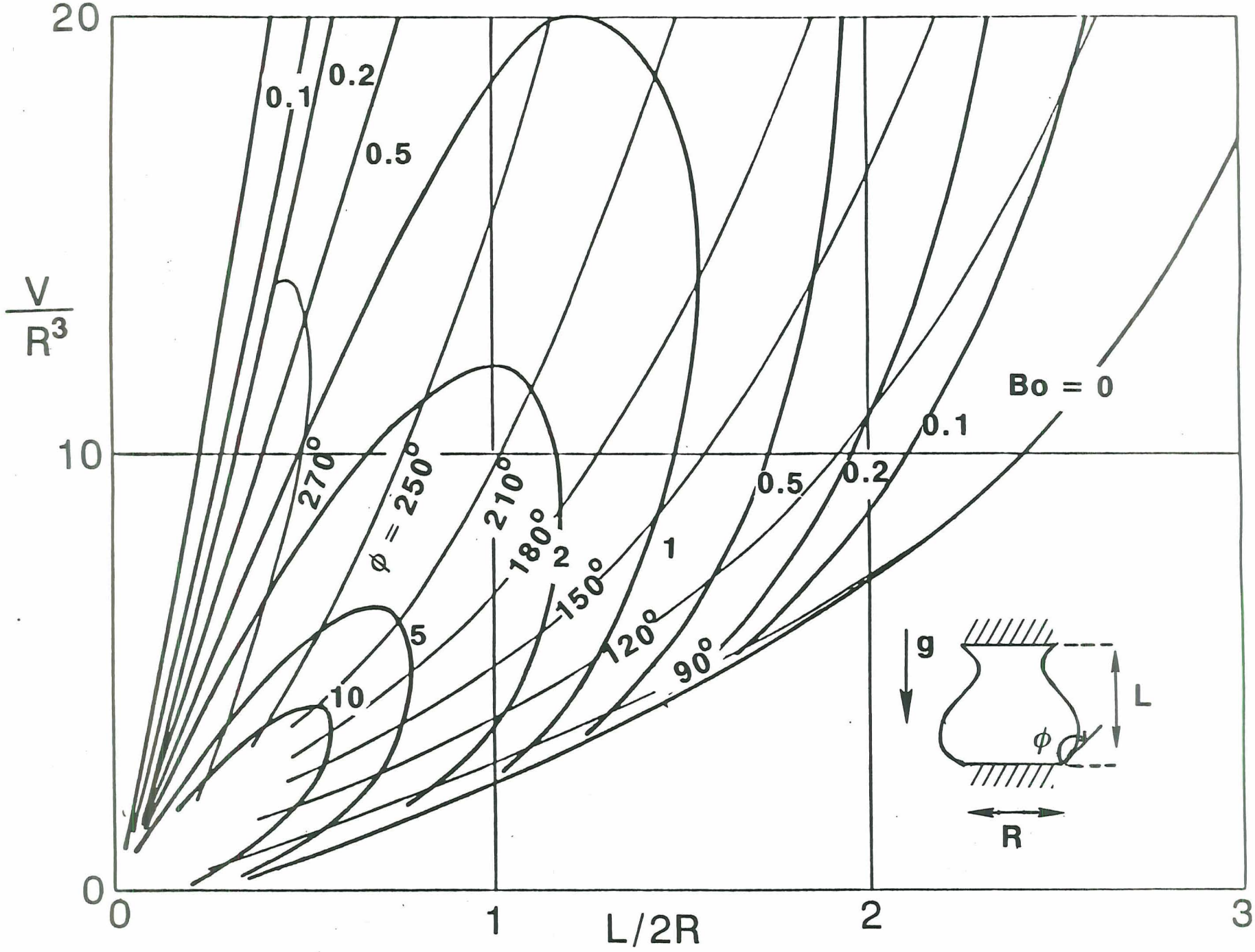
20
10
0
0
1
2
3
V/R³
L/2R
0.1
0.2
0.5
1
2
5
10
Bo = 0
0.1
0.2
0.5
270°
250°
210°
180°
150°
120°
90°
φ
g
L
R

Fig. 10

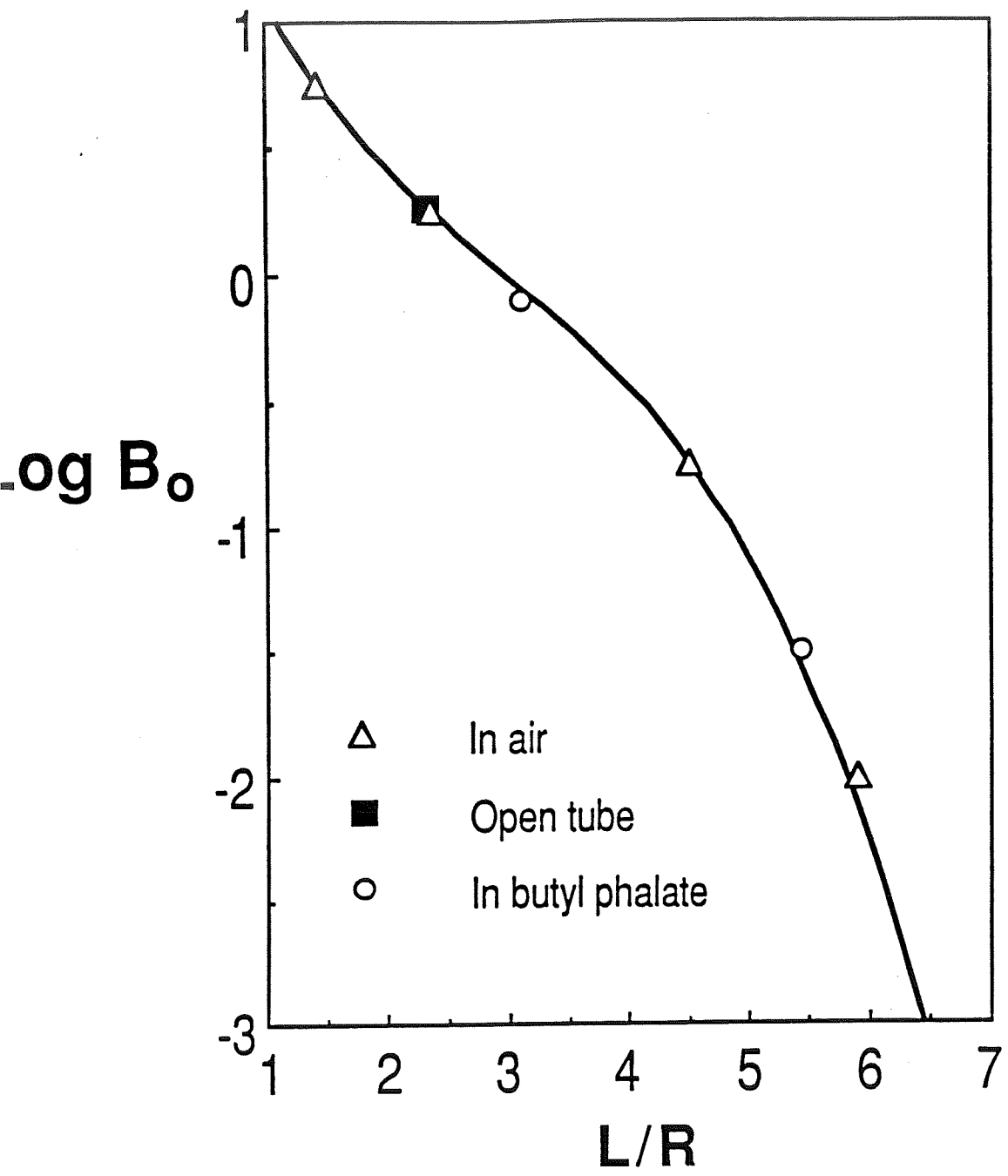

Fig. 11

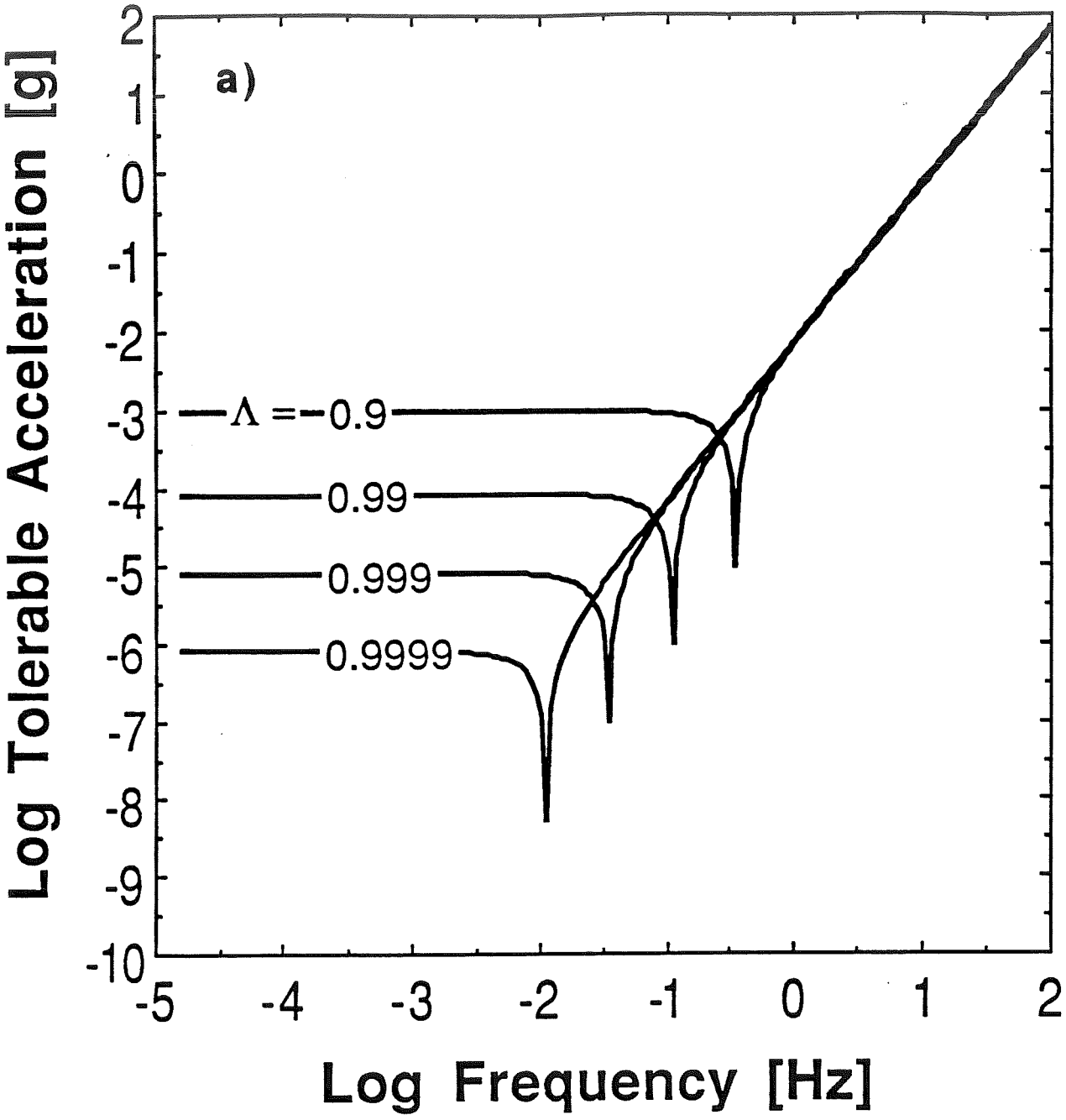
a)
Log Tolerable Acceleration [g]
Log Frequency [Hz]
Λ = 0.9
0.99
0.999
0.9999
2
1
0
-1
-2
-3
-4
-5
-6
-7
-8
-9
-10
-5
-4
-3
-2
-1
0
1
2

Fig. 12 a

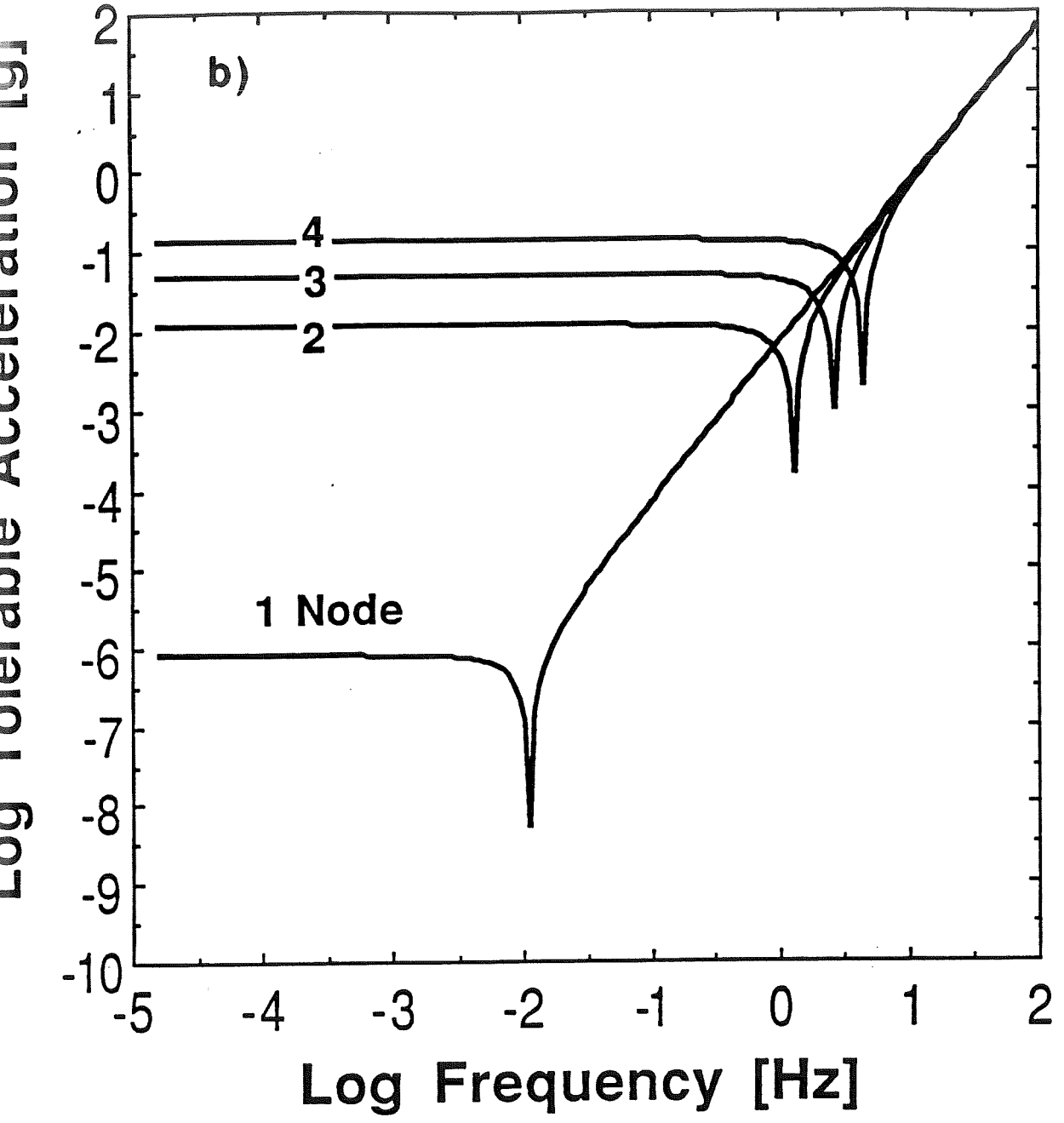
b)
4
3
2
1 Node
Log Tolerable Acceleration [g]
Log Frequency [Hz]
2
1
0
-1
-2
-3
-4
-5
-6
-7
-8
-9
-10
-5
-4
-3
-2
-1
0
1
2

Fig. 12 b

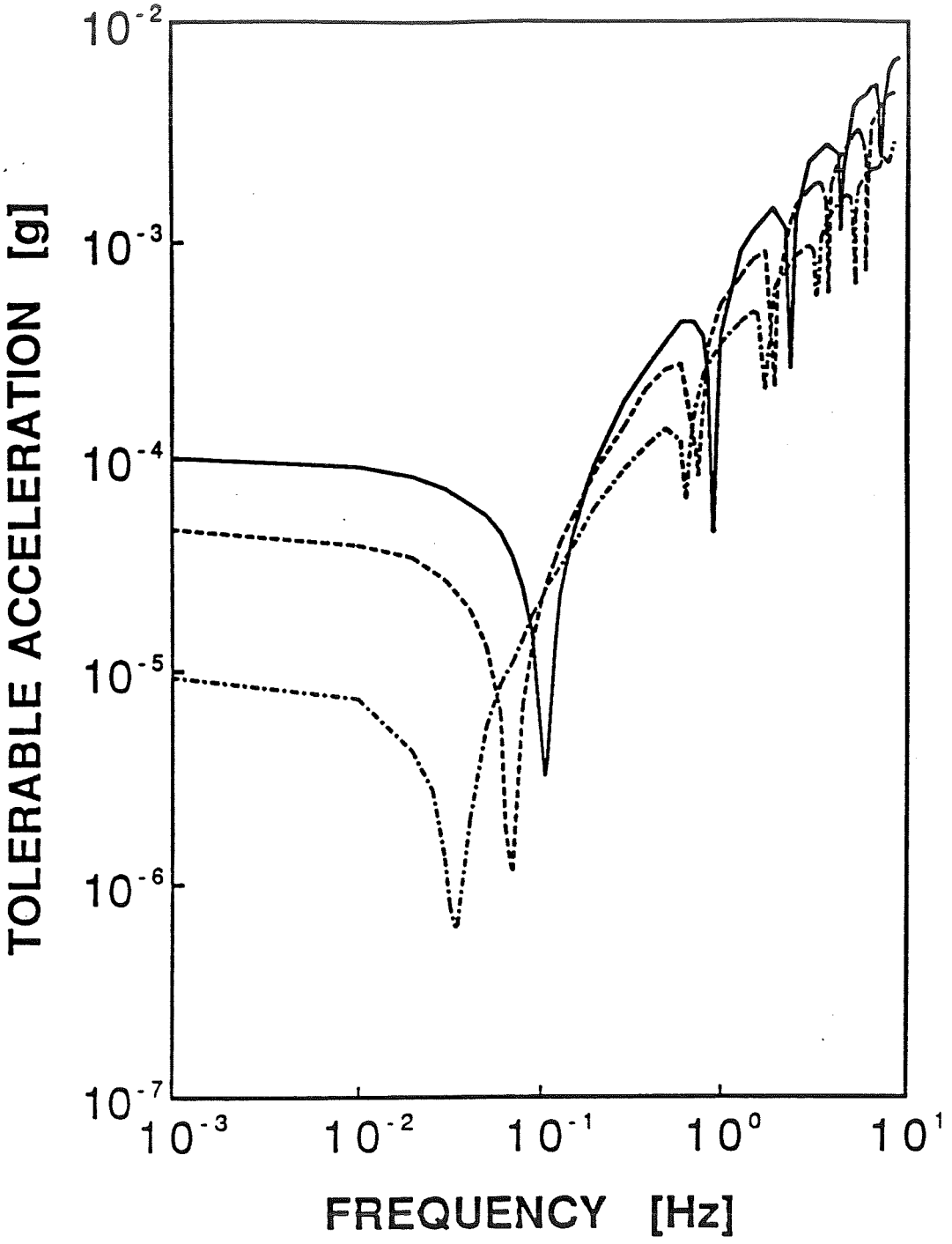
TOLERABLE ACCELERATION [g]
10-2
10-3
10-4
10-5
10-6
10-7
10-3
10-2
10-1
100
101
FREQUENCY [Hz]

Fig. 13

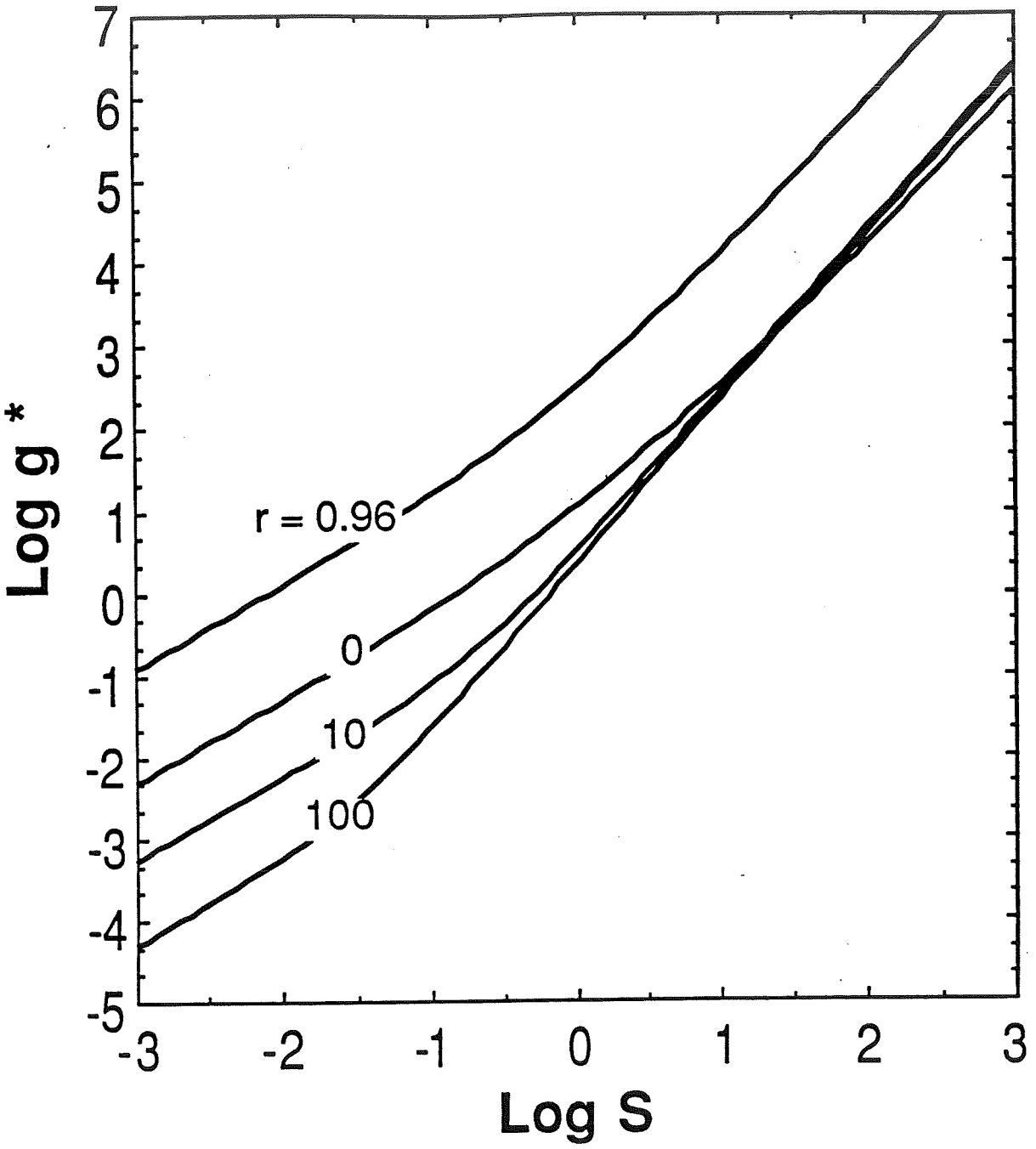

Fig. 14

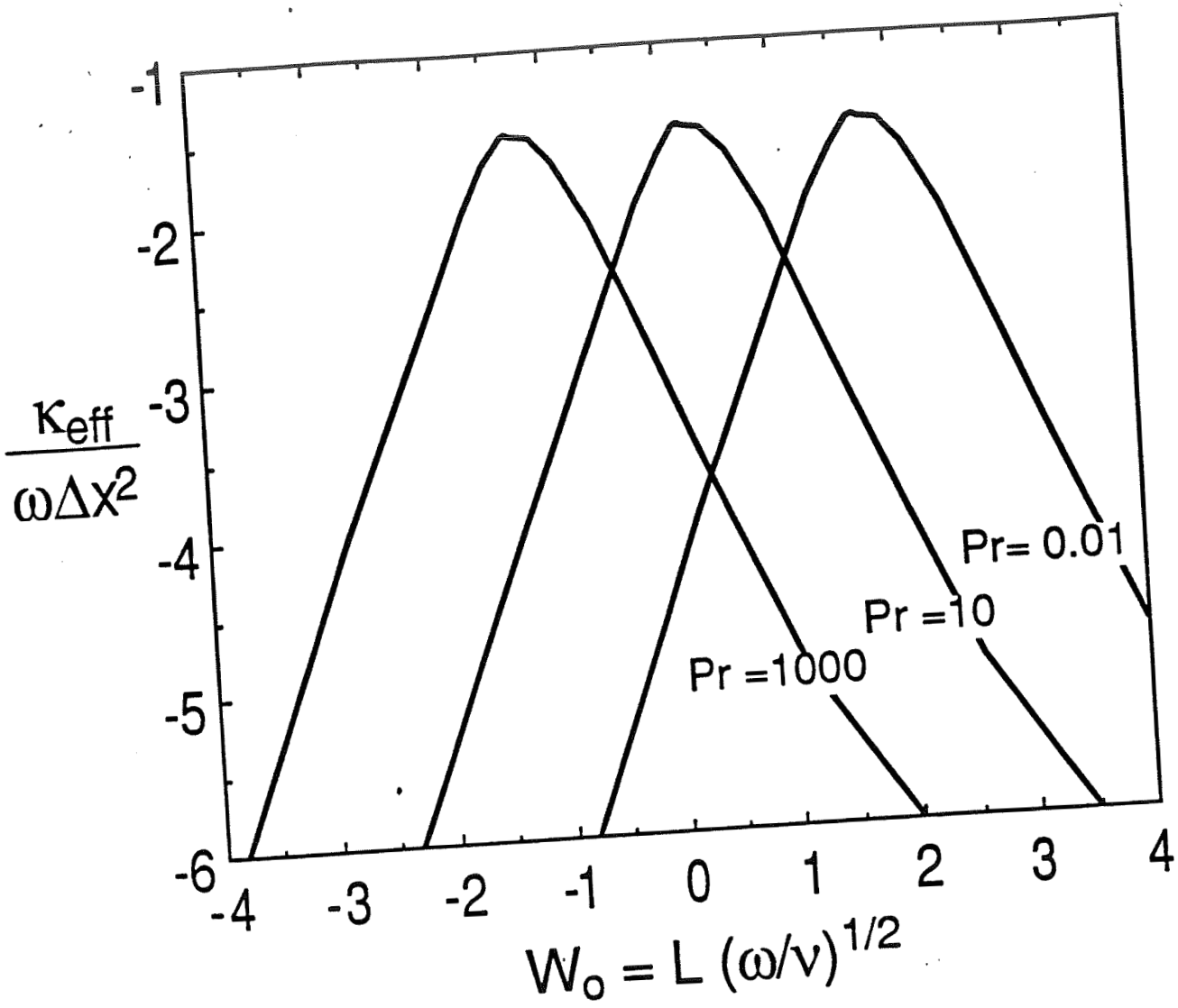

Fig. 15

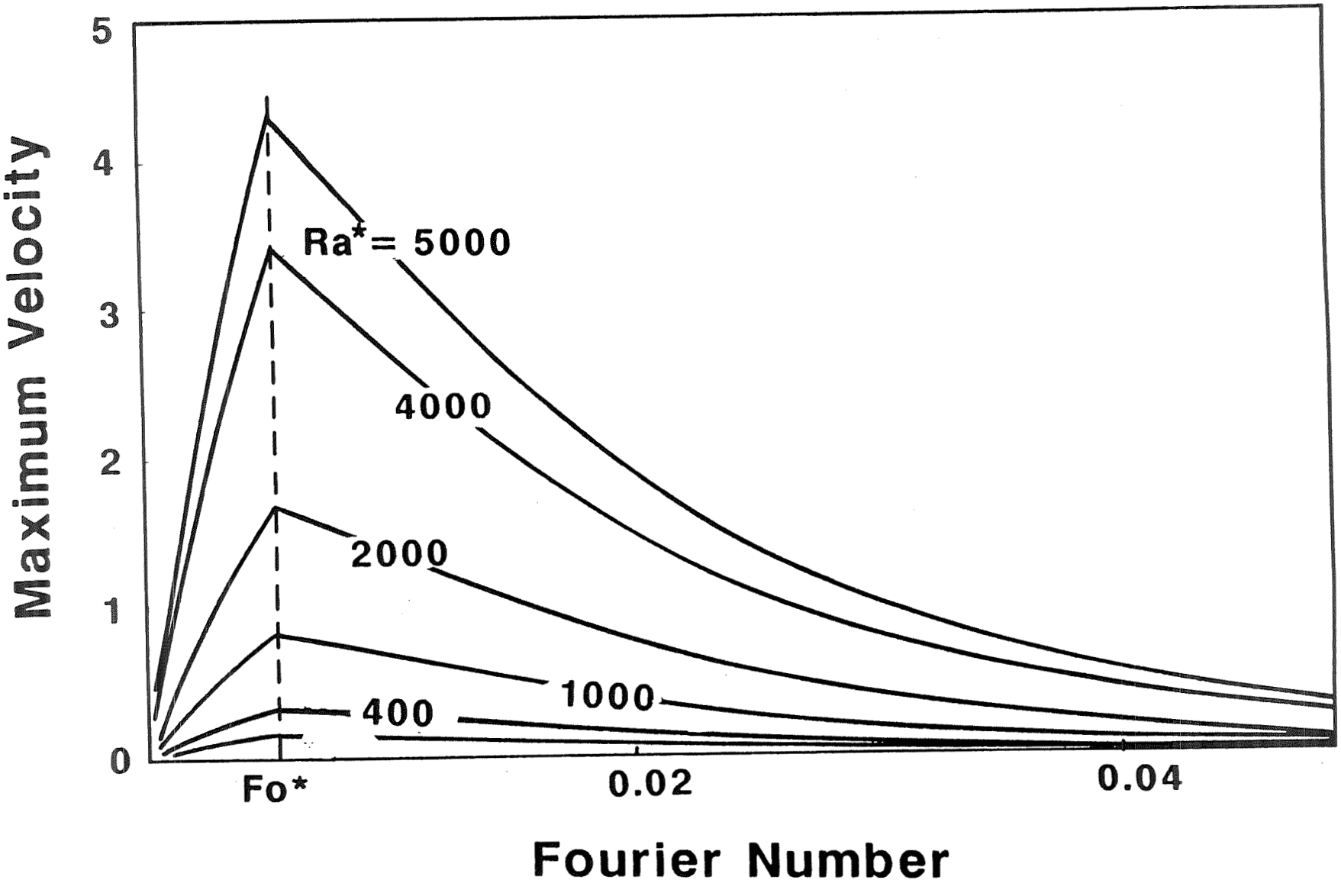
Maximum Velocity
5
4
3
2
1
0
Ra* = 5000
4000
2000
1000
400
Fo*
0.02
0.04
Fourier Number

Fig. 16

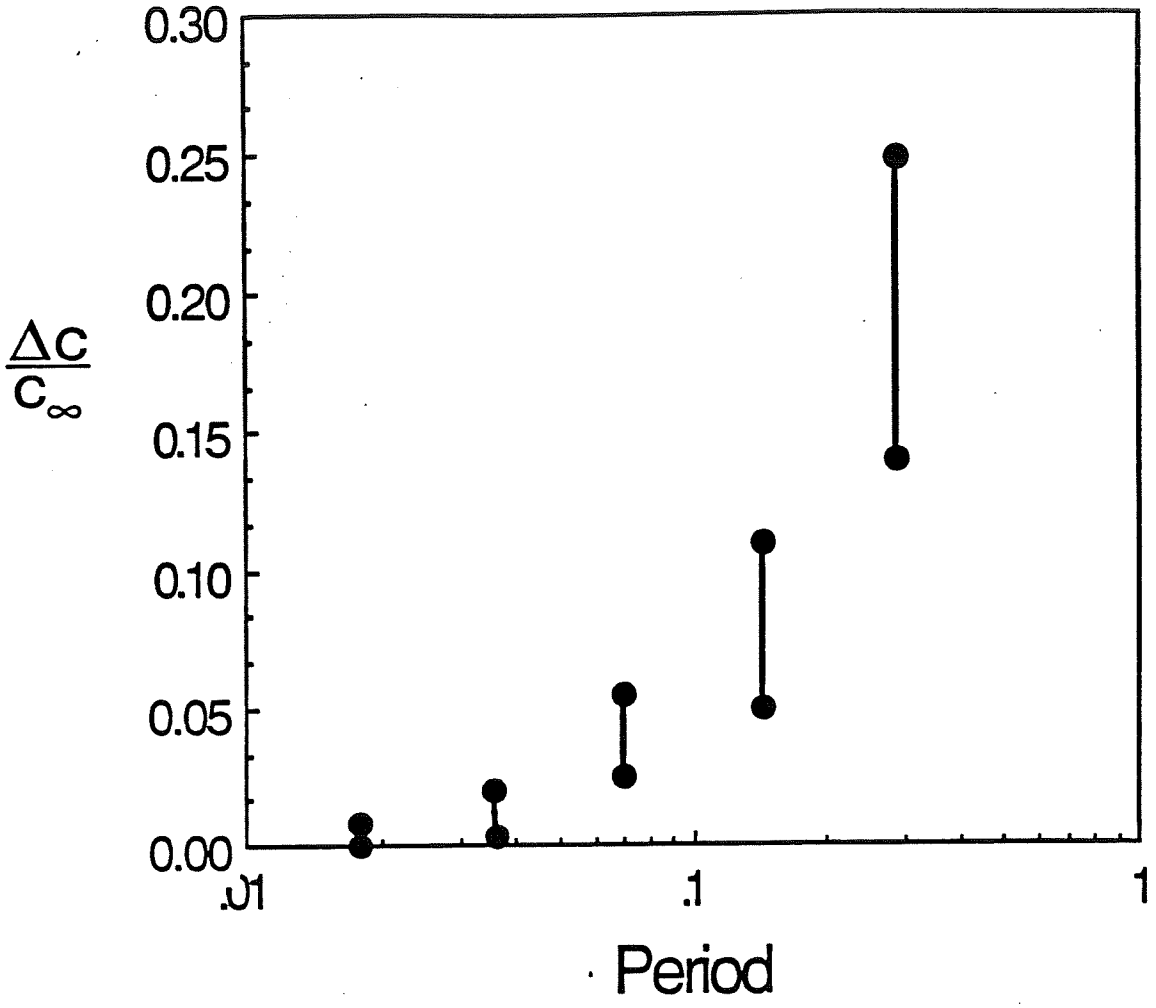

Fig. 17

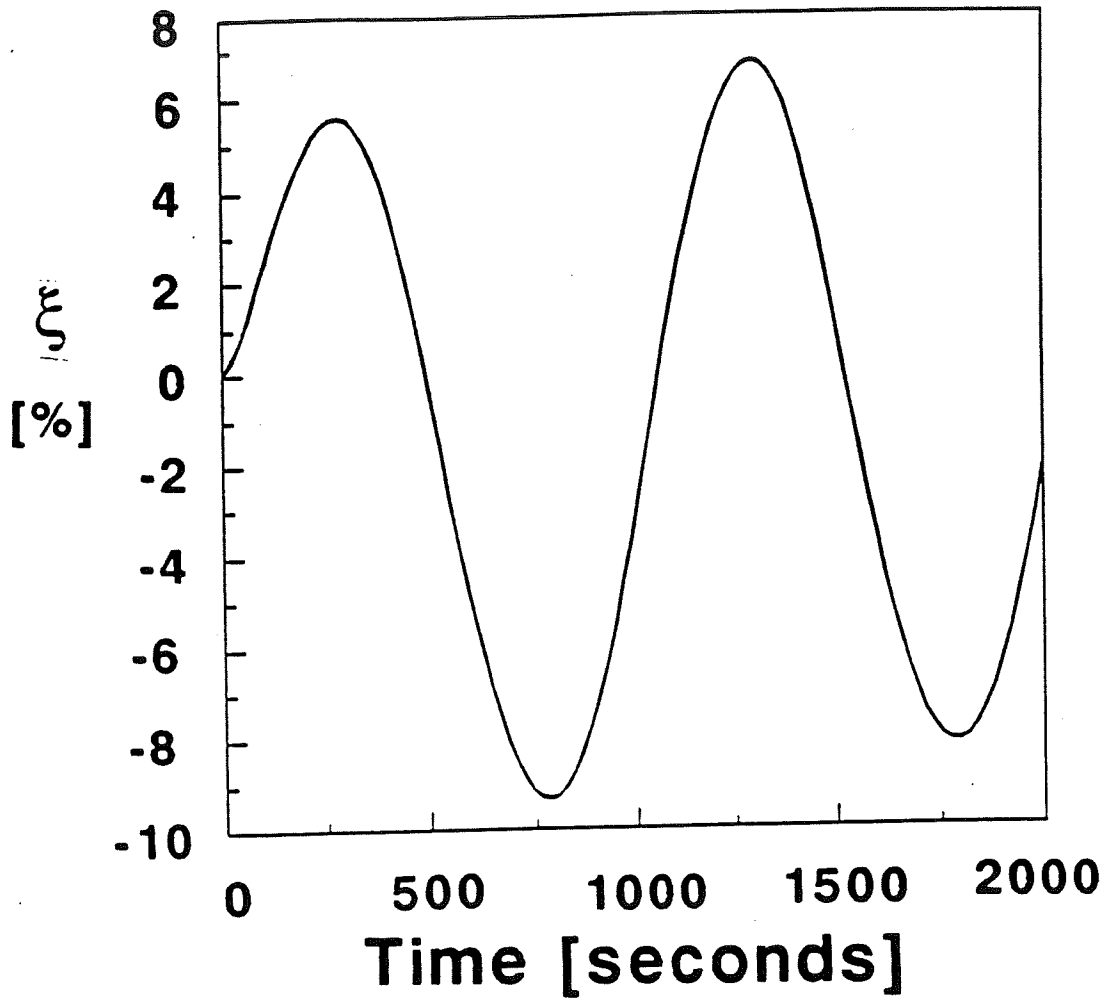

Fig. 18

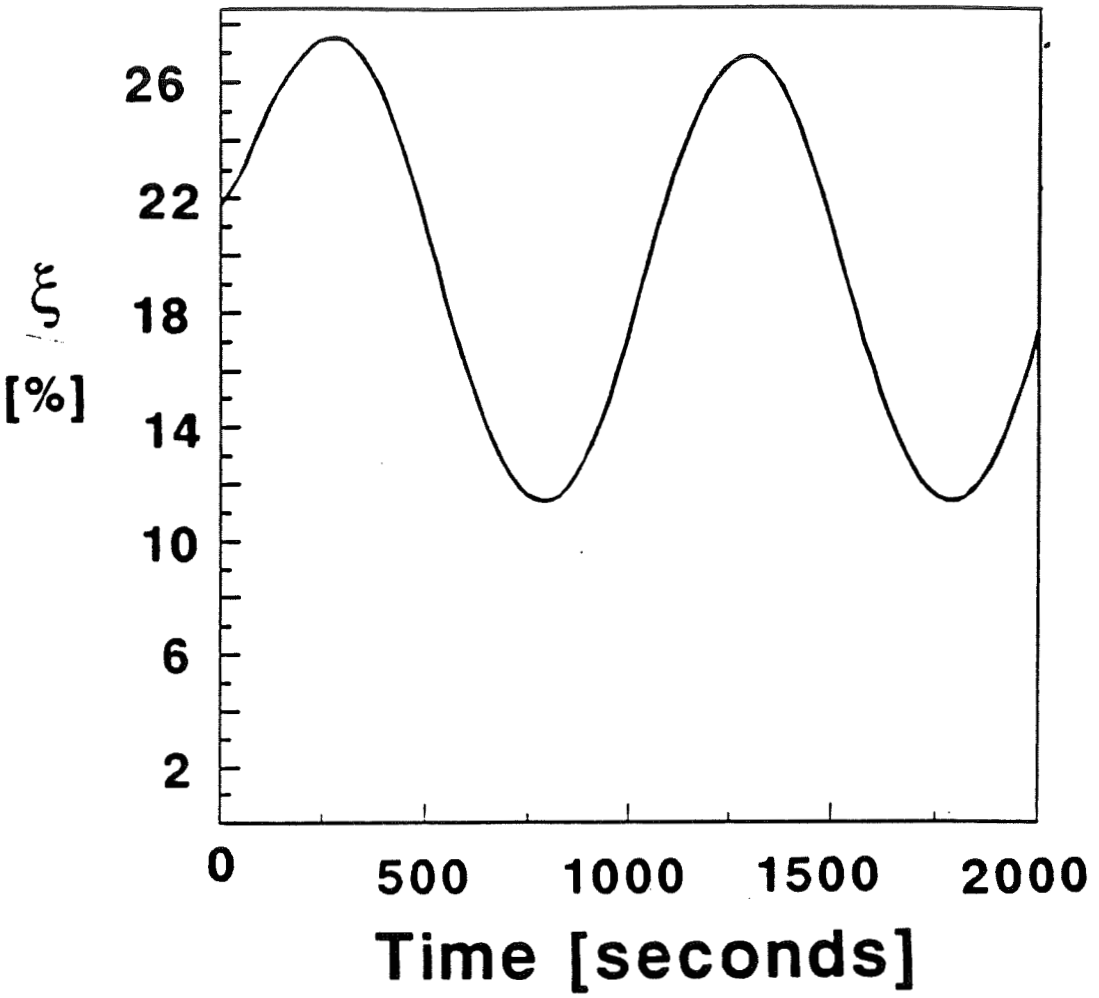

Fig. 19

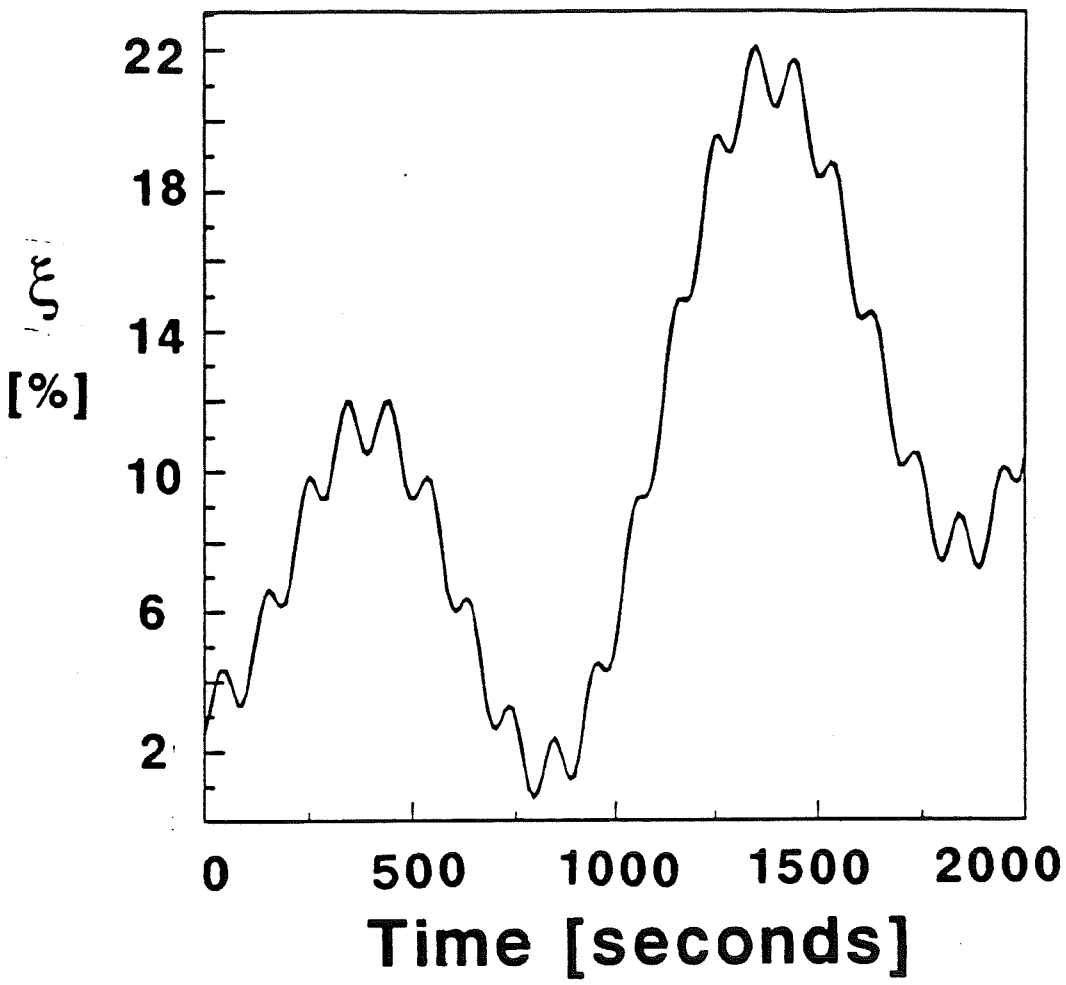

Fig. 20

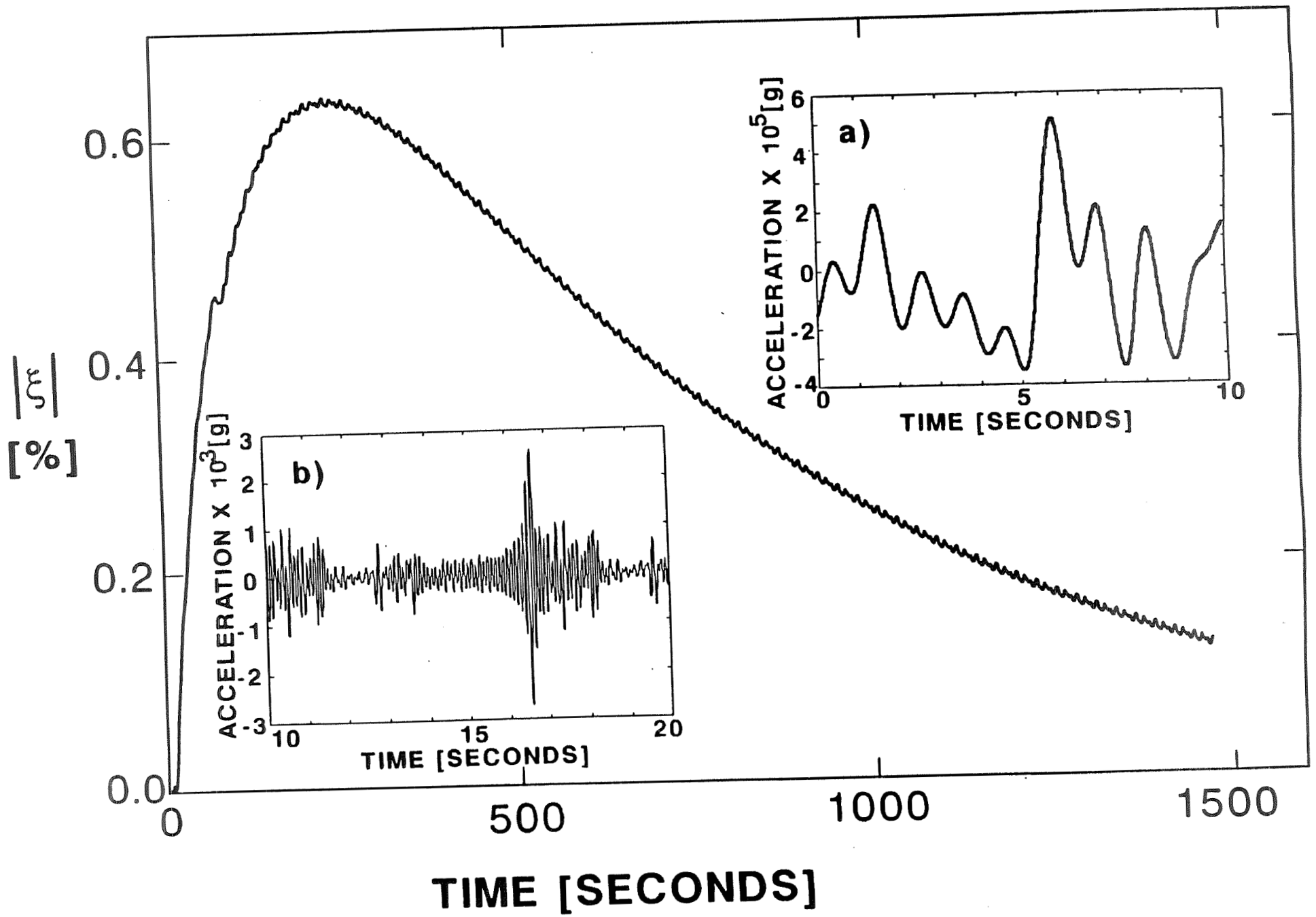
0.6
0.4
0.2
0.0
0
500
1000
1500
|ξ| [%]
TIME [SECONDS]
a)
ACCELERATION X 10^5[g]
6
4
2
0
-2
-4
0
5
10
TIME [SECONDS]
b)
ACCELERATION X 10^3[g]
3
2
1
0
-1
-2
-3
10
15
20
TIME [SECONDS]

Fig. 21

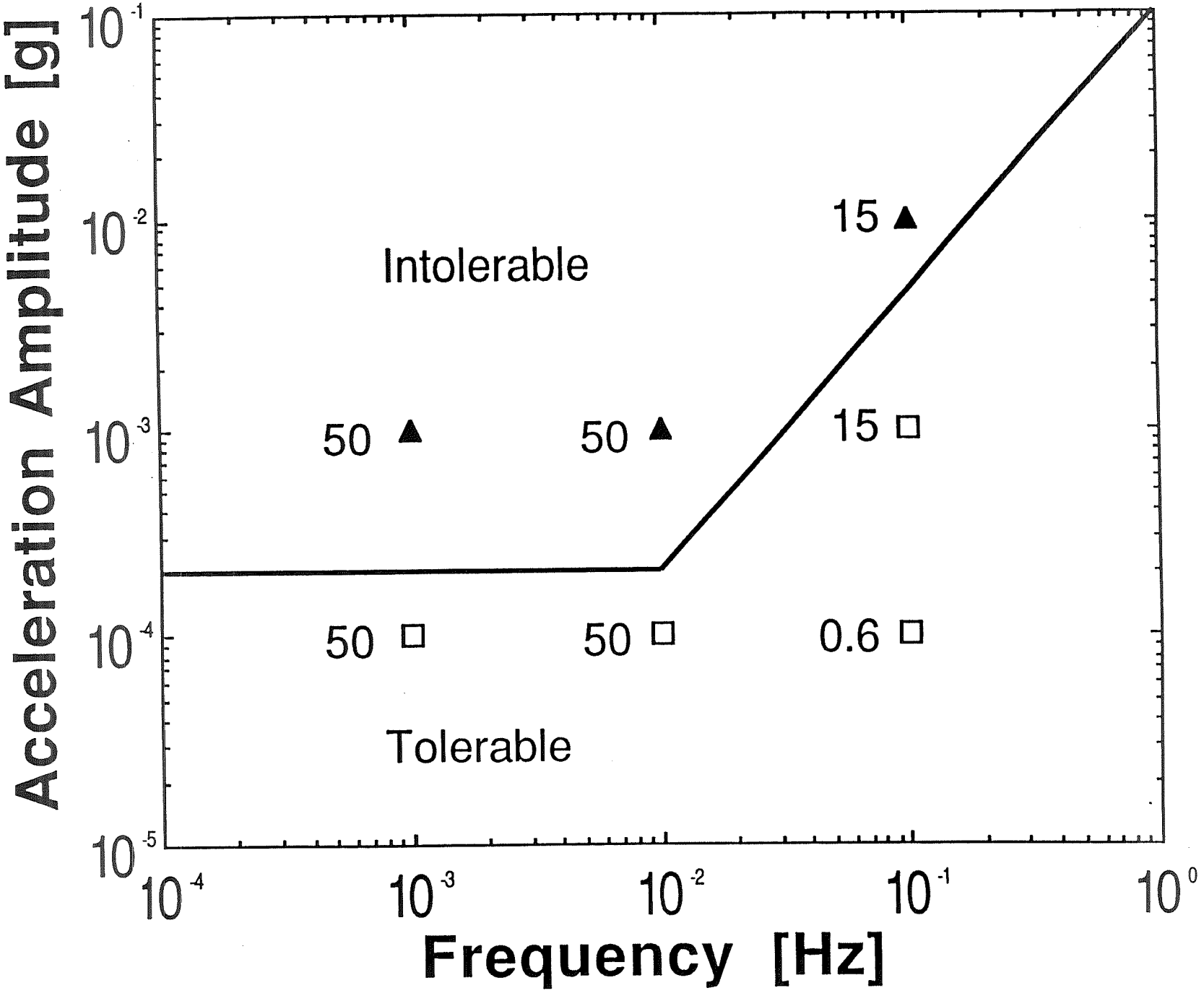
Acceleration Amplitude [g]
10^-1
10^-2
10^-3
10^-4
10^-5
Intolerable
15 ▲
50 ▲
50 ▲
15 □
50 □
50 □
0.6 □
Tolerable
10^-4
10^-3
10^-2
10^-1
10^0
Frequency [Hz]

Fig. 22

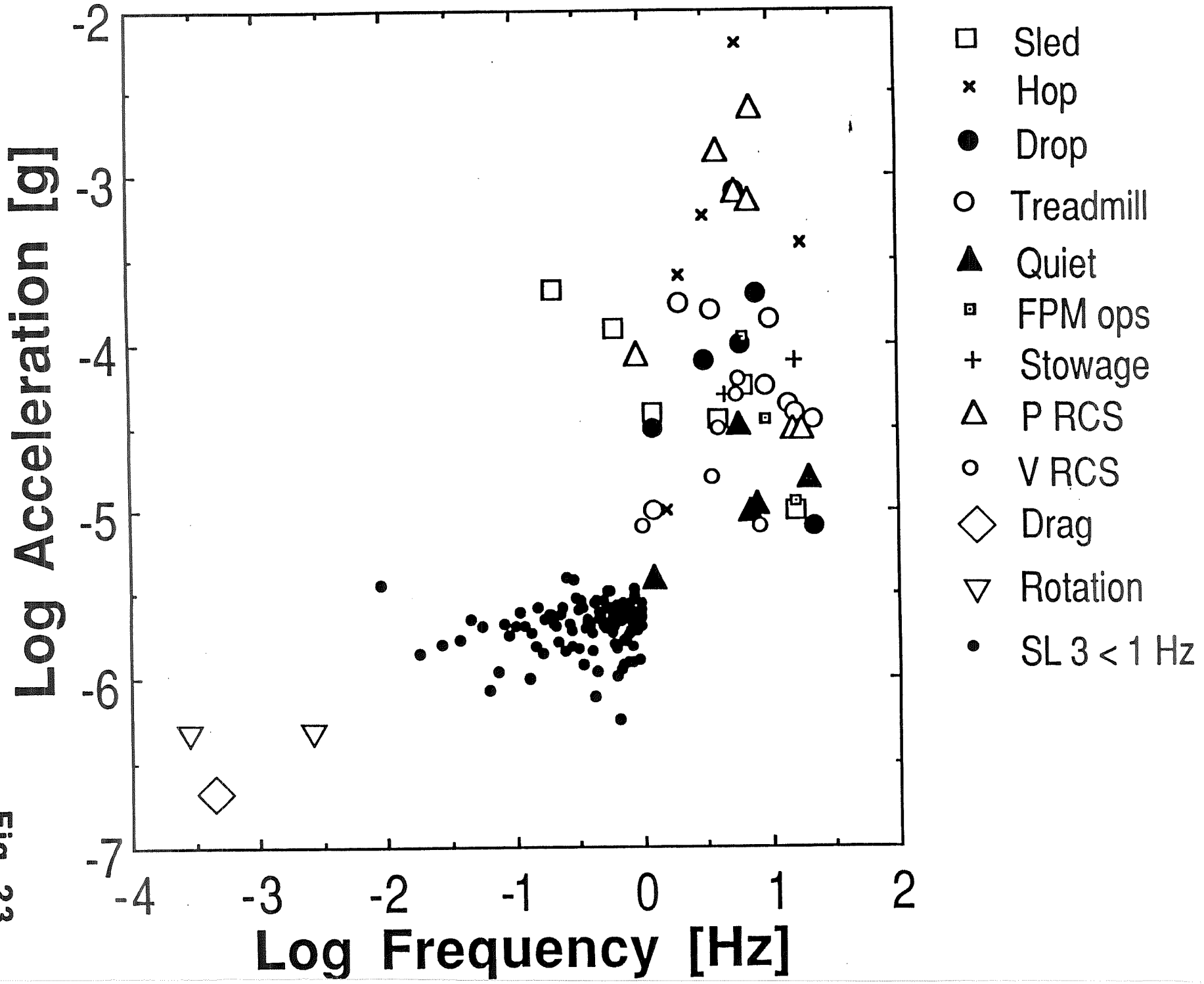
Log Acceleration [g]
-2
-3
-4
-5
-6
-7
-4
-3
-2
-1
0
1
2
Log Frequency [Hz]
Sled
Hop
Drop
Treadmill
Quiet
FPM ops
Stowage
P RCS
V RCS
Drag
Rotation
SL 3 < 1 Hz

Fig. 23

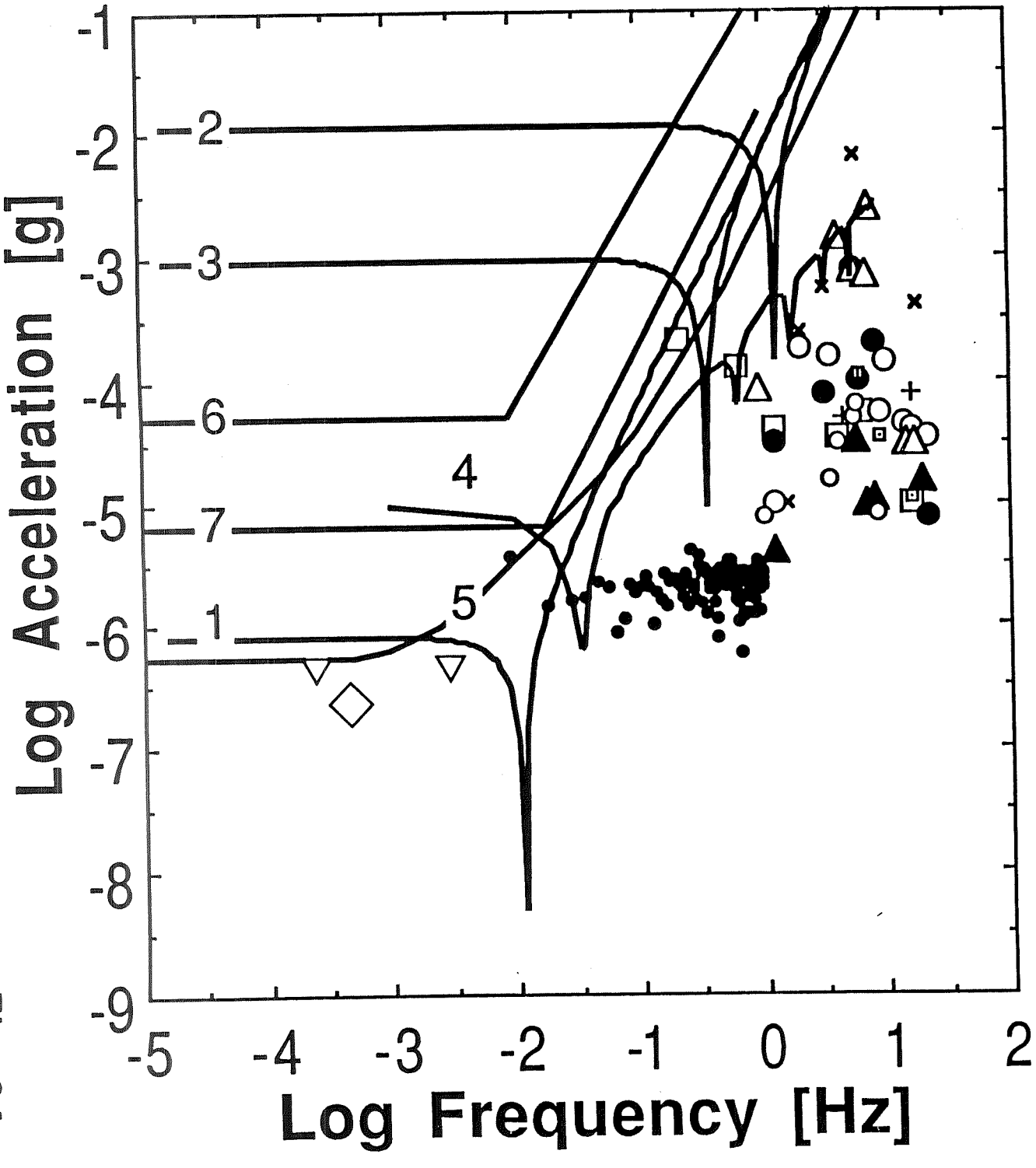
Log Acceleration [g]
-1
-2
-3
-4
-5
-6
-7
-8
-9
2
3
6
4
7
5
1
-5
-4
-3
-2
-1
0
1
2
Log Frequency [Hz]

Fig. 24

Page intentionally left blank

3. A NUMERICAL ANALYSIS OF LOW GRAVITY TOLERANCE OF THE BRIDGMAN-STOCKBARGER TECHNIQUE : TIME-DEPENDENT ACCELERATION

3.1. Introduction

In this work we extend our investigation of the sensitivity of directional solidification by the Bridgman-Stockbarger technique to residual acceleration and examine the effects of periodic accelerations and acceleration profiles synthesized from data recorded on Spacelab 3 (SL-3). The effects of low-gravity on the transport of heat and momentum have been examined in a number of articles [1-13]. Robertson et al. [2,3] found that for convection in circular cylinders with azimuthal variations in temperature at the boundary and the gravity vector applied perpendicular to the cylinder axis, the intensity of convection follows the prediction of Weinbaum's first order theory [14] for low Rayleigh numbers. Weinbaum's first order theory predicts a simple sinusoidal dependence of the maximum velocity as a function of orientation of the gravity vector. The effects of a variety of acceleration vectors (sinusoidal, cycloidal and linear periodic) on motion in three fluids corresponding to mercury, helium and water ($10^{-2} < Pr < 10$) were studied by Spradley et al. [4]. They found that the steady mean part of the applied disturbance is more important than the oscillatory part (frequency =1 Hz) in determining the flow field and heat transfer. Kamotani et al. [1] solved a linearized approximation of the Boussinesq equations and investigated the effect of an applied acceleration consisting of a time mean part and an oscillatory part on the temperature and flow fields in a rectangular enclosure. They found that the thermal convection was predominantly oscillatory in nature. In addition they found that the acceleration perpendicular to the temperature gradient is the most important for the generation of fluid motion.

The response of natural convection of a Boussinesq fluid in a cylinder to residual acceleration has been examined by Heiss et al. [6], and Schneider and Straub [7]. In the work of Heiss et al. the calculations are three-dimensional and involve gravity pulses and a rotating gravity vector. The ends of the cylinder are held at different temperatures. The cylinder walls were taken to be either perfectly insulating or perfectly conducting. Schneider and Straub [7] examined the effect of Prandtl number on the response to g-jitter for the same system as Heiss et al. They examined the response of the system to pulses of infinite length and sinusoidally varying pulses. For sinusoidal pulses they found for systems with Pr =0.71 and 7.0 (air and water) that the maximum velocity decreased with increasing frequency for dimensionless frequencies, $F=f L^2/\kappa$, greater than 10. At Pr=7 a maximum in the velocity was observed between F = 10 and 100 for the maxium amplitude pulse examined (Ra = 2×10^5, or $|\mathbf{g}| \approx 3\times10^{-4}$ g for a fluid with the properties of water, a 1 cm diameter cylinder and a temperature difference of 10 K). They determined that the system was least sensitive when the transient accelerations acted along the cylinder axis.

The extent to which gravity causes buoyancy-driven fluid motion (and thus, solute redistribution) during directional solidification has been examined using numerical models of buoyancy-driven convection in cylindrical and rectangular geometries [7-11,15-20]. Except for [6-11,20] these studies are restricted to axisymmetric situations in which a steady gravity vector is

oriented parallel to the axis of a cylindrical ampoule. McFadden and Coriell [9] have undertaken 2-D calculations of the effects of time-dependent accelerations on lateral compositional variations during directional solidification. The gravitational acceleration was assumed to have a uniform magnitude and rotation rate. The amount of compositional nonuniformity was found to increase with decreasing rate of rotation (see Fig. 17).

Griffin and Mokatef [21,22] modelled the nature of melt convection in a Bridgman system subject to steady and unsteady axial acceleration. They also found that at conditions corresponding to low-gravity, the response time of the melt velocity is proportional to the momentum diffusion time (i.e. it is controlled by the characteristic system length scale and melt viscosity). They found that the velocity response to sinusoidal g-jitter decreased as the inverse square of the momentum diffusion time.

Two- and three- dimensional models of directional solidification from dilute gallium-doped germanium melts have been used to determine the sensitivity of crystal compositional uniformity to both time-dependent and steady residual accelerations [10,11,20] (see also **section 5.1**). The specific boundary conditions, thermo-physical properties of the melt, growth rates and ampoule size are all found to play a role in the determination of the experiment sensitivity. For a given set of operating conditions, it is found that at growth rates on the order of 6.5 mm s^{-1} the orientation of the experiment with respect to the steady component of the residual gravity is a crucial factor in determining the suitability of the spacecraft as a means to suppress or eliminate unwanted effects caused by buoyant fluid motion. The worst case appears to be when the acceleration vector is parallel to the crystal interface. At growth rates on the order of microns per second, this orientation leads to compositional non-uniformities of 10-20% when the magnitude of the acceleration is of the order 10^{-6} g. If, however, the growth rate is lowered by an order of magnitude, the nonuniformity is reduced significantly (down to 1- 5% in this case). Table 5 in **section 5.1** summarizes the results obtained for steady accelerations.

3.2. Formulation

The basic model and governing equations were introduced in paper I. The physical situation under investigation involves an ampoule containing a dilute two-component melt. Directional solidification takes place as the ampoule is translated through fixed "hot " and "cold" zones. The zones are separated by a thermal barrier [23] which is modelled using adiabatic sidewalls. Translation of the ampoule is modelled by supplying a doped melt of dilute bulk composition c_∞ at a constant velocity V_g at the top of the computational space (inlet), and withdrawing a solid of composition $c_s = c_s(x,t)$ from the bottom. The crystal-melt interface is located at a distance L from the inlet. The temperature at the interface is taken to be T_m, the melting temperature of the crystal, while the upper boundary is held at a higher temperature T_h. Since we wish to confine our attention to compositional non-uniformities caused by bouyancy convection, rather than variations resulting from non-planar crystal-melt interfaces, the interface is held flat in our model.

The governing equations are cast in dimensionless form using L, κ/L (κ is the melt's thermal diffusivity), $\rho_m\kappa^2/L^2$, T_h-T_m, and c_∞ to scale the lengths, velocity, pressure, temperature, and solute concentration. The dimensionless equations governing momentum, heat and solute transfer in the melt are then

$$\frac{\partial \mathbf{u}}{\partial t} + (\text{grad}\mathbf{u})\mathbf{u} = \text{Pr}\Delta\mathbf{u} + \text{GrPr}^2\mathbf{g}, \tag{1}$$

$$\text{div}\,\mathbf{u} = 0, \tag{2}$$

$$\frac{\partial \theta}{\partial t} + \mathbf{u} \cdot \text{grad}\theta = \Delta\theta, \tag{3}$$

$$\frac{\text{Sc}}{\text{Pr}}\left(\frac{\partial s}{\partial t} + \mathbf{u} \cdot \text{grads}\right) = \Delta s, \tag{4}$$

where, $\mathbf{u}(\mathbf{x})$ represents the velocity, $\theta = (T(\mathbf{x}) - T_m)/(T_h - T_m)$ the temperature and $s = c_m(\mathbf{x})/c_m^\infty$ represents the solute concentration. Pr, Ra and Sc are defined in **section 5.1**. The magnitude of g used in the Rayleigh number, Ra, will be the magnitude of the actual acceleration. For the calculations presented here we have used the thermo-physical properties corresponding to gallium-doped germanium melts (see section **section 2.6** p. 28 and **section 5.1**). The term **g** in (1) has a specifies the orientation of the gravity vector. The Rayleigh number is taken to be the value of Ra at the earth's surface, thus the magnitude of **g** represents the acceleration magnitude relative to 1 g.

The following boundary conditions apply at the crystal-melt interface:

$$\frac{\text{Sc}}{\text{Pr}}\left(\frac{\partial s}{\partial t} + \mathbf{u} \cdot \text{grads}\right) = \Delta s, \tag{5}$$

where **N** is the unit vector normal to the planar crystal melt interface. We define the measure of compositional nonuniformity in the crystal at the interface to be the lateral range in concentration given by

$$\xi(t) = \frac{c_{smax} - c_{smin}}{c_{sav}}\%, \tag{6}$$

where c_s is the (dimensional) solute concentration in the crystal, and c_{av} is the average concentration. The following boundary conditions are applied at the "inlet" (y=0)

$$\theta = 1, \quad \mathbf{u}\cdot\mathbf{N} = \frac{\text{Pe}_g\text{Sc}}{\text{Pr}}\sigma, \quad \mathbf{u}\wedge\mathbf{N} = 0, \quad \frac{\partial s}{\partial y} = \frac{\text{Pe}_g\text{Sc}}{\text{Pr}}(s\text{-}1). \tag{7}$$

At the side walls the conditions are

$$\mathbf{u}\cdot\mathbf{N} = \frac{\text{Pe}_g\text{Sc}}{\text{Pr}}\sigma, \quad \mathbf{u}\cdot\mathbf{e}_w = 0, \quad \text{grads}\cdot\mathbf{e}_w = 0, \tag{8}$$

with $\theta = 1$ in the isothermal zone and grad$\theta \cdot e_w$ in the adiabatic zone. Here e_w is the normal to the ampoule wall.

In an actual experiment, owing to the finite length of the ampoule, there is a gradual decrease in length of the melt zone during growth. In this model transient effects related to this change are ignored. This assumption is referred to as the quasi-steady assumption and is frequently used in melt-growth modelling[15,19,20]. It is thus assumed that the ampoule is sufficiently long for these effects to be negligible, a condition which should be checked from case to case.

3.2.1. Solution Method

The governing equations were recast in the stream-function vorticity formulation and solved using a pseudo-spectral Chebyshev technique [20,24] which incorporated the influence matrix method [25,26]. This allowed us to avoid the artificial compressibilty method used to examine steady and transient accelerations and, thus, avoid iterating to satisfy (2) at each time step.

3.2.2. Types of transient acceleration examined

The form of accelerations examined was taken to be

$$\mathbf{g}(t) = \sum_{n=1}^{N} g_n \sin(2\pi f_n t + \phi_n)\mathbf{k}, \qquad (1)$$

where f_n is the frequency, $\mathbf{k}$ is a unit vector parallel to the crystal melt interface, ϕ_n is the phase and g_n represents the amplitude of the n^{th} acceleration component. We examine single, triple component accelerations as well as accelerations synthesized from accelerations recorded on SL-3.

The computations were performed on a CRAY XMP computer. The results of the calculations were compared with results obtained using the primitive variable formulation and artificial compressibility method used in paper I. The results were found to be practically identical. For the time dependent cases examined we systematically varied the number of spatial points as well as the time step size. In all cases a 33×33 Chebyshev points were found to be sufficient. The results presented here were calcualted using 41×41 Chebyshev points.

3.3. Results

We examined single and multiple frequency acceleration and synthesized accelerations from sample time series obtained on SL-3. Our results showed that, qualitatively, the transient response of the system to single and multiple frequency accelerations is independent of the type of disturbance. If examined over short time periods, that is $t < L^2/D$, the sensitivity can be a factor of ten higher than at later times.

a) Single frequency oscillatory disturbances

Table 1gives the short time response of ξ for single frequency oscillatory disturbances. We shall see later that results obtained for longer simulation times indicates that a better estimate of the long time sensitivity is obtained after times on the order of L^2/D

We have examined the system response to disturbances in the frequency range 10^{-3}-1 Hz. The most sensitive response was found to be for the longer period disturbances. The development of the velocity field is characterized by a plot of u_{max} and v_{max} as a function of time in Fig. 1. Note that for the 10^{-3} Hz disturbance the largest magnitudes are attained at 250, 750 1250 and 1750 seconds. The velocity field is in phase with the residual acceleration. The short time sensitivity is greatest at the end of the velocity transient. On the other hand, the compositional nonuniformity (see Fig. 2) exhibits a local maximum at about 600, 1000, and 1500 seconds. For the first two periods of the 10_{-3} Hz disturbance the solute field is not in phase with the velocity field. The solute field at 500, 1000, 1500 and 2000 seconds for this case is shown in Fig. 3.

At higher frequencies the response of the velocity field changes character. The difference between the behavior for 1 Hz, 10^{-1} Hz and 10^{-2} Hz is marked. The maximum velocity exhibits a short transient of between 20-50 seconds before it begins to oscillate regularly. Note that, in comparison to the 10^{-3} Hz case, the maximum value of ξ for the 10^{-2} and 10^{-1} Hz cases was reached between 200-300 seconds, whereupon it decays significantly. Figures 4-7 show the maximum velocities and concentrations as a function of time for the 10^{-2} Hz and 10^{-1} Hz cases. Note the appearance of two local maxima of ξ per period at about 1200 seconds for the 10 Hz case.

Fig. 8 shows the velocity field at .25 s, 0.5s, 0.75 s and 1s for a 10^{-2} g 1 Hz acceleration oriented parallel to the crystal surface. Note that in all the velocity plots, the velocity vectors have been rescaled such that the velocity at the inlet and the crystal boundary is always of magnitude 6.5×10^{-4} cm s^{-1}. During first half of the cycle the acceleration vector points from right to left. The maximum magnitude occurs at 0.25 s. The hot melt moves anti-parallel to the acceleration vector. The velocity reaches a maximum at 0.25 seconds and then decreases as the acceleration magnitude decreases. At 0.75 seconds the acceleration vector has reached a value of 10^{-2} g but is now oriented from left to right. The fluid motion at this time, however, still has the same sense as the motion during the first half of the cycle, although the magnitude is diminished. At 1 second, significant convection occurs only at the boundaries. The flow direction has reversed and a weak clockwise circulation has been established. This is short-lived since the acceleration direction then changes for the next 0.5 seconds. This behavior repeats itself for some time, although the relative strength of the clockwise rotation increases at the expense of the counter-clockwise flow. This is seen in Fig. 9. Here the component (u,v) maximum velocity magnitude are seen to fluctuate with twice the period of the driving force. During the first second, a strong counter-clockwise cell is established followed by a weak clockwise cell. This is indicated by the appearance of two velocity maxima, the first representing the counter-clockwise cell which is approximately 2.5 times the magnitude of the clockwise cell. During subsequent cycles, the difference between these two peaks decreases. At about 80 seconds the peaks have approximately the same magnitude. Fig. 10 shows the component maximum velocities from 802 to 808 seconds. The behavior is quite regular and

about $\pi/2$ out of phase with the driving force. Notice the slight difference between adjacent peak velocity magnitudes. If the two maxima per period are the same, then no net flow will have occurred in the system over that period. Careful examination of Fig. 10b reveals a barely perceptible difference in the two maxima.This reflects a small net circulation with velocities on the order of the growth velocity,

Fig. 11 depicts the solute concentration field at 1, 6, 200 and 800 seconds. At 1 second the solute field appears to be slightly disturbed, at 6 seconds the isoconcentrates away from the crystal-melt interface are clearly distorted, although the nonuniformity at the surface is negligible. At 200 seconds a distinct nonuniformity has been established. At 800 seconds the magnitude of the nonuniformity has decreased but is still significant. The variation of ξ with time is depicted in Fig. 12. Here, ξ reaches a value of 19% at about 300 seconds and decays to almost 6 % after 3000 seconds. As shown in the inset b) ξ is modulated slightly with a frequency of 1 Hz.

b) multiple frequency oscillatory disturbance

In order to assess the contribution to solute transport of a combination of oscillatory acceleration components, we examined several cases of a three component disturbance. As for the single component cases, for the range of amplitudes chosen, the greatest sensitivity was to the low frequency component of the disturbance. In these cases the lowest frequency was 10^{-3} Hz.

Fig. 13 depicts the velocity field at 3,6,8 and 10 seconds in response to a disturbance with frequency components 10^{-2}, 10^{-1}, and 1 Hz and amplitudes 10^{-4}, 10^{-3} and 10^{-2} g. Development of the velocity field during the first 10 seconds is illustrated by Fig. 14. Fig 15 gives the corresponding solute concentration fields. For this case the maximum solute nonuniformity was almost 60% . While the effects of the individual components are additive, the higher frequency accelerations cause only relatively small modulations of the basic trend. For a disturbance with frequency components 10^{-2}, 10^{-1}, and 1 Hz and amplitudes 10^{-5} 10^{-4} and 10^{-3} g, the maximum velocity and composition nonuniformity as a function of time are shown in Figs. 16-17. As for the case of the single frequency disturbances, the velocity field gives rise to a counter clock-wise net circulation during the transient phase. The maximum value of ξ is 6%. This is attained at around 250 seconds and decays to value which fluctuates between 0.18 and 0.65% after some 3000 seconds have elapsed. Clearly, this case is only marginally sensitive for long times. In addition, it is interesting to note the behavior of the nonuniformity fluctuation which is sinusoidally modulated during its overall decay after 200 seconds. The most obvious modulations occur with a frequency of 10^{-2} Hz (Fig. 18a) and these are not manifested until 80 seconds have elapsed. Fig. 18b shows the long time behavior of ξ from 1200 seconds onward. The mean value of ξ(averaged over 100 seconds) continues to decay until about 2000 seconds whereupon it fluctuates about a value of 0.4 %. Notice also that at 2000 seconds an additional local maximum in ξ appears such that the modulation period is 50 seconds. This merely reflects that the composition field is finally responding to the basic flow which had been established some 1900 seconds earlier. Now the flow results in two maximum values of ξ per period. The second maximum, which is related to the clockwise motion of the melt, is suppressed until ξ_p reaches a steady value. The velocity at a point

x=0.7, y=0.7 as a function of time from 800-1000 seconds is shown in Fig. 19. For this case, the 10^{-2} Hz component of the acceleration is responsible for the largest fluctuations.

In all the cases examined, the velocity field exhibited a greater response than the solute field. For single frequency oscillatory disturbances, the degree to which the fluid motion affected the time-dependent redistribution of solute in the melt is dependent on the characteristic time for the fluid to reach an oscillatory state compatible with the driving force. If the the Schmidt number is large the solute field will be disturbed during the velocity transient. At the time the velocity transient ends and the fluid velocities oscillate between fixed values at the frequency of the driving force, the solute field will still be in a transient state. In fact, since during the transient there will have been net rotation of the fluid in one direction, the composition nonuniformity will reach a maximum toward the end of the velocity transient. Once the fluid behaves regularly the solute field slowly adjusts to this state. The composition nonuniformity gradually reduces and reaches a significantly smaller value after an elapsed time on the order of the characteristic diffusion time τ_D (more than 2000 seconds for the Ge:Ga system examined here).

c) Acceleration synthesized from SL-3 sample time series

Of the cases examined all but one are on the margin of sensitivity for the model Ge:Ga system. The results are presented in Figs. 20-24. The compositional nonuniformity was insensitive ($\xi < 0.1$ %) to the disturbance shown in Fig. 20, although the maximum velocity fluctuated on the order of the growth rate (see Fig. 21). For the acceleration depicted in Fig. 20, the amplitudes of the component accelerations are given in Table 2. In order to find the margin of sensitivity of a disturbance with these frequency components we increased the amplitudes by a factor of 10.Fig. 22 shows the time variation of u_{max} and v_{max} is shown. Note that the sample series used to synthesize the disturbance has a period of 10 s which is evident in Figs.21, 22 and 23. As might be expected, the tenfold increase in the component amplitudes resulted in a tenfold increase in the maximum value of ξ.

In Fig. 24 the response to a disturbance synthesized from spacelab-3 acceleration data is shown. The disturbance consists of two repeated sample time series (a) (0-10 seconds, 20-80 seconds and from 90 seconds on, combined with sample time series (b) (from 10-20 and 80-90 seconds. Table 3 gives the component frequencies and amplitudes of disturbance (a). The sample series (b) represents a thruster firing event. For the amplitude-frequency components present in these disturbances (see Table 3), the system was marginally sensitive. The maximum value of ξ was 0.6% which was attained after some 200 seconds had elapsed. The nonuniformity subsequently decayed to less than 0.2% after 1500 seconds. In order to asses the impact of the two thruster firing events we ran the simulation with only the series (a). While the velocity field responded directly to the thruster sequence, the composition nonuniformity exhibited the same behavior in both cases. In order to check the sensitivity limits we increased the all the amplitudes series (a) by a factor of ten. Again, the tenfold increase in the acceleration amplitudes resulted in a corresponding increase in the maximum value of ξ~60%.

3.4. Discussion

We have investigated the sensitivity of the Bridgman-Stockbarger technique to residual accelerations corresponding to single and multi-component oscillatory disturbances. The multi-component disturbances included simple 3-component accelerations and complex acceleration profiles synthesized from Fourier series analyses of acceleration data obtained on SL-3. For the Ge:Ga system examined, we found that for accelerations less than 10^{-2} Hz large amplitude fluctuations were found to occur in ξ for acceleration amplitudes above 10^{-6} g. The system response to 10^{-5} g accelerations at 10^{-3} Hz led to composition non-uniformities on the order of 60%. For single component disturbances, larger accelerations are required to give significant non-uniformities as the frequency is increased. The most noticeable difference in the response of the Ge:Ga system to different frequency accelerations was in the behavior of the velocity and composition transients as the system adjusted from the zero velocity initial state to the final state where the system oscillated with the frequency of the driving force. The difference is clearly seen upon comparison of the results for 10^{-3} with those of higher frequencies. The maxium velocity behavior, for example, shows a distinct transient behavior for frequencies greater than or equal to 10^{-2} Hz, which is not observed at 10^{-3} Hz. For the 10^{-3} Hz frequency acceleration, the nonuniformity exhibits large amplitude oscillations with twice the frequency of the acceleration, although there is a phase lag during the first two periods. For higher frequency disturbances, the larger accelerations required to obtain significant non-uniformities are sufficient to modify the solute field such that the modulation of ξ is barely noticeable at early times owing to the steady riase in the nonuniformity magnitude during the velocity transient. Between 200 and 300 seconds the composition nonuniformity reaches a maximum and clearly exhibits modulations with the frequency of the driving force. As time proceeds the solute field slowly adjusts to the regularly oscillating velocity field. By 2000-3000 seconds the solute field has relaxed into a reglarly oscillating state and the value of ξ is diminished considerably. Furthermore, ξ is modulated about a fixed non-zero value at twice the frequency of the driving force which indicates that composition field has finally adjusted from the state with high lateral nonuniformity which resulted from the velocity transient.

The system was insenstitive to disturbances synthesized from SL-3 measurements with frequencies in the range 10^{-1}-10 Hz, and only exhibited marginal sensitivity for amplitudes of the individual frequency components that were a factor of ten higher than the measured amplitudes.

3.5. References

[1] *Kamotani, Y., Prasad, A., Ostrach, S.* : AIAA Journal 19 (1981) 511.
[2] *Robertson, S. J., Nicholson, L. A.*: Lockheed Report LMSC-HREC TR D867640 (1987).
[3] *Robertson, S. J., Nicholson, L. A., Spradley, L. W.*: Lockheed Report LMSC-HREC TR D867624 (1982).
[4] *Spradley, L. W. Bourgeois, S. W. , Lin, F. N.*: AIAA paper 75-695 (1975).
[5] *Grodzka, P. G., Bannister, T. C.*: AIAA paper 74-156 (1974).
[6] *Heiss, T., Schneider, S., Straub, J.*: Proc. 6th European Symposium Materials Sciences in Microgravity Conditions, Bordeaux, France (ESA SP-256 1987) 517.
[7] *Schneider, S., Straub, J.*: J. Crystal Growth 97 (1989) 235.

[8] *Polezhaev, V. I., Lebedev, A. P., Nikitin, S. A.*: Proc. 5th European Symposium on Materials Sciences under Microgravity, Schloss Elmau FRG, ESA SP-222 (1984), 237.
[9] *McFadden, G. B., Coriell, S. R.*: in Proc. AIAA/ASME/SIAM/APS 1st National Fluid Dynamics Congress, Cincinnati, July 25th-28th (1988) p. 1572.
[10] *Alexander, J. I. D., Ouazzani, J., Rosenberger, F.*: Proc. 3rd International Colloquium on Drops and Bubbles, AIP Conference Proceedings 197, ed. Taylor G. Wang (American Institute of Physics, New York, 1988) p.112.
[11] *Alexander, J. I. D., Ouazzani, J.*: Proc. 6th International Conference on Num. Methods in Laminar and Turbulent Flow, C. Taylor, P. Gresho, R. L. Sani and J. Haüser (eds.) Pineridge, Swansea 1989 1035.
[12] *Arnold, W. A., Jacqmin, D. A., Chang, R., Chait, A.*: AIAA paper No. 89 (1989).
[13] *Ramachandran, N., Winter, C.* AIAA Paper No. 90-0654 (1990).
[14] *Weinbaum, S.*: J. Fluid Mech. 18 (1964) 409.
[15] *Chang, C. J., Brown, R. A.*: J. Crystal Growth 63 (1983) 353.
[16] *Clark, P. A., Wilcox, W. R.*: J. Crystal Growth 50 (1980) 461.
[17] *Kobayashi , N., Wilcox, W. R.*: J. Crystal Growth 59 (1982) 616.
[18] *McFadden, G. B., Rehm, R. G., Coriell, S. R., Clark, W., Morrish, K. A.*: Metall. Trans. A15 (1984) 2125.
[19] *Adornato, P. M., Brown, R. A.*: J. Crystal Growth 80 (1987) 155.
[20] *Alexander, J. I. D., Ouazzani, J. , Rosenberger, F.*: J. Crystal Growth 97 (1989) 285.
[21] *Griffin, P. R., Mokatef, S.*: Appl. Microgravity Tech. 2 (1989) 121.
[22] *Griffin, P. R., Mokatef, S.*: ibid. 128.
[23] *Dahkoul, Y.M., Farmer R., Lehoczky S. L. and Szofran F.*: J. Crystal Growth **86** (1988) 49.
[24] *Peyret, R.*, The Chebyshev Multidomain Approach to Stiff Problems in Fluid Mechanics, Proc. ICOSAHOM 89, June 26-29, 1989, Como (Italy)
[25] *Ehrenstein, U., Guillard, H., and Peyret R.*: Int. J. Numer. Meth. Fluids **9** (1989) 499-515.
[26] *Canuto, C., Quatrteroni, A., Hussaini, M.Y., and Zang, T.A.*: Spectral Methods in Fluid Dynamics (Springer Verlag, Berlin, 1988).

3.7. TABLES

3.6. Tables

Table 1. Short time response of ξ to single frequency disturbances.

magnitude [g]	frequency [Hz]	duration [s]	ξ [%]
10^{-3}	10^{-2}	500	14.0
10^{-4}	10^{-1}	120	1.5
10^{-3}	10^{-1}	20	5.5
10^{-3}	1	12	0.26
10^{-2}	1	2	0.5

Table 2. Acceleration profile components used to obtain the results depicted in Fig. 20

MAGNITUDE (g)	FREQUENCY (Hz)	PHASE (radians)	MAGNITUDE (g)	FREQUENCY (Hz)	PHASE (radians)
0.6678974E-05	0.3222656E+01	-0.1023456E+00	0.4157672E-05	0.6591797E+01	0.1069476E+01
0.1168701E-04	0.3369141E+01	-0.2171423E+01	0.8624586E-05	0.6738281E+01	0.2299790E+01
0.4029183E-05	0.3515625E+01	-0.2680568E+01	0.4860019E-05	0.6884766E+01	-0.5513560E+00
0.5767611E-05	0.3662109E+01	-0.1120755E+01	0.1024745E-04	0.7031250E+01	0.1441972E+01
0.7336796E-05	0.3808594E+01	-0.2688848E+01	0.8487802E-05	0.7177734E+01	-0.3315119E+00
0.2979588E-05	0.3955078E+01	-0.1051489E+00	0.9614520E-05	0.7324219E+01	-0.2408829E+01
0.7084803E-05	0.4101563E+01	-0.1396236E+01	0.1111080E-04	0.7470703E+01	-0.1942924E+01
0.2380885E-05	0.4248047E+01	0.4626593E+00	0.4023313E-05	0.7617188E+01	0.2730639E+01
0.1256049E-04	0.4394531E+01	-0.1144225E+01	0.1338748E-05	0.7763672E+01	-0.6898107E-01
0.1908798E-04	0.4541016E+01	-0.2954485E+01	0.1156079E-04	0.7910156E+01	-0.1999173E+01
0.1414271E-04	0.4687500E+01	0.1487755E+01	0.2205120E-05	0.8056641E+01	0.9450552E+00
0.1242372E-04	0.4833984E+01	-0.2697886E+01	0.6399363E-05	0.8203125E+01	0.3106058E+01
0.5044114E-05	0.4980469E+01	-0.5252368E+00	0.1163937E-04	0.8349609E+01	0.2999920E+01
0.1122994E-04	0.5126953E+01	0.1805229E+01	0.7708650E-05	0.8496094E+01	0.2374351E+01
0.3820708E-05	0.5273438E+01	-0.5802202E+00	0.4804912E-05	0.8642578E+01	0.2401585E+01
0.6576809E-05	0.5419922E+01	0.1198942E+01	0.8501992E-05	0.8789063E+01	0.2369910E+01
0.3735003E-05	0.5566406E+01	0.1164908E+00	0.1167328E-04	0.8935547E+01	0.2706169E+01
0.2560308E-05	0.5712891E+01	0.2914079E+01	0.9668714E-05	0.9082031E+01	0.2292677E+01
0.2788814E-06	0.5859375E+01	0.1549920E+01	0.5459605E-05	0.9228516E+01	0.2345090E+01
0.1614620E-04	0.6005859E+01	-0.1767729E+01	0.9634379E-05	0.9375000E+01	0.1297546E+01
0.1469397E-04	0.6152344E+01	-0.2948359E+01	0.4274781E-05	0.9521484E+01	0.2430201E+01
0.6047145E-05	0.6298828E+01	-0.1647892E+01	0.7036096E-05	0.9814453E+01	0.3016870E+01
0.2211998E-04	0.6445313E+01	0.2799345E+01	0.4917858E-05	0.9960938E+01	-0.3074690E+01

Table 3a. Acceleration components used for background for results in Fig. 24.

MAGNITUDE (g)	FREQUENCY (Hz)	PHASE (radians)	MAGNITUDE (g)	FREQUENCY (Hz)	PHASE (radians)
0.2051083E-05	0.3662109E-01	0.2722871E+01	0.2299556E-05	0.5493164E+00	0.5712527E-01
0.3877013E-05	0.7324219E-01	0.2648538E+01	0.3156646E-05	0.5859375E+00	-0.2943187E+01
0.3535946E-05	0.1098633E+00	-0.2834018E+01	0.3780498E-06	0.6225586E+00	0.3755093E+00
0.2020149E-05	0.1464844E+00	-0.2707997E+01	0.1398821E-05	0.6591797E+00	-0.1829336E+01
0.4987608E-05	0.1831055E+00	-0.1178820E+00	0.1847642E-05	0.6958008E+00	0.2193359E+01
0.2028721E-05	0.2197266E+00	-0.1539647E+00	0.1234316E-05	0.7324219E+00	0.9030567E+00
0.2897678E-05	0.2563477E+00	-0.1277694E+01	0.1469757E-05	0.7690430E+00	-0.1069827E+01
0.3776532E-05	0.2929688E+00	0.2503309E+01	0.2028031E-05	0.8056641E+00	-0.1359947E+01
0.4340377E-06	0.3295898E+00	-0.8924237E+00	0.1607328E-05	0.8422852E+00	0.8610225E+00
0.1476338E-05	0.3662109E+00	0.9381254E-01	0.2306742E-05	0.8789063E+00	0.1889095E+01
0.1008826E-05	0.4028320E+00	-0.6826349E+00	0.4854811E-05	0.9155273E+00	-0.6913710E+00
0.4067975E-05	0.4394531E+00	-0.2601777E+01	0.1340891E-05	0.9521484E+00	-0.1410856E+01
0.3092643E-05	0.4760742E+00	-0.1353911E+01	0.3400232E-06	0.9887695E+00	0.4895686E+00
0.2499588E-05	0.5126953E+00	0.1620389E+01			

Table 3 b. Acceleration components for thruster firing

MAGNITUDE (g)	FREQUENCY (Hz)	PHASE (radians)	MAGNITUDE (g)	FREQUENCY (Hz)	PHASE (radians)
0.1140294E-04	0.1464844E+00	-0.6030687E+00	0.7271495E-04	0.5126953E+01	-0.6024272E+00
0.9509653E-05	0.2929688E+00	-0.2491597E+01	0.5785038E-04	0.5273438E+01	-0.2669662E+01
0.3754365E-05	0.4394531E+00	-0.5223967E+00	0.5360622E-04	0.5419922E+01	-0.2476458E+00
0.9918378E-05	0.5859375E+00	-0.2804558E+01	0.2124587E-04	0.5566406E+01	0.1014042E+01
0.2464890E-05	0.7324219E+00	-0.3086868E+00	0.5234673E-04	0.5712891E+01	0.8560771E+00
0.1546870E-04	0.8789063E+00	0.2448875E+01	0.7330361E-05	0.5859375E+01	0.7808214E-01
0.8610295E-05	0.1025391E+01	-0.2492758E+01	0.5052985E-04	0.6005859E+01	0.3010761E+01
0.3151318E-05	0.1171875E+01	-0.2377229E+00	0.4433946E-04	0.6152344E+01	-0.4996738E+00
0.1032598E-04	0.1318359E+01	-0.7560444E+00	0.5526816E-04	0.6298828E+01	-0.2421690E+01
0.8860652E-05	0.1464844E+01	-0.8895736E+00	0.5564178E-04	0.6445313E+01	0.3093696E+00
0.1105441E-04	0.1611328E+01	0.9257343E-01	0.4753912E-04	0.6591797E+01	-0.1798343E+01
0.1503079E-05	0.1757813E+01	0.2136720E+01	0.8398587E-04	0.6738281E+01	0.1045000E+01
0.9216345E-05	0.1904297E+01	-0.2327524E+01	0.8855044E-05	0.6884766E+01	-0.9388244E+00
0.6179209E-05	0.2050781E+01	0.2664295E+01	0.7329257E-04	0.7031250E+01	0.2976783E+01
0.1986734E-04	0.2197266E+01	-0.2010437E+01	0.8345300E-04	0.7177734E+01	-0.3053698E+01
0.1236275E-04	0.2343750E+01	0.6686478E+00	0.8957948E-04	0.7470703E+01	-0.3556173E+00
0.3020275E-04	0.2490234E+01	0.2269750E+01	0.3759252E-04	0.7617188E+01	-0.1476801E+01
0.2345829E-04	0.2636719E+01	0.1499383E+00	0.4840786E-04	0.7763672E+01	0.1300743E+01
0.1733246E-04	0.2783203E+01	-0.3016654E+01	0.7912557E-04	0.7910156E+01	-0.8301902E+00
0.1302133E-04	0.2929688E+01	-0.1257968E+01	0.7635894E-04	0.8056641E+01	0.1833709E+01
0.6113684E-05	0.3076172E+01	0.2914706E+00	0.4677792E-04	0.8203125E+01	0.9043092E-01
0.1626974E-04	0.3222656E+01	-0.2269336E+01	0.6698716E-04	0.8349609E+01	-0.2321067E+01
0.8334577E-05	0.3369141E+01	-0.2960312E+01	0.1024659E-03	0.8496094E+01	0.8468162E+00
0.2110433E-04	0.3515625E+01	-0.1538641E+01	0.1090984E-03	0.8642578E+01	-0.1963995E+01
0.2329673E-04	0.3662109E+01	0.2187939E+01	0.7792140E-04	0.8789063E+01	0.1164153E+01
0.4597104E-04	0.3808594E+01	-0.1761344E+01	0.9283071E-04	0.8935547E+01	-0.9430396E+00
0.1087029E-04	0.3955078E+01	0.5420735E+00	0.1097537E-03	0.9082031E+01	0.2549556E+01
0.2991441E-04	0.4101563E+01	-0.1586179E+01	0.1056685E-03	0.9228516E+01	-0.4995980E+00
0.1452386E-04	0.4248047E+01	-0.4454126E+00	0.1023078E-03	0.9375000E+01	-0.2675524E+01
0.8852465E-05	0.4394531E+01	0.2433605E+01	0.7012900E-04	0.9521484E+01	0.1263102E+01
0.3346926E-04	0.4541016E+01	-0.6390298E+00	0.2513885E-03	0.9667969E+01	-0.1458808E+01
0.3887603E-04	0.4687500E+01	0.2700060E+01	0.2497189E-03	0.9814453E+01	0.1446993E+01
0.6244237E-04	0.4833984E+01	0.9014922E+00	0.3261188E-03	0.9960938E+01	-0.1155957E+01
0.3006418E-04	0.4980469E+01	-0.3005708E+01			

3.7. Figures and Figure Captions

Fig. 1 Maximum u-velocity a) and v-velocity b) as a function of time for a sinusoidal acceleration with magnitude 10^{-5} g and frequency 10^{-3} Hz oriented parallel to the crystal surface.

Fig. 2 Compositional nonuniformity ξ as a function of time for a sinusoidal acceleration with magnitude 10^{-5} g and frequency 10^{-3} Hz oriented parallel to the crystal surface.

Fig. 3 The solute field at a) 500, b) 1000, c) 1500 and d) 2000 seconds for a sinusoidal acceleration with magnitude 10^{-5} g and frequency 10^{-3} Hz oriented parallel to the crystal surface.

Fig. 4 Maximum u-velocity a) and v-velocity b) as a function of time for a sinusoidal acceleration with magnitude 10^{-4} g and frequency 10^{-2} Hz oriented parallel to the crystal surface.

Fig. 5 Compositional nonuniformity ξ as a function of time for a sinusoidal acceleration with magnitude 10^{-4} g and frequency 10^{-2} Hz oriented parallel to the crystal surface.

Fig. 6 Maximum u-velocity a) and v-velocity b) as a function of time for a sinusoidal acceleration with magnitude 10^{-3} g and frequency 10^{-1} Hz oriented parallel to the crystal surface.

Fig. 7 Compositional nonuniformity ξ as a function of time for a sinusoidal acceleration with magnitude 10^{-3} g and frequency 10^{-1} Hz oriented parallel to the crystal surface.

Fig. 8 Velocity fields at a) 0.25 b) 0.5 c) 0.75 and d) 1 second caused by a sinusoidal acceleration with magnitude 10^{-2} g and frequency 1 Hz oriented parallel to the crystal surface.

Fig. 10 Maximum u-velocity a) and v-velocity b) as a function of time from 802 to 808 seconds for a sinusoidal acceleration with magnitude 10^{-2} g and frequency 1 Hz oriented parallel to the crystal surface.

Fig. 11 The solute field at a) 1, b) 6 c) 200 and d) 800 seconds for a sinusoidal acceleration with magnitude 10^{-2} g and frequency 1 Hz oriented parallel to the crystal surface.

Fig. 12 Compositional nonuniformity ξ as a function of time for a sinusoidal acceleration with magnitude 10^{-2} g and frequency 1 Hz oriented parallel to the crystal surface. Note the low amplitude modulation of ξ with a frequency of 1 Hz between 802 to 808. Beyond 1200 seconds ξ fluctuates with a frequency of 2 Hz.

Fig.13 The velocity fields at a) 3 b) 6 c) 8 and d) 10 seconds caused by a sinusoidal 3-component acceleration with magnitudes 10^{-4} g, 10^{-3}g and 10^{-2} g frequencies 10^{-2}, 10^{-1} and 1 Hz oriented parallel to the crystal surface.

Fig. 14 Maximum u-velocity a) and v-velocity b) as a function of time for a sinusoidal 3-component acceleration with magnitudes 10^{-4} g, 10^{-3}g and 10^{-2} g frequencies 10^{-2}, 10^{-1} and 1 Hz oriented parallel to the crystal surface.

Fig. 15 The solute field at a) 3, b) 6 c) 8 and d) 10 seconds for a sinusoidal 3-component acceleration with magnitudes 10^{-4} g, 10^{-3}g and 10^{-2} g frequencies 10^{-2}, 10^{-1} and 1 Hz oriented parallel to the crystal surface.

Fig. 16 Maximum u-velocity a) and v-velocity b) from 0 -10 seconds as a function of time for a sinusoidal 3-component acceleration with magnitudes 10^{-5}g, 10^{-4}g and 10^{-3} g frequencies 10^{-2}, 10^{-1} and 1 Hz oriented parallel to the crystal surface.

Fig. 17 Maximum u-velocity a) and v-velocity b) for 0-200 seconds as a function of time for a sinusoidal 3-component acceleration with magnitudes 10^{-5}g, 10^{-4}g and 10^{-3} g frequencies 10^{-2}, 10^{-1} and 1 Hz oriented parallel to the crystal surface.

Fig. 18 Compositional nonuniformity ξ as a function of time for a sinusoidal 3-component acceleration with magnitudes 10^{-5}g, 10^{-4}g and 10^{-3} g frequencies 10^{-2}, 10^{-1} and 1 Hz oriented parallel to the crystal surface. a) 0 -1200 seconds, b) 1200-5500 seconds. Note that beyond 2000 seconds, ξ can be seen to fluctuate with a frequency of 2 Hz.

Fig.19 The velocity components at a point in the melt as a function of time for a sinusoidal 3-component acceleration with magnitudes 10^{-5}g, 10^{-4}g and 10^{-3} g frequencies 10^{-2}, 10^{-1} and 1 Hz oriented parallel to the crystal surface.

Fig. 20 Residual acceleration profile with the amplitudes and frequencies listed in Table 2 taken from acceleration data obtained on Spacelab 3.

Fig. 21 The velocity components at a point in the melt as a function of time for the acceleration profile shown in Fig. 20 oriented parallel to the crystal surface.

Fig. 22 Maximum u-velocity a) and v-velocity b) for 0-200 seconds as a function of time for an acceleration with the frequencies listed in Table 2 and amplitudes multiplied by a factor of 10. The acceleration is oriented parallel to the crystal surface.

Fig. 23 Compositional nonuniformity ξ as a function of time for an acceleration with the frequencies listed in Table 2 and amplitudes multiplied by a factor of 10. The acceleration is oriented parallel to the crystal surface.

Fig.24 Lateral non-uniformity ξ as a function of time for accelerations taken from a sample time series (see inset) constructed from data obtained on Spacelab 3. The acceleration consists of a repeated "noise" segment (length 10 seconds, 10^{-1} Hz $< f <$ 1 Hz) and a thruster firing event (length 10 seconds, 10^{-1} Hz $< f <$ 13 Hz). The latter is introduced at 10 and 80 seconds.

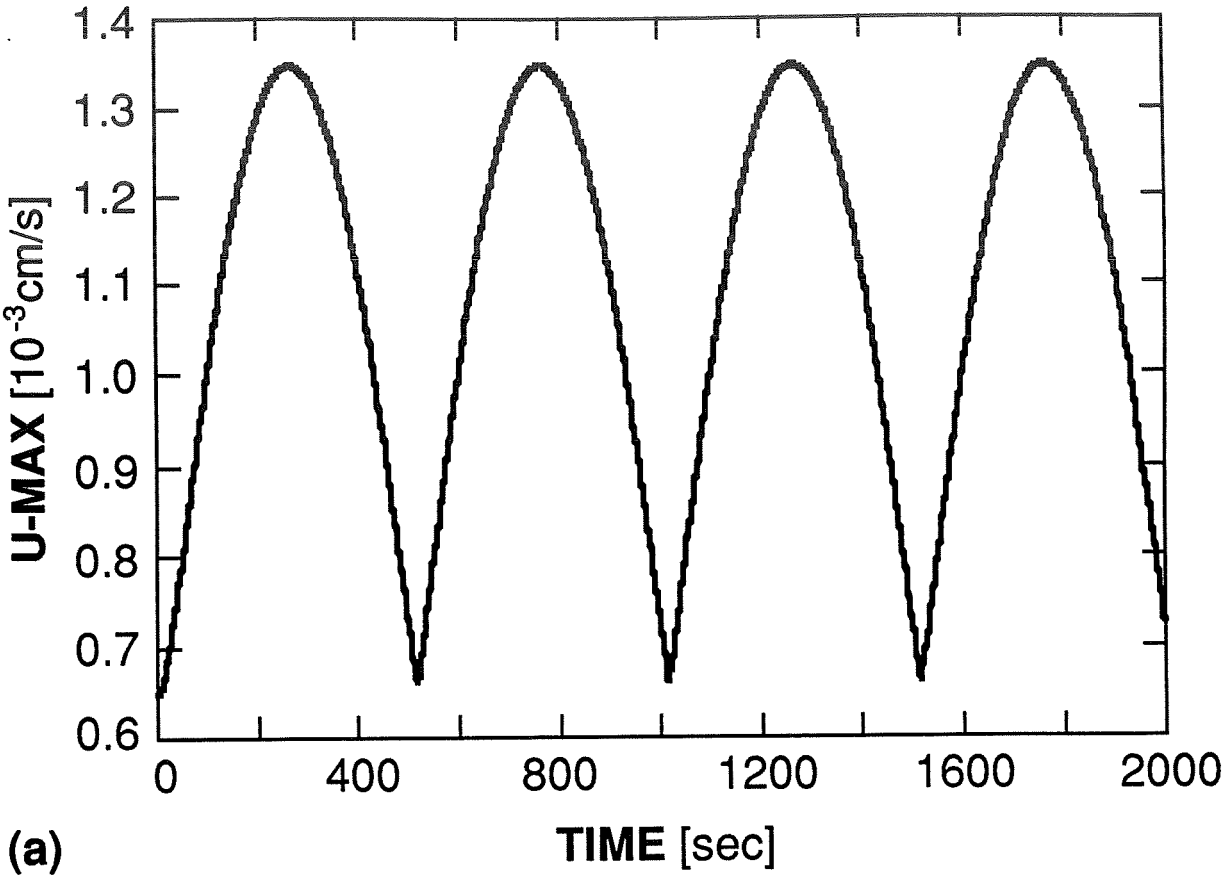
1.4
1.3
1.2
1.1
1.0
0.9
0.8
0.7
0.6
U-MAX [10-3cm/s]
0
400
800
1200
1600
2000
TIME [sec]

(a)

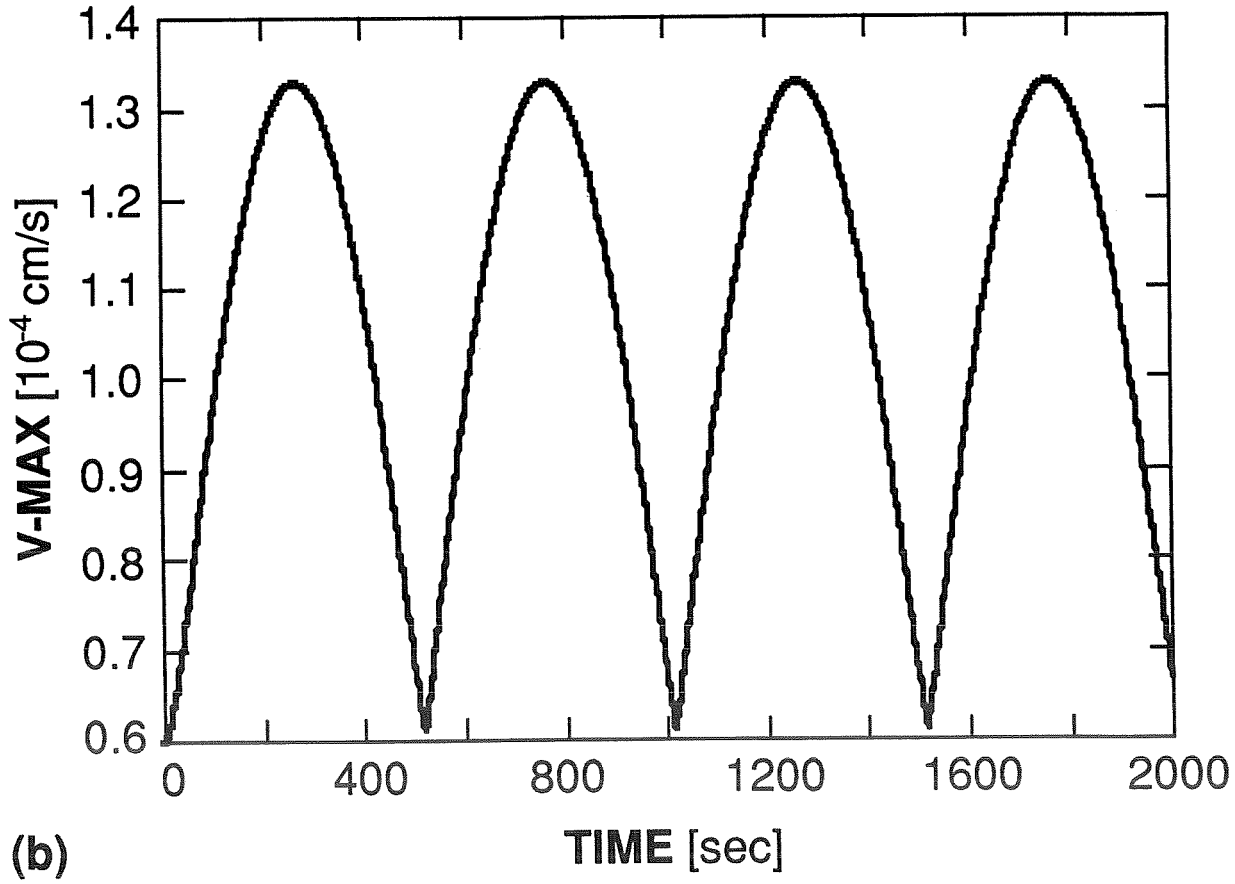
1.4
1.3
1.2
1.1
1.0
0.9
0.8
0.7
0.6
V-MAX [10-4 cm/s]
0
400
800
1200
1600
2000
TIME [sec]

(b)

FIG. 1

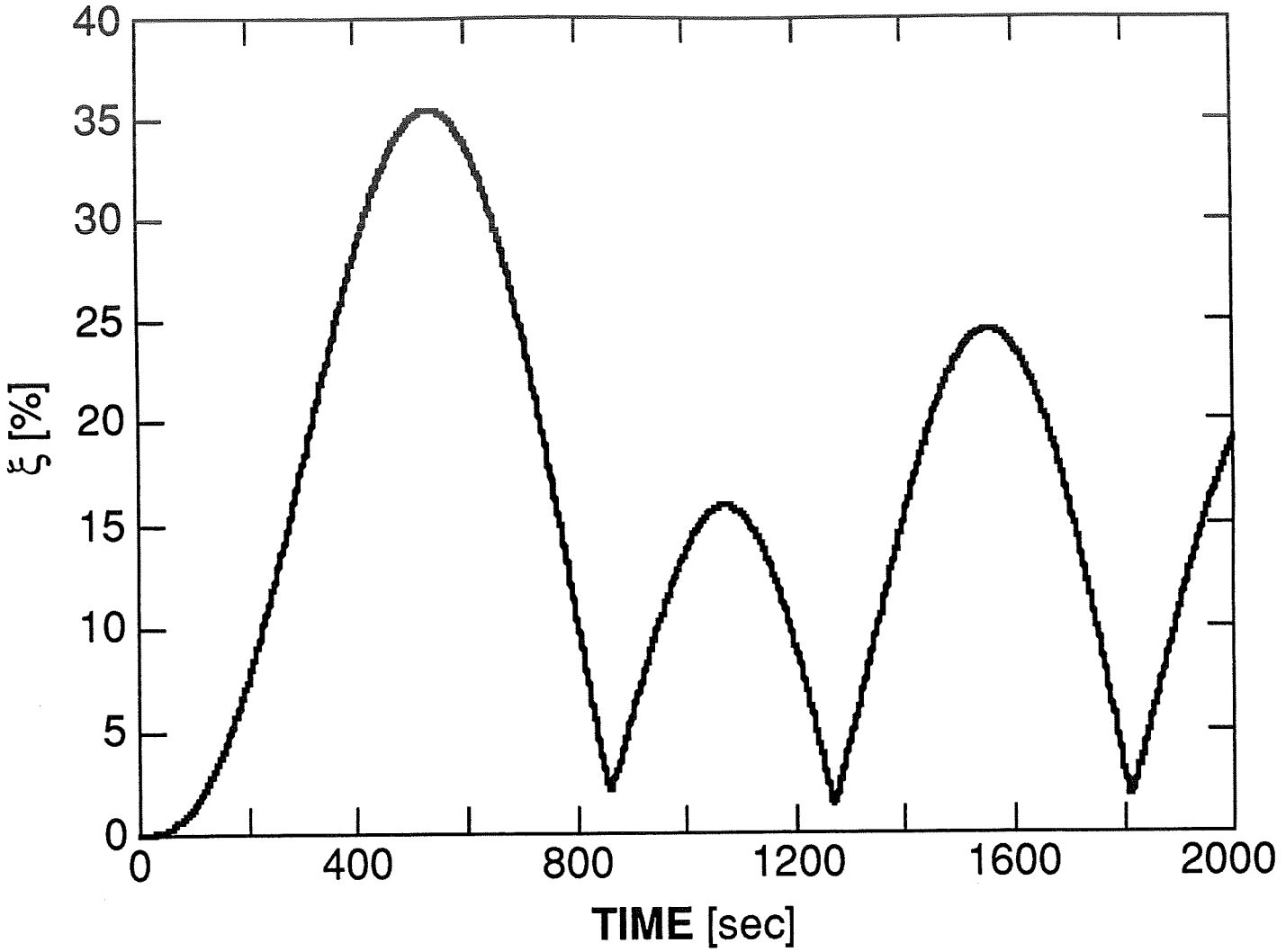

FIG. 2

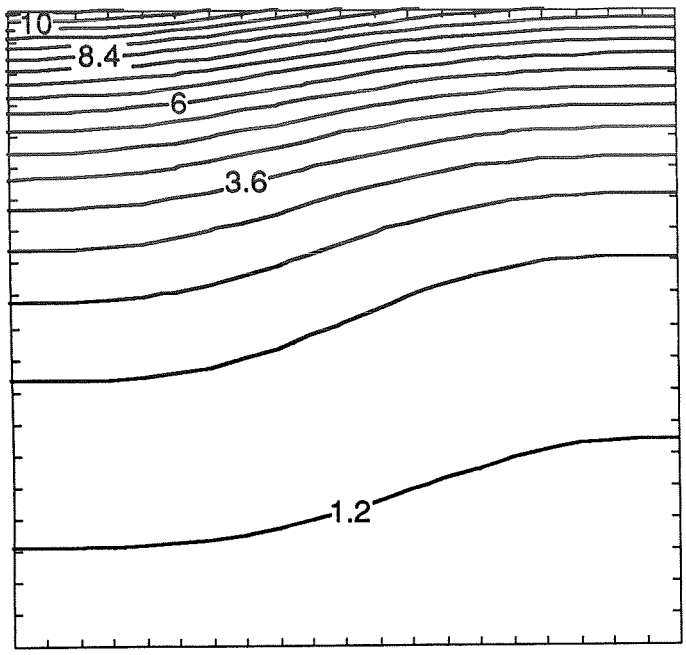

(a)

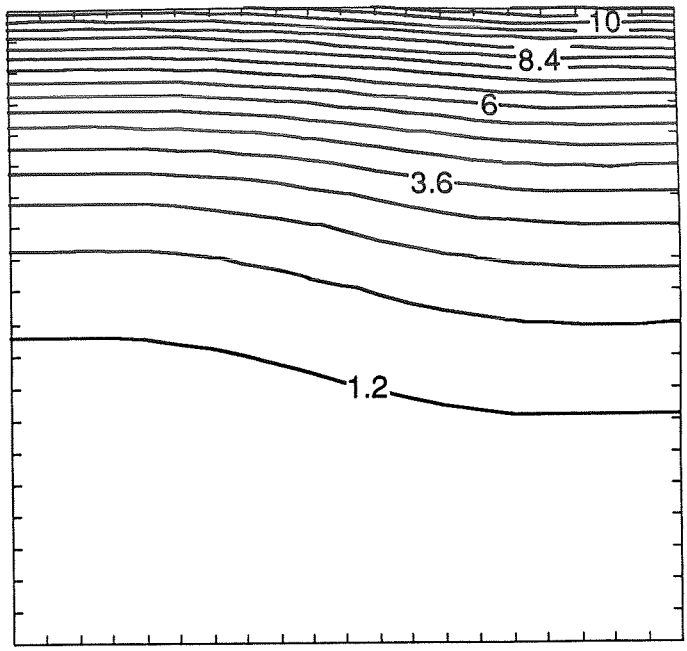

(b)

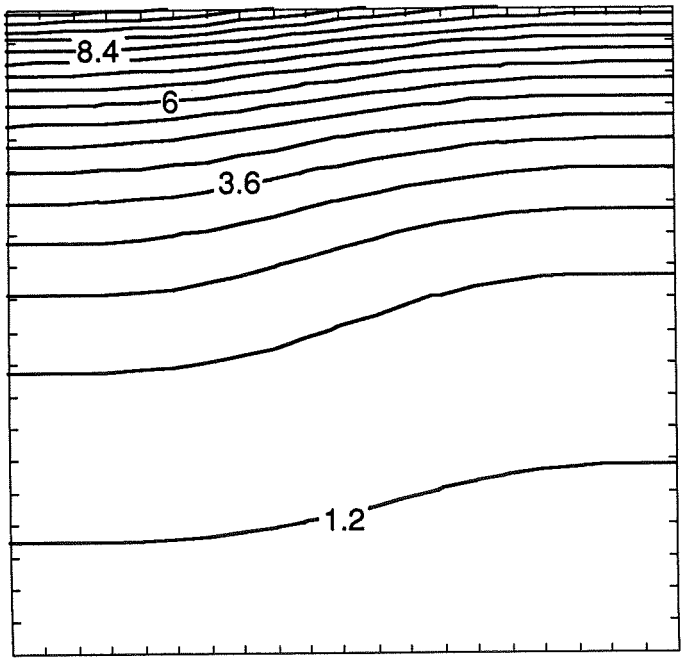

(c)

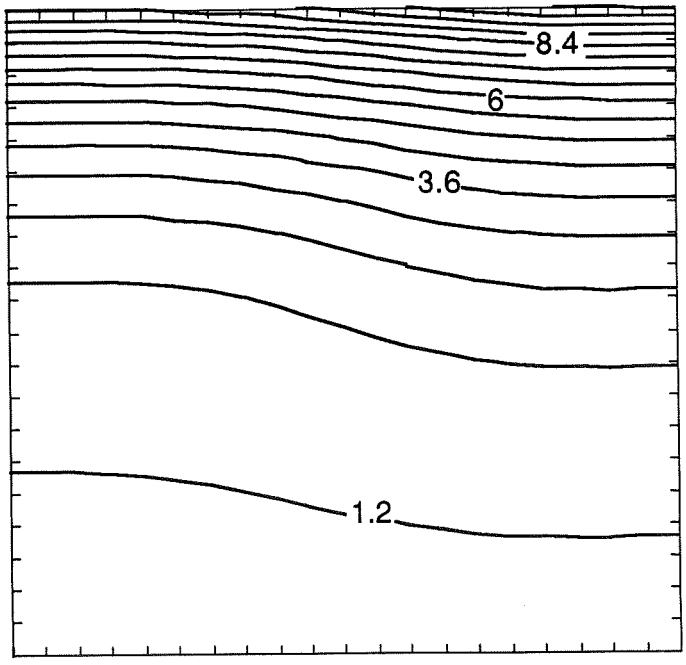

(d)

FIG. 3

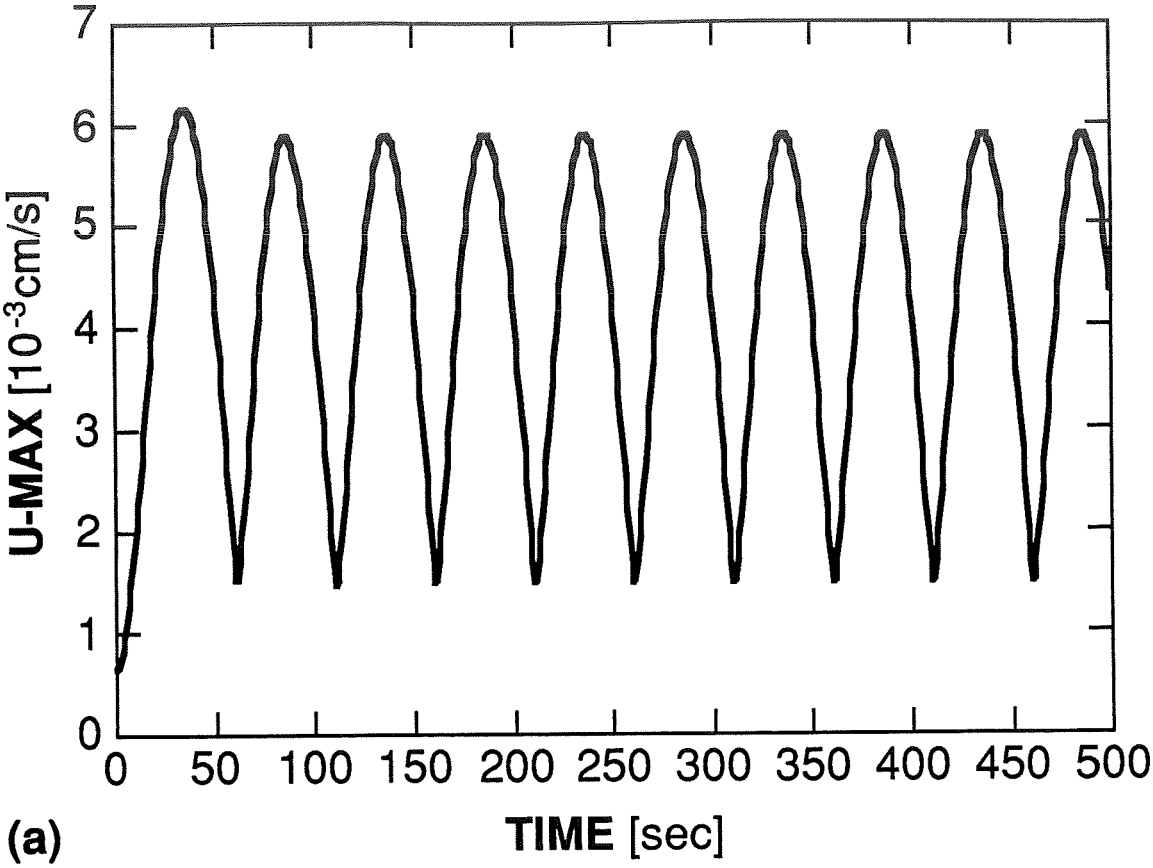
U-MAX [10-3cm/s]
0
1
2
3
4
5
6
7
0 50 100 150 200 250 300 350 400 450 500
TIME [sec]

(a)

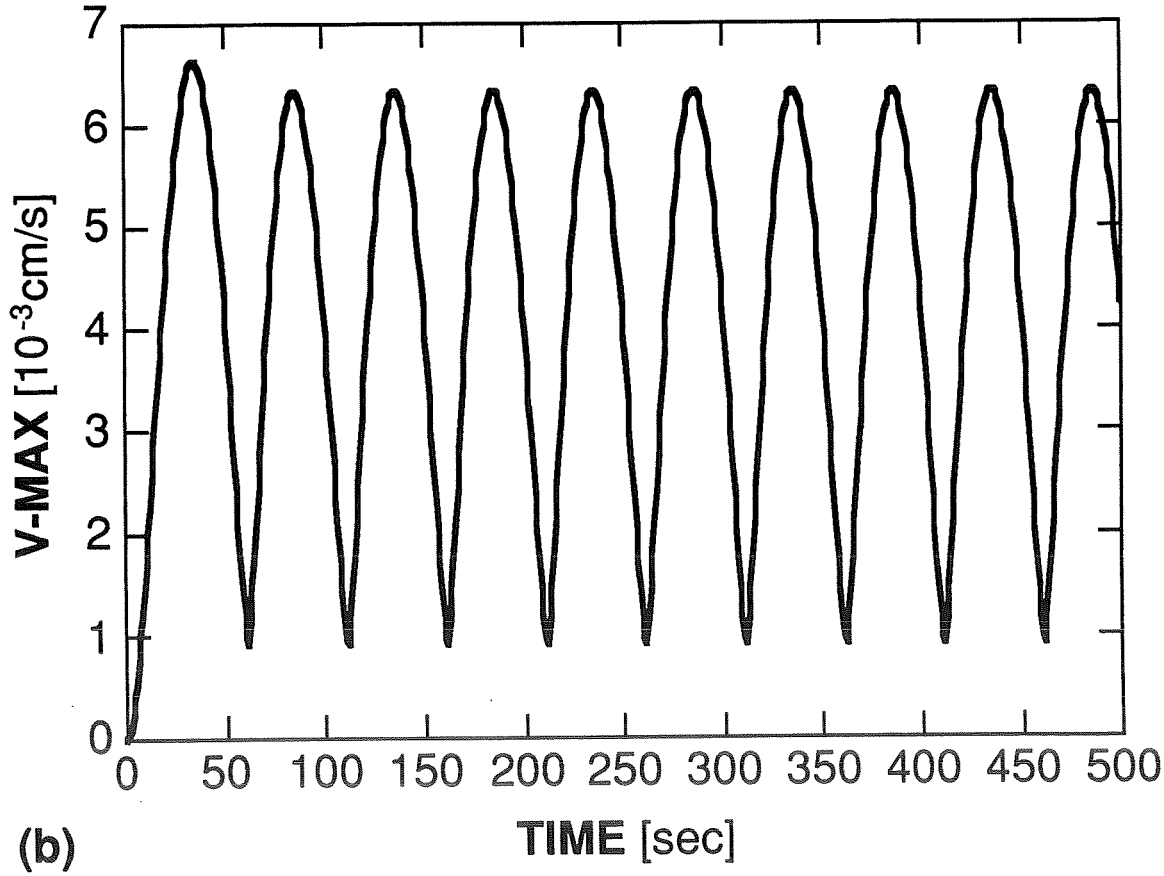
V-MAX [10-3cm/s]
0
1
2
3
4
5
6
7
0 50 100 150 200 250 300 350 400 450 500
TIME [sec]

(b)

FIG. 4

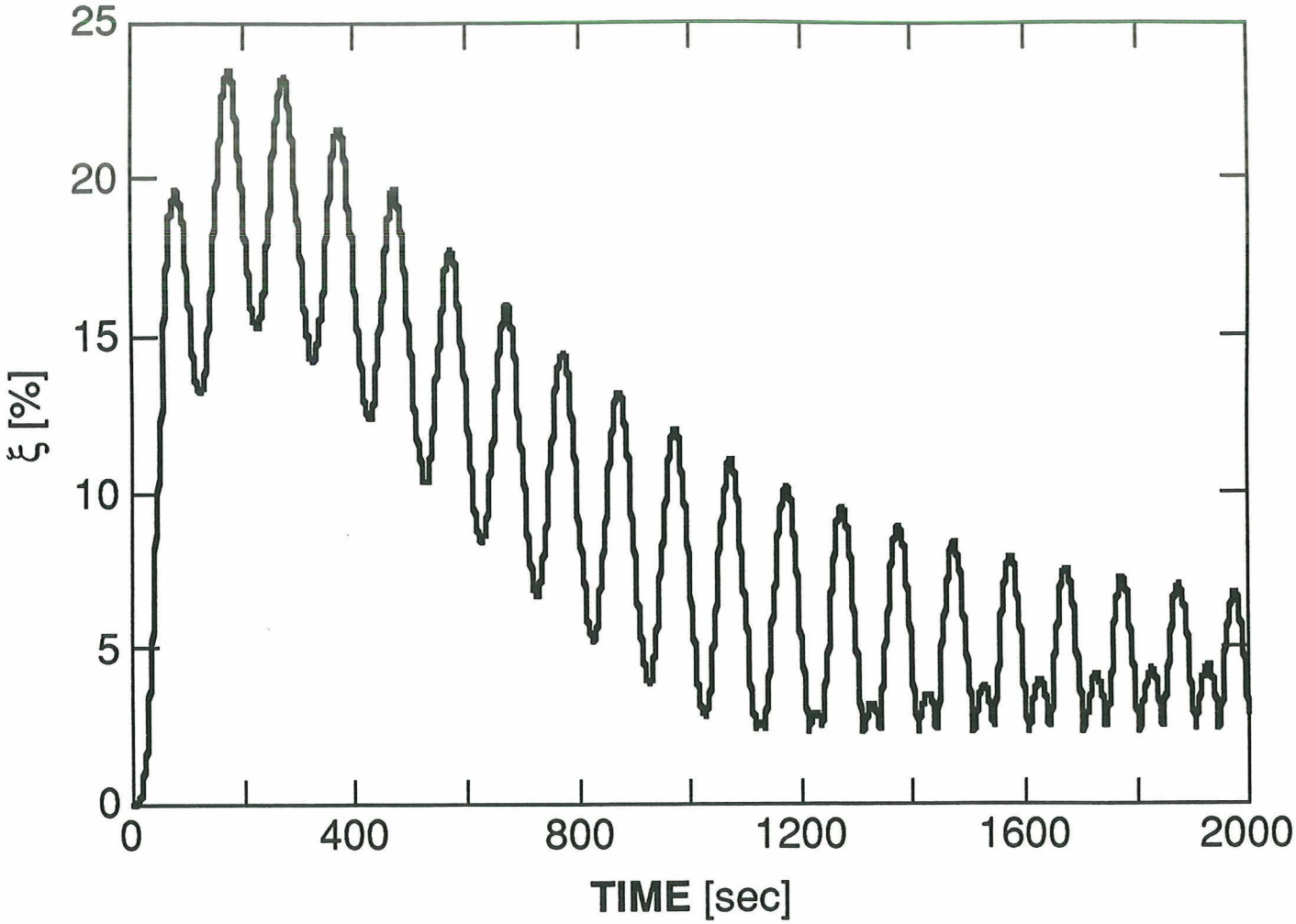

FIG. 5

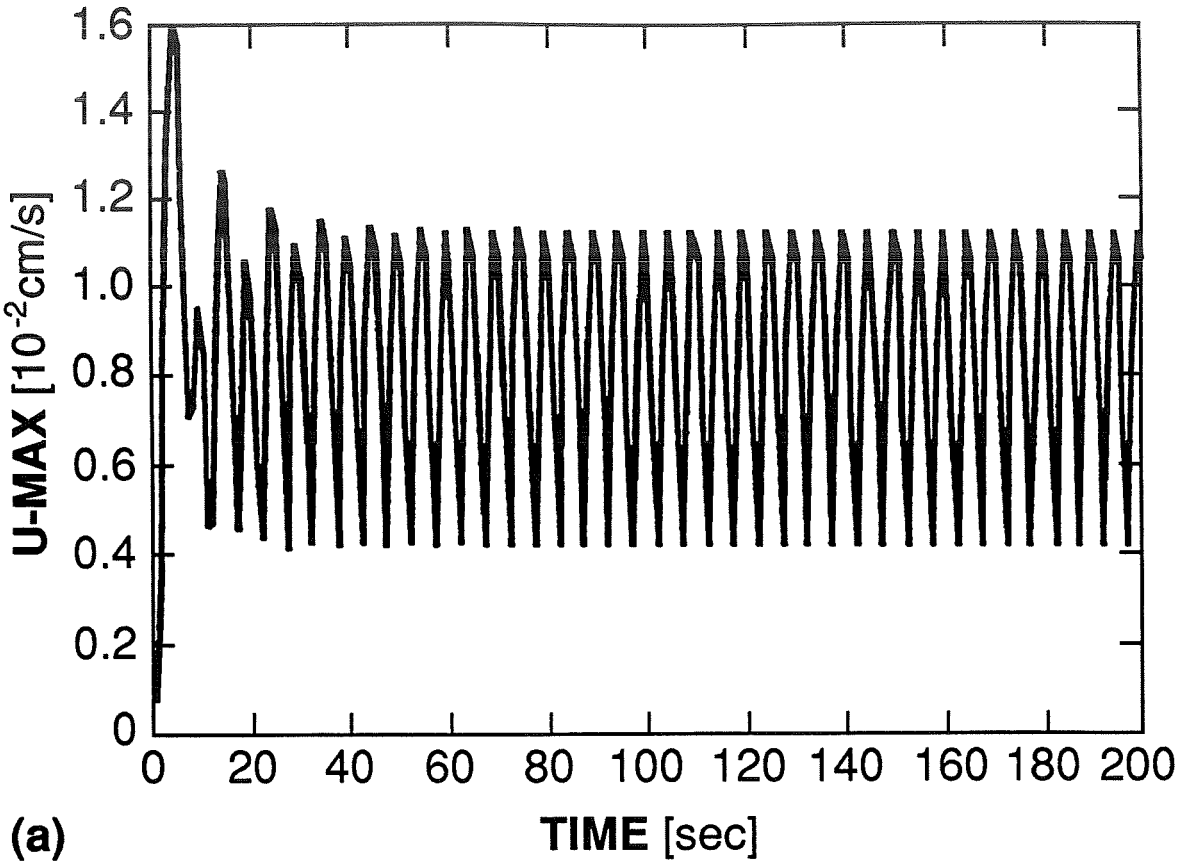
1.6
1.4
1.2
1.0
0.8
0.6
0.4
0.2
0
U-MAX [10-2cm/s]
0 20 40 60 80 100 120 140 160 180 200
TIME [sec]

(a)

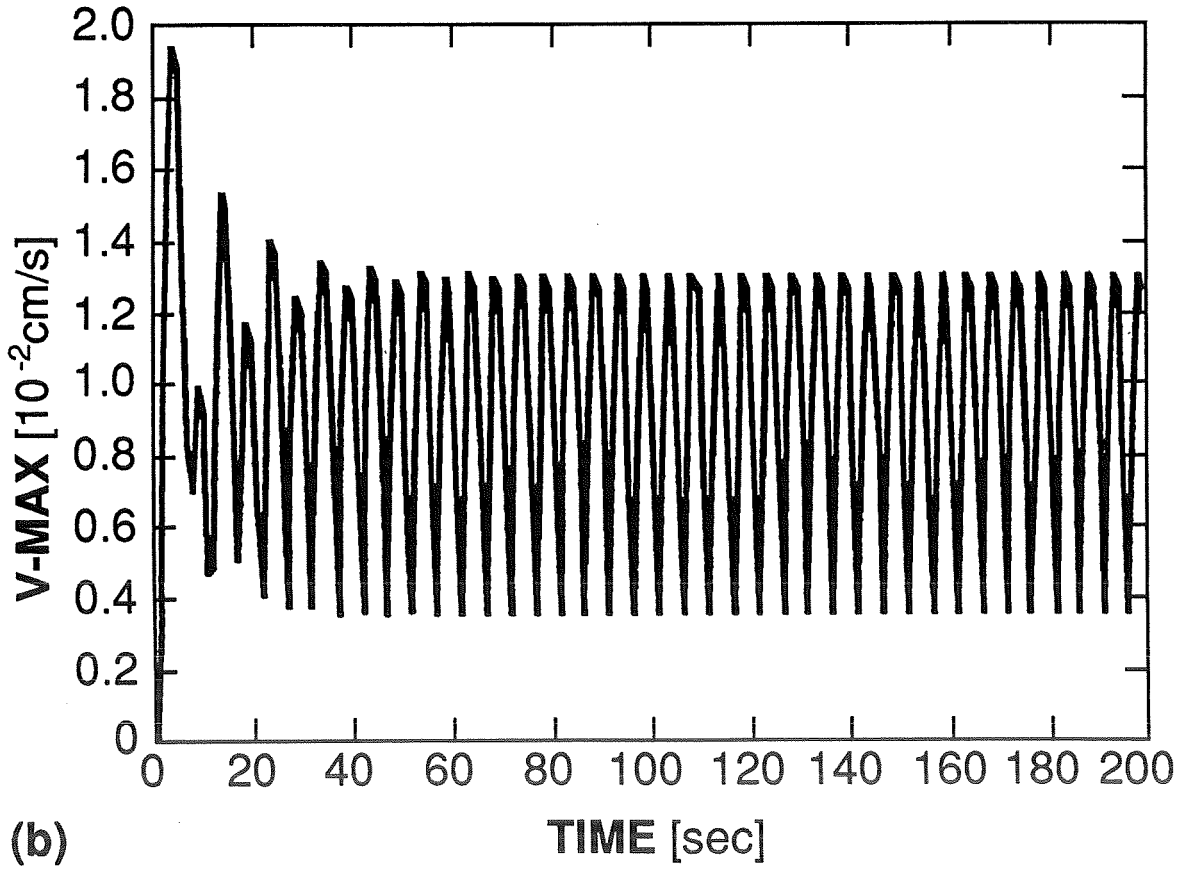
2.0
1.8
1.6
1.4
1.2
1.0
0.8
0.6
0.4
0.2
0
V-MAX [10-2cm/s]
0 20 40 60 80 100 120 140 160 180 200
TIME [sec]

(b)

FIG. 6

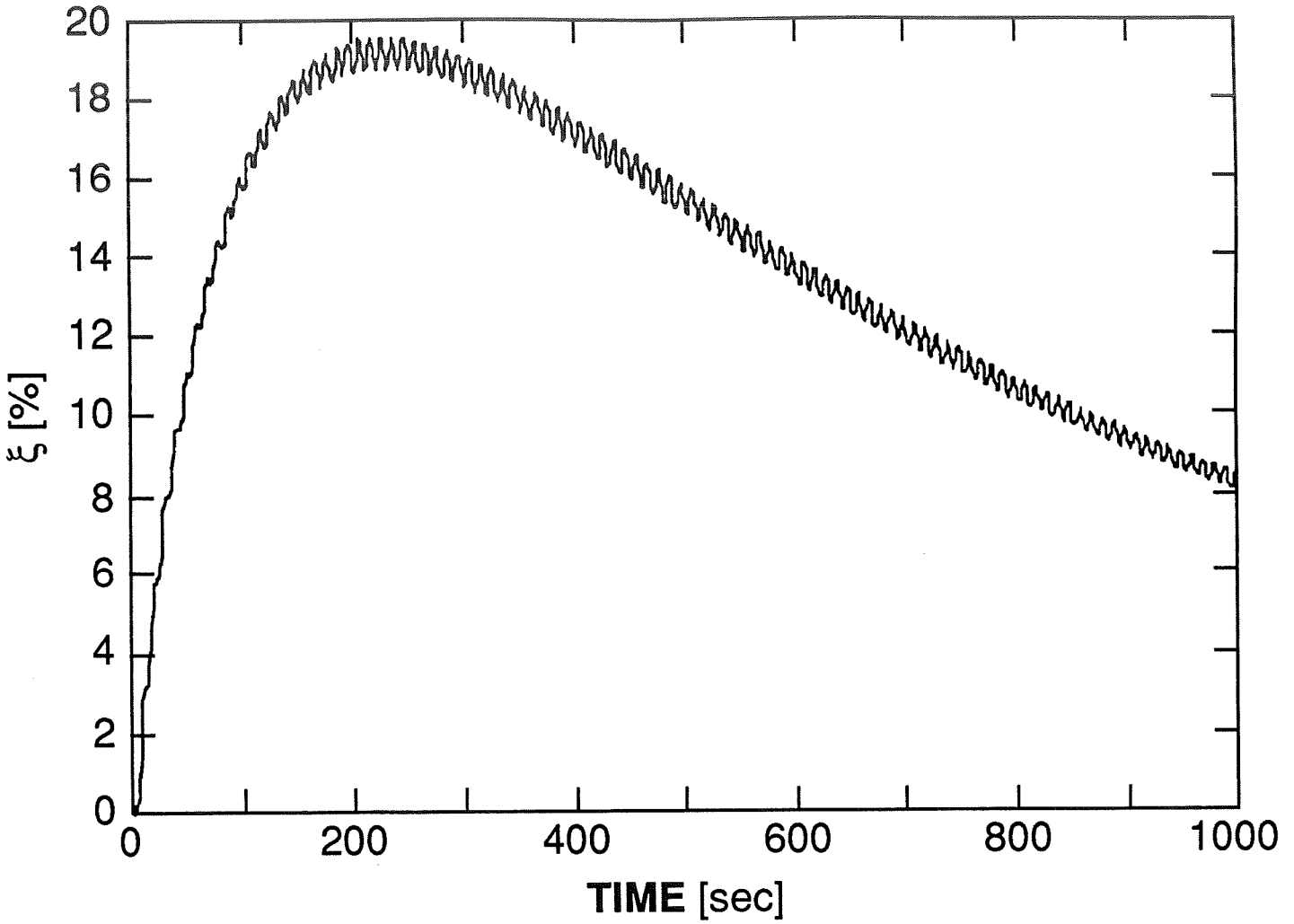

FIG. 7

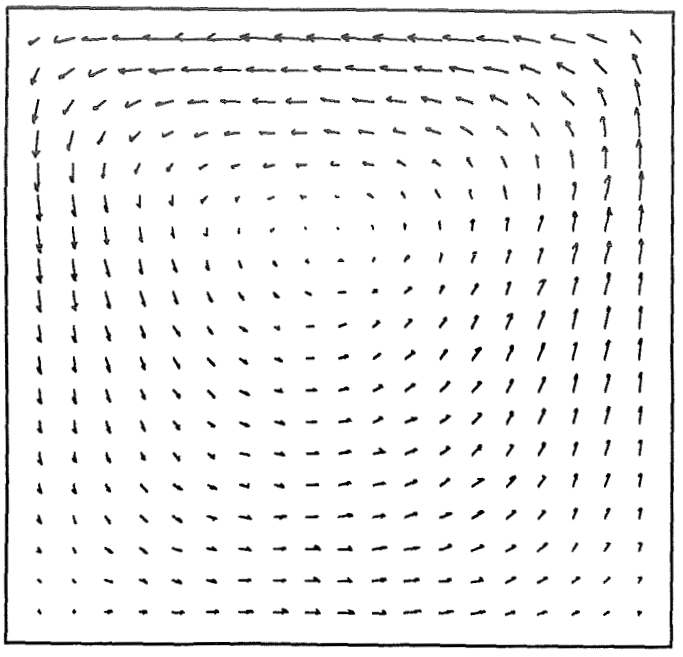

(a)

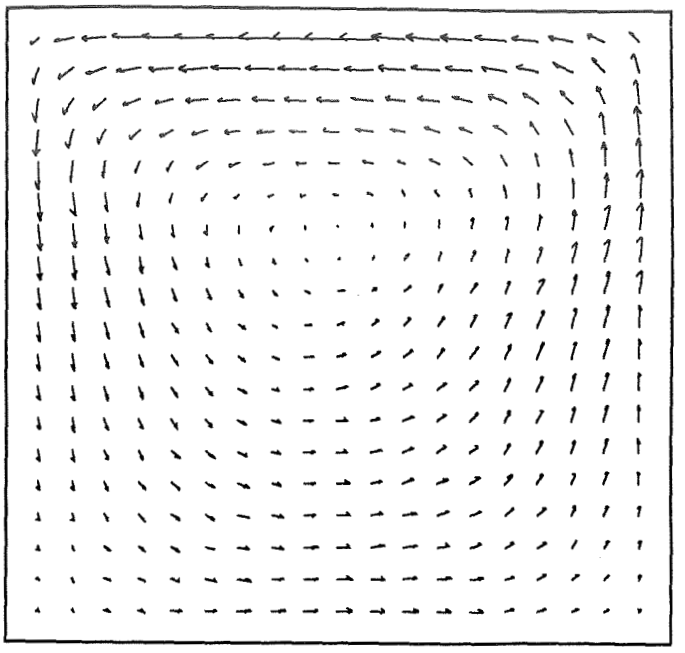

(b)

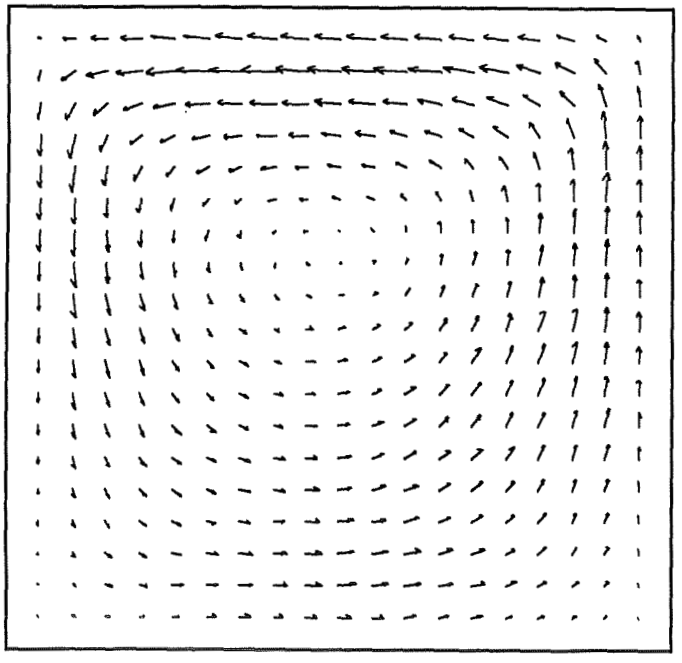

(c)

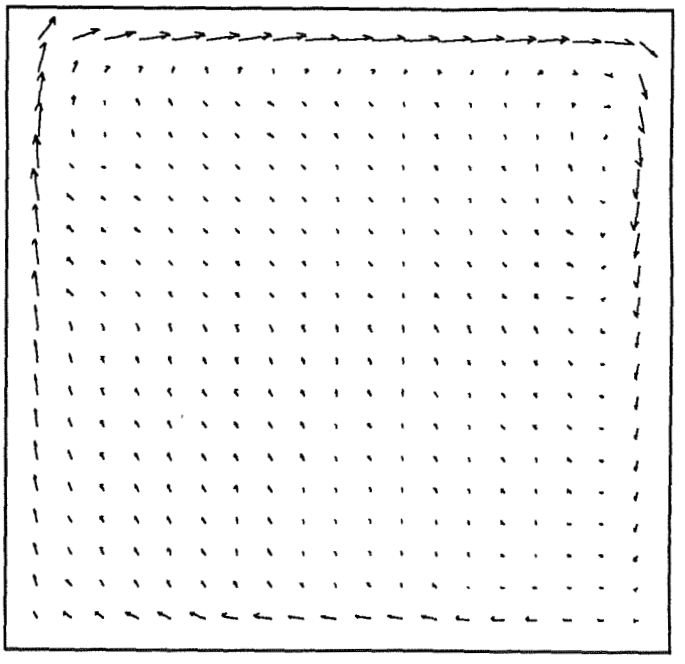

(d)

FIG. 8

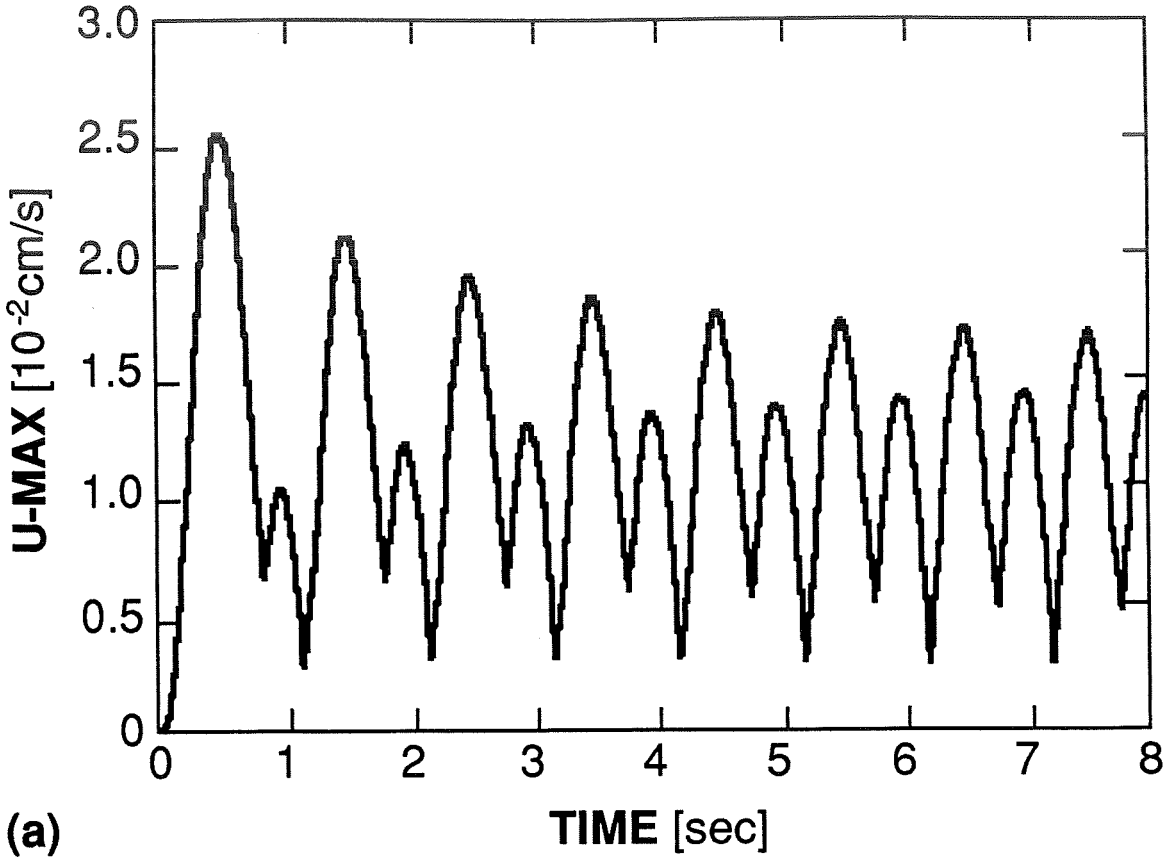
3.0
2.5
2.0
1.5
1.0
0.5
0
U-MAX [10-2cm/s]
0
1
2
3
4
5
6
7
8
TIME [sec]

(a)

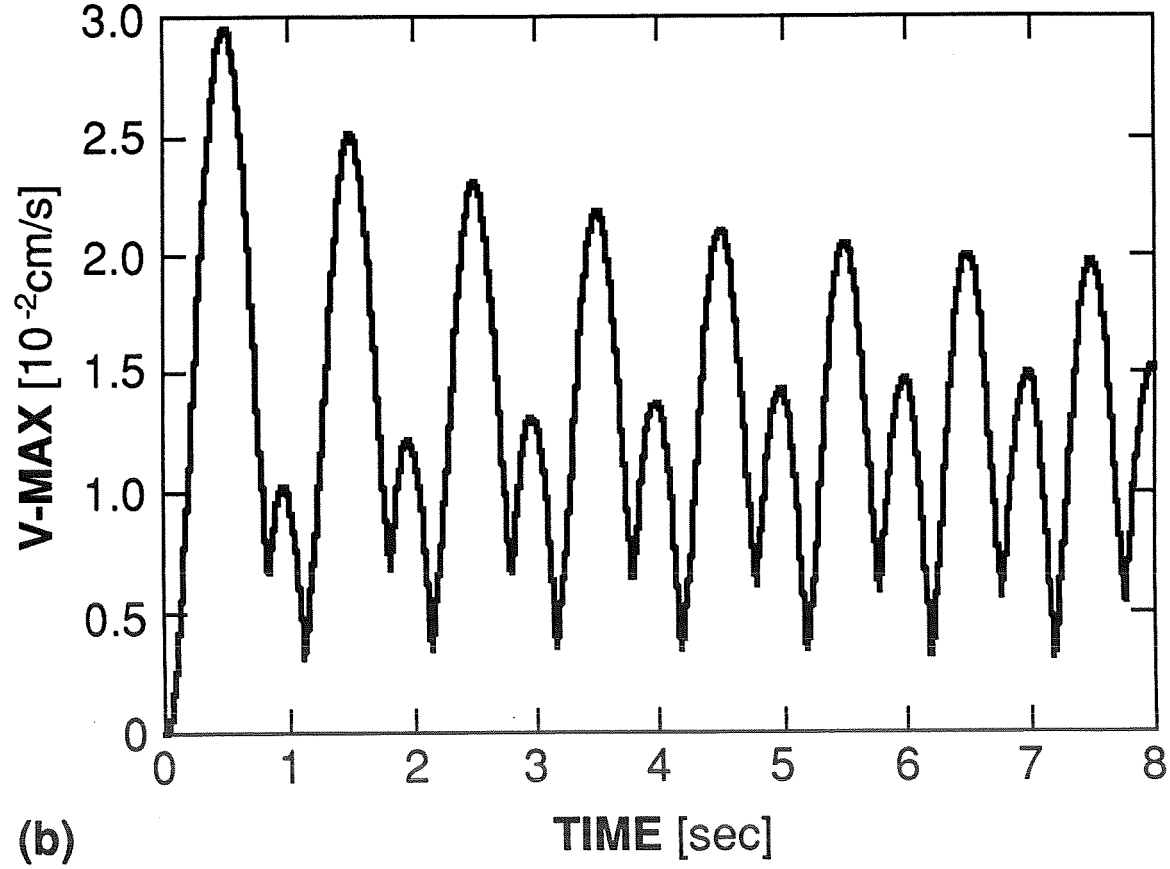
3.0
2.5
2.0
1.5
1.0
0.5
0
V-MAX [10-2cm/s]
0
1
2
3
4
5
6
7
8
TIME [sec]

(b)

FIG. 9

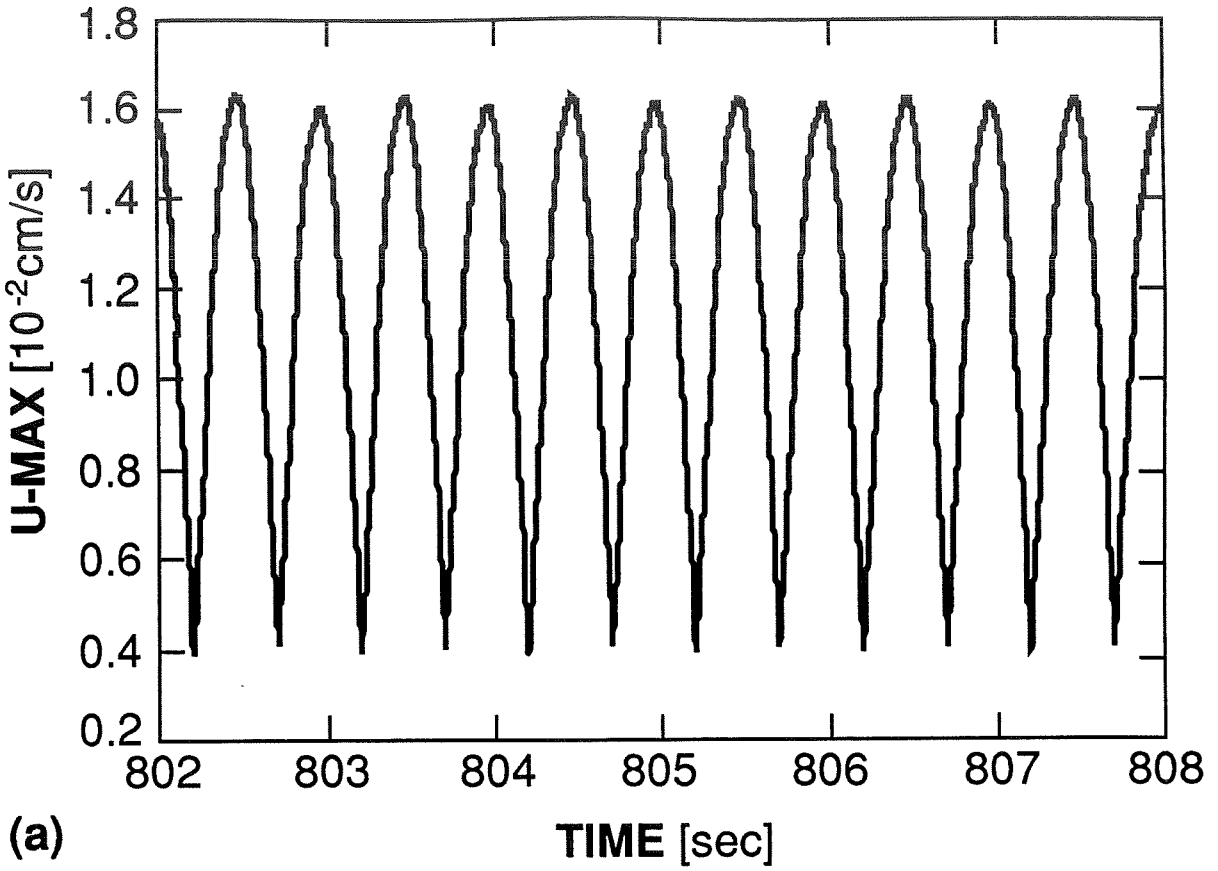
1.8
1.6
1.4
1.2
1.0
0.8
0.6
0.4
0.2
U-MAX [10-2cm/s]
802
803
804
805
806
807
808
TIME [sec]

(a)

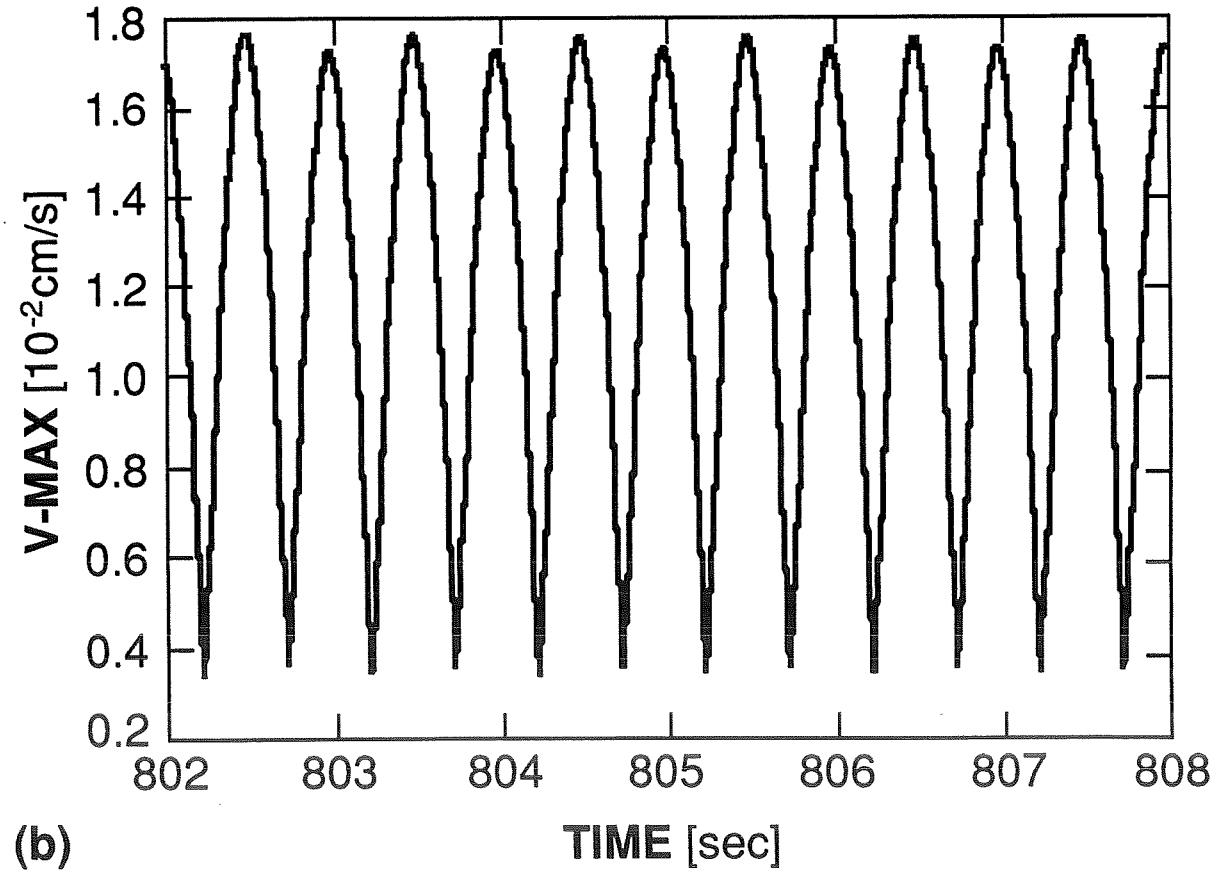
1.8
1.6
1.4
1.2
1.0
0.8
0.6
0.4
0.2
V-MAX [10-2cm/s]
802
803
804
805
806
807
808
TIME [sec]

(b)

FIG. 10

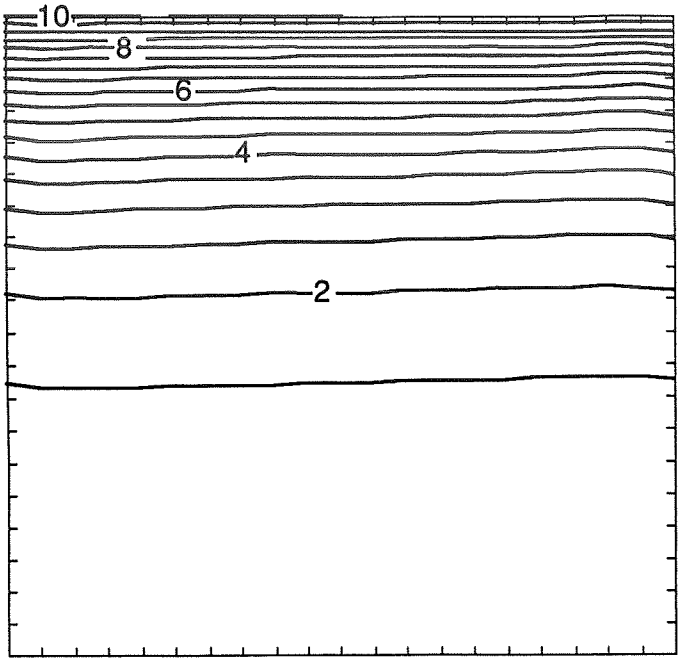

(a)

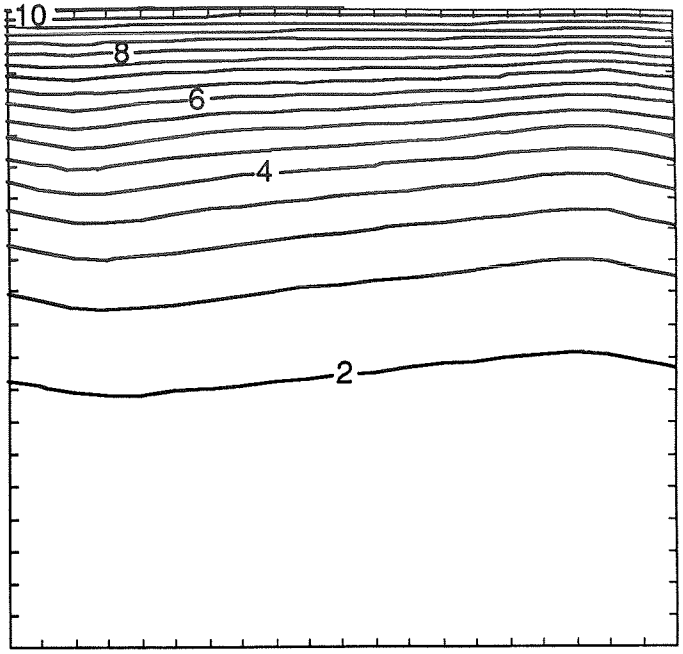

(b)

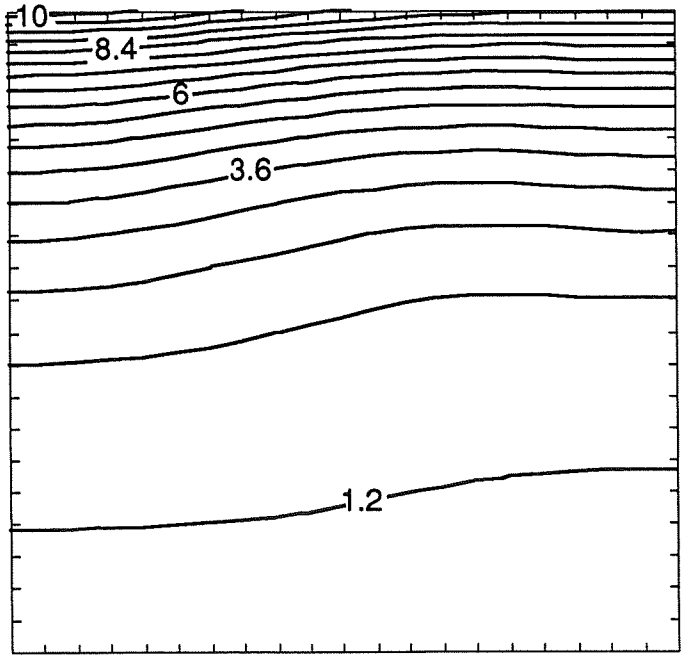

(c)

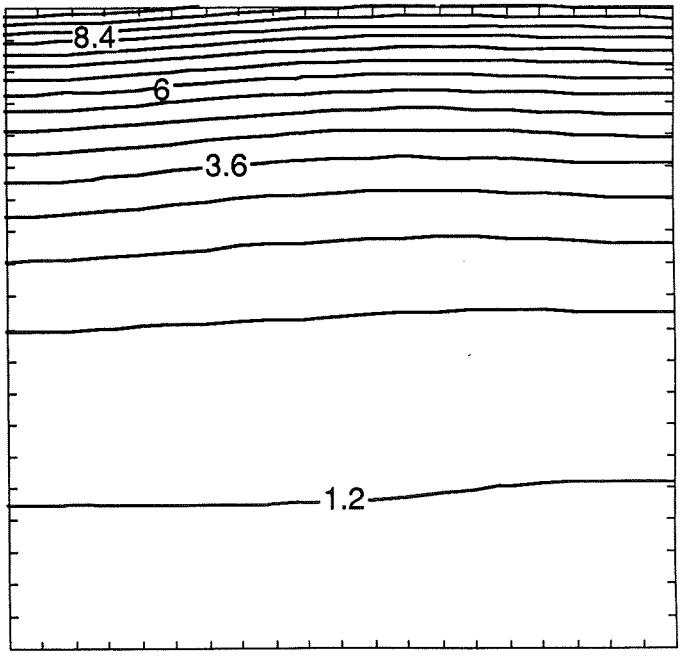

(d)

FIG. 11

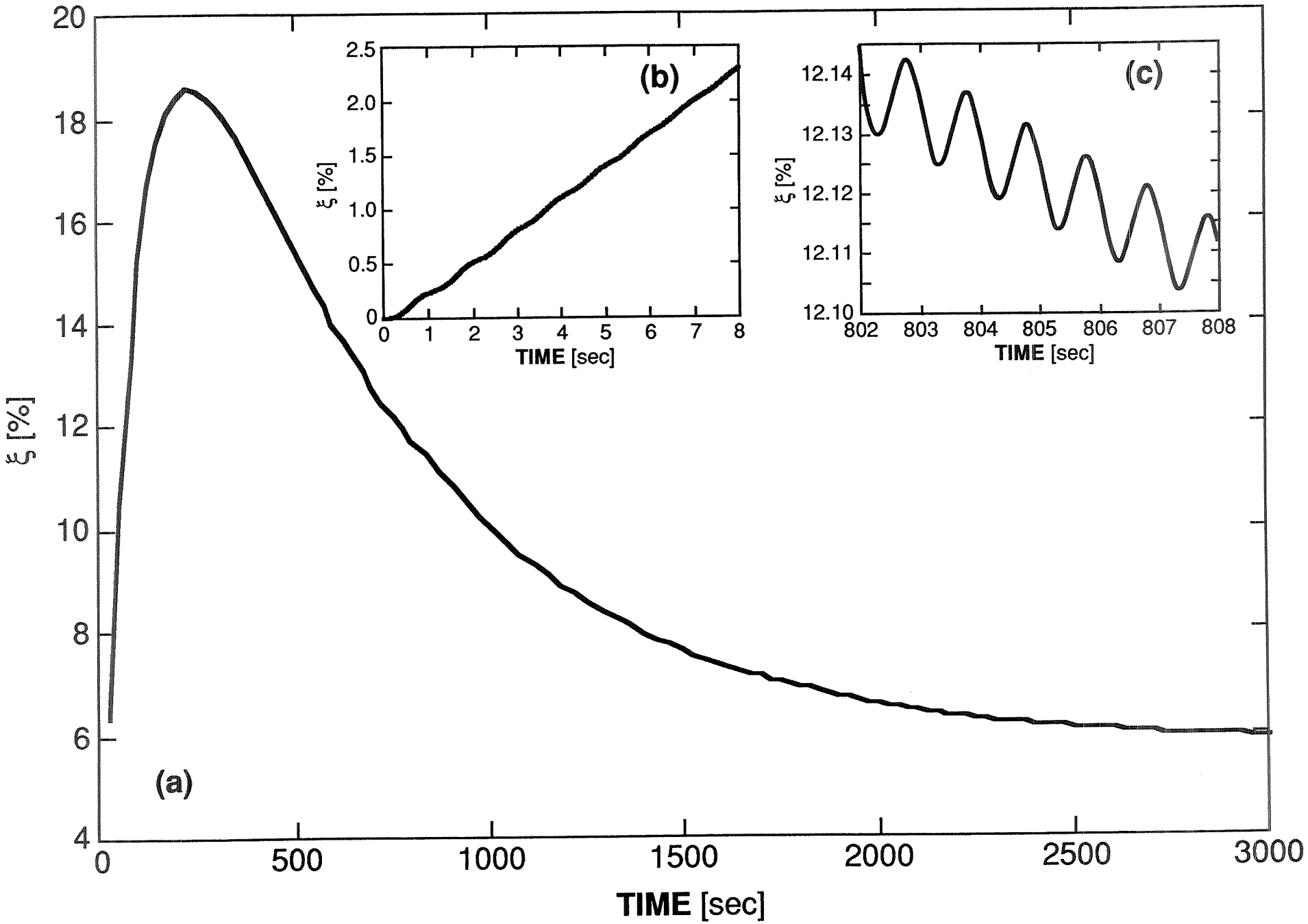
(a)
(b)
(c)
ξ [%]
TIME [sec]
20
18
16
14
12
10
8
6
4
0
500
1000
1500
2000
2500
3000
2.5
2.0
1.5
1.0
0.5
0
1
2
3
4
5
6
7
8
12.14
12.13
12.12
12.11
12.10
802
803
804
805
806
807
808

FIG. 12

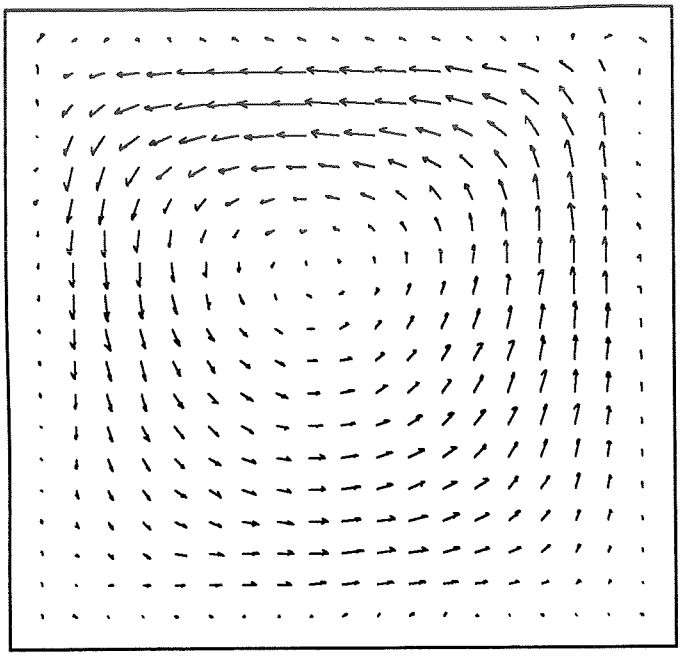

(a)

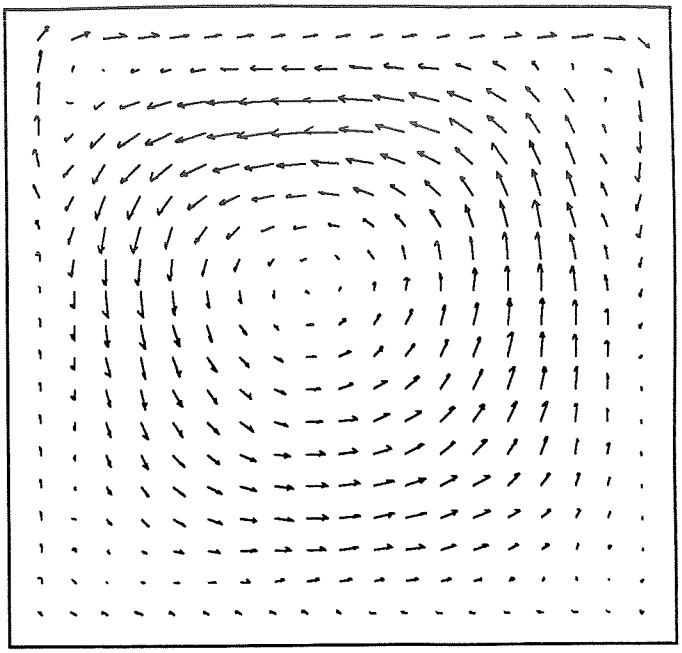

(b)

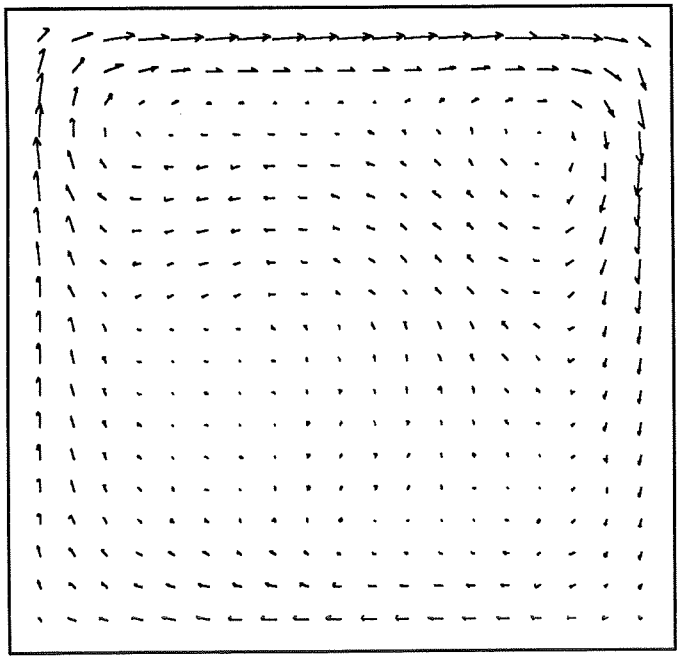

(c)

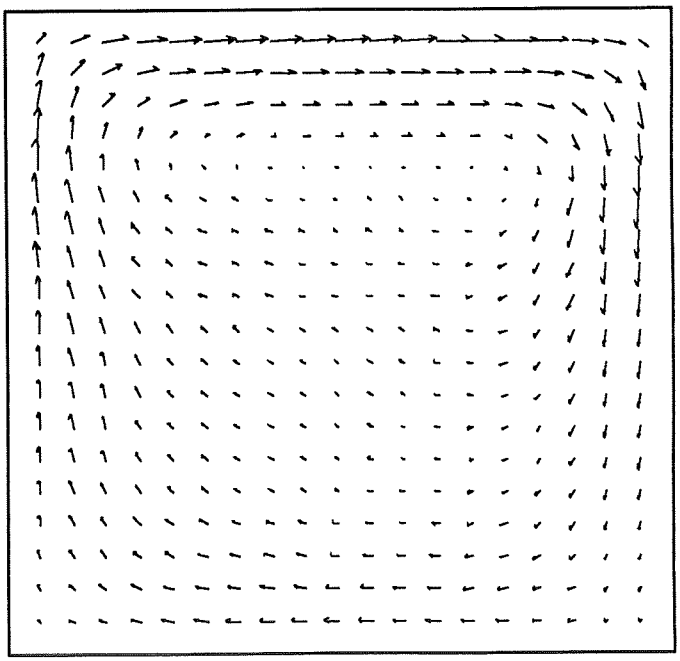

(d)

FIG. 13

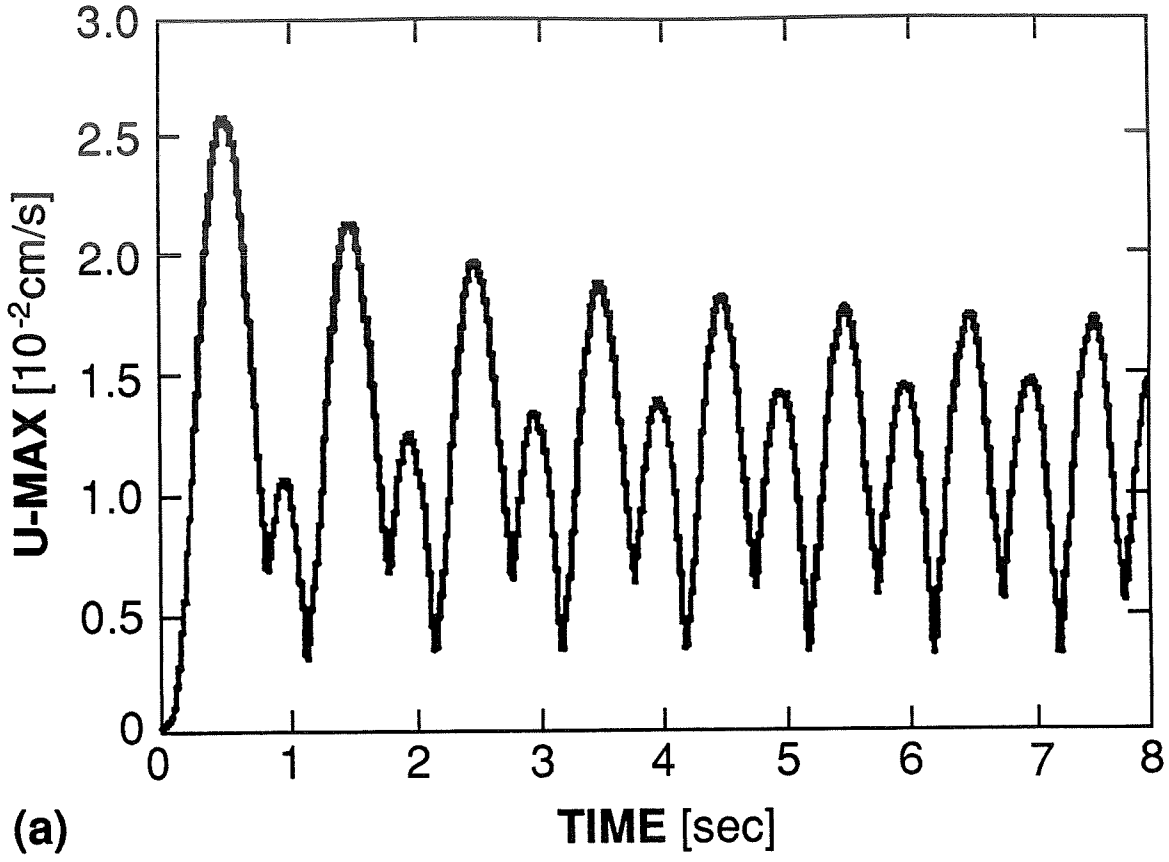
3.0
2.5
2.0
1.5
1.0
0.5
0
U-MAX [10-2cm/s]
0
1
2
3
4
5
6
7
8
TIME [sec]

(a)

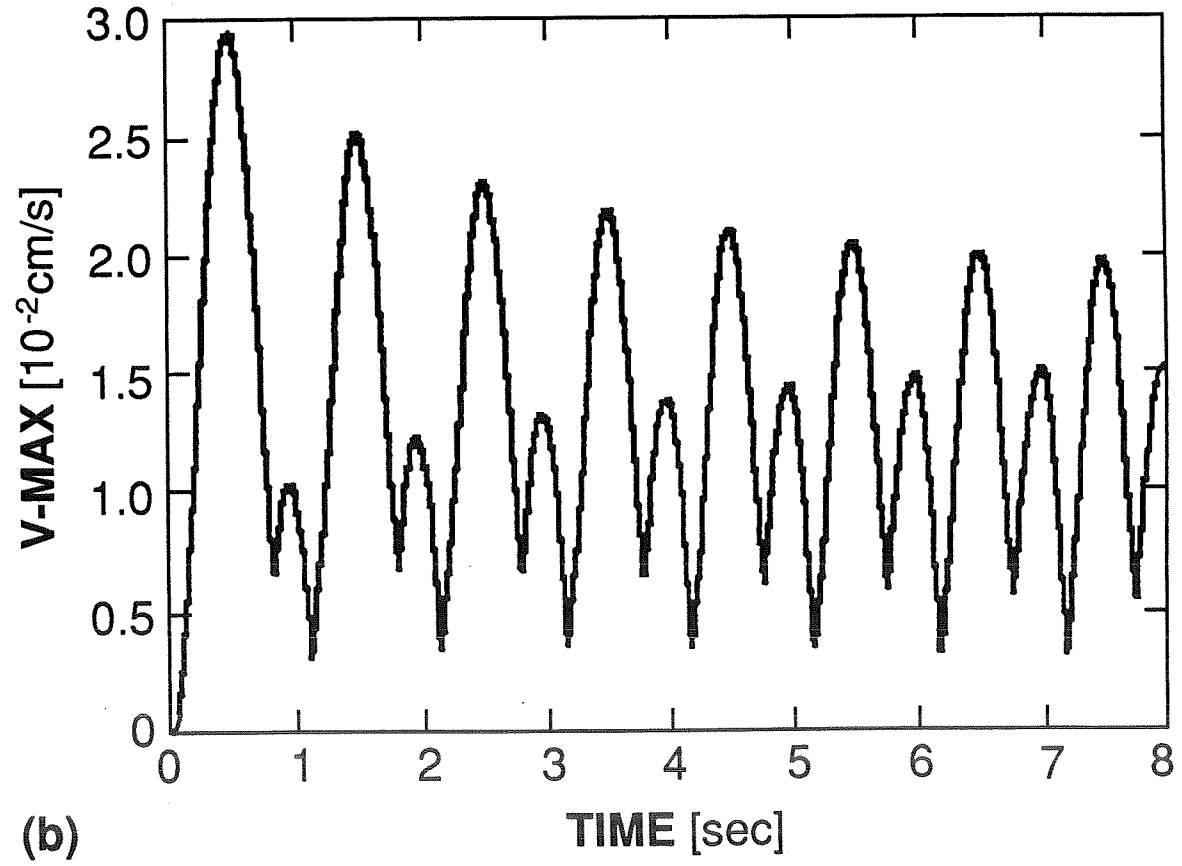
3.0
2.5
2.0
1.5
1.0
0.5
0
V-MAX [10-2cm/s]
0
1
2
3
4
5
6
7
8
TIME [sec]

(b)

FIG. 14

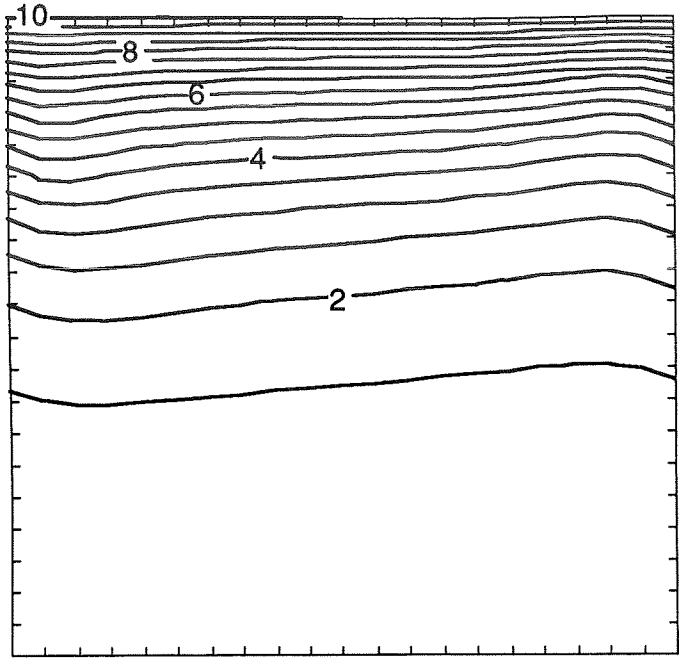

(a)

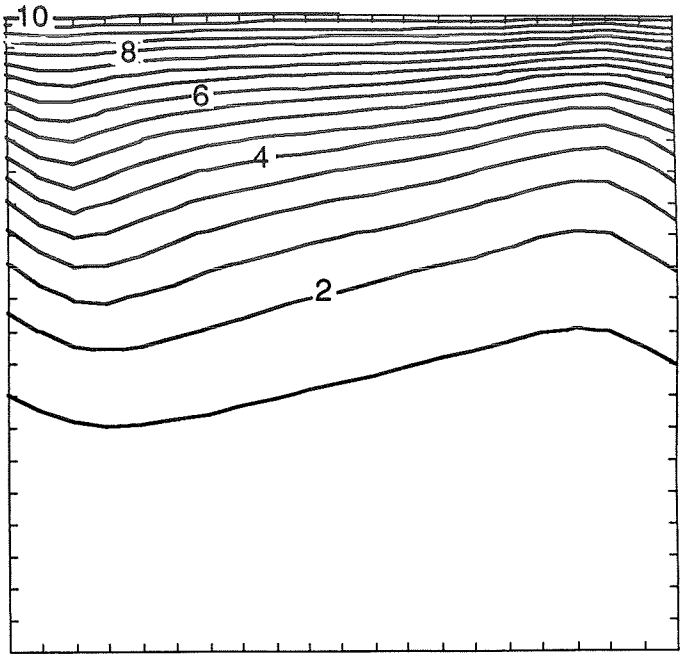

(b)

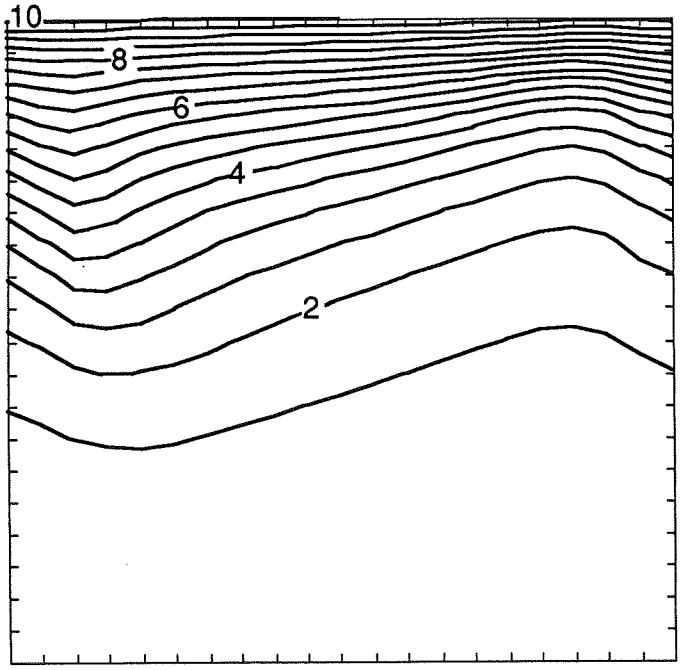

(c)

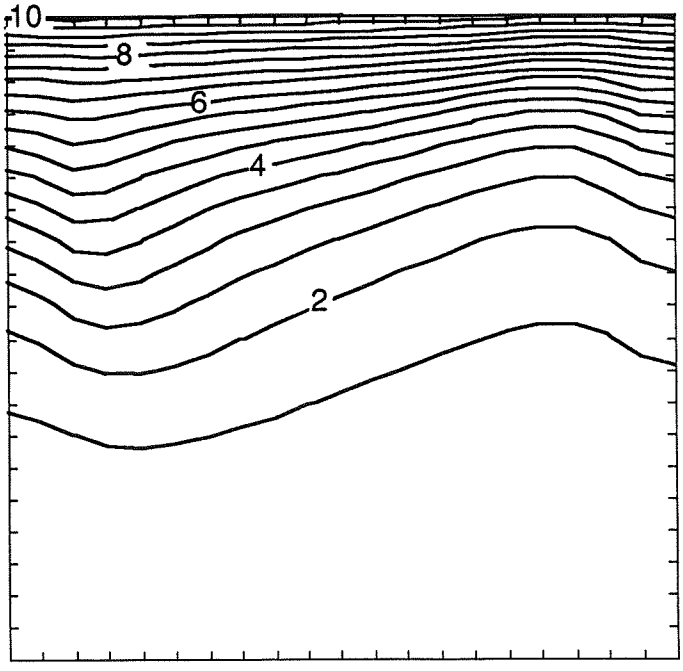

(d)

FIG. 15

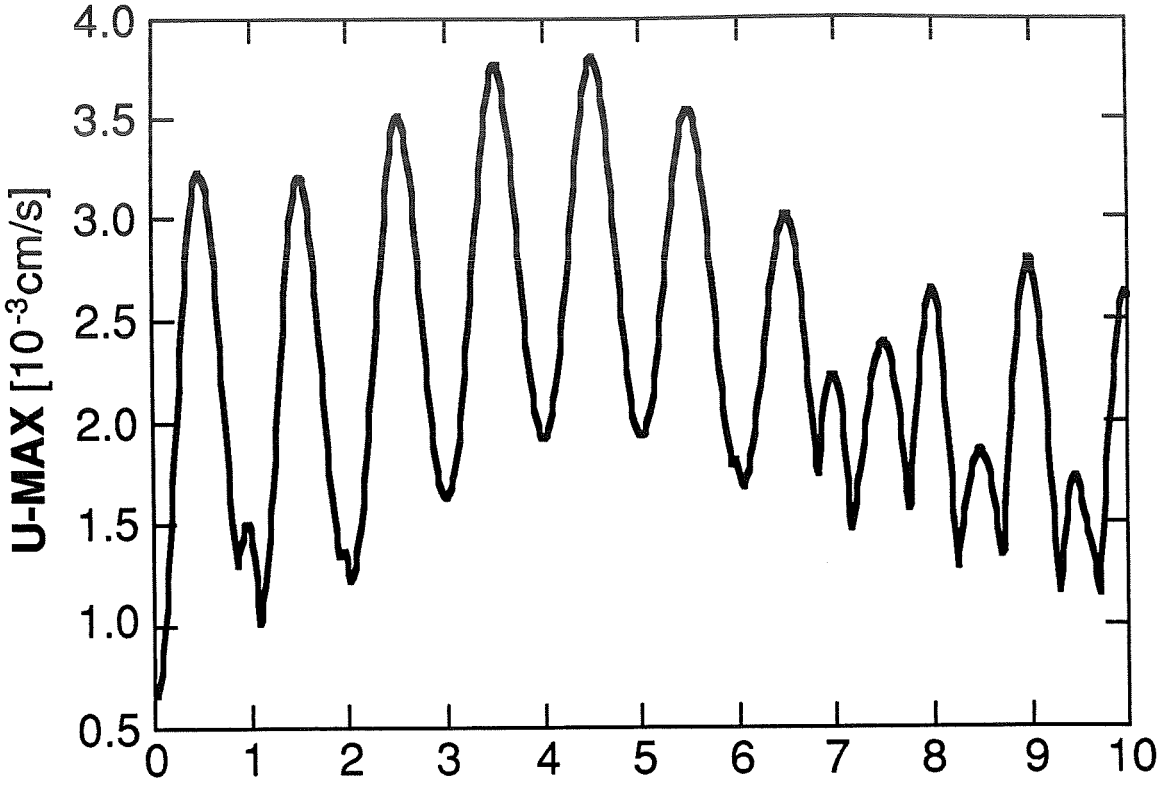
4.0
3.5
3.0
2.5
2.0
1.5
1.0
0.5
U-MAX [10-3cm/s]
0 1 2 3 4 5 6 7 8 9 10
TIME [sec]

(a)

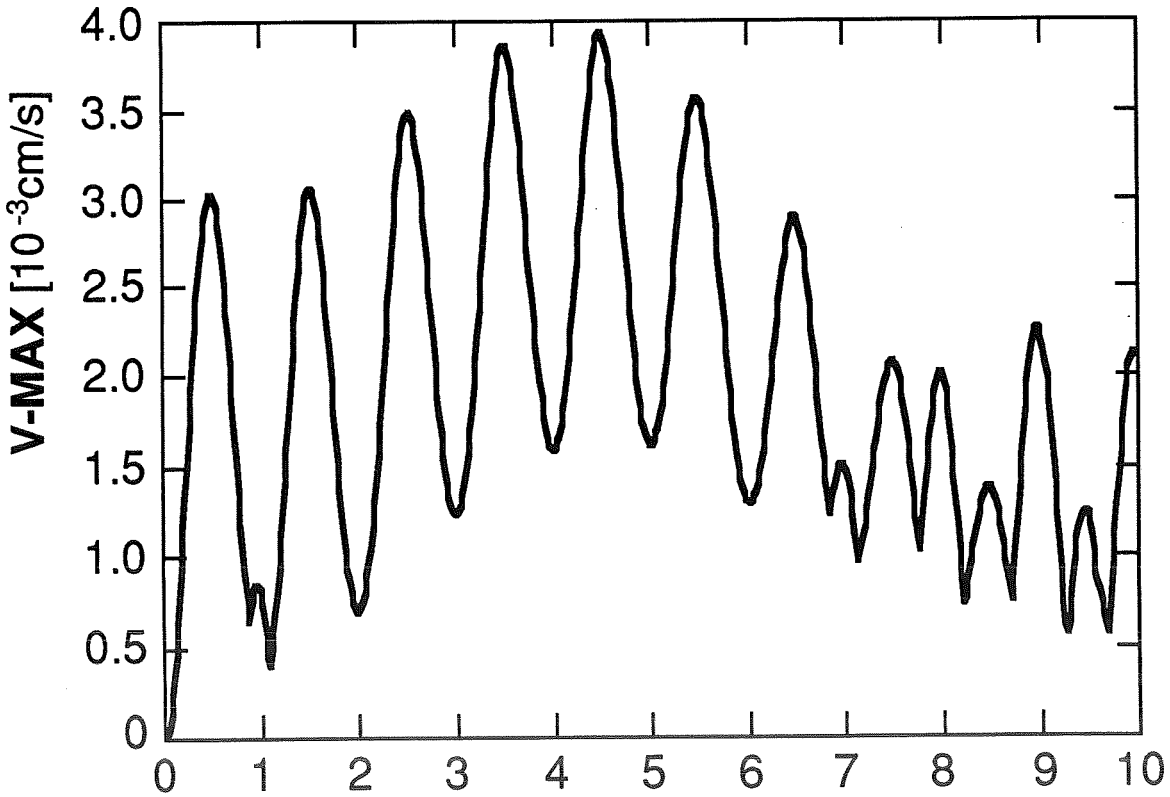
4.0
3.5
3.0
2.5
2.0
1.5
1.0
0.5
0
V-MAX [10-3cm/s]
0 1 2 3 4 5 6 7 8 9 10
TIME [sec]

(b)

FIG. 16

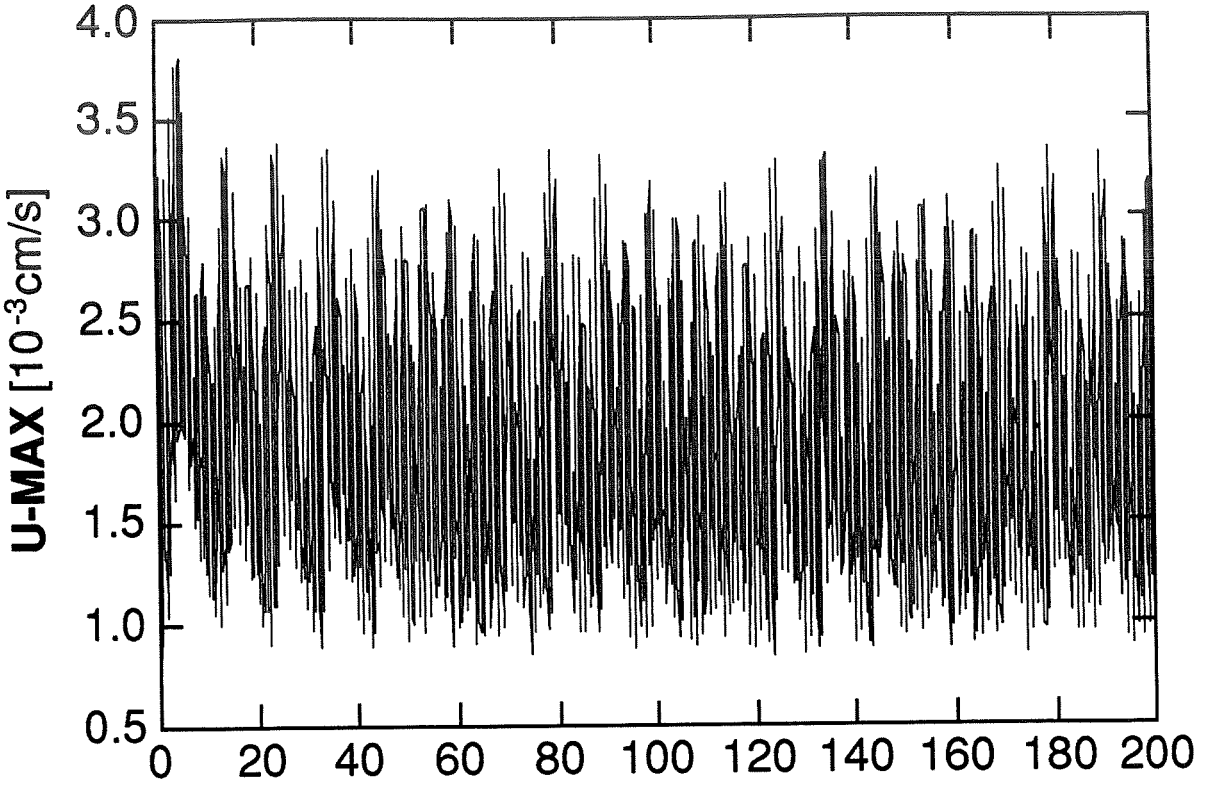
4.0
3.5
3.0
2.5
2.0
1.5
1.0
0.5
U-MAX [10-3cm/s]
0
20
40
60
80
100
120
140
160
180
200
TIME [sec]

(a)

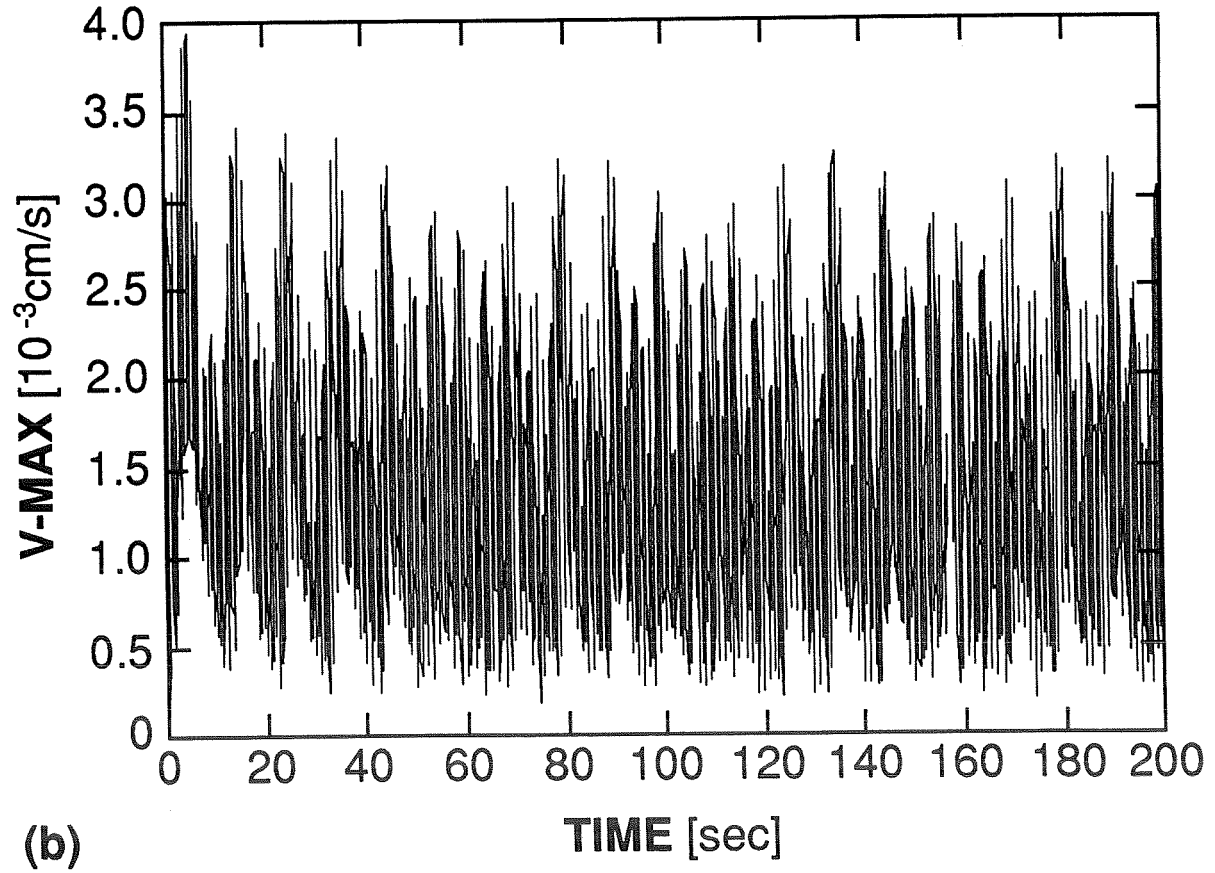
4.0
3.5
3.0
2.5
2.0
1.5
1.0
0.5
0
V-MAX [10-3cm/s]
0
20
40
60
80
100
120
140
160
180
200
TIME [sec]

(b)

FIG. 17

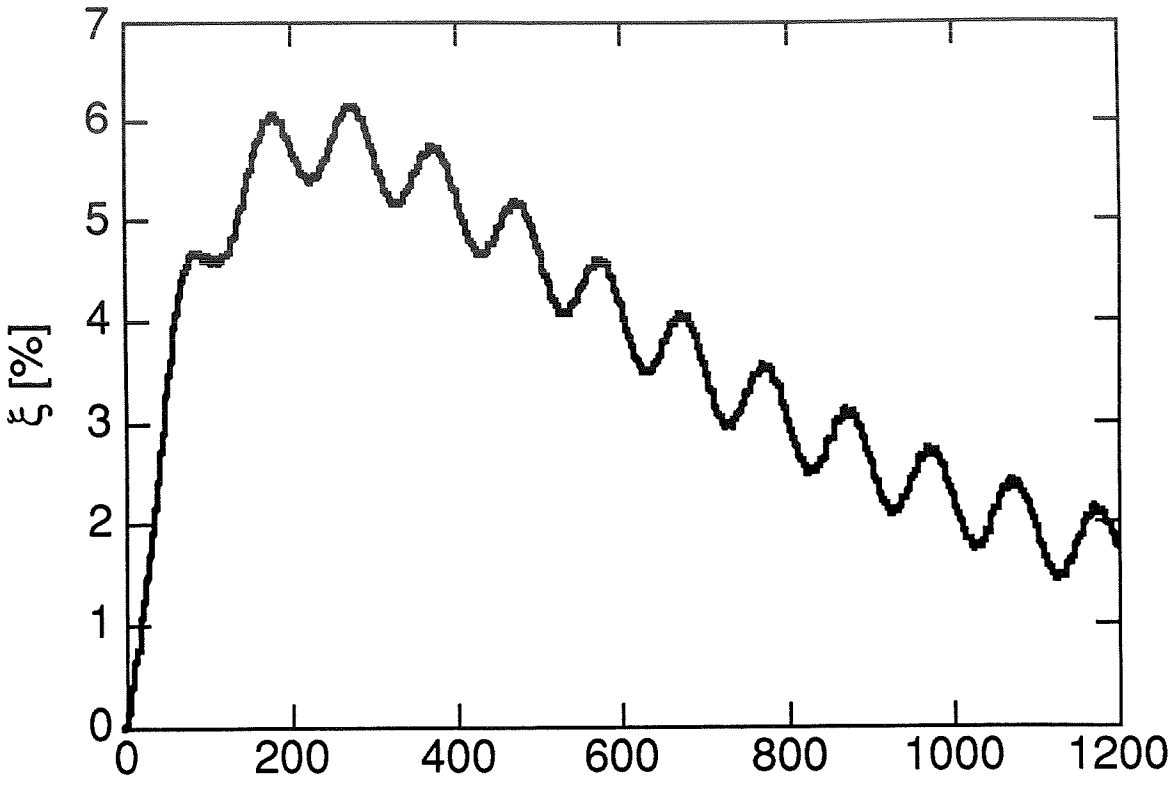
7
6
5
4
3
2
1
0
ξ [%]
0
200
400
600
800
1000
1200
TIME [sec]

(a)

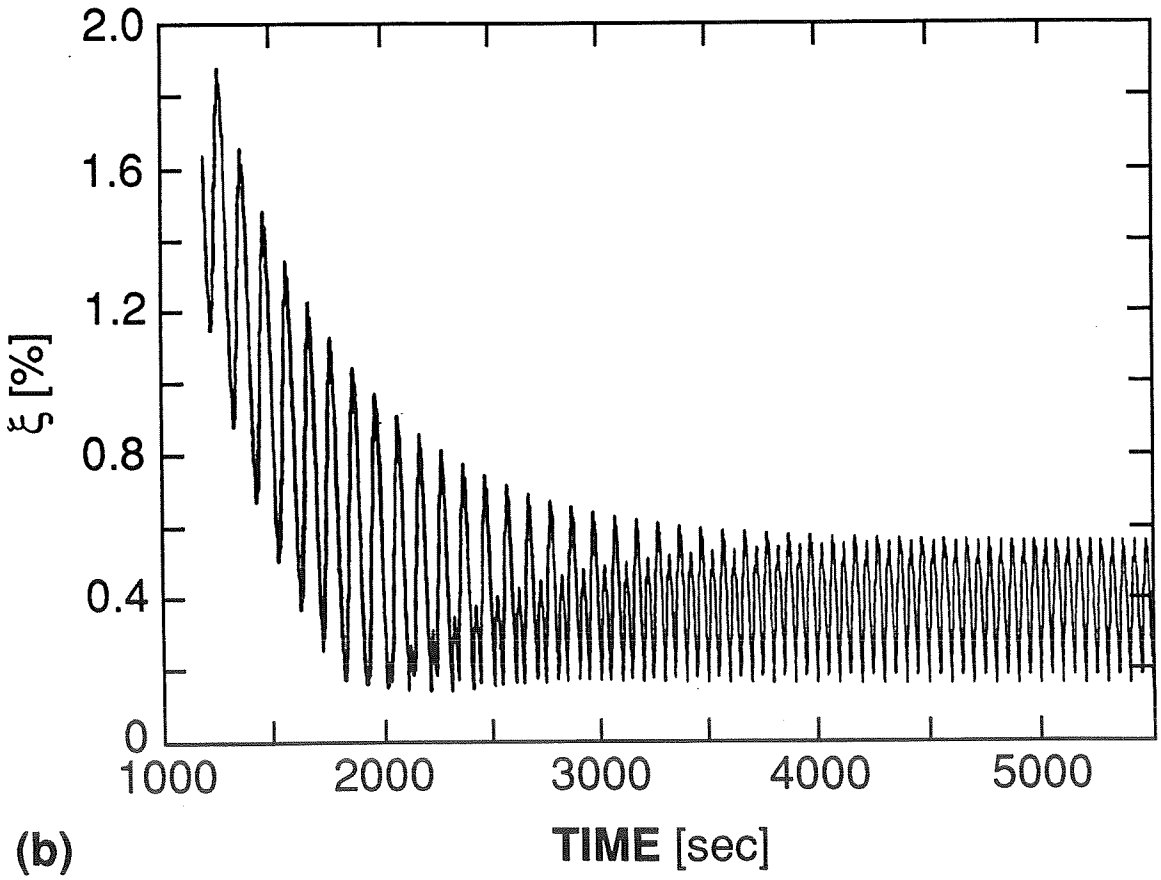
2.0
1.6
1.2
0.8
0.4
0
ξ [%]
1000
2000
3000
4000
5000
TIME [sec]

(b)

FIG. 18

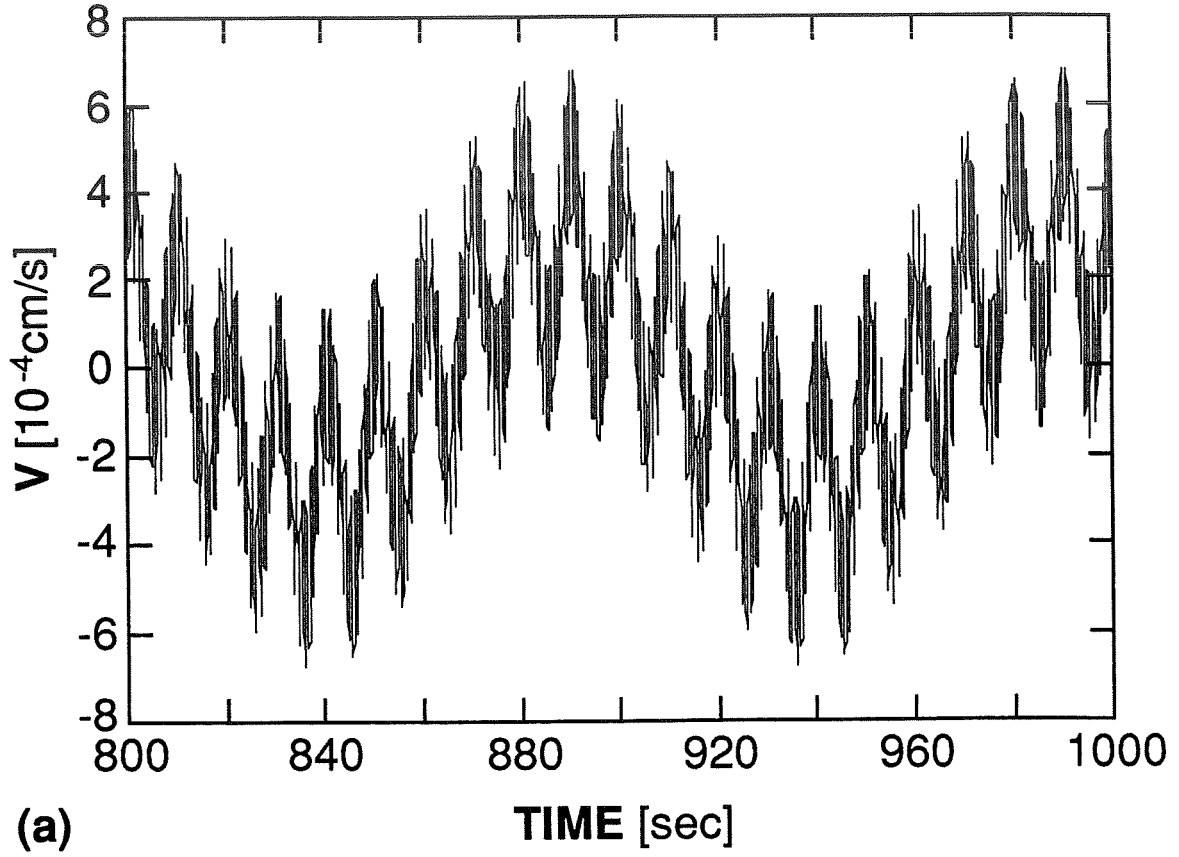
8
6
4
2
0
-2
-4
-6
-8
V [10-4cm/s]
800
840
880
920
960
1000
TIME [sec]

(a)

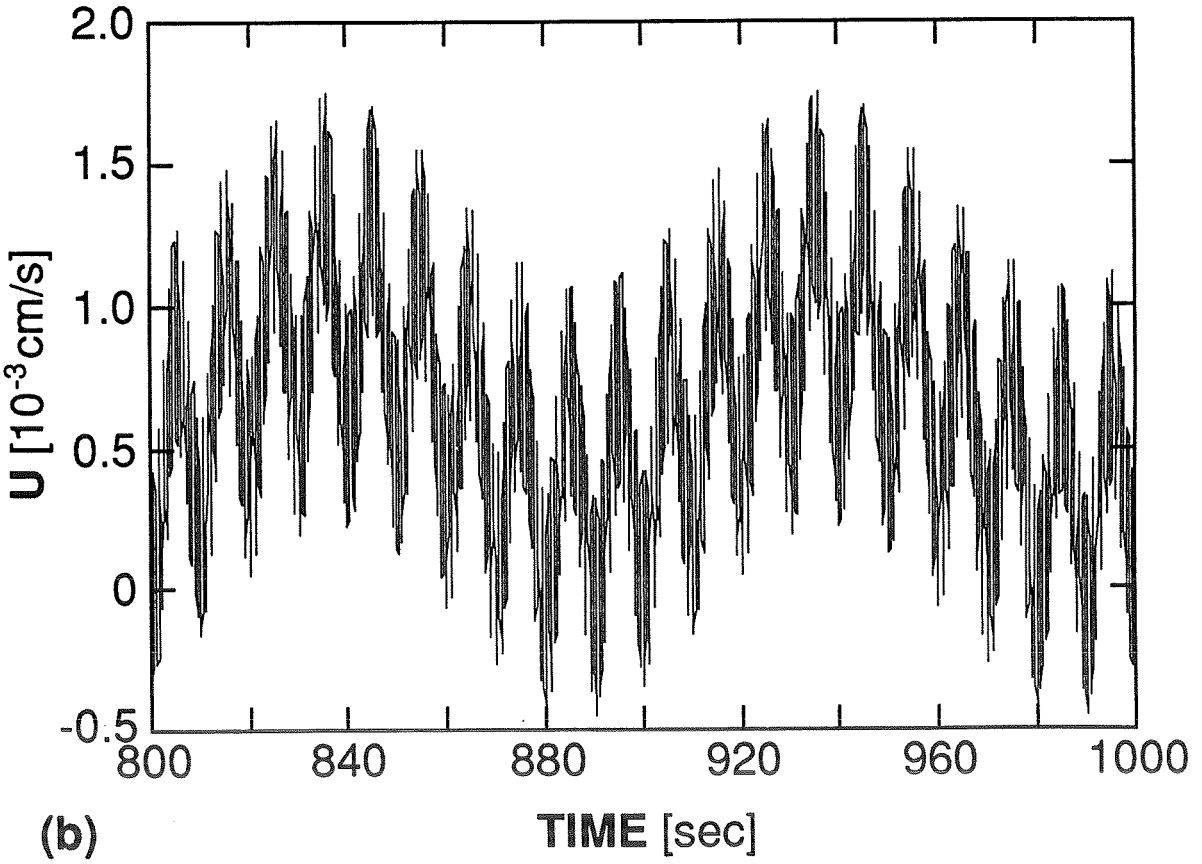
2.0
1.5
1.0
0.5
0
-0.5
U [10-3cm/s]
800
840
880
920
960
1000
TIME [sec]

(b)

FIG. 19

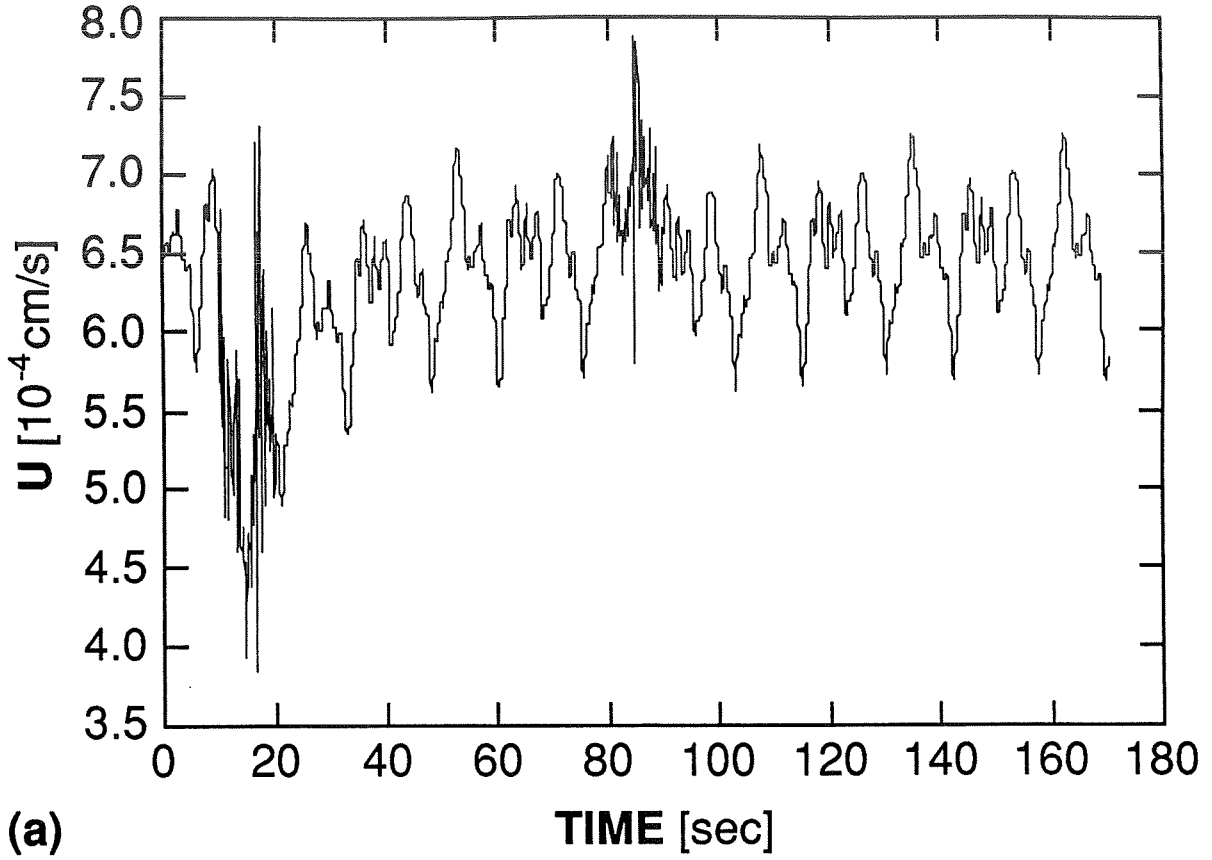
8.0
7.5
7.0
6.5
6.0
5.5
5.0
4.5
4.0
3.5
U [10-4cm/s]
0
20
40
60
80
100
120
140
160
180
TIME [sec]

(a)

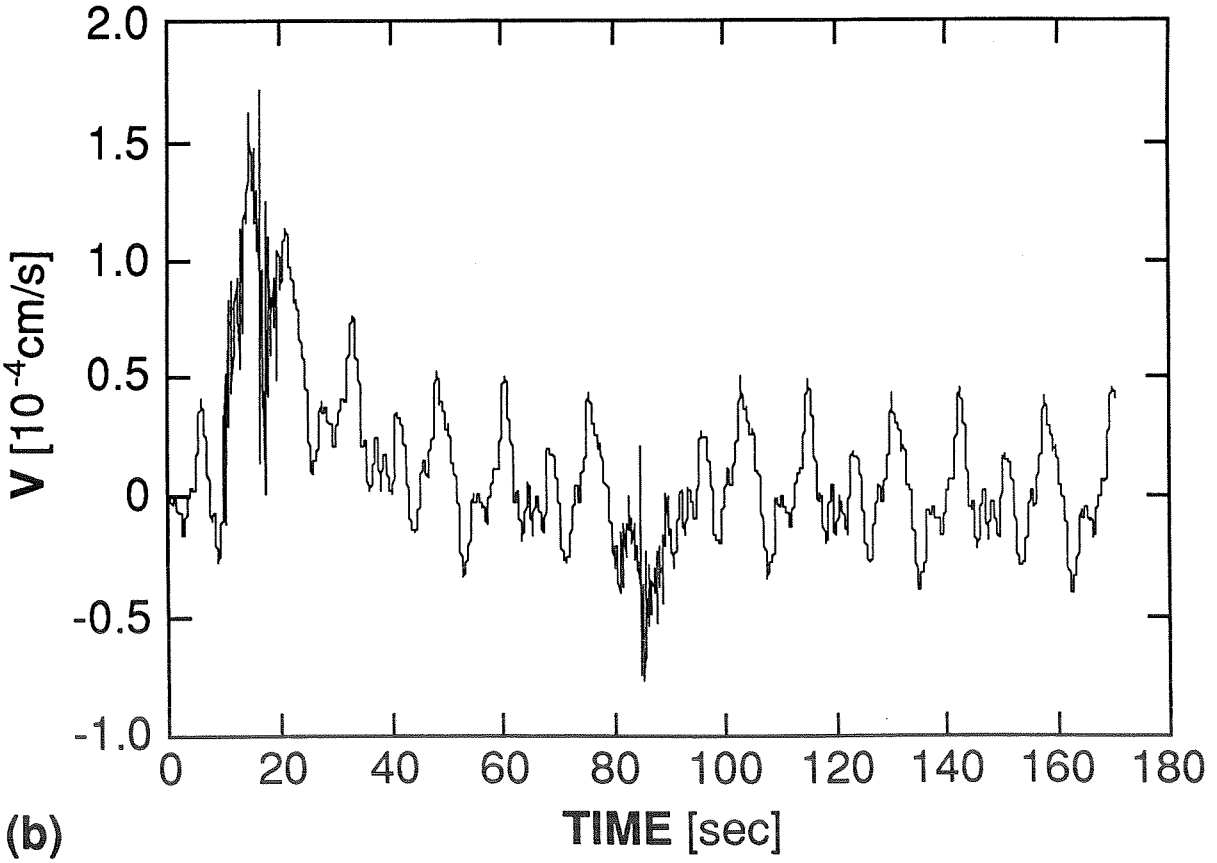
2.0
1.5
1.0
0.5
0
-0.5
-1.0
V [10-4cm/s]
0
20
40
60
80
100
120
140
160
180
TIME [sec]

(b)

FIG. 21

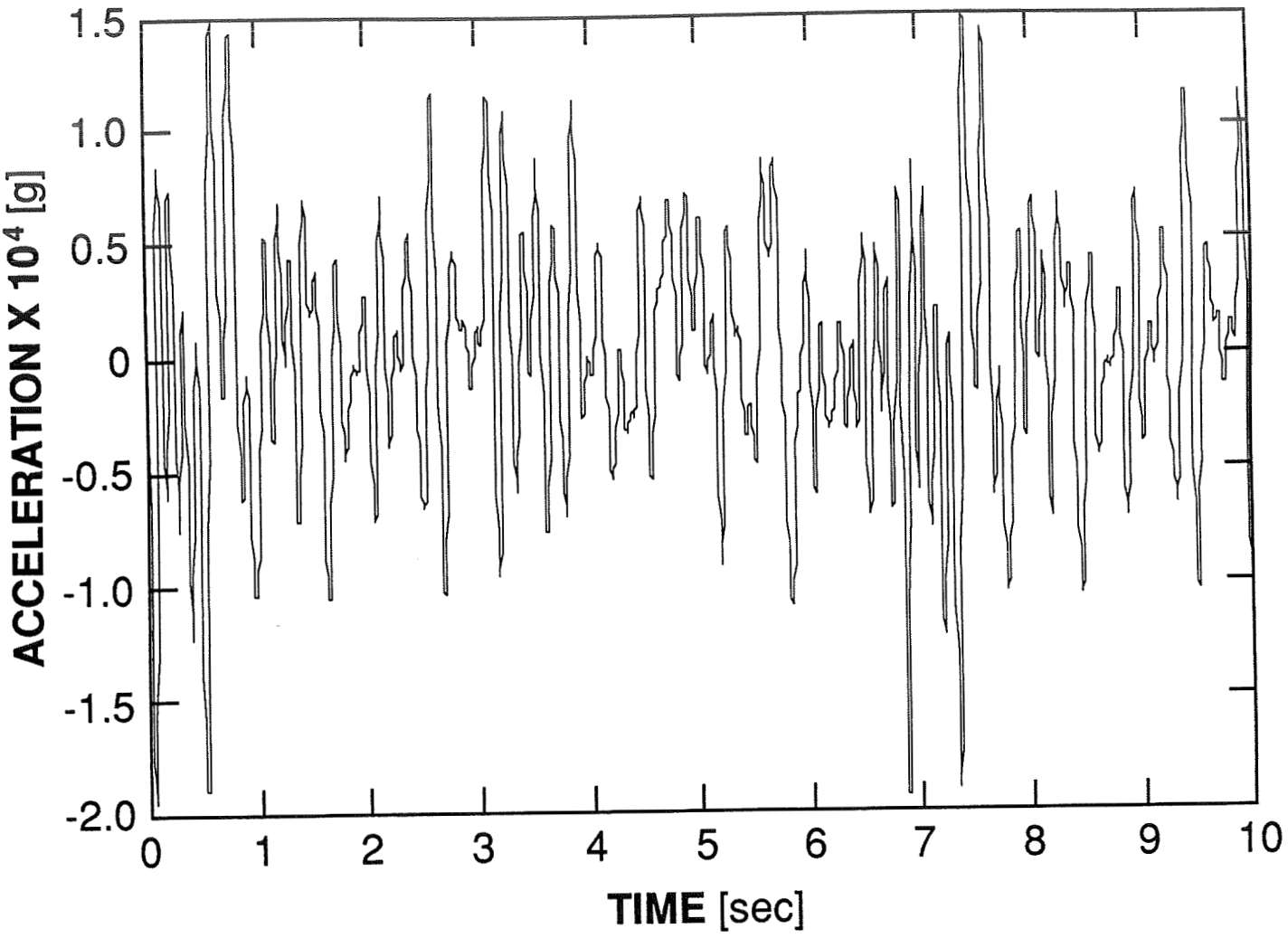
1.5
1.0
0.5
0
-0.5
-1.0
-1.5
-2.0
ACCELERATION X 10⁴ [g]
0
1
2
3
4
5
6
7
8
9
10
TIME [sec]

FIG. 20

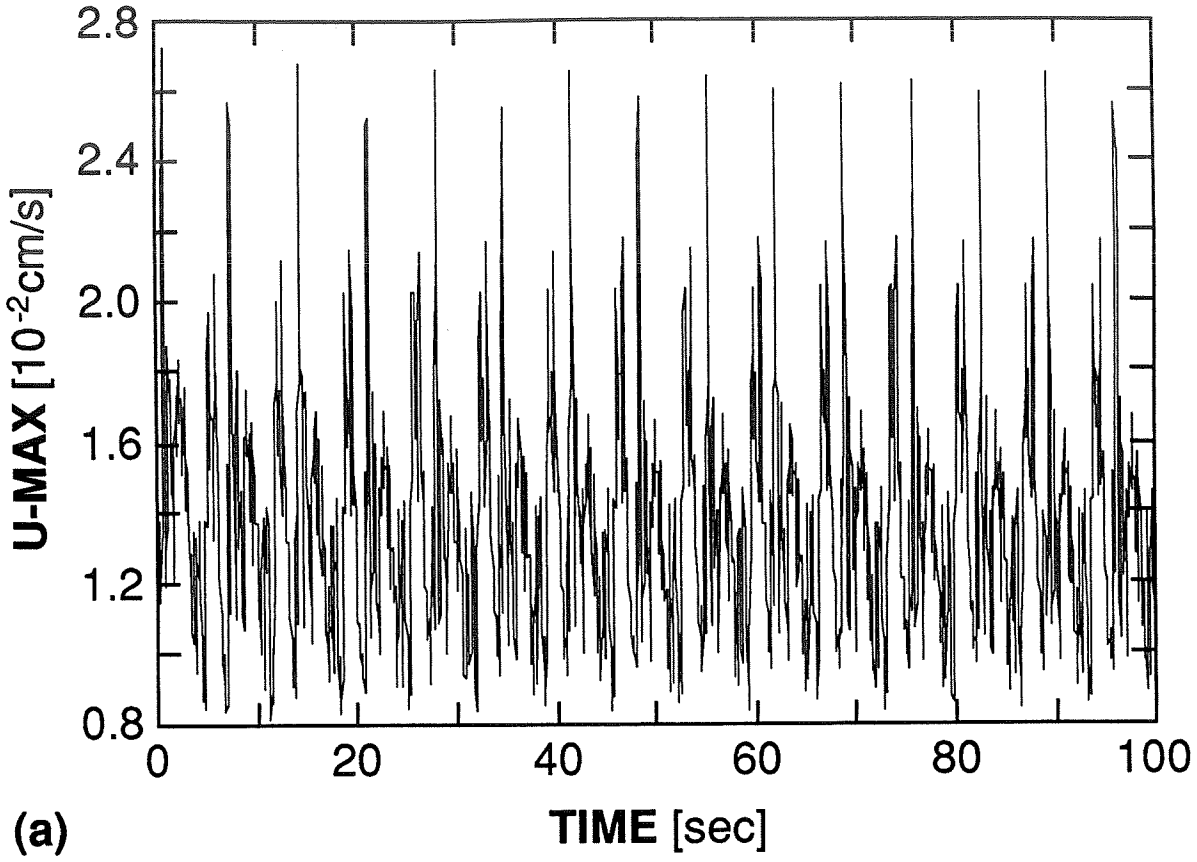
2.8
2.4
2.0
1.6
1.2
0.8
U-MAX [10-2cm/s]
0
20
40
60
80
100
TIME [sec]

(a)

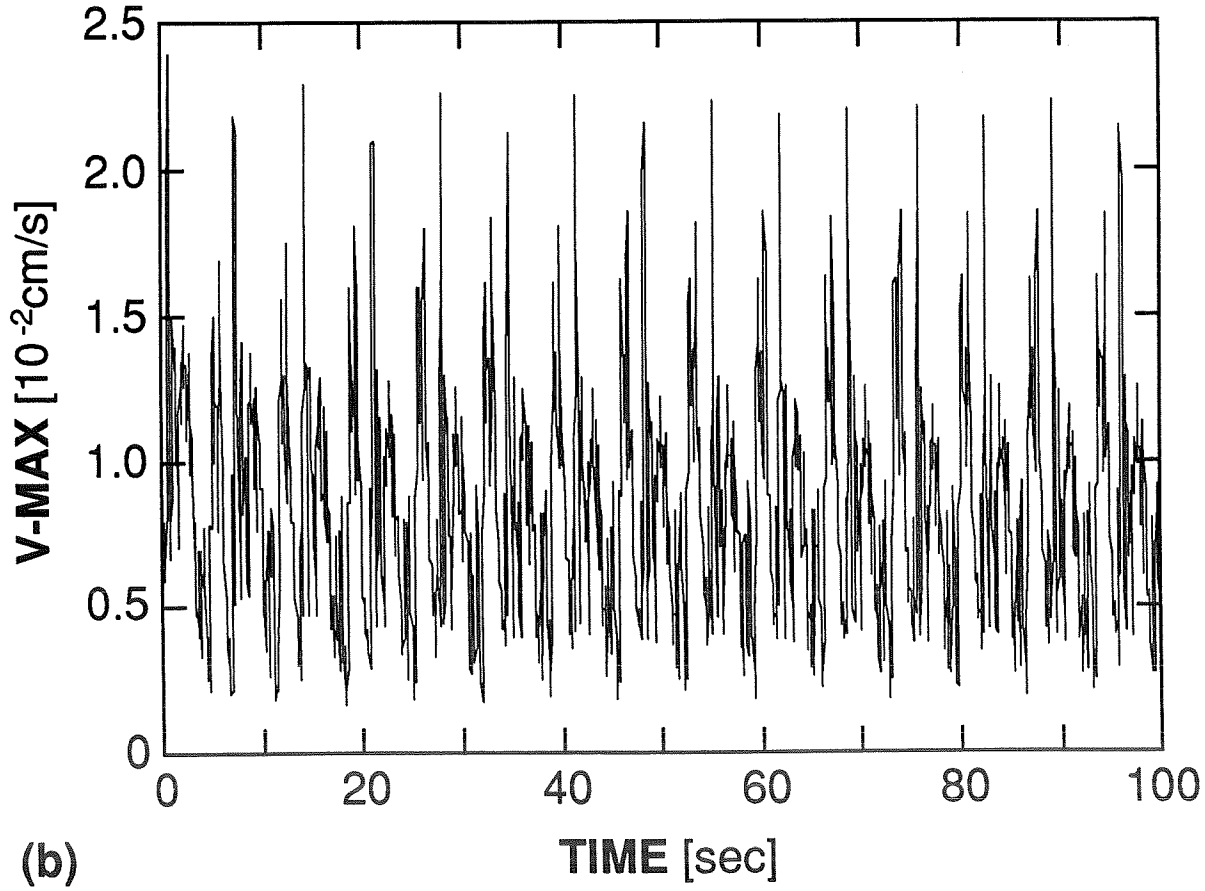
2.5
2.0
1.5
1.0
0.5
0
V-MAX [10-2cm/s]
0
20
40
60
80
100
TIME [sec]

(b)

FIG. 22

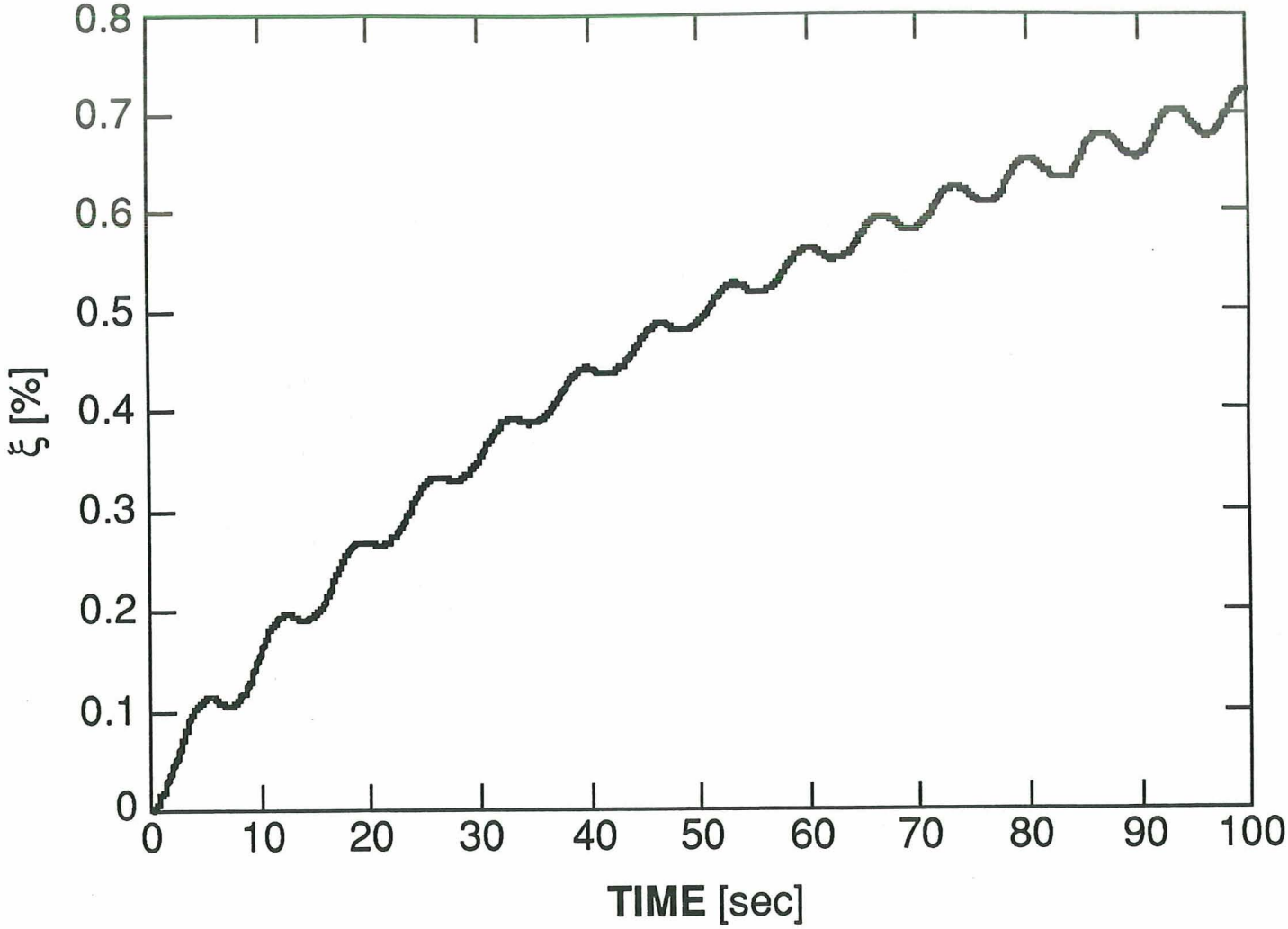

FIG. 23

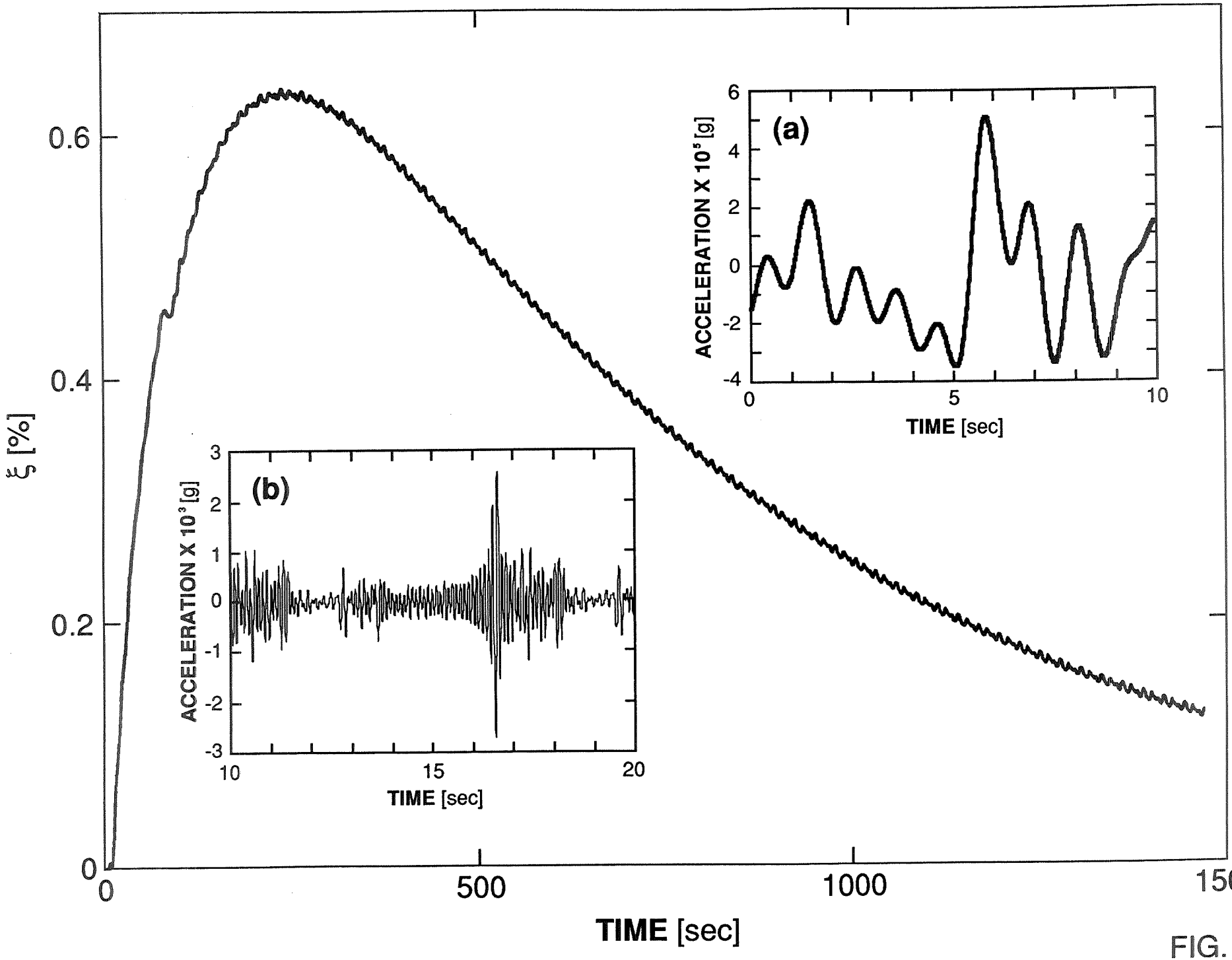
0.6
0.4
0.2
0
ξ [%]
0
500
1000
1500
TIME [sec]
(a)
ACCELERATION X 10⁵ [g]
6
4
2
0
-2
-4
0
5
10
TIME [sec]
(b)
ACCELERATION X 10³ [g]
3
2
1
0
-1
-2
-3
10
15
20
TIME [sec]

FIG. 24

Page intentionally left blank

4. MODELLING CRYSTAL GROWTH BY PHYSICAL VAPOR TRANSPORT IN CLOSED AMPOULES

4.1. Summary

There has been great interest in growing crystals by physical vapor transport in closed ampoules ever since mercuric iodide and cadmium telluride crystals were successfully grown on Spacelab missions in 1985. In order to ascertain if the transport modes prevailing in low gravity environments are beneficial to vapor growth and to determine tolerance limits of residual accelerations for such growth, we have developed a steady state two-dimensional model. This was solved using the finite volume code PHOENICS. Gravitational accelerations of less than 0.1g were found to be sufficient to suppress bouyancy-driven convection to an extent that diffusion was the dominant transport mode. Furthermore, we found that the convection is usually solutally-driven and that if convection is reduced enough there is greater uniformity in the growth rate. It is also shown that a linear temperature gradient on the ampoule walls will cause the vapor to be supersaturated throughout the ampoule resulting in undesireable nucleation at the walls. A "hump" in the wall temperature profile can be used to avoid this. The size of the hump could be used to avoid this. The prevailing transport conditions determine the size of the hump needed.

4.2. Introduction

In 1985 van den Berg and co-workers grew a single crystal of mercuric iodide (HgI_2) on Spacelab 3 by physical vapor transport [1]. That crystal was shown to have significantly better structural and electronic properties than Earth-grown crystals. Two reasons were suggested for this improvement in quality. The first one is the propensity for slippage of HgI_2 crystals under terrestrial gravity and the resulting decrease in structural quality. The second is the reduction of convective flows in a low gravity environment which was expected to produce a more uniform growth rate and, hence, crystals of greater homogeneity. Even if the former reason was specific to soft crystals like HgI_2, the latter, if correct, would suggest that a low gravity environment is beneficial for all crystals grown by physical vapor transport (PVT). These improvements in crystal quality realtive to earth-grown crystals were further confirmed by Nitsche and co-workers [2] for the vapor growth of cadmium telluride crystals on the Spacelab D-1 mission in 1985.

These results and those of the earlier experiments with GeSe and GeTe by Wiedemeier and co-workers [3,4] have sparked interest in growing other crystals by PVT in future shuttle missions and on the Space Station. The interplay of diffusion and convection in such systems is very complex and quantitative results cannot be predicted by simple models or purely physical arguments. However, as has been demostrated for crystal growth from the melt and solution, "generic" models of the growth process can be used to identify trends in the response of the condition to different transport conditions. In this work we will attempt to arrive at a better understanding of the role of convection in a simplified PVT model and to predict the effect of low

gravity on the growth system. In addition, it is hoped that the results of this study will lead to improvements in the growth methods employed.

The first systematic attempt to model PVT in a closed ampoule with convective flow was made by Klosse and Ullersma [5]. They ignored the net mass transport resulting from crystal growth and also solutal convection which makes their results of limited validity in real growth situations. Rosenberger and co-workers have demonstarted the complexity of the transport even in a simplified two-dimensional model, showing that recirculation of the inert gas can result in convective flows even in the absence of gravity [6]. Also they incorporated the compressible form of the Navier-Stokes equation (rather than the Boussinesq approximation), used the exact boundary conditions at the source and crystal interfaces to obtain the most realistic model used so far for PVT [7-9]. They were able to investigate the effect of a variety of growth parameters like aspect ratio and the orientation of the ampoule with respect to gravity. More importantly, they made clear the nature of the flow field during PVT and showed that non-uniformities in the growth rate can occur even in the best of situations.

Bontoux and co-workers have modelled 3-D convective flow during PVT [10,11]. Despite their use of the Boussinesq approximation their results compared favourably with experiments [12]. The relationship of the crystal growth rate to the convective flow for different experimental conditions cannot be readily deduced from their work.

In our study we will concentrate mainly on exploring the advantages or disadvantages of low gravity environments for vapor growth though some of the conclusions should also be relevant to ground-based experiments. We will employ a "generic" model which includes aspects of PVT important to crystal growers which have been neglected in previous models, such as the use of nonlinear wall temperature gradients to prevent spurious nucleation, and the use of different total pressures and inert gases in the ampoule. We will present our model in the next section and the numerical scheme employed in section 3. In section 4 present and discuss our results and draw conclusions in section 5.

4.3. The Model

We restrict our model to examine how a typical convective flow field will affect the crystal growth rate. A two-dimensional model will suffice and we have used a rectangle to represent the ampoule with a source and crystal of material A on the two ends. In addition, the domain contains an inert gas B.

The other major assumption we have made is to postulate the existence of a basic steady state. While this can never be achieved in real growth situations, it is nonetheless usfeul for a qualitative interpretation of the response of the system to different transport conditions. Not only is the temperature gradients at the walls hard to maintain with moving source and crystal interfaces but, more importantly, a steady state would require dopant incorporation at the same rate as sublimation at all times, a very unlikely prospect. Time-dependent calculations are a time consuming and unless absolutely necessary should be avoided. Besides, the main interest in using a time dependent model is to study dopant incorporation and compositional uniformity, but this also requires a knowledge of the composition of the vapor and the vapor-solid equilibrium

relationships for the dopant and host crystal. Unfortunately for most systems this information is not available. Thus, the effort involved in such detailed calculations is of limited practical use.

We have also assumed that all physical properties except density and diffusivity are constant and this is reasonable for most vapor growth systems. The conservation equations for a compressible gas then become:

$$\nabla\cdot\rho\mathbf{v} = 0, \tag{1}$$

$$\rho\mathbf{v}\cdot\nabla\mathbf{v} = -\nabla p + \mu\nabla^2\mathbf{v} + \rho\mathbf{g}, \tag{2}$$

$$\mathbf{v}\cdot\nabla T = \kappa\nabla^2 T, \tag{3}$$

and

$$\mathbf{v}\cdot\nabla W_A = \nabla\cdot D_{AB}\nabla W_A\ . \tag{4}$$

Here $\mathbf{v}$, p, T, W_A and $\mathbf{g}$ are the mass averaged velocity [13], pressure, temperature, mass fraction of the transported material A and gravitational acceleration respectively. The physical properties ρ, μ, κ and D_{AB} are the density, viscosity, thermal diffusivity and the binary diffusion coefficient, respectivley. We have assumed an ideal gas relationship in relating the density to the pressure.

The boundary conditions on velocity are that the mass averaged velocity vanishes at the ampoule walls (for a discussion of this point see [6,14]) and that at the source and crystal ends there will be a perpendicular component of velocity due to the inflow and outflow of component A. These conditions are

$$\mathbf{v} = 0 \text{ at } x = 0 \text{ and } x = a, \tag{5}$$

$$\mathbf{v}\cdot\mathbf{n} = -\frac{D_{AB}}{1-W_A}\nabla W_A\cdot\mathbf{n} \text{ at } y = 0 \text{ and } y = l\ . \tag{6}$$

The two ends are held at different constant temperatures. The walls are maintained at a specified temperature profile. We will not consider the case of insulated walls as this is difficult to achieve in practice and also since most vapor growth experiments are conducted with an imposed temperature profile to avoid nucleation at the ampoule walls. Thus,

$$T = T_s \text{ at } y = 0 \text{ and } T = T_c \text{ at } y = l, \tag{7}$$

and

$$T = f(y) \text{ at } x = 0 \text{ and } x = a\ . \tag{8}$$

The boundary conditions on the mass fraction of component A are impermeability at the ampoule walls and vapor-solid equilibrium at the source and crystal:

$$\nabla W_A\cdot\mathbf{n} = 0 \text{ at } x = 0 \text{ and } x = a \tag{9}$$

and

$$p_A = P_{eq}(T) \text{ at } y = 0 \text{ and } y = l, \tag{10}$$

where p_A is the partial pressure of component A and $P_{eq}(T)$ is the equilibrium vapor pressure of A. Since we will be using the iodine-hydrogen system for most of our calculations, with iodine the crystallizing material and hydrogen the inert gas, we have used the relationship suggested by Gillespie and Fraser [15] for the vapor pressure of iodine:

$$P_{eq}(T) = 760\exp(\ 30.795 - 8088.64/T - 2.013\ln T\ )\ \text{mm Hg}. \tag{11}$$

The diffusion coefficient is a strong function of temperature and pressure but for vapor growth the total pressure is essentially constant over the ampoule and the temperature differences

are usually too small to cause significant variations. Nevertheless some simulations were carried out where the diffusion coefficient, as suggested by Rosenberger [13], was given by

$$D_{AB} = D_0(p_0/p)(T/T_0)^{1.82}, \qquad (12)$$

where D_0 is the diffusion coefficient at temperature T_0 and pressure p_0. However, the results so obtained hardly differed from those with constant coefficients. Hence, most of the simulations were carried out with constant coefficients though for each simulation at an assumed total pressure D_{AB} was recalculated using eqn. (12). The physical properties used in the simulations are listed in table 1.

4.4. Numerical Method

The coupled conservation equations (1-4) were solved subject to the boundary conditions (5-11) using the commercial code PHOENICS. This code is based on a finite volume method with a fully implicit time scheme and allows the solution of the transport equations in the compressible form [16]. Convergence was not easy to obtain and the mesh size and the relaxation parameters had to be adjusted for each simulation. A particular difficulty was to have mass conservation between inlet and outlet, as this is not automatically satisfied when the boundary conditions are discretized. The mesh we used was finer near the crystal and the source and coarser elsewhere. Typically a simulation with an ampoule of aspect ratio (Length/Width) $l/a = 2$ required a 24x36 mesh and one with an aspect ratio of 5 required a 24x52 mesh.

All computations were carried out on the Cray-XMP of the Alabama Supercomputer Network. Computer time for each run varied according to the complexity of the formulation (eg. the use of a polynomial for the imposed wall temperature profile and the use of a temperature dependent diffusion coefficient), the magnitude and orientation of the gravitational acceleration and the relative magnitudes of the thermal and solutal density gradients when they opposed each other. Most of the simulations required between 5 to 10 minutes of Cray CPU time.

4.5. Results and Discussion

The first question examined was the effect of gravitational acceleration on the crystal growth rate. Greenwell et al. [8] first demonstrated that the convective flow can cause nonuniformities in the growth rate. We examined this in more detail using a linear temperature profile at the ampoule walls. It was found that when solutal convection dominates, the imposed temperature profile has no effect on the growth rate. For most of our calculations weused the properties of iodine as the crystallizing material A and hydrogen as the inert gas B. For some of the calculations we varied the molecular weight of B from 2 up to 254 in order to study the effect of thermally driven convection in isolation.

Fig. 2 shows our results for a horizontal ampoule of aspect ratio 5 (length=5cm, width=1cm)), with a temperature of 370.5 K at the source end and 358.1 K at the crystal end, and a total pressure of 100 torr. The most important observation from the point of view of space processing is that even at 0.1g convective effects become very small and we have essentially diffusive transport in the vapor. Moreover, when the same ampoule was kept vertical (with source both up and down) even a gravitational level of 1g was not enough to cause significant changes in

growth rate compared to the diffusive case. This is quite unlike other crystal growth methods being tested in low gravity environments which require gravitational levels of 10^{-6}g or lower to avoid convective effects [17,18], which may be difficult to obtain in the currently available low gravity environments. For vapor growth these environments would seem quite adequate and problems of "g-jitter" which are a cause of concern for other experiments should have little effect on vapor growth systems. The experiments of Launay and co-workers [19] who grew Ge by chemical vapor transport on the Spacelab D1 mission in 1985 confirms this, as their measurements of the mass transport in the ampoule indicated a purely diffusive regime. However it must be mentioned that in their numerical model of this experiment they reported significant convection even at 10^{-2}g and observed a purely diffusive solution only at 10^{-4}g [20].

This leaves us with the question of whether there is anything to be gained by suppressing convection. From fig. 2 we can see that convection does enhance the mass transport of component A, and consequently also the growth rate, but at the expense of nonuniformity in the growth rate. It also can be seen that convection and, hence, the nonuniformity, is more likely to be significant when the ampoule is horizontal rather than vertical. In the vertical position the thermal and solutal gradients oppose each other and for convection to occur the solutal gradient must exceed the thermal gradient and overcome the viscous resistence. In the horizontal position convective effects are a more likely occurrence. In the vertical position we can have diffusive growth, especially if the ampoule is held in the convectively stable position. Suppressing convection should be possible even without resorting to a low gravity environment.

Fig. 3 shows the results for an aspect ratio 2 (length=2cm). The growth rates are much larger than for aspect ratio 5 but the nonuniformity due to convection is also far greater. The increase in the convection level is visible from the fact that even in the vertical position convection will be significant. However, even for this case, a factor of ten reduction in the gravitational level is enough to suppress convective effects on growth rate. Increasing the temperature difference between source and crystal gave similar results (fig. 4). This suggests that one benefit of the low gravity environment would be to increase the growth rates by using ampoules of smaller aspect ratios or using larger temperature differences between source and crystal and still avoid the drawback of increased convection, which normally would rule out such methods on Earth.

Next we examined situations for which thermal convection might be larger than the solutal. This could occur when inert gases other than hydrogen and having a molecular weight closer to that of the crystallizing material are used. Thermal convection, if dominant, is very hard to eliminate on Earth. Unlike the mass fraction it is difficult to maintain a uniform temperature across a cross section of the ampoule, which means radial temperature gradients are invariably present. The results for a horizontal ampoule are shown in fig. 5. As the molecular weight of B is increased we can see that the effect of solutal convection first increases and then decreases rapidly and eventually the transport becomes largely diffusive. Its only when the molecular weights of A and B are almost equal that the thermal gradient overcomes the stabilizing solutal gradient. When the molecular weights were equal the thermal gradient gave rise two convection rolls, unlike the single

rolls of solutally driven convection seen so far, and resulted in significant nonuniformities in the growth rate. From this it is possible to say that unless the two components have molecular weights very close to each other, the dominant mode of convection is likely to be solutal. But it should be mentioned that when the two gradients were comparable it was difficult to get the computer code to converge possibly suggesting that oscillatory convection may have been present.

A very important concern in vapor growth is the avoidance of parasitic nucleation at the ampoule walls [21]. Figs. 6 and 7 show the equilibrium vapor pressure of component A computed from eqn. (11) and the partial pressures of A at the ampoule walls resulting from the transport, when a linear temperature profile is used. The results are for a source temperature of 378.1 K and the crystal at 358.1 K with fig. 6 for the case of purely diffusive transport and fig. 7 for the ampoule kept horizontal with respect to gravity. It is easy to see why a linear temperature profile is rarely used in practice, as the vapor of component A is in a supersaturated state throughout the ampoule.

The commonly used experimental technique to prevent nucleation at the walls is to impose a wall temperature profile with a maximum between the crystal and the source, usually referred to as a temperature "hump" [21-23]. We ran some simulations in a horizontal ampoule for a source temperature of 378.1 K and the crystal at 358.1 K with a temperature hump of 4 K, the functional form of the temperature profile being:

$$f(b) = 378.1 + 26.67b - 55.66b^2 + 28.04b^3 + 115.46b^4 - 134.61b^5 \ \text{K} \qquad (13)$$

where b is y/l. Fig. 8 shows the results and we can see that even though the supersaturation has been eliminated, the profile is an overcorrection for the problem of nucleation at the walls. A smaller hump would have sufficed. But this result is valid only when the diffusion coefficient is large as in hydrogen pairs. When inert gases of larger molecular weight are used D_{AB} is likely to be much smaller. Even for hydrogen pairs at pressures close to 1 atm. D_{AB} will be 0.16 from eqn. (12). In fig. 9 we have plotted the results with a diffusion coefficient of 0.25 and it can be seen that component A becomes supersaturated near the crystal and a larger hump would be needed to avoid it. This also explains why nucleation is more likely to occur near the crystal end and also why the temperature maximum has to be located closer to this end. It is worth mentioning that this problem at low diffusion coefficients occurs only due to convection. At low gravity smaller humps would be quite adequate to avoid supersaturation. If the variation of the diffusion coefficient with temperature is significant it is likely the effect will be felt most in determining the magnitude of the hump. We performed one simulation with D_{AB} as a function of temperature given by eqn. (12). Owing to the small temperature differences employed, the results were indistinguishable from those for a constant coefficient .

One consequence of using temperature humps is that when thermal convection is dominant it is confined to a small region near the crystal end of the ampoule as shown in fig. 10. Here the convection is strong enough to cause nonuniformities in the growth rate but as it is confined to a

small region we do not have the benefit of enhanced mass transfer across the ampoule for, as can be seen in fig. 11, there is no overall increase in the growth rate. Barring this instance, when the molecular weights of both components are comparable, the temperature hump had no effect on the growth rate. So any conclusions obtained from a linear temperature profile would be applicable here as well.

4.6. Conclusions

Convective effects can easily be suppressed in vapor growth systems for most low gravity environments. A gravitational acceleration level of less than 0.1g is adequate to ensure purely diffusive transport. The more important question is then: What are the benefits of purely diffusive transport conditions?

The benefits are by no means overwhelming but they do exist. Nonuniformities in the growth rate caused by convection can be eliminated, freeing the experimenter to use methods to enhance the growth rate like smaller aspect ratios and larger temperature differences between source and crystal, which would not have been feasible otherwise. In addition in order to avoid nucleation at the walls the size of the temperature hump for purely diffusive conditions can be smaller than that needed in the presence of than convection.

Finally we must reemphasize that a thorough study of physical vapor transport in closed ampoules would require (1) an experimental program to determine the composition of the vapor and equilibrium relationships between vapor and solid for both host and dopant components, and (2) a time-dependent numerical model to investigate the effects of experimental conditions on the compositional uniformity of the crystals grown. Proper evaluation of the (improved) quality of crystals for device applications can only be made if there is a well-defined link between transport conditions and the characteristics of the grown crystal which are necessary for high quality device fabrication.

4.7. References

[1] L. van den Berg and W.F. Schnepple, Nucl. Instr. and Meth. Phy. Res. A283 (1989) 335.

[2] P. Siffert, B. Biglari, M. Samimi, M. Hage-Ali, J.M. Koebel, R. Nitsche, M. Bruder, R. Dian and R. Schönholz, Nucl. Instr. and Meth. Phy. Res. A283 (1989) 363.

[3] H. Wiedemeier, F.C. Klaessig, E.A. Irene and S.J. Wey, J. Crystal Growth 31 (1975) 36.

[4] H. Wiedemeier, H. Sadeek, F.C. Klaessig, M. Norek and R. Santandrea, J. Electrochem. Soc. 124 (1977) 1095.

[5] K. Klosse and P. Ullersma, J. Crystal Growth 18 (1973) 167.

[6] B.L. Markham and F. Rosenberger, Chem. Eng. Commun. 5 (1980) 287.

[7] D.W. Greenwell, B.L. Markham and F. Rosenberger, J. Crystal Growth 51 (1981) 413.

[8] D.W. Greenwell, B.L. Markham and F. Rosenberger, J. Crystal Growth 51 (1981) 426.

[9] B.L. Markham and F. Rosenberger, J. Crystal Growth 67 (1984) 241.

[10] E. Crespo, P. Bontoux, C. Smutek, B. Roux, G. Hardin, R. Sani and F. Rosenberger, in: Proc. 6th European Symposium on Materials Sciences under Microgravity Conditions, (ESA SP-256, February 1987) p529.
[11] G.P. Extrémet, B. Roux, P. Bontoux and F. Elie, J. Crystal Growth 82 (1987) 761.
[12] C. Smutek, P. Bontoux, B. Roux, G.H. Schiroky, A.C. Hurford, F. Rosenberger and G. de Vahl Davis, Numerical Heat Transfer 8 (1985) 613.
[13] F. Rosenberger, Fundamentals of Crystal Growth I (Springer, Berlin, 1979).
[14] G. Mo and F. Rosenberger, Phys. Rev. A (1990), in print.
[15] L.J. Gillespie and L.H.D. Fraser, American Chem. Soc. J. 58 (1936) 2260.
[16] H.I. Rosten and D.B. Spalding, The PHOENICS Reference Manual (CHAM, Wimbledon, UK, 1987).
[17] J.I.D. Alexander, J. Ouazzani and F. Rosenberger, J. Crystal Growth 97 (1989) 285.
[18] A. Nadarajah, F. Rosenberger and J.I.D. Alexander, J. Crystal Growth 104 (1990) 218.
[19] J.C. Launay, H. Debegnac, B. Zappoli and C. Mignon, J. Crystal Growth 92 (1988) 323.
[20] B. Zappoli, C. Mignon, J.C. Launay and H. Debegnac, J. Crystal Growth 94 (1989) 783.
[21] J.R. Abernathy, D.W. Greenwell and F. Rosenberger, J. Crystal Growth 47 (1979) 145.
[22] J. Omaly, M. Robert and R. Carodet, Materials Res. Bull. 16 (1981) 785.
[23] J.C. Launay, J. Crystal Growth 60 (1982) 185.

4.8. Tables

Table 1. Physical properties and operating conditions

Property	Value
Viscosity (μ)	1.5×10^{-4} poise
Diffusion Coefficient at 360 K and 100 torr	1.25 cm^2 sec^{-1}
Prandlt number ($\mu/\rho K$)	1.0
Molecular weight of A (M_A)	254
Operating Conditions	
Total Pressure (p)	100 mm Hg
Crystal Temperature (T_C)	358.1 K
Source Temperature (T_S)	370.5 and 378.1 K
Ampoule Width (a)	1 cm
Ampoule Length (l)	2 and 5 cm

4.9. Figure Captions

Fig. 1 Ampoule geometry used in the model showing location of source and crystal.

Fig.2 Crystal growth rates for an ampoule of aspect ratio 5 (length = 5cm) and a linear temperature gradient of 2.48 K cm^{-1} along the walls.

Fig.3 Crystal growth rates for an aspect ratio 2 (length = 2cm) and a linear temperature gradient of 6.2 K cm^{-1} along the walls.

Fig. 4 Crystal growth rates for an aspect ratio 5 and a linear temperature gradient of 4 K cm^{-1} along the walls.

Fig. 5 Crystal growth rates for various species of B with differing molecular weights for a horizontal ampoule of aspect ratio 5 and a linear temperature gradient of 4 K cm^{-1} along the walls.

Fig. 6 Plot of the equilibrium vapour pressure and the component A partial pressure at the walls for diffusive transport for an ampoule with an aspect ratio of 5 and a linear temperature gradient of 4 K cm^{-1} along the walls.

Fig. 7 Plot of the equilibrium vapour pressure and the partial pressures of A at the walls horizontal ampoule of aspect ratio 5 and a linear temperature gradient of 4 K cm^{-1} along the walls.

Fig. 8 Plot of the equilibrium vapour pressure and the partial pressures of A at the walls when the ampoule is kept horizontal. The aspect ratio is 5 and the imposed wall temperature profile is given by (13). The temperature hump is 4K.

.Fig. 9 Plot of the equilibrium vapour pressure and the partial pressures of A at the walls when the ampoule is kept horizontal for a D_{AB} of 0.25. The aspect ratio is 5 and the imposed wall temperature profile is non-linear.

Fig. 10 Velocity in a horizontal ampoule of aspect ratio 5 with a non-linear imposed wall temeperature profile. The molecular weights of A and B are equal. Only half the ampoule is shown.

Fig. 11 Crystal growth rates with a non-linear temperature profile at the walls and when the molecular weights of components A and B are equal. The aspect ratio is 5.

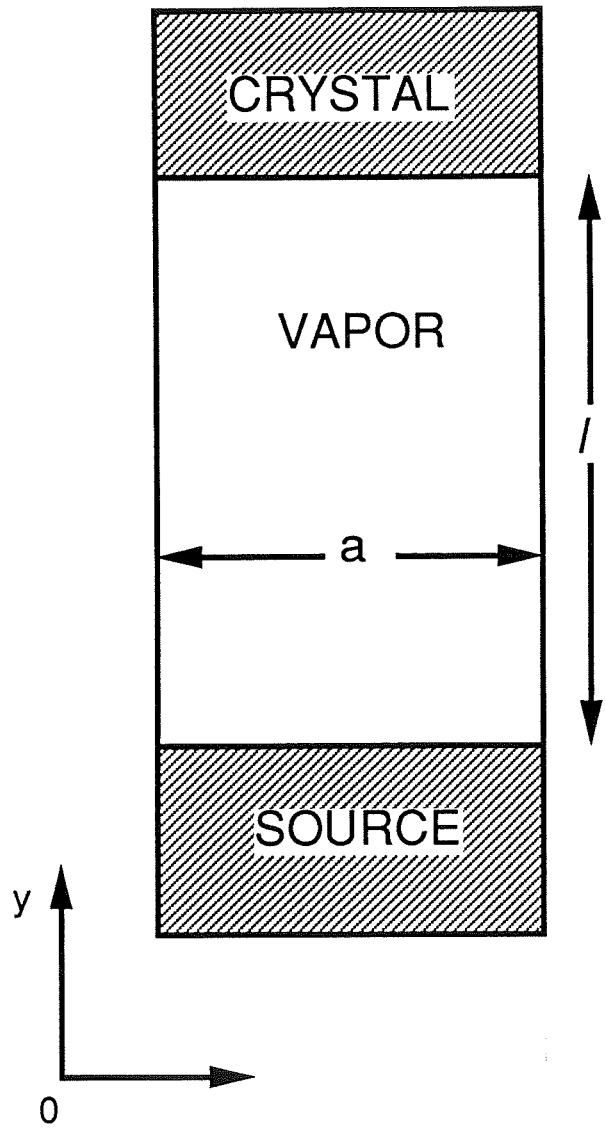

Fig. 1

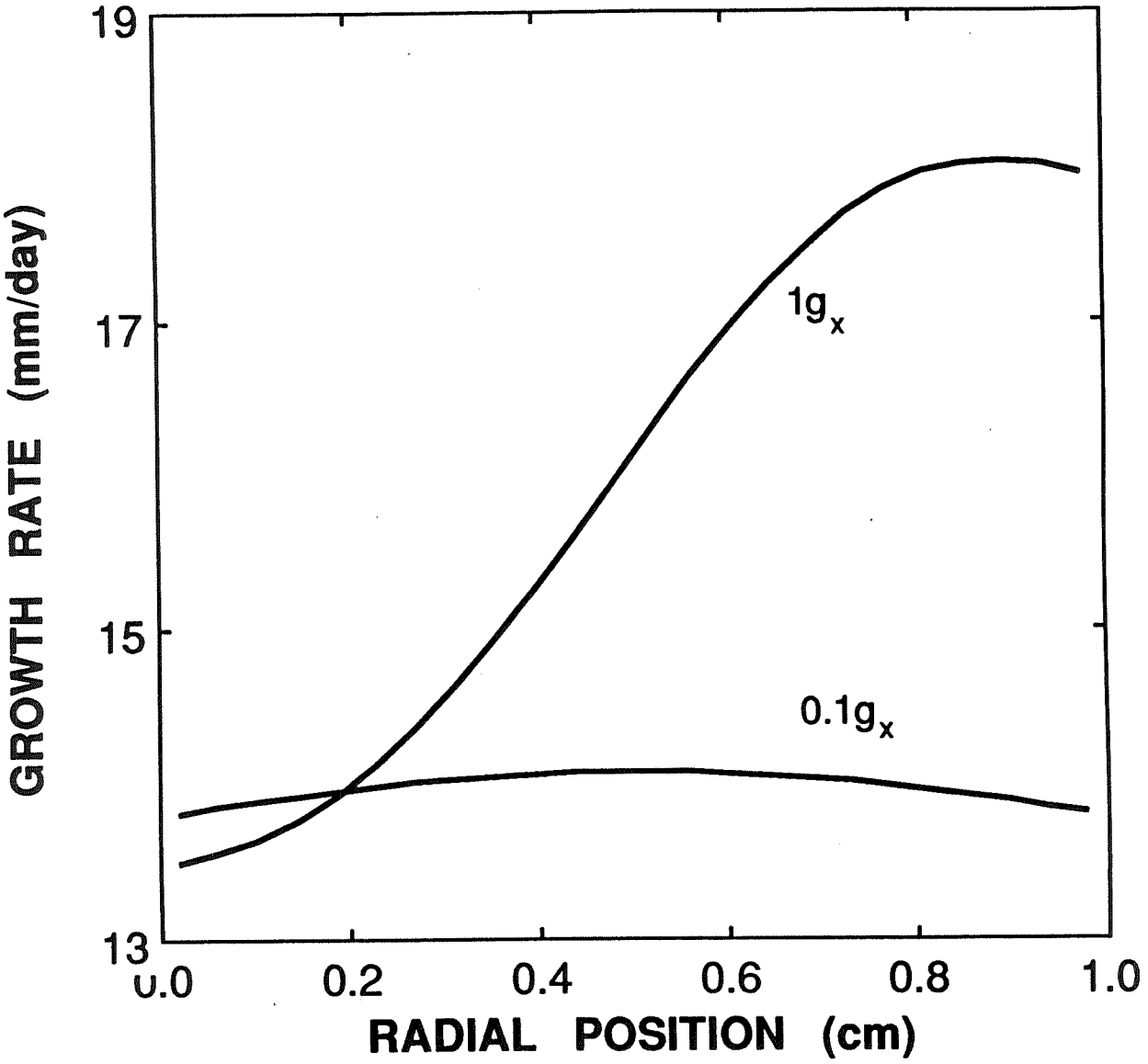
19
17
15
13
GROWTH RATE (mm/day)
1g$_x$
0.1g$_x$
0.0
0.2
0.4
0.6
0.8
1.0
RADIAL POSITION (cm)

Fig. 2

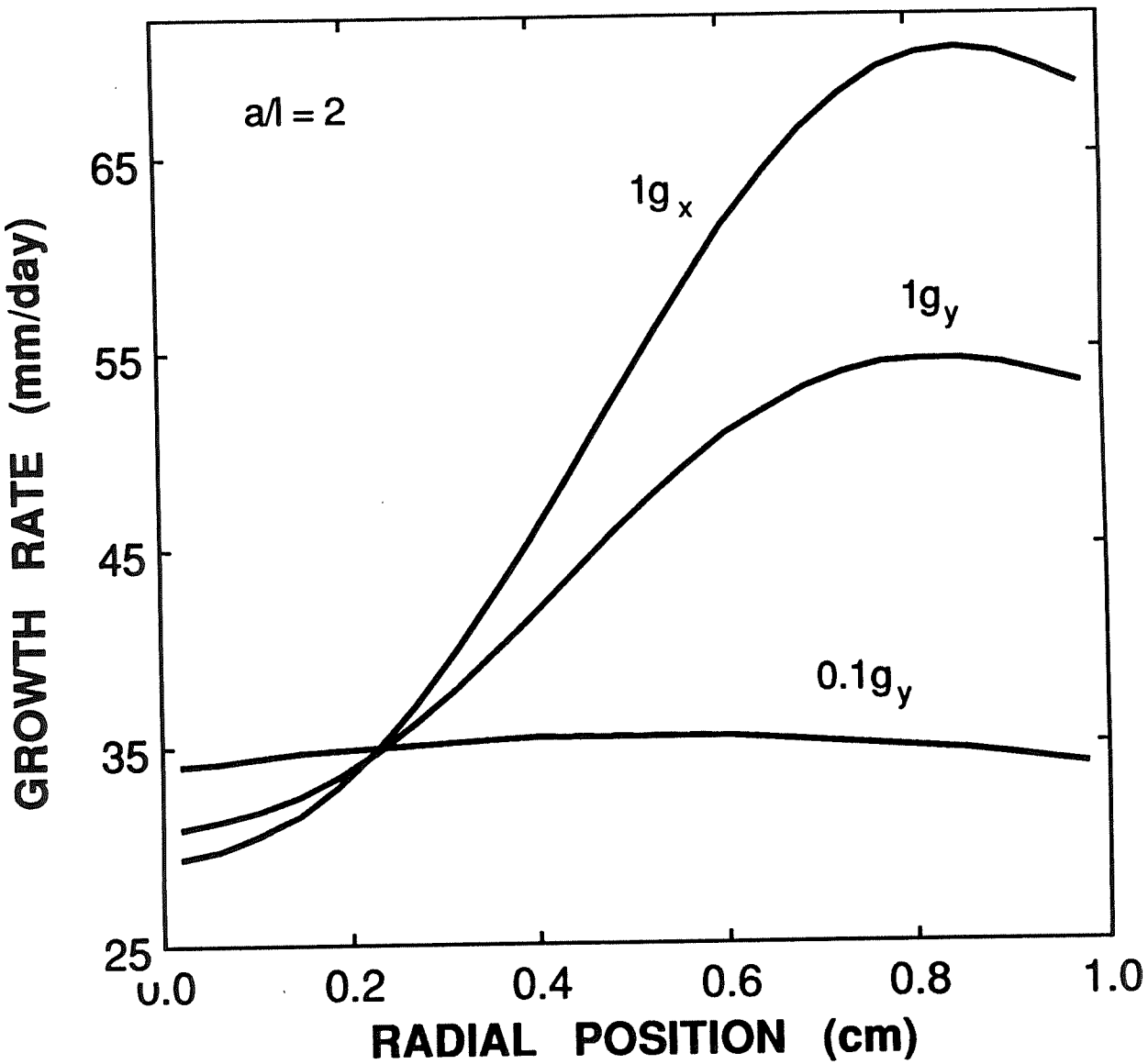
a/l = 2
1g x
1g y
0.1g y
GROWTH RATE (mm/day)
65
55
45
35
25
0.0
0.2
0.4
0.6
0.8
1.0
RADIAL POSITION (cm)

Fig. 3

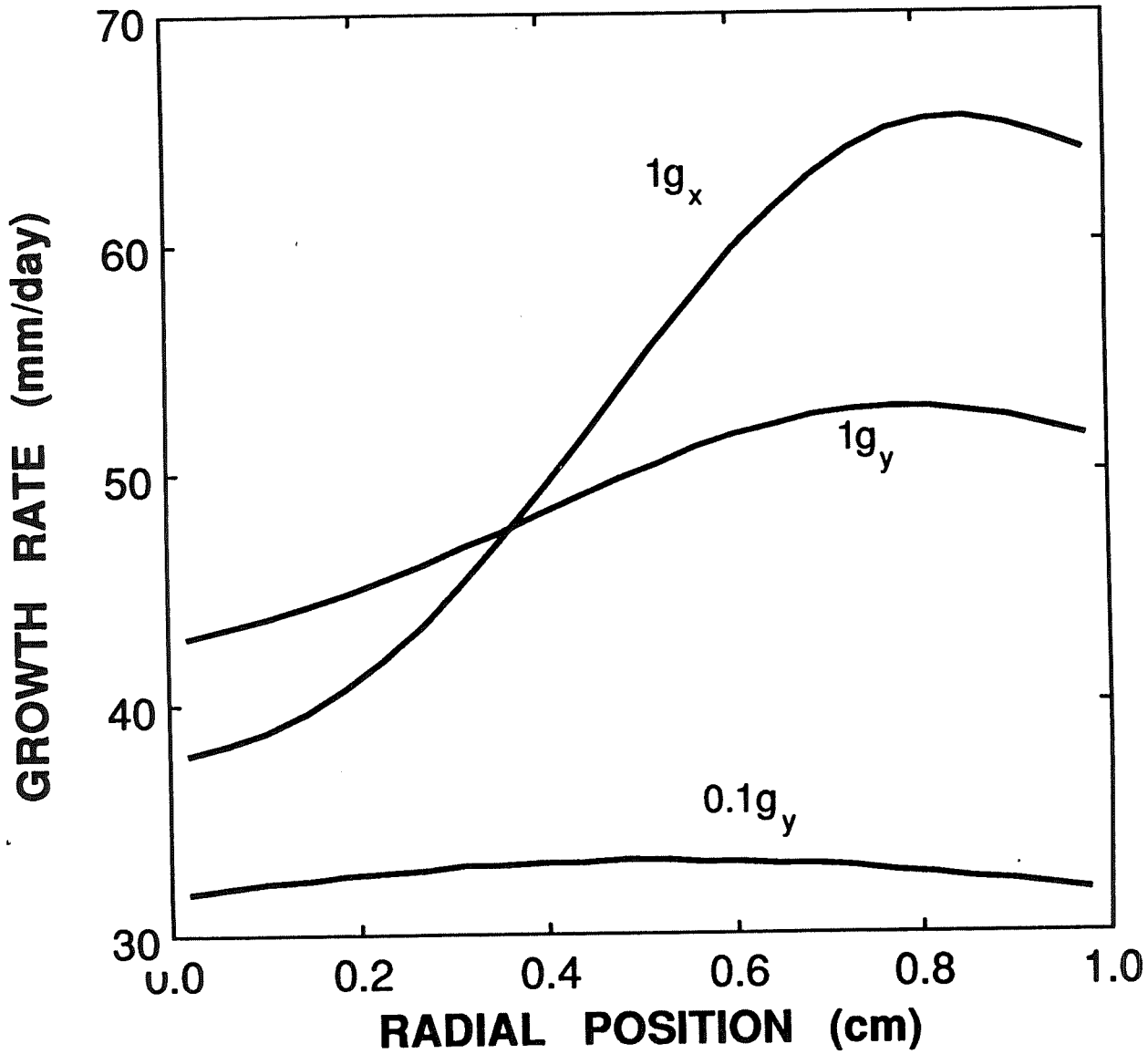
70
60
50
40
30
GROWTH RATE (mm/day)
1g_x
1g_y
0.1g_y
0.0
0.2
0.4
0.6
0.8
1.0
RADIAL POSITION (cm)

Fig. 4

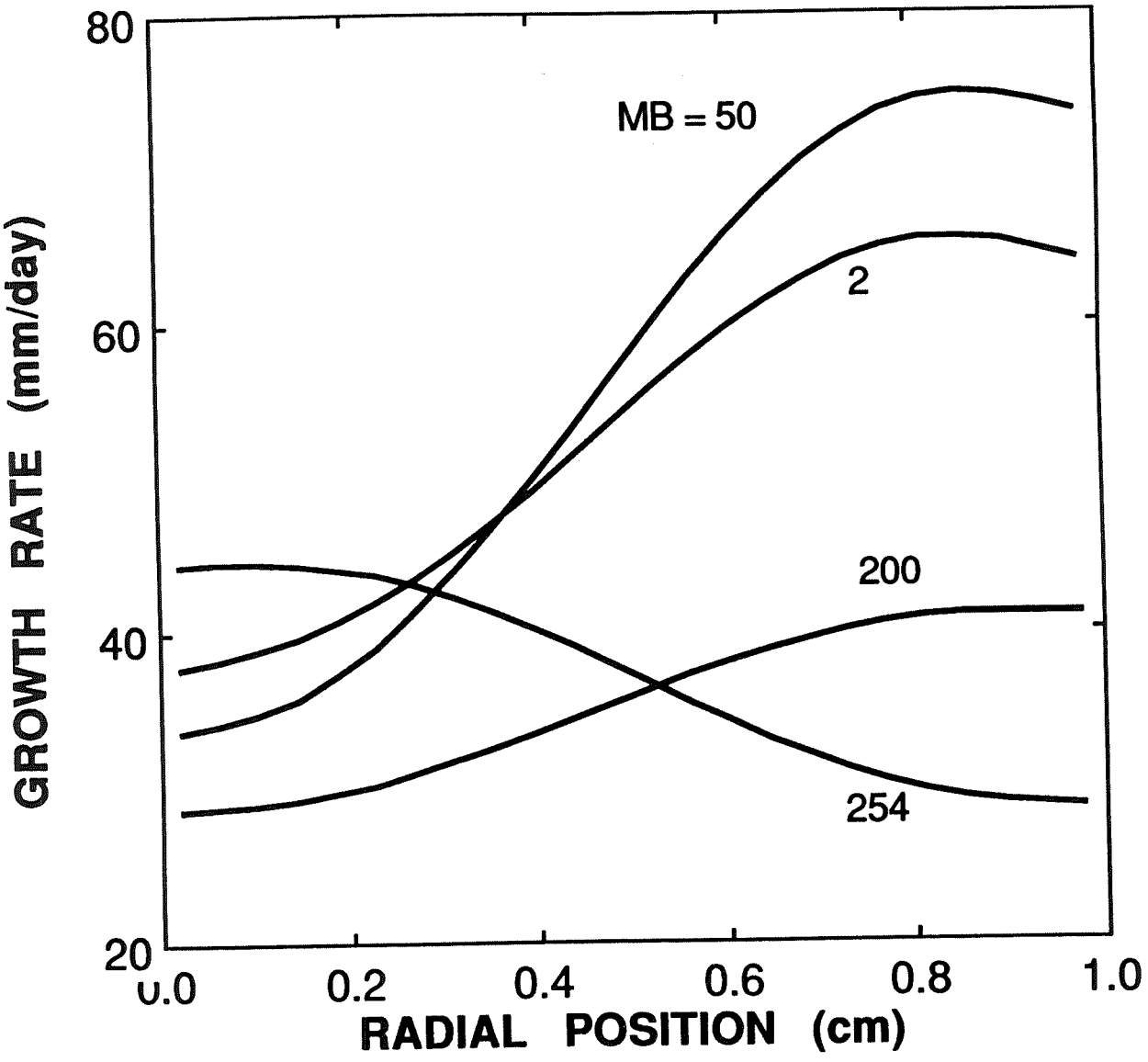
80
60
40
20
GROWTH RATE (mm/day)
MB = 50
2
200
254
0.0
0.2
0.4
0.6
0.8
1.0
RADIAL POSITION (cm)

Fig. 5

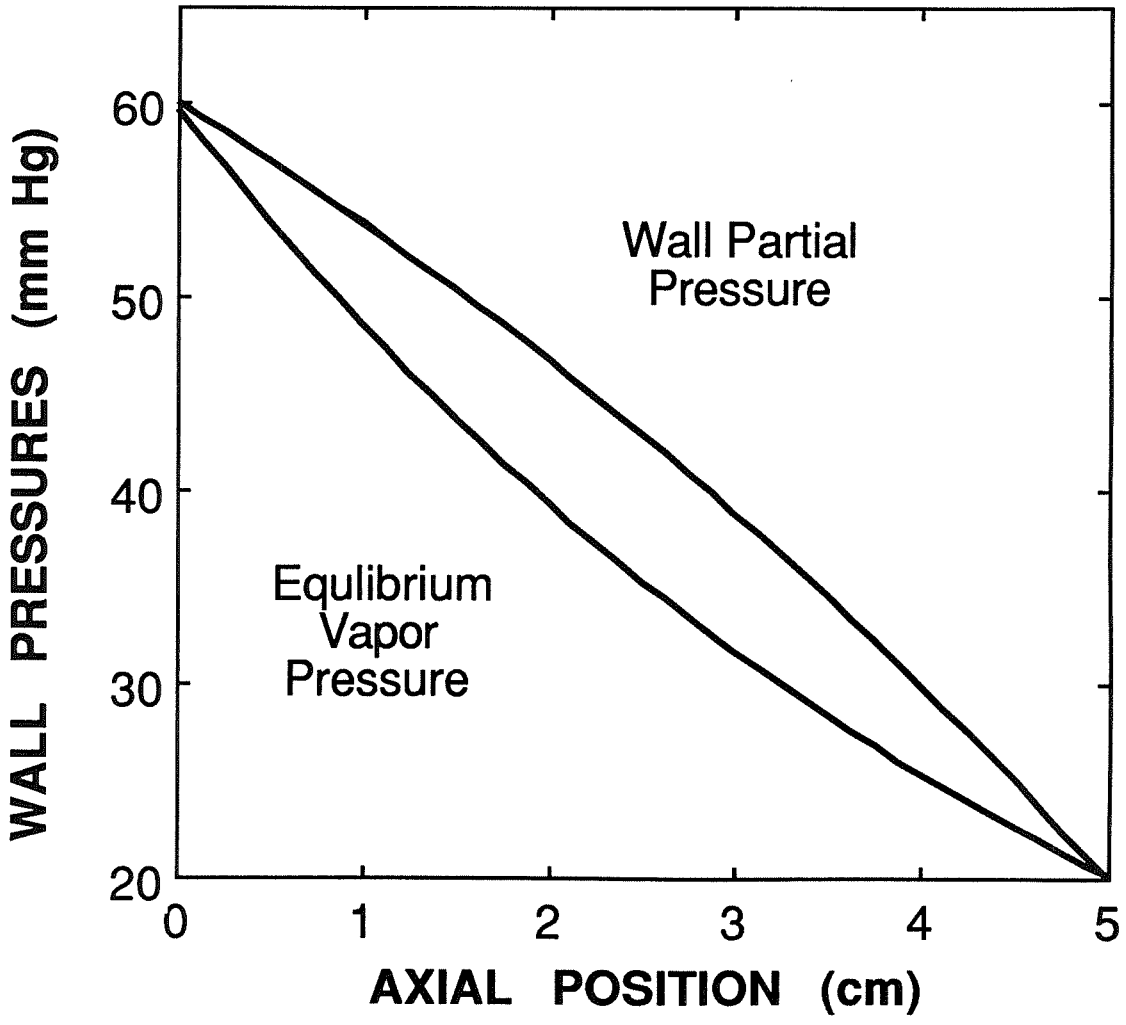
WALL PRESSURES (mm Hg)
60
50
40
30
20
0
1
2
3
4
5
AXIAL POSITION (cm)
Wall Partial Pressure
Equlibrium Vapor Pressure

Fig. 6

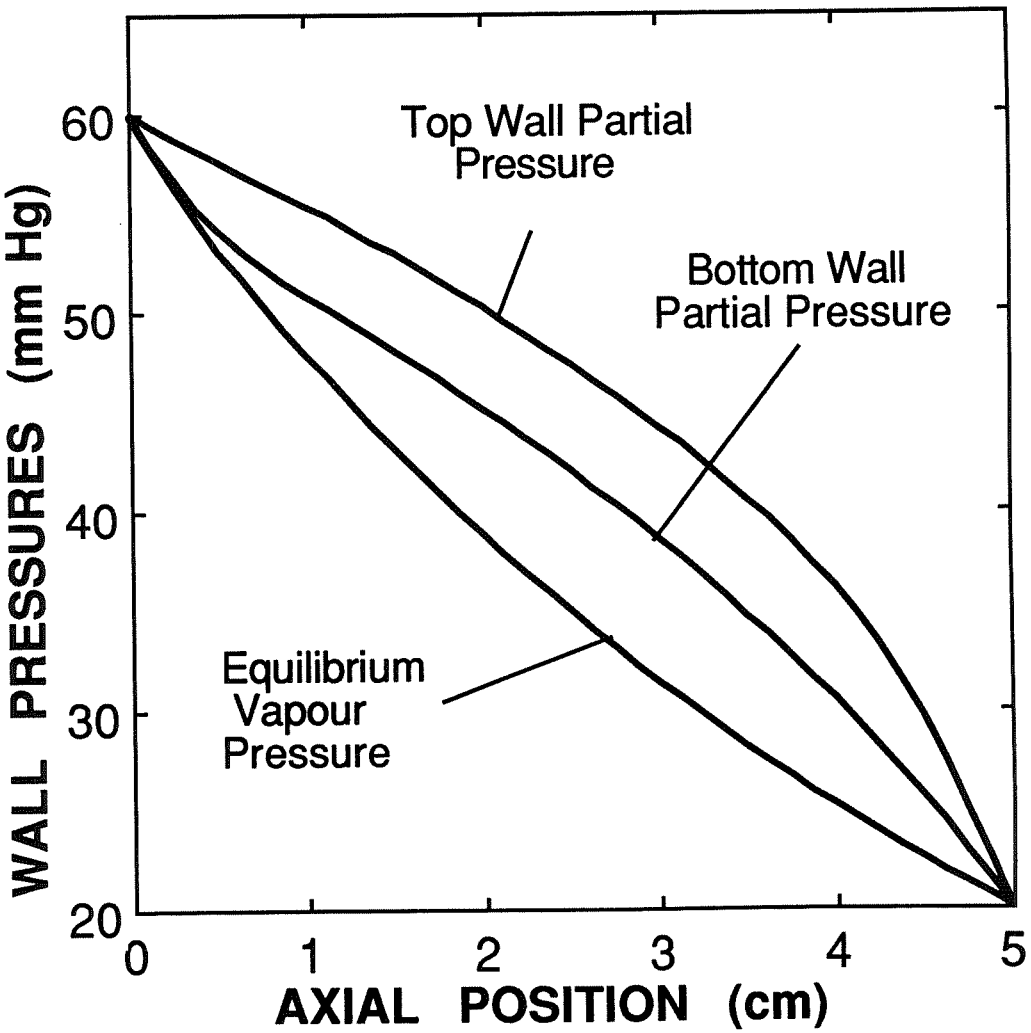
Top Wall Partial Pressure
Bottom Wall Partial Pressure
Equilibrium Vapour Pressure
WALL PRESSURES (mm Hg)
60
50
40
30
20
0
1
2
3
4
5
AXIAL POSITION (cm)

Fig. 7

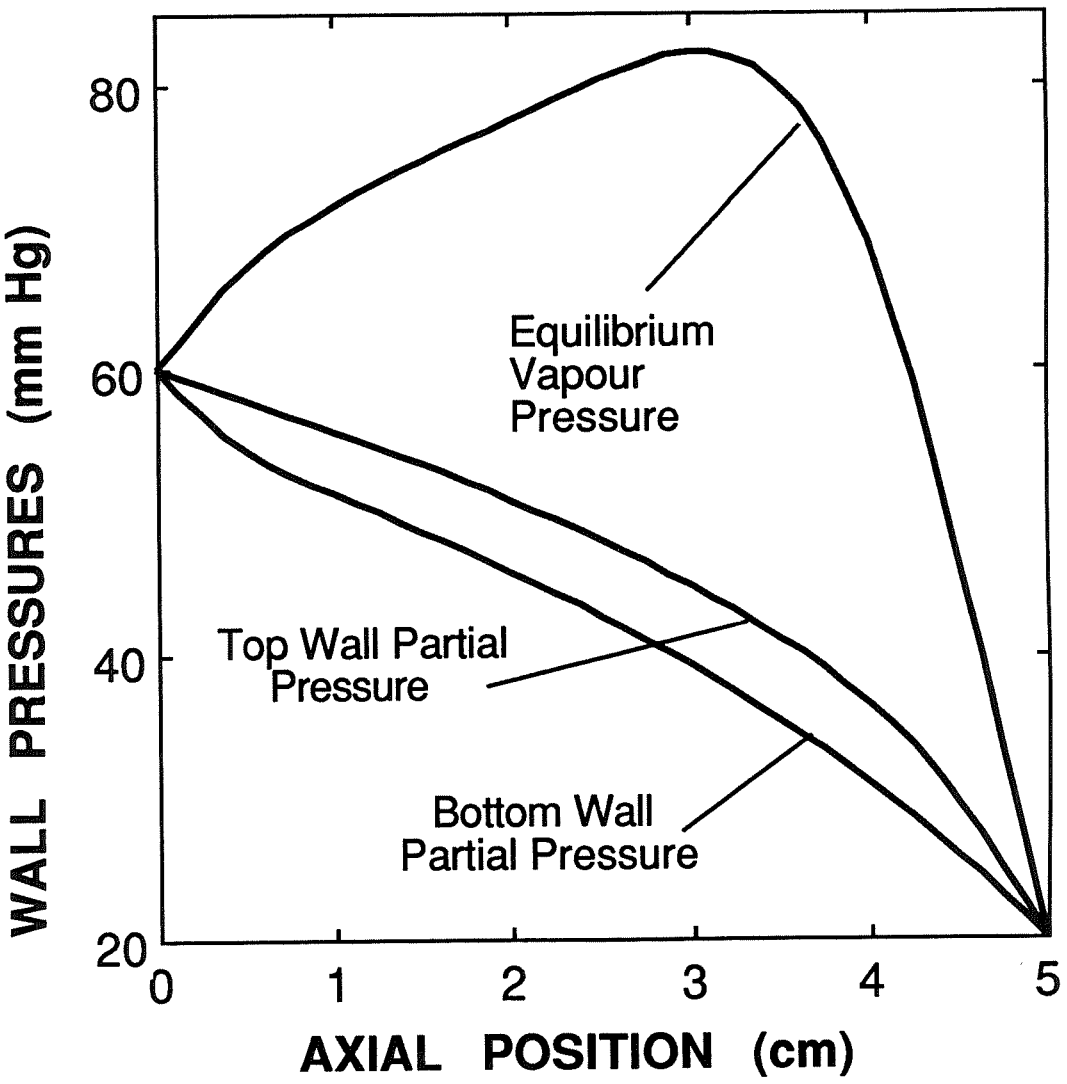
80
60
40
20
0
1
2
3
4
5
WALL PRESSURES (mm Hg)
AXIAL POSITION (cm)
Equilibrium
Vapour
Pressure
Top Wall Partial
Pressure
Bottom Wall
Partial Pressure

Fig. 8

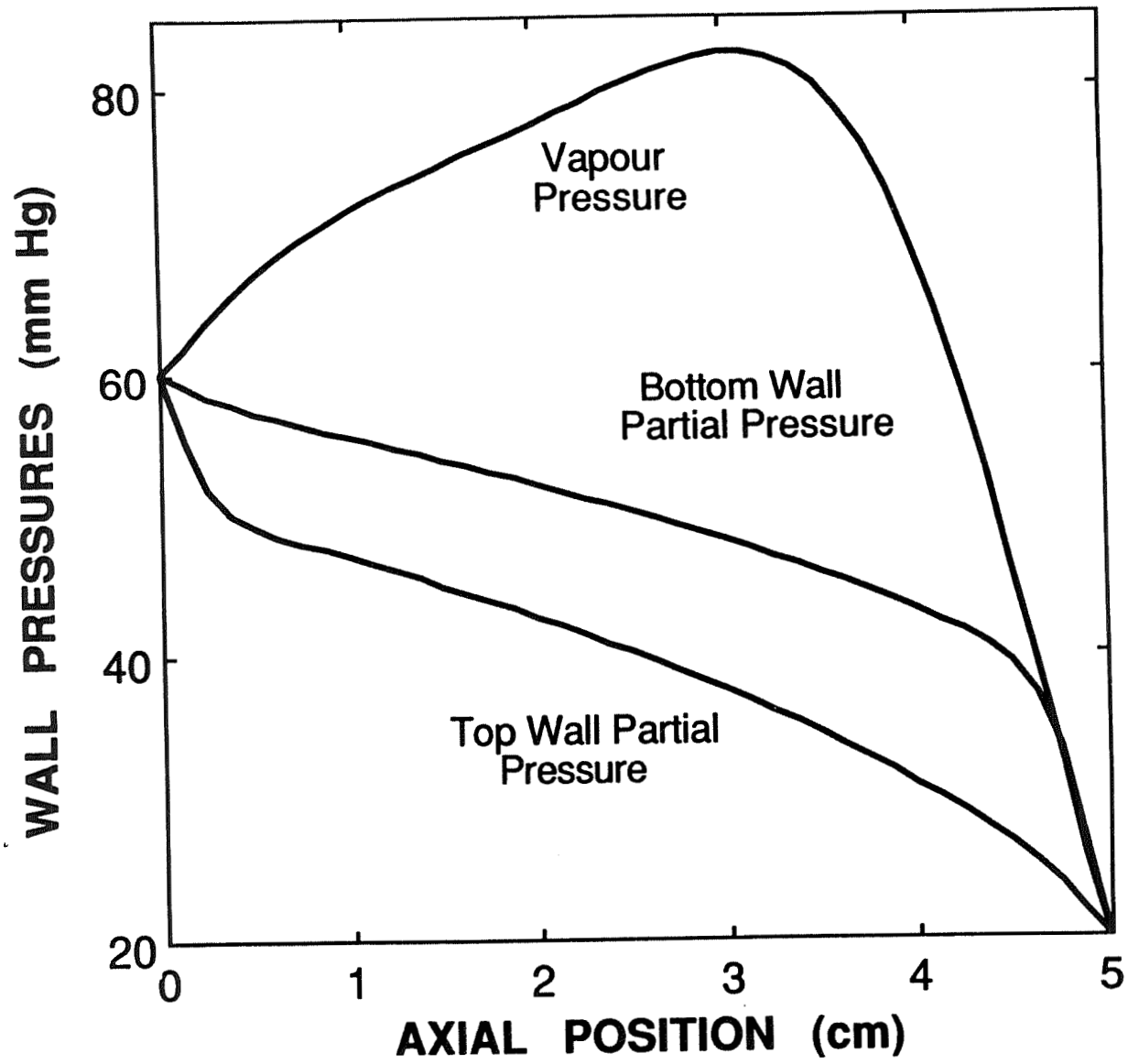
80
60
40
20
0
1
2
3
4
5
Vapour
Pressure
Bottom Wall
Partial Pressure
Top Wall Partial
Pressure
WALL PRESSURES (mm Hg)
AXIAL POSITION (cm)

Fig. 9

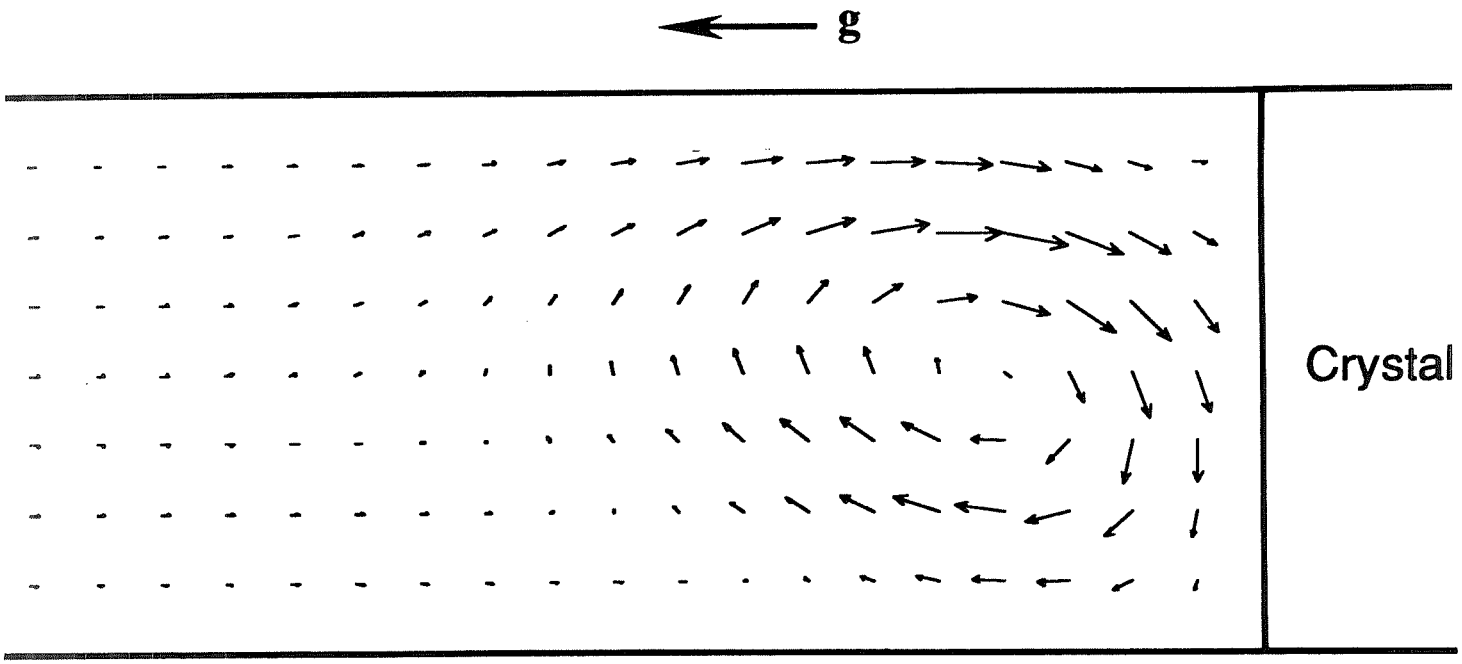

Fig. 10

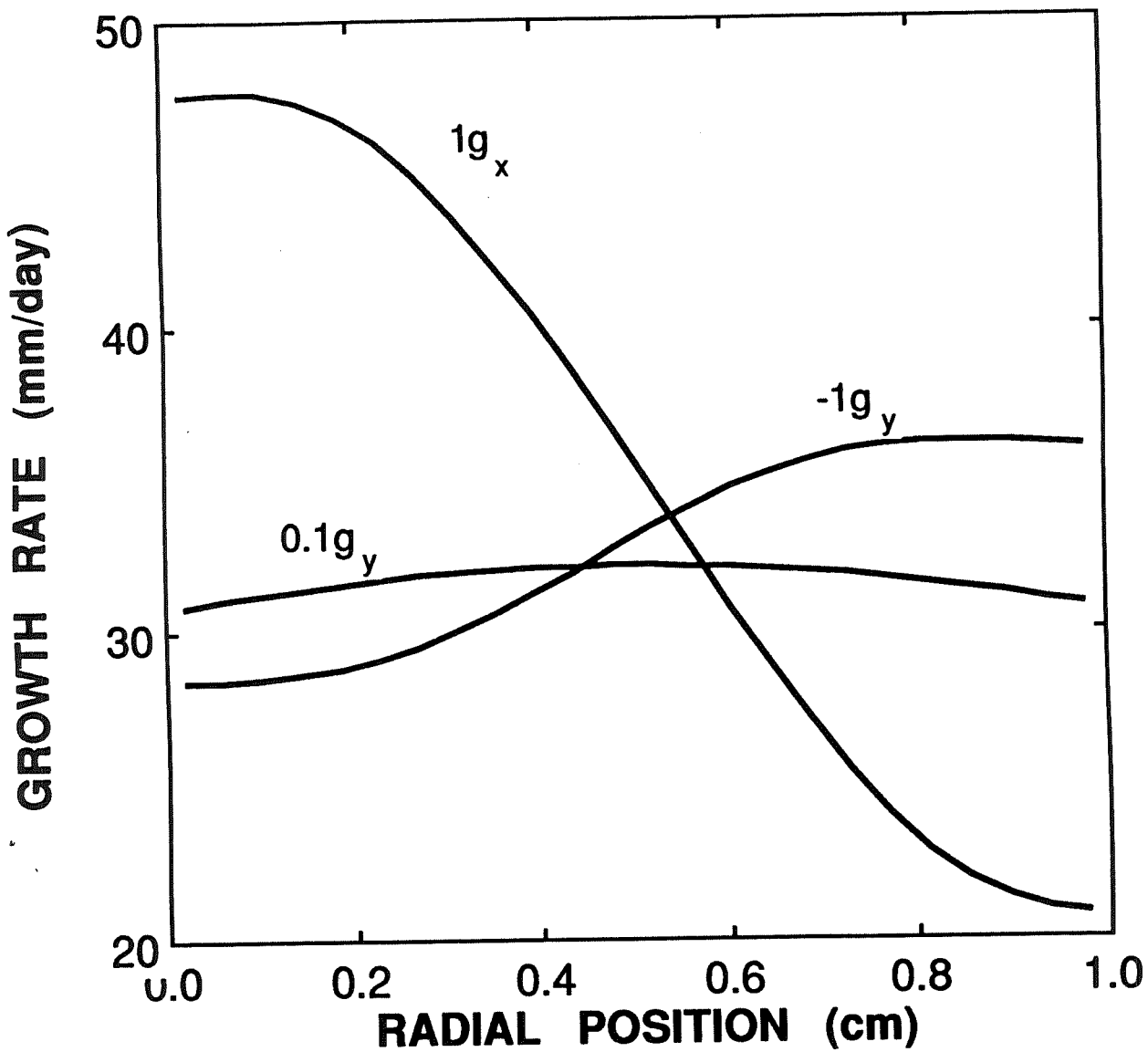
50
40
30
20
0.0
0.2
0.4
0.6
0.8
1.0
GROWTH RATE (mm/day)
RADIAL POSITION (cm)
1g x
-1g y
0.1g y

Fig. 11

Page intentionally left blank

5. APPENDICES

5.1 A Numerical Analysis of the Sensitivity of the Bridgman-Stockbarger Technique to Residual Acceleration: I Steady and Impulse Acceleration

5.2 Modelling the solution growth of Triglycine Sulfate crystals

Journal of Crystal Growth 97 (1989) 285–302
North-Holland, Amsterdam

ANALYSIS OF THE LOW GRAVITY TOLERANCE OF BRIDGMAN–STOCKBARGER CRYSTAL GROWTH
I. Steady and impulse accelerations

J. Iwan D. ALEXANDER, Jalil OUAZZANI and Franz ROSENBERGER

Center for Microgravity and Materials Research, University of Alabama in Huntsville, Huntsville, Alabama 35899, USA

Received 12 February 1989; manuscript received in final form 14 April 1989

The effects of steady and impulse-type residual accelerations on dopant distributions during directional solidification in 2D and 3D "generic" models of the Bridgman–Stockbarger technique have been investigated using numerical models. The calculations are based on the thermo-physical properties of molten germanium doped with a low concentration of gallium. A novel Chebyshev collocation pseudo-spectral method was used for the solution of the governing momentum-, mass-, species- and heat-transfer equations. Only convection caused by temperature gradients was considered. It was found that lateral non-uniformity in composition is very sensitive to the orientation of the steady component of the residual gravity vector and to the particular operating conditions under consideration. For growth rates of several microns per second a steady background level of 10^{-6} times that of normal gravity can be tolerated provided that the acceleration vector is aligned with the axis of the growth ampoule. For reduced growth rates, higher (steady) background acceleration levels are acceptable. It was also found that laterally or radially averaged composition profiles are alone insufficient to describe the extent of residual convection in a spacecraft environment. The effects of impulse-type disturbances can be severe and can extend for times on the order of one thousand seconds after the termination of the impulse. A so-called "compensating double pulse" will not result in completely offsetting effects.

1. Introduction

During the past decade there has been considerable interest in the possibility of using the almost weightless environment of an orbiting spacecraft as a laboratory in which to study crystal growth processes. The attraction of such a laboratory is that buoyancy-driven convection in nutrient phases may be reduced or practically eliminated so that mass transfer is more likely to be controlled by diffusion [1–3]. It has been recognized for some time that convection can lead to undesirable compositional variations in melt grown (semi-conductor) crystals [2,4–6]. In many of these cases the convection is buoyancy-driven [7]. Thus, as far as crystal growth is concerned, the diffusion-controlled conditions which may result in a spacecraft should favor compositional uniformity in the crystal [1,2].

That the magnitude of the effective gravity vector may be reduced as much as six orders of magnitude is well known, and has led to the use of the term *microgravity* to describe the spacecraft's residual acceleration environment. However, our experience in space laboratories has led to the realization that, while in principle the accelerations could be as low as 10^{-5}–10^{-6} gal *, in practice this is not always the case [8,9]. The many sources of residual acceleration [8–10] include the earth's gravity gradient, atmospheric drag, basic orbital attitude motions, crew motions, machinery induced perturbations, and attitude corrections. The latter three can give rise to disturbances on the order of 10^{-3} to 10^{-2} gal. While these accelerations may be orders of magnitude lower than that experienced at the earth's surface, they are nonetheless finite and pose potential problems for certain types of experiment, especially those for which minimization of accelerations is desirable.

In this work, we examine the extent to which buoyancy-driven convection, caused by small

* 1 gal = 9.8 m s^{-2}, and is a unit of acceleration (named after Galileo) commonly used in geophysics.

0022-0248/89/$03.50

accelerations characteristic of the steady component of the residual acceleration vector in a spacecraft, result in non-uniform solute distribution in a directionally solidified crystal. The physical system under consideration involves crystals grown from a two component melt via the Bridgman–Stockbarger technique. In particular, the importance of ampoule orientation relative to the gravity vector is studied. The effects of impulses are also examined. The consequences of other types of time-dependent disturbances will be discussed in a companion paper.

In previous work involving the use of numerical models to study melt convection, the thermal boundary conditions have been modelled with varying degrees of fidelity. Early work [11–13] includes a variety of imposed temperature boundary conditions. These range from purely vertical temperature gradients in which the flow ensues after a critical value of the Rayleigh number is exceeded [14], to idealized conditions associated with Bridgman–Stockbarger furnaces [13] which are imposed directly on the melt and crystal without consideration of the heat transfer between the ampoule, furnace and sample. For these boundary conditions, flow always occurs owing to the presence of radial temperature gradients. Later models [15,16] have accounted for the presence of the ampoule, and the furnace design. In an actual growth situation the characteristic thermal profile of the inner surface of the furnace is not realized at the ampoule wall; it is modified by heat transfer between the crystal, melt, ampoule and the furnace itself. The tendency is to reduce axial temperature gradients, while radial temperature gradients may increase or decrease depending on the specific nature of the heat transfer between the charge and ampoule [15]. The influence of melt convection on dopant distribution has been examined for dilute and non-dilute melts [13,15]. For a given furnace-ampoule combination the amount of compositional non-uniformity (or radial segregation) was shown to be a non-linear function of the Rayleigh number. The growth rate and physical properties of the melt also influence the degree of compositional uniformity in the grown crystal.

That residual accelerations on the order of 10^{-6}–10^{-5} gal are sufficient to cause observable fluid motion has been established [10,17–19] and can be inferred from work such as [13]. The sensitivity to low gravity has also been estimated for a wide variety of experiments by dimensional analysis [20,21]. The extent to which gravity causes solute redistribution, via buoyancy-driven fluid motion, during directional solidification in geometries characteristic of the Bridgman–Stockbarger technique has been examined using numerical models [11–14,19,22]. Apart from McFadden and Coriell [22] who examined a two-dimensional situation in which the gravity vector continuously rotates relative to the container, and Polezhaev et al. [19], other work is restricted to axisymmetric situations in which a steady gravity vector is oriented parallel to the axis of a cylindrical ampoule.

A general conclusion that can be drawn from all previous attempts to characterize gravity-driven convective effects on directional solidification from two component melts (and from the results of the work presented here) is that the maximum lateral solute non-uniformity (radial segregation for the axisymmetric cases) occurs near the transition from diffusion dominated to convection dominated growth conditions [20,23]; that is, when convective velocities are of the same order of magnitude as the diffusive velocities. The conditions under which this "transition" takes place will depend on the specific nature of the forces driving convection. We demonstrate in this work that the orientation of the steady component of the gravity vector is crucial in determining the magnitude of the gravity vector at which this transition occurs. Thus, for a given set of operating conditions the orientation of the gravity vector can determine the suitability of a low gravity environment for directional solidification experiments.

In the following sections we formulate the basic model, define the range of operating conditions under consideration and examine the effects of magnitude and orientation of steady and impulse-type acceleration vectors on compositional uniformity in directionally solidifying crystals. The objective of this work is to identify trends. Rather than attempt to model the thermal conditions corresponding to a specific furnace, we adopt a generic model which is based on the pioneering

work of Chang and Brown [13], in which the thermal profile is imposed on the melt and crystal.

2. Formulation

The following physical situation, which corresponds to directional solidification by the Bridgman–Stockbarger technique, is considered. An ampoule containing a (dilute) two-component melt is translated at a constant rate between fixed hot and cold zones of a furnace. The upper and lower parts of the furnace are maintained at a uniform temperature by means of heat pipes and the two zones are separated by a thermal barrier [24]. Directional solidification takes place as the ampoule is translated. In an actual growth situation the heat transfer conditions between the crystal, melt and ampoule can result in a non-planar crystal–melt interface (for a summary, see ref. [24]). Curvature of the solid–liquid interface can result in significant lateral compositional non-uniformity [25,26]. Since we wish to focus attention on the influence of convection on the composition of the crystal we choose to constrain the interface to be planar.

Two- and three-dimensional models are considered. For the 2D model the dilute binary melt is assumed to occupy a rectangular region Ω of height L and width W, which is bounded by planar surfaces (see fig. 1). In the 3D model the rectangular region is replaced by a circular cylinder with radius $W/2$.

Translation of the ampoule is modelled by supplying a doped melt of dilute bulk composition c_∞ at a constant velocity V_M at the top of the computational space, and withdrawing a solid of composition c_s (which, in general, will be a function of both space and time) from the bottom. The crystal–melt interface is located at a fixed distance L from the top of the computational space. Thus, the assumption that the ampoule translation rate and the growth rate are equal is implicit. The thermal barrier which separates the zones is modelled using adiabatic sidewalls of length $L/4$ (see fig. 1). The temperature at the interface is taken to be T_M, the melting temperature of the crystal, while the upper boundary is held at a higher

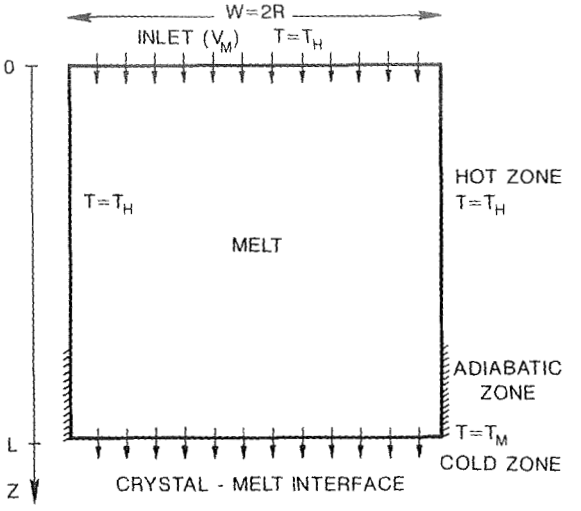

Fig. 1. Idealized model of the Bridgman–Stockbarger system.

temperature T_H. In an actual experiment, owing to the finite length of the ampoule there is a gradual decrease in length of the melt zone during growth. In this model transient effects related to this change are ignored. Thus, it is assumed that the ampoule is sufficiently long for steady state temperature, concentration and growth rate to be established. The appropriate boundary condition to adopt in this case is the pseudo-steady state condition used by Chang and Brown [13]. The only transient effects to be considered will arise directly from the time-dependent nature of the residual gravity field. We also assume that the contribution of the solute (dopant) to convection is negligible. Free convection is driven by thermal gradients only.

The governing equations are cast in dimensionless form using L, κ/L (where κ is the melt's thermal diffusivity), $\rho_M \kappa^2/L^2$ (where ρ_M is the melt's density), $T_H - T_M$, and c_∞ to scale the lengths, velocity, pressure, temperature and solute concentration, respectively. The dimensionless equations governing momentum, heat and solute transfer in the melt are then

$$\frac{\partial \boldsymbol{u}}{\partial t} + (\operatorname{grad} \boldsymbol{u})\,\boldsymbol{u} = -\operatorname{grad} p + \operatorname{Pr} \Delta \boldsymbol{u} + \operatorname{Ra} \operatorname{Pr} \theta\, \boldsymbol{g}(t), \tag{1}$$

$$\operatorname{div} \boldsymbol{u} = 0, \tag{2}$$

Table 1
Forms of the acceleration vector examined in this work

Steady
$\boldsymbol{g}_0 = g_{0x}\boldsymbol{i} + g_{0z}\boldsymbol{k}$;
$\|\boldsymbol{g}\| = 10^{-4}, \sqrt{2}\times10^{-5}, 10^{-5}, 5\sqrt{2}\times10^{-6}, 5\times10^{-6}, \sqrt{2}\times10^{-6}, 10^{-6}, 10^{-7}$
Impulse
$\boldsymbol{g}(t) = [g_0 + g(t)]\boldsymbol{k}$, $g_0 = 10^{-6}, \sqrt{2}\times10^{-6}$,
$g(t) = 0$ for $t < t_1$ and $t > t_2$ and $g(t) = g_1$ for $t_1 < t < t_2$
$g(t) = 0$ for $t < t_1$, $t_2 < t < t_3$ and $t > t_4$ and $g(t) = g_1$ for $t_1 < t < t_2$, $t_3 < t < t_4$
$g(t) = 0$ for $t < t_1$, $t_3 < t < t_2$ and $t > t_4$ and $g(t) = g_1$ for $t_1 < t < t_2$, $g(t) = -g_1$ for $t_3 < t < t_4$, $g_1 = 5\times10^{-3}, 3\times10^{-3}$

$$\frac{\partial\theta}{\partial t} + \boldsymbol{u}\cdot\text{grad}\ \theta = \Delta\theta, \tag{3}$$

$$\frac{\text{Sc}}{\text{Pr}}\left(\frac{\partial C}{\partial t} + \boldsymbol{u}\cdot\text{grad}\ C\right) = \Delta C, \tag{4}$$

where $\boldsymbol{u}(\boldsymbol{x}, t)$, $\theta = (T(\boldsymbol{x}, t) - T_M)/(T_H - T_M)$ and C, respectively represent the velocity, temperature and solute concentration. The parameters $\text{Pr} = \nu/\kappa$, $\text{Ra} = g\beta(T_H - T_M)L^2/\kappa\nu$ and $\text{Sc} = \nu/D$ are, respectively, the Prandtl, Rayleigh and Schmidt numbers. The term $\boldsymbol{g}(t)$ in eq. (1) represents the steady or time-dependent gravity vector. The value of g in Ra is taken to be 1 gal, i.e. equal to the gravitational acceleration at the earth's surface. Thus, the magnitude of $\boldsymbol{g}$ represents the ratio between the actual residual acceleration and g. Table 1 lists the forms of $\boldsymbol{g}(t)$ used in these calculations.

The following boundary conditions are applied at the crystal-melt interface

$$\theta = 0, \tag{5}$$

$$\boldsymbol{u}\cdot\boldsymbol{N} = \text{Pe}/\sigma, \tag{6}$$

$$\boldsymbol{u}\times\boldsymbol{N} = \boldsymbol{0}. \tag{7}$$

$$\frac{\partial C}{\partial z} = \frac{\text{Pe Sc}}{\text{Pr}}(1-k)\,C, \tag{8}$$

where $\boldsymbol{N}$ points into the melt and is the unit vector perpendicular to the planar crystal melt interface, $\text{Pe} = V_{ML}/\kappa$ is the Peclet number, $\sigma = \rho_M/\rho_S$ and k is the segregation coefficient. We define the measure of compositional non-uniformity in the crystal at the interface to be the lateral range in concentration given by

$$\xi = \frac{(c_{\text{smax}} - c_{\text{smin}})\times 100\%}{c_{\text{av}}},$$

where c_s is the (dimensional) solute concentration in the crystal, and c_{av} is the average interface concentration. At the "inlet" ($z = 0$) the following boundary conditions are applied

$$\theta = 1, \tag{9}$$

$$\boldsymbol{u}\cdot\boldsymbol{N} = \text{Pe}\ \sigma, \tag{10}$$

$$\boldsymbol{u}\times\boldsymbol{N} = \boldsymbol{0}. \tag{11}$$

$$\frac{\partial C}{\partial z} = \frac{\text{Pe Sc}}{\text{Pr}}(C-1), \tag{12}$$

Eqs. (8) and (12) express conservation of mass at the crystal–melt interface and the inlet respectively. Eqs. (6) and (10) guarantee continuity of the melt with the crystal and with the supply of melt at the inlet, while eqs. (7) and (11) ensure no-slip tangent to the interface and the top surface. At the side walls the following conditions are applied

$$\text{grad}\ C\cdot\boldsymbol{e}_w = 0, \quad \boldsymbol{u}\cdot\boldsymbol{N} = \text{Pe}\ \sigma, \quad \boldsymbol{e}_w\cdot\boldsymbol{u} = 0, \tag{13}$$

along with

$$\theta = 1 \tag{14}$$

in the isothermal zone, and

$$\text{grad}\ \theta\cdot\boldsymbol{e}_w = 0 \tag{15}$$

in the adiabatic zone. Here $\boldsymbol{e}_w$ is the normal to the

Table 2
Thermo-physical properties of gallium-doped germanium [13] and operating conditions used in the calculations

Property	Value
Thermal conductivity of the melt	0.17 W K^{-1} cm^{-1}
Heat capacity of the melt	0.39 J g^{-1} K^{-1}
Density of the melt (ρ_M)	5.6 g cm^{-3}
Density of the solid (ρ_S)	5.6 g cm^{-3}
Kinematic viscosity of the melt (ν)	1.3×10^{-3} cm^2 s^{-1}
Melting temperature (T_M)	1231 K
Solute diffusivity (D)	1.3×10^{-4} cm^2 s^{-1}
Thermal diffusivity of the melt (κ)	1.3×10^{-1} cm^2 s^{-1}
Segregation coefficient (k)	0.1
Thermal expansion coefficient (β)	2.5×10^{-4} K^{-1}
Associated dimensionless parameters	**Value**
Prandtl number $Pr = \nu/\kappa$	0.01
Peclet number $Pe = V_M L/\kappa$	
Schmidt number $Sc = \nu/D$	10
Density ratio σ	1.0
Operating conditions	**Value**
(A) Hot zone temperature (T_H)	1331 K
Distance between inlet and interface (L)	1.0 cm
Height of adiabatic zone	2.5 mm
Ampoule width (diameter)	1.0 cm
(B) Hot zone temperature (T_H)	1346 K
(C) Hot zone temperature (T_H)	1251 K
(D) Ampoule width	2.0 cm
(E) Ampoule width	0.5 cm
(V1) Translation (supply) rate (V_M)	6.5 μm s^{-1}
(V2) Translation (supply) rate (V_M)	3.25 μm s^{-1}
(V3) Translation (supply) rate (V_M)	0.65 μm s^{-1}

ampoule wall. While the above model will rarely apply to a specific furnace (since details of the heat transfer at the ampoule walls, and between ampoule and furnace are neglected), it nonetheless serves as a reasonable "generic" model with which to carry out a preliminary analysis of a directional solidification experiment under conditions characteristic of the low gravity environment of space.

For the most part, our calculations are limited to thermo-physical properties corresponding to dilute gallium-doped germanium, although the effect of different Schmidt numbers are considered for a limited range of steady low gravity conditions. The values of the thermo-physical properties and the associated dimensionless groups and operating are given in table 2.

3. Method of solution

The governing equations (1)–(15) were solved by two different methods; a pseudo-spectral Chebyshev collocation method and a finite volume method implemented by the code PHOENICS [28]. The latter method was used to obtain most of the results pertaining to the Ge : Ga system. Only those results corresponding to B (2D and 3D) in table 2 and to the 2D impulse accelerations were computed using PHOENICS.

The pseudo-spectral method employed is an orthogonal collocation pseudo-spectral method which uses Chebyshev polynomial expansions for spatial discretization [27,29]. Only the two-dimensional calculations were tackled using this approach, although the method is readily extended to three dimensions. Steady solutions are obtained using a pseudo-unsteady method which involves a generalized ADI procedure [27]. The momentum equations are linked to the continuity equation via the method of artificial compressibility. Both steady and time-dependent solutions were computed using an Adams–Bashforth–Crank–Nicolson scheme [27]. (For more details see [30].) The results presented in this paper were computed using 33×33 points. This was found to yield sufficient resolution for the range of Schmidt numbers considered. For the impulse-type residual accelerations a variable time step was employed. In order to assess the consequences of adopting the pseudo-steady state conditions, (9)–(12), we varied the aspect ratio of the computational space. While, for accelerations between 10^{-4} and 10^{-3} gal (oriented parallel to the interface) this altered the flow pattern in the upper part of the ampoule, the computed values of ξ differed only by a few percent from the values computed with aspect ratio 1. For the lower acceleration magnitudes (and for orientations perpendicular to the interface) no significant difference in ξ was found.

PHOENICS embodies a finite volume or finite domain formulation [28,31]. It represents the governing equations introduced in the previous section as a set of algebraic equations. These equations represent the consequence of integrating the differential equation over the finite volume of a computational cell (and, for transient problems,

over a finite time) and approximating the resulting volume, area and time averages by interpolation. For the 2D and axisymmetric calculations discussed in this paper we employed a 40×39 grid. The 3D calculations were performed in a circular cylindrical domain with 20 nodes in the radial direction, 12 in the azimuthal direction and 39 in the axial direction. We found that for the 2D calculation less than 40 points in the direction parallel to the interface resulted in poor convergence of the solute field.

The scheme employed by PHOENICS has the same accuracy as a finite difference scheme which is of the order Δx, where Δx is the distance between the grid nodes. The time scheme is implicit and thus unconditionally stable. However, small time steps are required to obtain accurate solutions. For highly non-linear flows the use of underrelaxation is necessary to eliminate divergence and to ensure good convergence of the solutions.

A comparison of the two methods was made for different acceleration magnitudes and for different Schmidt numbers. The spectral method was found to cope better with the steep solute gradients which occur in the high Schmidt number cases. For $\mathrm{Sc} = 10$, and steady acceleration magnitudes of less than 10^{-3} gal, the results of the two methods compared favorably. For example, the computed concentration values differed by at most 5%, the difference being less at lower acceleration magnitudes. A comparison of interface concentration values for accelerations oriented parallel to the interface with magnitudes of $\sqrt{2} \times 10^{-6}$ and $\sqrt{2} \times 10^{-5}$, yielded differences of 2% or less. The average interface concentration computed by both methods being less than 0.1%. The calculated values of ξ for these two cases were 21.5% and 18.5% for the lower acceleration magnitude and 152% and 123% for the higher magnitude; in both cases the lower value of ξ was computed using the spectral method. Hence, the percentage difference in ξ computed by both methods is about a factor of 10 (for $k = 0.1$) higher than the differences in the computed values of concentration.

Steady calculations using the pseudo-spectral method with 33×33 collocation points required 2000–2500 iterations to achieve good convergence for the steady calculations. This typically took around 5–10 min of (CRAY XMP) CPU time. The finite volume calculations were carried out on a VAX-785 and required 3–4 h of CPU time.

4. Results

4.1. Steady accelerations: 2D

The temperature field is insensitive to the convective motion owing to the low Prandtl number of the melt ($\mathrm{Pr} = 10^{-2}$) and the low magnitude of the residual accelerations considered. It is characterized by the conduction profile shown in fig. 2. Note that there are lateral (radial) as well as axial temperature gradients in the system. The consequent density gradient is responsible, as we shall see, for driving convection in the melt even when residual acceleration magnitudes are as low as 10^{-6} gal. The temperature fields for all the cases listed in table 2 are qualitatively similar, the major differences are the magnitudes of the temperature gradients which reflect the temperature difference $T_H - T_M$.

The velocity and concentration distributions, together with the interfacial ξ values, have been obtained for various combinations of orientations

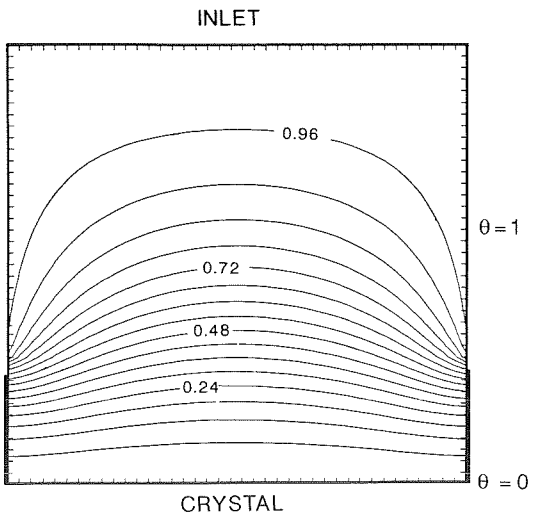

Fig. 2. The dimensionless temperature field, θ, for 2D calculations corresponding to operating conditions B-V1 in table 2. Note that there is no difference between this and a purely conductive profile (i.e. g = 0).

Table 3
Compositional non-uniformity ξ[%] for Ge:Ga

Residual acceleration magnitude (gal)		Orientation		Ampoule width (cm)				
		N	e_g	1	1	1	0.5	2.0
				Growth rate (μm s^{-1})				
				6.5	3.25	0.65	6.5	6.5
(A)	10^{-4}	↑	←	80				
	10^{-5}		←	92.7		11.9	12.0	
			↙	70.9		11.3		
			↓	6.4		0.95		
	5×10^{-6}		↓	3.2				
			↙	39				
			←	54.2				
	10^{-6}		←	11.3		2.0		
			↙	8.0				
(B)	10^{-4}	↑	↓	36				
			↑	32				
	$\sqrt{2}\times10^{-5}$		↙	110				
			←	152 (91)				
	10^{-5}		↓	7.5	4.6	0.7		
	$5\sqrt{2}\times10^{-6}$		↙	57				
	$\sqrt{2}\times10^{-6}$		↙	10				
			↑	4.0				
			↓	2.0				
			←	21.5 (26)		1.5		
	10^{-6}		↓	0.7	0.4	0.0		3.8
	10^{-7}		↑	1.0	0.5	0.2		
(C)	10^{-5}	↑	←	22.6				64.5
	10^{-6}		←	2.3				

e_g is the unit vector parallel to g, N is the normal vector to the crystal.
$L = 1$ cm for all cases.
Values in parentheses indicate 3D results.
(A), (B) and (C) refer to the operating conditions listed in table 2.

and magnitudes of the acceleration vector, growth rates, ampoule (Ω) dimensions and temperature differences $T_H - T_M$. The results are summarized in table 3.

Figs. 3–5 illustrate the velocity and solute fields for three cases where the residual acceleration is parallel to the crystal–melt interface and the operating conditions correspond to A-V1 in table 2. Note that the vectors in these figures are scaled by the growth velocity and have been obtained by interpolation from the computed values obtained on the unevenly spaced Chebyshev mesh. If the conditions were purely diffusive, the velocity vectors would all be the same length and perpendicular to the crystal–melt interface. Furthermore, the isoconcentrates and crystal–melt interface would be parallel. A single roll is calculated at 10^{-5} gal, resulting in $\xi = 92.7\%$. Between 10^{-5} and 10^{-6} gal the roll is no longer present and at 10^{-6} gal the convective motion results in a barely perceptible deflection of the velocity vectors from a purely longitudinal flow. The compositional variations in the melt are, however, still significant even at 10^{-6} gal.

In contrast to the single roll flow depicted in fig. 3a, fig. 6 shows that when the same magnitude gravity vector is oriented perpendicular to the crystal-melt interface there are no rolls. The flow is deflected symmetrically about the ampoule axis. The associated compositional non-uniformity is

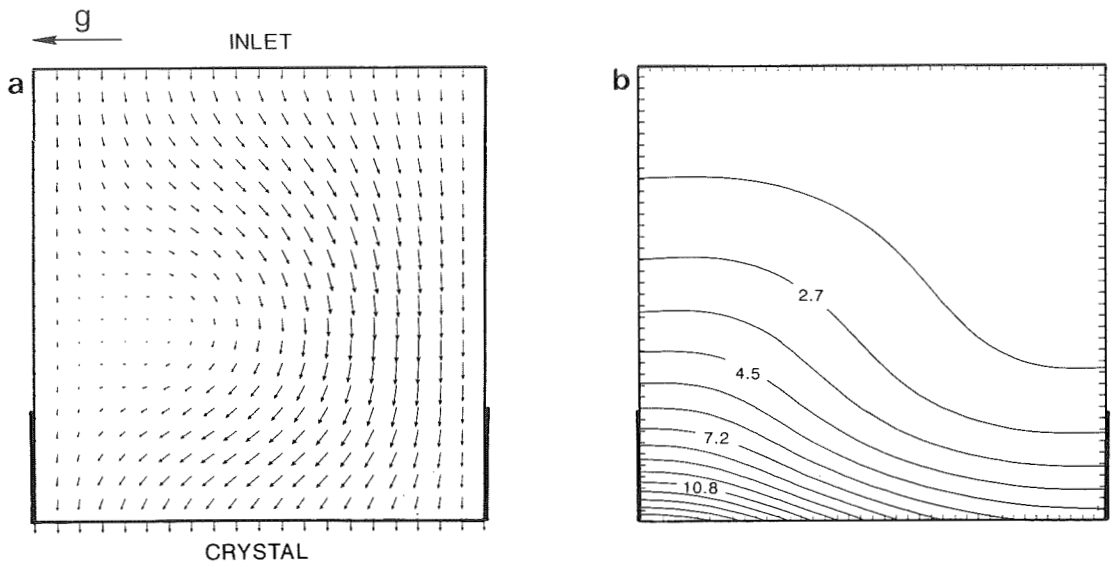

Fig. 3. (a) The steady flow field produced by a residual acceleration with a magnitude 10^{-5} gal acting parallel to the crystal–melt interface. The maximum speeds are approximately twice the growth speed. (b) The dimensionless solute field, C, associated with the flow depicted in (a). The contour interval is 0.9. For this case $\xi = 92.7\%$.

symmetric about the centerline of the ampoule and, with $\xi = 6.4\%$, is significantly smaller than for the asymmetric case.

Figs. 7a–7c depict the lateral variation in composition of the crystal for gravity orientations parallel, at 45° and perpendicular to the interface.

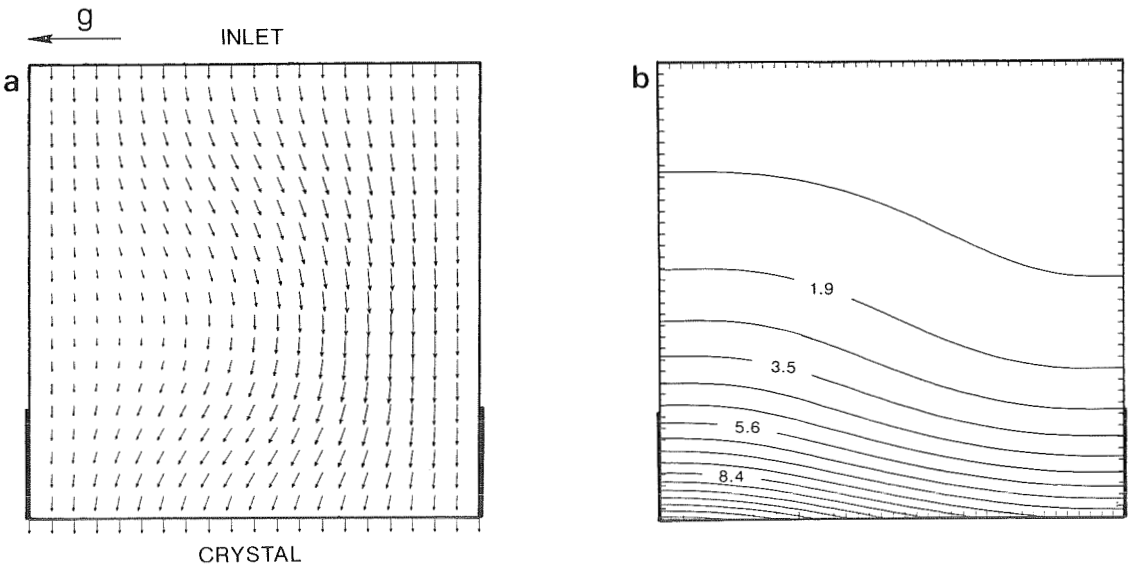

Fig. 4. (a) The steady flow field produced by a residual acceleration with a magnitude 5×10^{-6} gal acting parallel to the crystal–melt interface. The maximum speeds are slightly greater than the growth speed. (b) The dimensionless solute field, C, associated with the flow depicted in (a). The contour interval is 0.7. For this case $\xi = 39\%$.

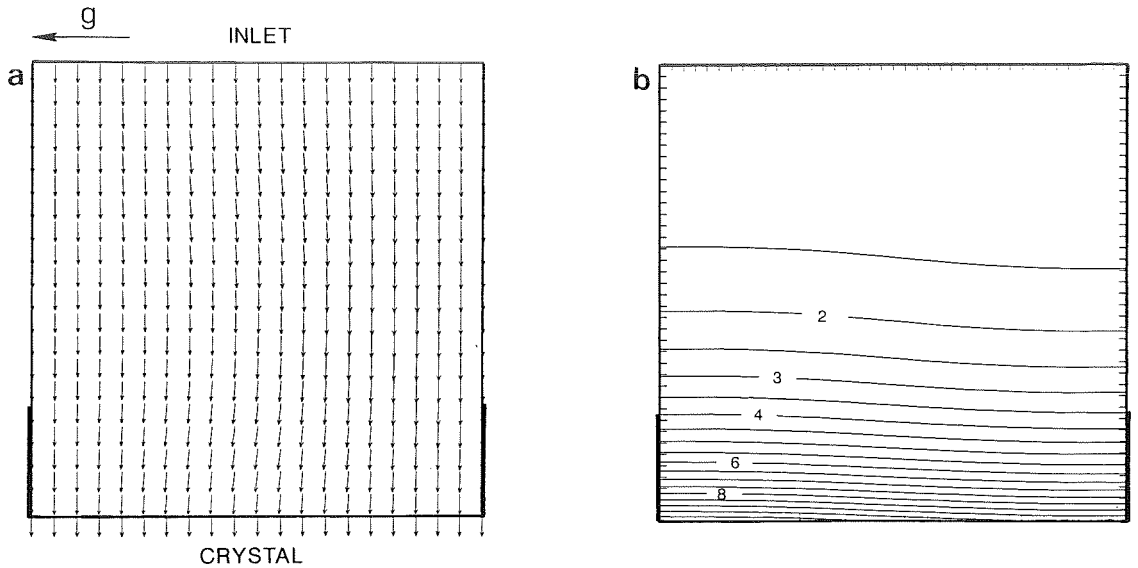

Fig. 5. (a) The steady flow field produced by a residual acceleration with a magnitude 10^{-6} gal acting parallel to the crystal–melt interface. The maximum speeds are slightly greater than the growth speed. (b) The dimensionless solute field, C, associated with the flow depicted in (a). For this case $\xi = 11.3\%$.

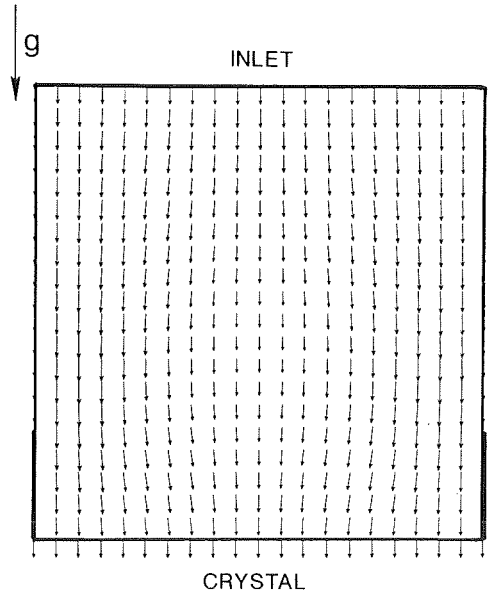

Fig. 6. The steady flow field produced by a residual acceleration with a magnitude 10^{-5} gal acting perpendicular to the crystal-melt interface, otherwise the operating conditions are the same as for figs. 3–5. The contour interval is 0.5. For this case $\xi = 6.4\%$.

These figures further illustrate the importance of ampoule orientation with respect to the residual acceleration vector. For a fixed acceleration magnitude, as the ampoule axis and acceleration vector are brought into alignment, the transition from asymmetric to symmetric compositional non-uniformity is accompanied by a reduction in the magnitude of the non-uniformity. For these, and other cases corresponding to gallium-doped germanium crystals, the values of lateral non-uniformity ξ are listed in table 3 along with the associated operating conditions.

Characterization of melt grown crystals often includes radially or laterally averaged crystal composition profiles [32–34]. Laterally averaged *melt* composition profiles are shown in fig. 8 for operating conditions corresponding to A-V1 in table 2 and for a selection of residual accelerations. Note that in fig. 8b these profiles are indistinguishable from the pure diffusion case. In addition, these profiles, reveal a high concentration gradient region adjacent to the interface with an approximate width of 0.2 cm. This agrees well with the simple

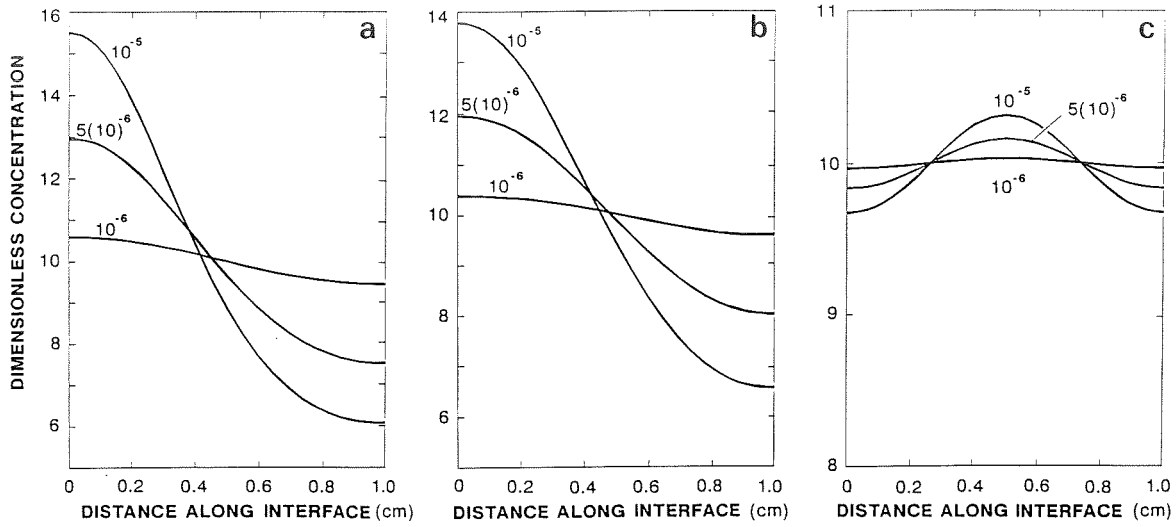

Fig. 7. Lateral variations in melt composition at the interface for operating conditions corresponding to A-V1 in table 2 with acceleration magnitudes of 10^{-5}, 5×10^{-6} and 10^{-6} gal with (a) parallel, (b) 45°, and (c) perpendicular orientation with respect to the crystal–melt interface.

characteristic length obtained from the relation $\delta = D/V_M$.

The consequences of reducing the growth rate are illustrated by fig. 9 which was obtained for 10^{-5} gal parallel to the interface and operating conditions A-V3 (i.e. $V_M = 0.65\ \mu m\ s^{-1}$). A comparison of figs. 3a and 9a shows that due to the reduced melt translation rate the buoyancy-driven recirculation now dominates. Thus, the axial concentration gradient is reduced (figs. 3b and 9b)

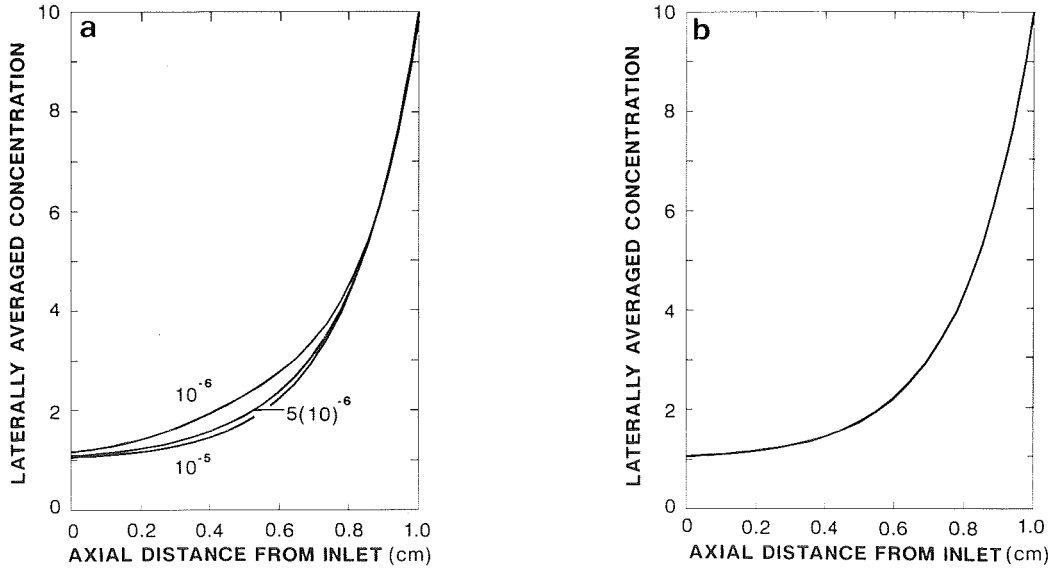

Fig. 8. Laterally averaged, axial composition profiles in the melt for operating conditions corresponding to A-V1 in table 2 for accelerations with magnitudes of 10^{-5}, 5×10^{-6} and 10^{-6} gal oriented (a) parallel and (b) perpendicular to the crystal–melt interface. Note that the latter are indistinguishable from the pure diffusion profile.

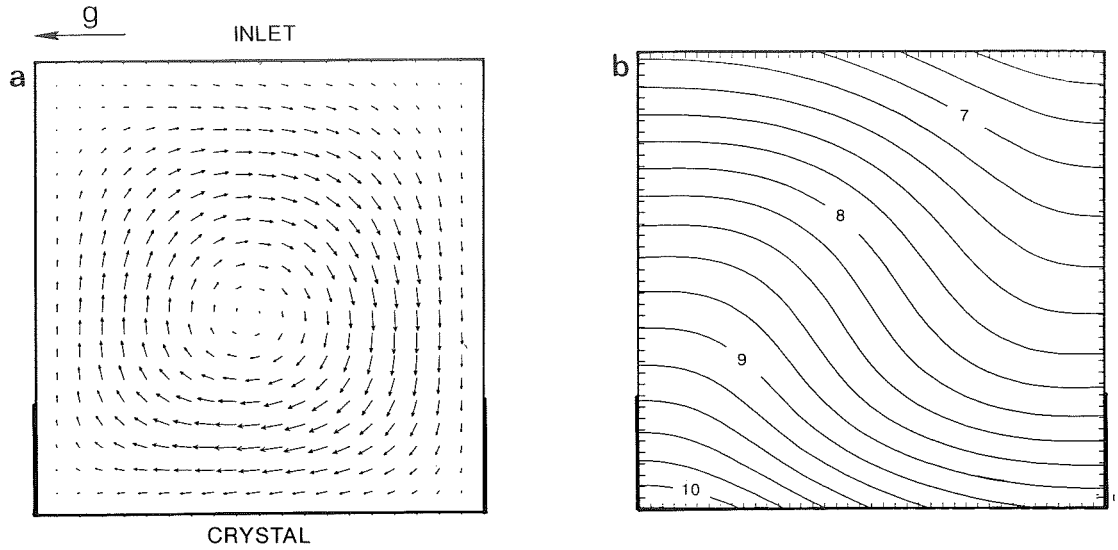

Fig. 9. (a) The velocity field associated with a residual acceleration of magnitude 10^{-5} gal acting parallel to the crystal–melt interface. The operating conditions correspond to A-V3 in table 2, i.e. the growth rate is 0.65 μm s^{-1}. (b) The dimensionless solute field associated with flow depicted in (a). The contour interval is 0.2. For this case $\xi = 11.9\%$.

and a smaller concentration gradient along the interface results (in fig. 9b, $\xi = 11.9\%$ as compared to 92.7% in fig. 3b).

Table 3 also illustrates the effect of changing the temperature gradient and the ampoule dimensions. For an acceleration of 10^{-5} gal oriented parallel to the interface a reduction of the temperature difference between the hot zone and the crystal–melt interface from 100 to 20 K changes ξ from 92.7% to 22.6%. An increase in the width of

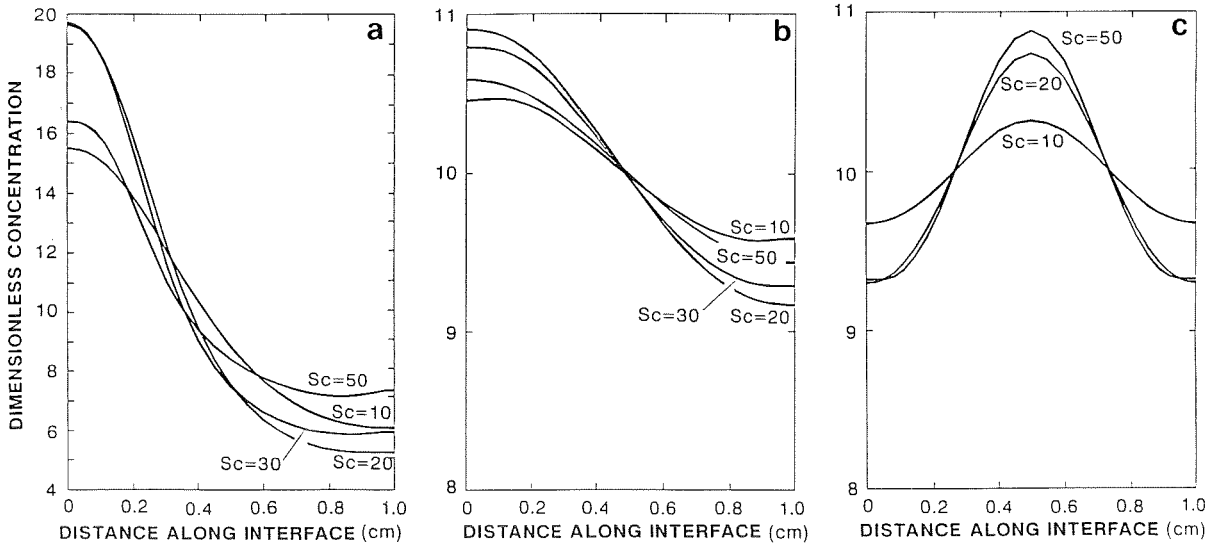

Fig. 10. Lateral variations in melt composition at the interface in crystals grown from melts with different Schmidt numbers for accelerations with the following magnitudes and orientations with respect to the crystal–melt interface: (a) 10^{-5} gal parallel, (b) 10^{-6} gal parallel and (c) 10^{-5} gal perpendicular.

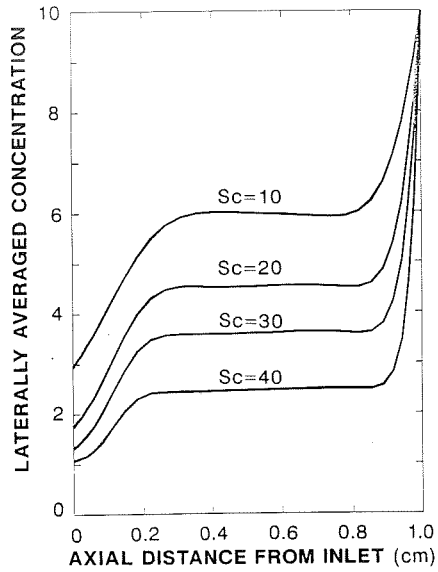

Fig. 11. Laterally averaged axial composition profiles for melts with different Schmidt numbers, for a 10^{-4} gal acceleration oriented parallel to the crystal–melt interface.

the ampoule from 1 to 2 cm with the 20 K temperature difference yields $\xi = 64.5\%$. Clearly, for a given steady acceleration the value of ξ is sensitive to the particular operating conditions employed.

In order to ascertain the importance of the diffusivity of the dopant we have also examined cases with Sc = 10, 20, 30, and 50 for operating conditions otherwise corresponding to A-V1. (Recall that in the relative weighting of convective and diffusive fluxes, an increase in Sc corresponds to a reduction in diffusive transport.) The results are displayed in fig. 10. It is clear that, all other things being equal, the relationship between Sc and ξ is not linear. In particular, for acceleration magnitudes of 10^{-6} and 10^{-5} gal oriented parallel to the interface, the maximum value of ξ is attained for Sc = 20, while at 10^{-5} gal oriented perpendicular to the interface there is little difference in the degree of non-uniformity between Sc = 20 and 50. Laterally averaged composition profiles for 10^{-4} gal acting parallel to the interface are depicted for Sc = 10, 20, 30, and 50 in fig. 11. In comparison to fig. 8 the laterally averaged composition profiles at 10^{-4} gal exhibit a flat section owing to the increase in convective transport.

4.2. Steady accelerations: 3D and axisymmetric

Five three-dimensional calculations were undertaken for $R = 0.5$ cm and $V_M = 6.5\ \mu m\ s^{-1}$ in order to examine the influence of a more realistic geometry. In all cases the operating conditions corresponded to B-V1 in table 2. Three runs were axisymmetric, with $\boldsymbol{g}$ antiparallel and parallel to $\boldsymbol{N}$. These calculations were carried out (for comparison purposes) with $\| \boldsymbol{g} \| = 10^{-4}$ gal, 10^{-3} gal and 10^{-2} gal. Values of the radial segregation were found to be within 5% of the values computed for these conditions by Chang and Brown. The compositional non-uniformity ξ was found to be approximately 10% lower for the 10^{-4} gal axisymmetric case for the 2D analog.

The remaining calculations were fully three-dimensional with $\boldsymbol{g}$ parallel to the crystal–melt interface. The fully 3D cases were carried out for $\| \boldsymbol{g} \| = \sqrt{2} \times 10^{-5}$ gal and $\sqrt{2} \times 10^{-6}$ gal. The melt isoconcentrates at the interface are shown in figs. 12 and 13 for sections cut perpendicular to the ampoule axis at $z = 1$. At the higher value of the residual acceleration, $\xi = 91\%$, which is approximately half the 2D value. At $\sqrt{2} \times 10^{-6}$ gal,

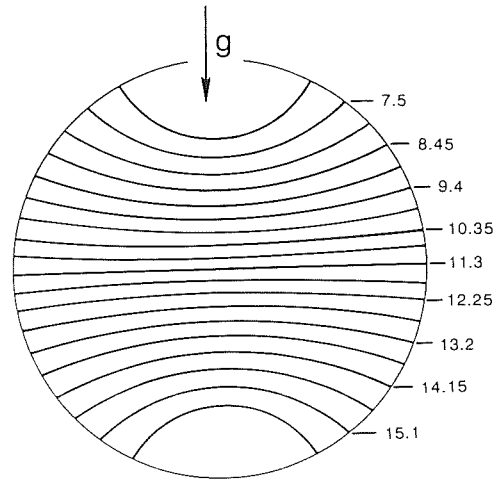

Fig. 12. The solute field at the crystal–melt interface consequent to a $\sqrt{2} \times 10^{-5}$ gal acceleration oriented parallel to the interface for the 3D case. The cross section is taken perpendicular to the ampoule axis. $\xi = 91\%$. The contour interval is 0.95.

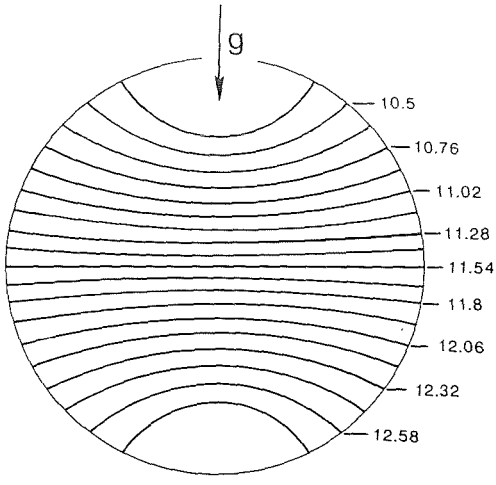

Fig. 13. The solute field at the crystal–melt interface consequent to $\sqrt{2}\times10^{-6}$ gal acceleration oriented parallel to the interface for the 3D case. The cross section is taken perpendicular to the ampoule axis. $\xi = 26\%$. The contour interval is 0.26.

$\xi = 26\%$. Thus, for this case, there was little difference between the 2D and 3D predictions (see table 3).

4.3. *Impulse-type accelerations*

Five cases of impulse-type disturbances were examined for a 2D geometry. All impulses were superimposed onto a steady background acceleration which was oriented parallel to the crystal–melt interface. The results are summarized in table 4.

Figs. 14a–14d illustrate the development of the solute field following a one second 5×10^{-3} gal impulse oriented anti-parallel to a background acceleration of 10^{-6} gal for operating conditions corresponding to A-V1. The effects are long lasting. The velocity field relaxes back to the initial state after some 300 s have elapsed. The response of the solute field is slower. The effect of the impulse is to initially re-orient the flow field. This has the effect of first reducing the lateral compositional nonuniformity. Thirty seconds after the termination of the impulse the composition nonuniformity is beginning to increase but has the opposite sense in comparison to the initial nonuniformity (see figs. 14a and 14b). At approximately 260 s after the termination of the impulse, ξ reaches a maximum value of 40%. It than slowly decreases in value (figs. 14c and 14d), reverses sense and eventually reaches its initial steady level (fig. 5b) after more than 2000 s have elapsed.

A shorter duration (10^{-1} s) pulse, with the same orientation and magnitude, resulted in a maximum deviation of the lateral nonuniformity of only 5% from the initial steady level 350 s after the termination of the pulse.

The effects of two one-second pulses separated by one second were also calculated. The magnitude of the pulses was 3×10^{-3} gal. They were oriented parallel to the crystal interface and superimposed onto a steady background acceleration of

Table 4
Summary of results for impulses

Magnitude (gal)	Duration (s)	ξ_{init}	ξ_{max}	ξ_{min}	τ_v (s)	τ_ξ (s)	τ_c (s)
5×10^{-3} (ap 10^{-6})	1	11	40	0	3–400	260	2200
3×10^{-3} (ap $\sqrt{2}\times10^{-6}$)	1	22	26	0	3–400	260	> 2000
3×10^{-3} (ap $\sqrt{2}\times10^{-6}$)	0.1	22	22	17	50	350	> 1000
3×10^{-3} (ap $\sqrt{2}\times10^{-6}$)	1*	22	76	17	3–450	225	> 2000
3×10^{-3} (ap $\sqrt{2}\times10^{-6}$)	1						
($\sqrt{2}\times10^{-6}$)	No pulse	22	24	22	300	100	> 1000
3×10^{-3} (p $\sqrt{2}\times10^{-6}$)	1						

ap and p denote a pulse anti-parallel and parallel to the background acceleration. All pulses are parallel to the crystal–melt interface. The background accelerations are given in parentheses and the asterisk denotes a 1 s pulse that was was repeated once after a 1 s interval.

The relaxation time τ_v refers to the decay time for the velocity field. τ_ξ denotes the time to reach the maximum value of ξ, and τ_c the time for the solute field to return to its initial steady state distribution.

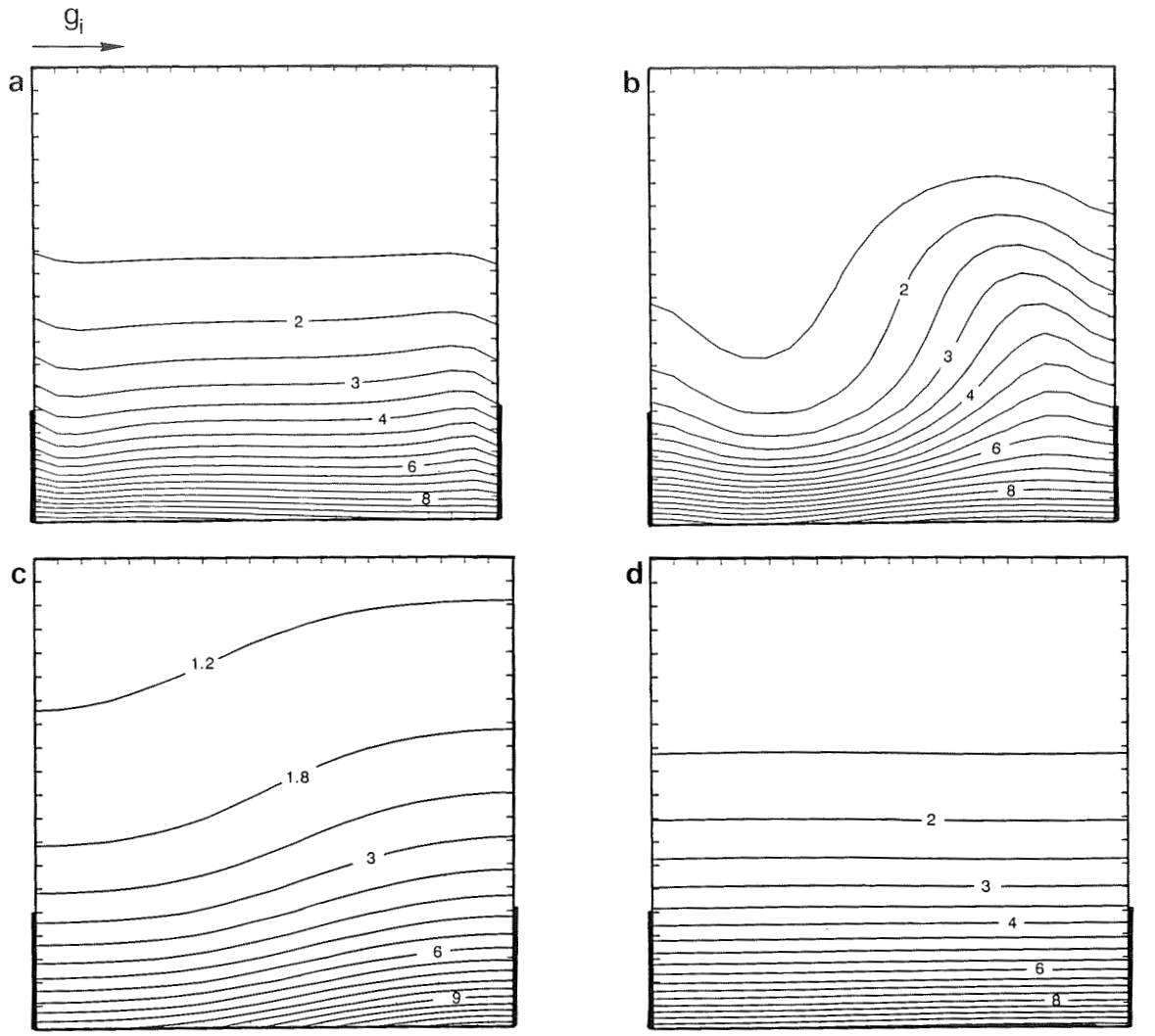

Fig. 14. The solute field after the termination of a one second duration 0.5×10^{-2} gal impulse ($\mathbf{g}_i$) oriented parallel to the crystal–melt interface and anti-parallel to a steady 10^{-6} gal background: (a) 1 s ($\xi = 11.3\%$), (b) 30 s ($\xi = 0.67\%$), (c) 250 s ($\xi = 40\%$) and (d) 1250 s ($\xi = 3.4\%$).

$\sqrt{2}\times10^{-6}$ gal oriented parallel to the interface. The main effect was to drive ξ from 21.5% (the initial value) to 76% after 225 s.

In addition, double pulses were examined. A pulse anti-parallel to the background steady acceleration followed by an equal but opposite pulse does not result in a "null" effect. While the flow generated by the first pulse is reversed by the second pulse there is a net flow following the termination of the second pulse. This flow is in the same sense as the initial steady flow and results in an increase of the lateral non-uniformity in composition to a maximum of 24% at 100 s, whereupon it decays slowly to its initial value.

5. Summary and discussion

The effects on dopant uniformity during directional solidification of steady and impulse-type

residual accelerations have been calculated using 2D and 3D "generic" models of the Bridgman–Stockbarger crystal growth technique. The salient results of our calculations for materials with properties and growth conditions corresponding to those listed in table 2 can be summarized as follows:

For a fixed growth rate, the amount of lateral non-uniformity in composition is very sensitive to the orientation of the steady component of the residual gravity vector. The worst case appears to be when the acceleration vector is parallel to the crystal interface. At growth rates on the order of microns per second, this orientation can lead to non-uniformities of 10–20% when the magnitude of the acceleration is 10^{-6} gal. If, however the growth rate is lowered by an order of magnitude, the non-uniformity is reduced significantly. A steady background level on the order of 10^{-6} gal can be tolerated for a wide range of the operating conditions examined provided that the acceleration vector is *aligned with the axis of the growth ampoule*.

When $\boldsymbol{g}$ is oriented parallel to the crystal–melt interface, the maximum compositional non-uniformity occurs between 10^{-4} and 10^{-5} gal compared to 10^{-2} gal for the axisymmetric case. It is evident upon examination of table 3 and figs. 3–7 that for a given orientation the relationship between the magnitude of the gravity vector and the amount of compositional non-uniformity is clearly not linear. (This result was first obtained by Chang and Brown [13] for the axisymmetric case.)

The effect of a reduction in growth rate on the velocity profile is to shift the center of the convective roll (see figs. 9a and 3a). This can be explained in terms of the superposition of the uniform solidification flow and a single convective roll. When convective velocities have the same order of magnitude as the solidification velocity the roll center is shifted to one side because only here does the addition of the convective and uniform solidification flow result in no motion.

For the cases examined, a reduction in compositional non-uniformity was also associated with a reduction in $T_H - T_M$. The presence of the adiabatic zone results in lateral as well as axial temperature gradients. Thus, convection always occurs in this system since there is always a location where the temperature gradient has a component normal to the acceleration vector. We compared our results with those of Chang and Brown's axisymmetric calculations [13]. Our 3D axisymmetric computations were found to be in agreement with their work. In addition we carried out full 3D (*non-axisymmetric*) steady calculations in order to calibrate our 2D results. For one set of examples we found that with $\sqrt{2} \times 10^{-5}$ gal parallel to the interface the percentage compositional non-uniformity predicted by the 2D calculation ($\xi = 152\%$) was 50% higher than predicted by the full 3D calculation. This difference may be attributed to the increased surface to volume ratio which increases the effect of the "no-slip" boundary condition. The presence of the rigid walls somewhat retards the flow and, thus, in comparison to the 2D case, the degree of solute redistribution is decreased. A comparison between 2D and 3D calculations for $\sqrt{2} \times 10^{-6}$ gal revealed no significant difference in ξ. At this magnitude of the gravity vector, convection is localized and weak. The increase in surface to volume ratio for this 3D case thus has little influence on the transport conditions.

There are some instances in the literature where radially or laterally averaged *crystal* composition profiles are used to compare space and earth grown samples [32–33]. In their interpretation of laterally averaged composition profiles in earth- and space-grown Ge : Ga crystals [32], Witt et al. concluded that for the space-grown crystal, convection was absent during growth. The theory of Tiller et al. [34], which considers only diffusion, gives a characteristic distance $z^* = D/kV$ at which the crystal composition reaches a value given by $c^* = c_0[1 - (1 - k)e^{-1}]$. The distance at which this composition was reached in the earth- and space-grown samples was compared with the theoretical distance z^*. Given the uncertainty associated with the relevant physical properties and the fact that the growth rate was not constant (as assumed in the theory of Tiller et al.), a range was given for the theoretical distance z^*. It was found that for the space-grown sample the measured characteristic distance fell within this range. The composition c^* was not reached in the earth-grown

sample. Thus, it seems appropriate to argue that convective transport is absent if the measured characteristic distance is equal to z^*. However, an analogous argument applied to the averaged melt composition profiles of figs. 8 and 11 leads us to a different conclusion. It has been proposed [35,36] that an appropriate measure of the influence of convective transport is the ratio, Δ, of the solute boundary layer thickness δ to the characteristic distance D/V_M. Corresponding transport regimes are then defined as [35,36]:

$\Delta \ll 1$: convective,
$\Delta = 1$: convective-diffusive,
$\Delta > 1$: diffusive.

As a working definition we take δ to be the distance from the interface where the rate of change of concentration gradient becomes small and evaluate Δ for the profiles given in figs. 8 and 11. In fig. 11, the approximate values of Δ range from 1 (Sc = 10) to 0.75 (Sc = 40). For all the profiles in figs. 8, which are virtually indistinguishable from the purely diffusive profiles, Δ is greater than 1. However, the profiles shown in fig. 8a are associated with significant lateral compositional non-uniformity that arises due to convection. Thus, even when the laterally averaged *melt* composition profiles have so-called diffusive (longitudinal) profiles, it may not be safe to assume that convection was absent. Thus, we propose that radially or laterally averaged composition profiles are alone insufficient to describe the extent of residual convection during solidification in a spacecraft environment.

The effects of impulse-type disturbances can be severe and can extend for a long time (on the order of 10^3 s) after the termination of the impulse. This is not surprising if one considers characteristic times for momentum and solute diffusion given by $t_m = L^2/\nu$ and $t_s = L^2/D$, respectively. For $L = 0.5$ cm (corresponding to the maximum distance from a wall in the 2D system considered) these characteristic times are $t_m \sim 200$ s, and $t_s \sim 2000$ s, which compare well with the order of magnitude of the decay times given in table 4. At growth rates of 6.5 μm s^{-1}, a pulse with a second duration, or a combination of such pulses has a drastic effect on the segregation levels at pulse amplitudes of 10^{-3} gal. The nature of the response depends on the magnitude, direction and duration of the impulse, and whether sequential, opposing impulses are involved. A so-called "compensating" double pulse will not result in completely offsetting effects. For the case we examined, however, the resulting compositional non-uniformity was not as severe as for sequential pulses with the same orientation. It should also be considered that the response will depend on the particular operating conditions employed. For example, the response to steady acceleration was shown to vary with the growth rate, and a similar dependence may exist for impulses. This remains to be verified. Further investigation of more realistic impulses (g-jitter) is necessary since the response of the system appears to depend on the nature of the impulse and our results indicate that impulses appear to have important consequences for transient behavior in crystal growth systems.

In addition to the results obtained for Ge : Ga, we have also examined the effects of different physical properties by examining a range of Schmidt numbers. Our results show that, for a given steady acceleration the sensitivity of the process also depends on the operating conditions and the physical properties of the melt. That is, the sensitivity to the residual acceleration depends on temperature conditions, the growth rate, and the ratio of the kinematic viscosity to the solute diffusivity. The fact that in a spacecraft buoyancy forces may be reduced by 5–6 orders of magnitude does not imply that the environment may be considered purely diffusive. Careful evaluation of the interaction between the operating conditions, physical properties and spacecraft acceleration environment must be made in order to ensure optimum use of limited spaceflight opportunities.

Space flight experiments involving germanium have been carried out on Skylab [32,33,37] and the Apollo–Soyuz Test Project (ASTP) [38,39]. The latter involved the directional solidification of seeded Ge melts. Melts were doped with galium and some were doped with 1% Si and 0.001% Sb [39]. These results have generated some controversy [1]; lateral compositional profiles revealed strong asymmetric non-uniformities in the space grown crystals. Lateral variations were also

observed in samples grown under terrestrial conditions but were much less pronounced [1]. In order to explain these observations it has been argued that the asymmetric redistribution of the dopant can be ascribed to "barometric diffusion" of the solutes due to the acceleration gradient in the melt arising from the rotational motion of the spacecraft [38,39]. The basis of the argument, however, appears to ignore the presence of gravity gradient and atmospheric drag effects and does not explicitly account for the spacecraft attitude motions. If it is assumed that during this phase of the ASTP mission the spacecraft flew in a radial attitude [9] (i.e. it continuously rotated relative to a fixed geocentric frame), then a steady residual acceleration vector would result from the gravity gradient, atmospheric drag and centrifugal contributions to the relative acceleration. It has been demonstrated in this work that melt convection can occur in response to a steady residual acceleration of rather small magnitudes. Furthermore, whenever the acceleration vector is not aligned with the ampoule axis strong asymmetries in the solute composition profiles can occur. Since the dependence of composition uniformity on convection is not linear, and since small asymmetries in temperature profiles can lead to asymmetric convection [40], there is always the possibility that the observed non-uniformities in the terrestrially grown samples will be smaller than those observed in space grown samples. Thus, the probability that the strong asymmetries in composition observed in the space-grown samples can be attributed to residual acceleration effects should not be discounted.

It should be emphasized that while some of the conditions examined have shown great sensitivity to residual acceleration, we have also shown that there are combinations of operating conditions for which the effects of realistic residual acceleration levels are small. It is therefore clear that residual gravity effects should be seriously considered when planning optimal operating conditions for space experiments. Furthermore, since our results are generic in nature they cannot be substituted for a detailed numerical examination of a particular Bridgman-type crystal growth system, although they can be expected to indicate trends in the expected response to the steady residual acceleration environment. As far as the response to time-dependent accelerations is concerned, impulses have been shown to be important, but more work is needed in this area, especially in terms of a more realistic representation of the residual acceleration vector. Continuous periodic accelerations are also a concern [21], particularly in the low frequency range ($\sim 10^{-3}$ Hz) and will be examined in a companion paper [41].

Acknowledgements

This work was supported by the National Aeronautics and Space Administration under grant NAG8-684, by the State of Alabama through the Center for Microgravity and Materials Research at the University of Alabama in Huntsville, and through the Alabama Supercomputer Network. We would like to thank Dr. Robert Naumann for stimulating our interest in this problem.

References

[1] D.T.J. Hurle, G. Müller and R. Nitsche, in: Fluid Sciences and Materials Science in Space, A European Perspective, Ed. H.U. Walter (Springer, Berlin, 1987) p. 315.
[2] F. Rosenberger, Fundamentals of Crystal Growth I, Springer Series in Solid-State Sciences, Vol. 5 (Springer, Berlin, 1979).
[3] R.F. Sekerka and S.R. Coriell, in: Proc. 3rd European Symp. on Materials Sciences in Space, Grenoble, April 1979 [ESA SP-142 (1979) 55].
[4] S.M. Pimputkar and S. Ostrach, J. Crystal Growth 55 (1981) 614.
[5] G. Müller, in: Convective Transport and Instability Phenomena, Eds. J. Zierep and H. Oertel (Braun, Karlsruhe, 1982) p. 441.
[6] G. Müller, G. Neumann and W. Weber, J. Crystal Growth 70 (1984) 78.
[7] W.E. Langlois, Ann. Rev. Fluid Mech. 17 (1985) 191.
[8] H. Hamacher, R. Jilg and U. Mehrbold, in: Proc. 6th European Symp. on Materials Sciences under Microgravity Conditions, Bordeaux, December 1986 [ESA SP-256 (1987) 413].
[9] J.I.D. Alexander and C.A. Lundquist, J. Astronautical Sci. 35 (1987) 193.
[10] J.I.D. Alexander and C.A. Lundquist, AIAA J. 26 (1988) 193.

[11] P.A. Clark and W.R. Wilcox, J. Crystal Growth 50 (1980) 461.
[12] N. Kobayashi and W.R. Wilcox, J. Crystal Growth 59 (1982) 616.
[13] C.J. Chang and R.A. Brown, J. Crystal Growth 63 (1983) 353.
[14] G.B. McFadden, R.G. Rehm, S.R. Coriell, W. Clark and K.A. Morrish, Met. Trans. A15 (1984) 2125.
[15] P.M. Adornato and R.A. Brown, J. Crystal Growth 80 (1987) 155.
[16] D.H. Kim, P.M. Adornato and R.A. Brown, J. Crystal Growth 89 (1988) 339.
[17] Y. Kamotani, A. Prasad and S. Ostrach, AIAA J. 19 (1981) 511.
[18] V.I. Polezhaev, Hydrodynamics, heat and mass transfer during crystal growth, in: Crystals, Vol. 10, Ed. H.C. Freyhardt (Springer, Berlin, 1984).
[19] V.I. Polezhaev, A.P. Lebedev and S.A. Nikitin, in: Proc. 5th European Symp. on Materials Sciences under Microgravity, Schloss Elmau (ESA SP-222 (1984) 237].
[20] D. Camel and J.J. Favier, J. Physique 47 (1986) 1001.
[21] R. Monti, J.J. Favier and D. Langbein, in: Fluid Sciences and Materials Science in Space, A European Perspective, Ed. H.U. Walter (Springer, Berlin, 1987) o. 637.
[22] G.B. McFadden and S.R. Coriell, in: Proc. AIAA/ASME/SIAM/APS 1st National Fluid Dynamics Congress, Cincinnati, July 1988, p. 1572.
[23] A. Rouzaud, D. Camel and J.J. Favier, J. Crystal Growth 73 (1985) 149.
[24] Y.M. Dakhoul, R. Farmer, S.L. Lehoczky and F.R. Szofran, J. Crystal Growth 86 (1988) 49.
[25] S.R. Coriell and R.F. Sekerka, J. Crystal Growth 46 (1979) 479.
[26] S.R. Coriell, R.F. Boisvert, R.G. Rehm and R.F. Sekerka, J. Crystal Growth 54 (1981) 167.
[27] R. Peyret and T.D. Taylor, Computational Methods for Fluid Flow (Springer, New York, 1983).
[28] H.I. Rosten and D.B. Spalding, in: Lecture Notes in Engineering, Vol. 18, Eds. C.A. Brennia and S.A. Orszag (Springer, New York, 1986) p. 3.
[29] J. Ouazzani and R. Peyret, in: Proc. 5th GAMM Conf. on Numerical Methods in Fluid Mechanics, Rome, October 1983, Eds. M. Pandolfi and R. Piva (Vieweg, Braunschweig, 1983) p. 275.
[30] J. Ouazzani, A new iterative method for unsteady incompressible fluid flows using a collocation pseudo-spectral technique, to be published.
[31] S.V. Patankar, Numerical Heat Transfer and Fluid Flow (Hemisphere, Washington, 1980).
[32] H.C. Gatos, in: Materials Processing in the Reduced Gravity Environment of Space, Mater. Res. Soc. Symp. Proc., Vol. 9, Ed. G.E. Rindone (North-Holland, New York, 1982) p. 355.
[33] A.F. Witt, H.C. Gatos, M. Lichtensteiger, M.C. Lavine and C.J. Herman J. Electrochem Soc. 125 (1975) 276.
[34] W.A. Tiller, K.A. Jackson, J.W. Rutter and B. Chalmers, Acta Met. 1 (1953) 428.
[35] A. Rouzaud, D. Camel and J.J. Favier, J. Crystal Growth 73 (1985) 149.
[36] J.J. Favier, Acta Metall. 28 (1981) 197, 205.
[37] J.T. Yue and F.W. Voltmer, J. Crystal Growth 29 (1975) 329.
[38] V.S. Zemskov, Soviet Phys.-Dokl. 22 (1977) 170.
[39] V.S. Zemskov, I.L. Shul'pina, A.N. Titkov, I. Belokurova, N.B. Guseva and V.I. Safarov, Soviet Phys. Solid State 21 (1979) 576.
[40] St. Krukowski, J.I.D. Alexander, J. Ouazzani and F. Rosenberger, Convection in an asymmetrically heated ampoule, to be published.
[41] J.I.D. Alexander, J. Ouazzani and F. Rosenberger, Analysis of the low gravity tolerance of Bridgman–Stockbarger crystal growth. II. Transient and periodic accelerations, in preparation.

Center for Microgravity and Materials Research
The University of Alabama in Huntsville